1

PM-1 3½"x4" PHOTOGRAPHIC MICROCOPY TARGET
NBS 1010a ANSI/ISO #2 EQUIVALENT

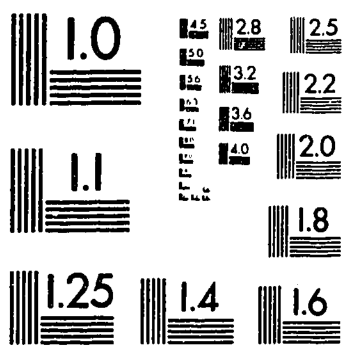

PRECISION℠ RESOLUTION TARGETS

National Library of Canada

Bibliothèque nationale du Canada

Acquisitions and Bibliographic Services Branch

Direction des acquisitions et des services bibliographiques

395 Wellington Street
Ottawa, Ontario
K1A 0N4

395, rue Wellington
Ottawa (Ontario)
K1A 0N4

Your file Votre référence

Our file Notre référence

NOTICE

The quality of this microform is heavily dependent upon the quality of the original thesis submitted for microfilming. Every effort has been made to ensure the highest quality of reproduction possible.

If pages are missing, contact the university which granted the degree.

Some pages may have indistinct print especially if the original pages were typed with a poor typewriter ribbon or if the university sent us an inferior photocopy.

Reproduction in full or in part of this microform is governed by the Canadian Copyright Act, R.S.C. 1970, c. C-30, and subsequent amendments.

AVIS

La qualité de cette microforme dépend grandement de la qualité de la thèse soumise au microfilmage. Nous avons tout fait pour assurer une qualité supérieure de reproduction.

S'il manque des pages, veuillez communiquer avec l'université qui a conféré le grade.

La qualité d'impression de certaines pages peut laisser à désirer, surtout si les pages originales ont été dactylographiées à l'aide d'un ruban usé ou si l'université nous a fait parvenir une photocopie de qualité inférieure.

La reproduction, même partielle, de cette microforme est soumise à la Loi canadienne sur le droit d'auteur, SRC 1970, c. C-30, et ses amendements subséquents.

Canada

UNIVERSITY OF ALBERTA

A Vortex Lattice Method in the Solution of Three Problems in Three Dimensional Aerodynamics: Winglet Performance, Vortex Sheet Roll-Up, and Anti-Icing Fluid Deposition on Runways

BY

CRAIG STA, ..EY MERKL ©

A thesis submitted to the Faculty of Graduate Studies and Research in partial fulfillment of the requirements for the degree of **Doctor of Philosophy**.

DEPARTMENT OF **Mechanical Engineering**

Edmonton, Alberta

FALL 1995

National Library of Canada
Bibliothèque nationale du Canada

Acquisitions and Bibliographic Services Branch
Direction des acquisitions et des services bibliographiques

395 Wellington Street
Ottawa, Ontario
K1A 0N4

395, rue Wellington
Ottawa (Ontario)
K1A 0N4

Your file Votre référence

Our file Notre référence

THE AUTHOR HAS GRANTED AN IRREVOCABLE NON-EXCLUSIVE LICENCE ALLOWING THE NATIONAL LIBRARY OF CANADA TO REPRODUCE, LOAN, DISTRIBUTE OR SELL COPIES OF HIS/HER THESIS BY ANY MEANS AND IN ANY FORM OR FORMAT, MAKING THIS THESIS AVAILABLE TO INTERESTED PERSONS.

L'AUTEUR A ACCORDE UNE LICENCE IRREVOCABLE ET NON EXCLUSIVE PERMETTANT A LA BIBLIOTHEQUE NATIONALE DU CANADA DE REPRODUIRE, PRETER, DISTRIBUER OU VENDRE DES COPIES DE SA THESE DE QUELQUE MANIERE ET SOUS QUELQUE FORME QUE CE SOIT POUR METTRE DES EXEMPLAIRES DE CETTE THESE A LA DISPOSITION DES PERSONNE INTERESSEES.

THE AUTHOR RETAINS OWNERSHIP OF THE COPYRIGHT IN HIS/HER THESIS. NEITHER THE THESIS NOR SUBSTANTIAL EXTRACTS FROM IT MAY BE PRINTED OR OTHERWISE REPRODUCED WITHOUT HIS/HER PERMISSION.

L'AUTEUR CONSERVE LA PROPRIETE DU DROIT D'AUTEUR QUI PROTEGE SA THESE. NI LA THESE NI DES EXTRAITS SUBSTANTIELS DE CELLE-CI NE DOIVENT ETRE IMPRIMES OU AUTREMENT REPRODUITS SANS SON AUTORISATION.

ISBN 0-612-06260-0

Canada

UNIVERSITY OF ALBERTA
LIBRARY RELEASE FORM

NAME OF AUTHOR: **CRAIG STANLEY MERKL**

TITLE OF THESIS: **A Vortex Lattice Method in the Solution of Three Problems in Three Dimensional Aerodynamics: Winglet Performance, Vortex Sheet Roll-Up, and Anti-Icing Fluid Deposition on Runways**

DEGREE: **Doctor of Philosophy**

YEAR THIS DEGREE GRANTED: **1995**

Permission is hereby granted to the University of Alberta Library to reproduce single copies of this thesis and to lend or sell such copies for private, scholarly or scientific research purposes only.

The author reserves all other publication and other rights in association with the copyright in the thesis, and expect as hereinbefore provided neither the thesis nor any substantial portion thereof may be printed or otherwise reproduced in any material from whatever without the author's prior written permission.

Craig Merkl

Box 396
Brooks, Alberta
Canada T1R 1B4

Date October 05, 1995

UNIVERSITY OF ALBERTA

FACULTY OF GRADUATE STUDIES AND RESEARCH

The undersigned certify that they have read, and recommend to the Faculty of Graduate Studies and Research for acceptance, a thesis entitled **A Vortex Lattice Method in the Solution of Three Problems in Three Dimensional Aerodynamics: Winglet Performance, Vortex Sheet Roll-Up, and Anti-Icing Fluid Deposition on Runways** submitted by **CRAIG STANLEY MERKLE** in partial fulfillment of the requirements for the degree of **Doctor of Philosophy**.

Dr. L. W. Sigurdson, Co-Supervisor
Professor, Mechanical Engineering

Dr. D. J. Marsden, Co-Supervisor
Professor Emeritus, Mechanical Engineering

Dr. R. W. Toogood
Professor, Mechanical Engineering

Dr. J. W. Yokota
Professor, Mechanical Engineering

Dr. N. Rajaratnam
Professor, Civil Engineering

for

Dr. R. J. Kind, External
Professor, Mechanical and Aerospace Engineering
Carleton University

Date 4 Oct 1995

Dedication

This thesis is dedicated to my Grandfather Steve Merkl, Sr. who has always been supportive of my attendance at university. Even though he never went to university or even knew all that was involved in the pursuit of a university degree, he has recognized the value of education. His influence began early, when as a child he challenged me to addition problems, something I recall enjoying and is likely responsible for my interest in math, science, and learning.

ABSTRACT

A simplified vortex lattice method (VLM) is used to gain additional insight into three problems in three dimensional aerodynamics. A literature review examines vortex systems pertaining to lifting wings of moderate aspect ratio and the design of winglets for aircraft wing tips. The VLM is used to investigate winglets with the focus being to determine the mechanism by which winglets produce a drag reduction. This drag reduction is shown to be due to both a forward thrust on the winglet and an induced drag reduction on the main wing. The magnitude of the forward thrust component is shown to vary significantly with winglet size and wing lift coefficient. Then the vortex sheet roll-up behind a lifting wing is considered using the VLM. The emphasis is on the effect of the boundary layer thickness on the wing and consequently the vortex sheet thickness on the developing vortex core. As well, the stretching and thinning of the vortex sheet in the vicinity of the core is demonstrated using multiple rows of vortices to represent the vortex sheet thickness. As a final application of the VLM, the topic of anti-icing fluid distribution on airport runways is considered. Three aircraft which are typically used in Canada during anti-icing fluid usage are modelled. The flow-off of the anti-icing fluid during the take-off ground roll results in anti-icing fluid being distributed on the runway. The calculations show the amount and distribution of the fluid deposition on and near the runway, along with the amount of anti-icing fluid which remains airborne.

Acknowledgements

Thanks to Dr. D.J. Marsden for his patient supervisory role and his many hours of openness in discussion with me about all facets of aerodynamics, aeronautics, and flight. This I'm sure springs from his understanding of the passion for flying. Also, appreciation is extended to Dr. L.W. Sigurdson, Dr. R.W. Toogood, and my many valuable friends who encouraged me forth toward completion of this thesis.

I also wish to thank my parents, especially Dad, for the way they taught me to learn to function and to think for myself. To Dad who instilled in me the philosophy to do things right the first time, so that you do not have to repeat the work. Dad has been a good model to look up to ... doing everything well and teaching integrity by his example. Also, I thank my parents who always have recognized the importance of friends through life. (Dad said once how he was happy living in and farming at Brooks because that was where his friends were.) Their love for their friends has been demonstrated by their continual effort to stay in touch with and continue to visit people that they have known over the years.

I give thanks to Jesus Christ, for His continuing love as my personal saviour, and for the ability and guidance to be able to attend the University of Alberta and to complete this thesis.

Table of Contents

List of Tables

List of Figures

List of Symbols for Chapter 2

a	radius of Rankine vortex core, m
A_R	aspect ratio of wing
b	wing span, m
b'	trailing vortex separation
C_D	drag coefficient
C_{Di}	coefficient of induced drag
ΔC_{Di}	change in induced drag coefficient
C_ℓ	local airfoil lift coefficient
C_L	wing lift coefficient
$dC_L/d\alpha$	lift curve slope, radian^{-1}
C_N	normal force coefficient of winglet
C_P	pressure coefficient
D	total drag, N
D_i	induced drag, N
ΔD_i	change in induced drag, N
d_{rup}	distance for vortex to roll up, m
e	induced efficiency factor
F_T	forward thrust component of winglet, N
ℓ	lift of incremental spanwise section of wing, N/m
L	lift, N
L/D	lift - drag ratio
$(L/D)_{max}$	maximum lift - drag ratio
M	Mach Number
P, P_o	local and stagnation pressure, N/m^2
n	number of vortex cores
r	radius from center of vortex, m
r_n	radius from center of vortex #n, m
r'	radius of viscous core of vortex, m
R	the radius for the fully developed vortex core within which all of the vorticity from each wing is contained
Re	Reynolds number
t	time, s
t_{rup}	time for vortex roll up, s
t^*	a dimensionless measure of time in a vortex flow
V, V_o	aircraft or freestream velocity, m/s
v_{dec}	velocity of descent of a vortex, m/s
$\bar{v}_{ind}$	induced velocity, m/s
v_{tan}	tangential velocity in vortex, m/s
v_{tot}	total velocity in vortex, m/s
x	x coordinate (streamwise), m
y	y coordinate (spanwise), m
$\bar{y}$	spanwise location of the centroid of vorticity shed by the wing outboard of the spanwise location y, m
$\bar{y}_t$	the spanwise location of the centroid of vorticity for the wing semi-span

GREEK SYMBOLS

α	angle of attack, degrees
β	angle of vortex core with respect to the helix axis, degrees
Γ	circulation of a vortex, m^2/s
$\Gamma(y)$, $\Gamma(\eta)$	spanwise distribution of circulation, m^2/s
$\Gamma'(r)$, $\Gamma'(\rho)$	radial distribution of circulation in an evolving trailing vortex system, m^2/s
Γ_o	total circulation of vortex or the total circulation for the semi-span, m^2/s
η	a dummy variable for y the semi-spanwise location
μ	absolute viscosity of air, kg/m s
ν	kinematic viscosity of air, μ/ρ, m^2/s
ρ	a dummy variable for the radial distance from the center of the evolving vortex core whose radius is indicated by r; or the density of the fluid or air, kg/m^3.

List of Symbols for Chapter 3

A_R	aspect ratio of wing
b	wing span, m
$c(y)$	wing chord at spanwise location y, m
c_r	root chord, m
c_t	tip chord, m
C_D	drag coefficient for wing, or the drag coefficient for the airfoil section
C_{dmin}	minimum drag coefficient for the airfoil section
C_{dfac}	drag coefficient factor for the airfoil section
C_L	total lift coefficient for wing
C_ℓ	local 2-D airfoil lift coefficient
$C_{\ell Cdmin}$	lift coefficient corresponding to the minimum drag coefficient for the airfoil section
$C_{\ell max}$	maximum local 2-D airfoil lift coefficient
$C_{\ell o}$	local 2-D aifoil lift coefficient at $\alpha = 0°$
$C_{\ell\alpha}$	$= dC_\ell/d\alpha$, local 2-D lift curve slope, radian^{-1}
ΔC_{Di}	change in induced drag coefficient of wing
C_{Dp}	profile drag coefficient of wing
ΔC_{DTotal}	change in total drag coefficient of wing
$D(s)$	drag along the arclength s of a wing
D_{Total}	total drag of wing
D	drag force, N
e	effictive aspect ratio factor.
$l(y)$	local lift per unit span, N/m
L	lift, N
L/D	lift to drag ratio
$\Delta L/D$	change in lift to drag ratio
r	the distance vector from a vortex element to the point being considered on the bound vortex arc, or the radius from the center of a vortex, m
r'	radius of core (i.e. to maximum v_{tan}) of Rankine vortex, m
s	arclength coordinate along a wing, or the distance around a circuit of a contour integral, m
Δt	time increment, s
V, $V(y)$	aircraft velocity, or air velocity, m/s
$v_{normal}(y)$	velocity normal to the local wing section, m/s
v_{tan}	tangential velocity in vortex, m/s
x_p, y_p, z_p	(x,y,z) coordinate of point P
x_v, y_v, z_v	(x,y,z) coordinate of vortex
x	x coordinate (streamwise), m
y	y coordinate (spanwise), m
z	z coordinate (vertical), m

Greek Symbols

α	local angle of attack of wing section, degrees
α_{init}	local angle of attack of wing section before induced velocity is added, degrees
β_1	angle to one end of vortex element
β_2	angle to second end of vortex element
$\gamma(y)$	trailing vortex filament circulation, m^2/s
Γ, $\Gamma(y)$	circulation of a line vortex, circulation of a bound vortex element, or the local circulation of a vortex, m^2/s
Γ_o	centerline or total circulation of vortex, m^2/s
ϵ	downwash angle, degrees
ρ, ρ_{air}	density of air, kg/m^3
$\underline{\omega}$	vorticity vector
Ω_Σ	vorticity intensity vector of an area of vortex sheet

List of Symbols for Chapter 4

a	radius of Rankine vortex core, m
b	wing span, m
b.l.t.	boundary layer thickness, m
C_D	drag coefficient
C_L	lift coefficient
D_i	induced drag, N
ΔD_i	change in induced drag, N
I_p	2nd moment of vorticity about the centroid of vorticity for the semi-span
$I_{p'}$	2nd moment of vorticity about the centroid of vorticity of an emerging vortex core
I_y	2nd moment of vorticity about the y axis
$I_{y'}$	2nd moment of vorticity about the y' axis through the centroid of vorticity of an emerging vortex core
I_z	2nd moment of vorticity about the z axis
$I_{z'}$	2nd moment of vorticity about the z' axis through the centroid of vorticity of an emerging vortex core
L	lift, N
r	radius from center of vortex, m
r'	radius to maximum v_{tan} of vortex, m
r^*	radius to v_{tan} corresponding to potential vortex, m
t	time, s
Δt	time step, s
u_{tan}	tangential velocity in vortex, m/s
u_θ	tangential velocity in vortex, m/s
V	aircraft velocity, m/s
v.s.t.	vortex sheet thickness, m
v_{tan}	tangential velocity in vortex, m/s
$v_{tan\text{-}max}$	maximum tangential velocity in vortex, m/s
x	x coordinate (streamwise), m
y	y coordinate (spanwise), m
z	z coordinate (vertical), m

GREEK SYMBOLS

α	angle of attack, degrees
γ_{max}	maximum value of the discretized shed vorticity, m^2/s
Γ	circulation of vortex, m^2/s
Γ_o	total circulation of vortex, m^2/s
ρ	density of air, kg/m^3

List of Symbols for Chapter 5

C_D	drag coefficient
C_L	local 2-D spanwise lift coefficient; or total lift coefficient
C_{Lmax}	maximum local 2-D lift coefficient
C_{Lo}	local 2-D lift coefficient at $\alpha = 0°$
$dC_L/d\alpha$	local 2-D lift curve slope, radian^{-1}
D	drag force, N
D_{drop}	diameter of drop, m
dm/dt	anti-icing fluid mass flow-off rate, kg/s
$dVol/dt$	anti-icing fluid volume flow-off rate, m^3/s
$l(y)$	local lift per unit span, N/m
q	dynamic pressure, $q = ½ \rho V_{rel}^2$
R_e	Reynolds number
s	distance around a circuit of a contour integral, m
t	time, s
Δt	time increment, s
V	air velocity, m/s
V_R	rotation speed of aircraft, m/s
V_{rel}	relative velocity of drop to air, m/s
V_S	stall speed of aircraft, m/s
x	x coordinate (streamwise), m
y	y coordinate (spanwise), m
z	z coordinate (vertical), m

Greek Symbols

α	angle of attack, degrees
$\Gamma(y)$	local circulation of vortex, m^2/s
Γ_o	centerline or total circulation of vortex, m^2/s
μ_{air}	absolute viscosity of air, kg/m s
δ_f	flap deflection angle, degrees (downward positive)
ρ_{air}	density of air, kg/m^3

CHAPTER 1

INTRODUCTION

1.1 Overview of the Problems

The research presented here involves the use of a simplified vortex lattice method (VLM) for the solution of various three dimensional aerodynamics related problems. This study shows that engineering problems can be treated with a relatively simple numerical technique to give solutions of engineering significance. The first part deals with a literature review of vortex systems and focuses on the design and analysis of winglets as applied to the aircraft wing tips. The VLM computer model is then applied to the actual case of winglets on aircraft wings. The use of even a vortex lattice model produces insight regarding the mechanism of the drag reduction produced by winglet application on a wing. The winglet problem is considered using a rigid wake (i.e. the vortex sheet not rolling up). The problem of the roll-up of a finite thickness vortex sheet to account for the wing boundary layer is discussed in the next part. Insight is provided into the vortex sheet roll-up process using a multiple row vortex model to allow for vortex sheet stretching and thinning during the roll-up. In the final part, the vortex lattice method is used to model the rolling up of the vortex wake and the movement of anti-icing fluid in the wake during a take-off ground run. The model handles the complex geometry of three commercial transport aircraft in the take-off configuration. Then the computer model determines the movement in the aircraft wake and the final ground deposition of anti-icing fluid which flows off the aircraft wings.

A necessary starting point for any research endeavor involves uncovering what has already been discovered. This involves a literature survey of past works. In the recent past, there have been several very good reviews of vortex systems and simulation of vortical flows (examples are: George (1985) and Sarpkaya (1989)). For one of the best reviews, the reader is referred to the paper by Sarpkaya (1989). Instead of repeating that work, the review which is presented here is an attempt to highlight significant contributions concerning the study of vortex systems, the trailing vortex wake, and winglets.

The first of the problems considered is the application of the VLM computer program to determine the mechanism by which winglets on a wing produce drag reductions. Winglets are currently used on numerous aircraft and can be shown to produce performance benefits. This problem is considered in the third chapter since the literature review showed that throughout all of the numerical and experimental work that has been done examining winglets, the drag reduction mechanism is still poorly understood. Specifically, this work was prompted by the lack of a clear understanding of the reason that a winglet on a wingtip can produce a drag reduction, and hence how to optimize a winglet design for a given wing. The computer program uses a vortex lattice method which is an inviscid, incompressible, potential flow fluid model. In addition, viscous effects (excluding separation) *are* included by way of a calculation of the profile drag of the airfoil sections along the wing span. This is done by calculating the profile drag based on the the local wing section lift coefficient and applying the relation for the C_D-C_L from the airfoil drag polar. This provides a reasonable ability to compare the relative importance of the profile drag and the induced drag components. The drag reduction produced by a winglet is then quantified and the components of the drag reduction are clearly demonstrated.

Numerical modelling of airfoils, wings, and vortex sheets has been the subject of much work over the years. Methods vary from point vortex methods, to Cloud in Cell (CIC), to vortex panel methods, and others. Yet with the availability of all of the methods and the vastly increasing computational power, there is yet to be shown a clear and accurate method for the vortex sheet roll-up into the developing core region behind a lifting wing. This study considers the boundary layer thickness, and consequently the vortex sheet thickness, since there does not exist a clear link between the wing boundary layer and the developing core behind the lifting wing. Thus, the fourth chapter uses the vortex lattice method to specify an elliptical wing loading, and then to examine the problem of the roll up of the vortex sheet behind the lifting wing. The vortex core development is determined with consideration given to the boundary layer thickness on the wing which is assumed to affect the vorticity distribution through the boundary layer and hence the shed vortex sheet thickness. The use of multiple rows of vortices to represent the vortex sheet provides insight into the phenomenon of vortex sheet stretching and thinning which is observable near the developing trailing vortex core region, as well as the sequence of roll-up of the upper and lower portion of the vortex sheet.

The trailing vortex wake has much significance since current air traffic is constrained by the need for sufficient spacing between aircraft to allow the trailing vortex system to lose its intensity and its danger. This requirement for spacing is a consideration during all phases of flight, but is especially true in the take-off and landing phases. The importance of the velocity distribution through a vortex core has to do with the maximum tangential velocity and the vortex core size. The maximum tangential velocity in a vortex core determines the roll rate of an aircraft intercepting a trailing vortex, particularly if the encountering aircraft is much smaller than the aircraft creating the vortex system. During the 1970s much research focused on the trailing vortex wake and methods of alleviation, without a great deal of success. Although vortex roll-up was not completely understood, the lack of funding seems to have led to reduced research concerning the trailing vortex hazard. Now again in the 1990s, the problems of air traffic congestion have revitalized the study of the trailing vortex hazard, and the need for greater understanding of the trailing vortex core development and structure.

Chapter five examines the movement of anti-icing fluid in the trailing vortex wake of aircraft during the ground run, and the final deposition of that fluid on and near the airport runway. The motivation for this study was twofold. First, since safety is a major issue in commercial aviation some concern exists regarding the change in coefficient of friction on a runway due to anti-icing fluid deposits, especially near the runway centerline. Landing aircraft may observe some reduction of braking coefficient during anti-icing fluid usage which is due to the fluid on the runway. The magnitude of this reduction is unknown at this time, largely due to the lack of information regarding the amount of anti-icing fluid on the runway. The second reason is due to the possible enviromental impact of the anti-icing fluid deposits near an airport runway. Type II anti-icing fluids are typically glycol based, and collection and treatment systems do not exist along the runways of most airports where Type II fluid is used. Collection of excess anti-icing fluid is done at the airport ramp area where the fluid is applied, but not elsewhere, specifically there is no collection of fluid which moves off the runway itself.

The study considers the use of the vortex lattice method to determine the wing loading of complex wing geometries. This is done for the aircraft considered prior to rotation during the take-off ground roll, hence ground effect is considered. The three jet aircraft considered possess complex wing geometry, especially during the take-off phase. This includes triple slotted flaps, single slotted flaps, leading edge slats, double taper, wing twist, and different airfoil sections. This wing geometry is considered with this computer model.

Note that this work is significantly different from the other two applications of the vortex lattice method. Now the VLM is used to predict the span loading of these more complex wing geometries, during the ground run before take-off and with ground effect included. Then the VLM is used to predict the wake roll-up within close proximity to the ground. Finally, anti-icing fluid flows off the wing and the fluid drop movement within that developing wake is calculated using a Lagrangian method. Appendix 5.A will elaborate on the theory and assumptions for the drop movement calculations.

Chapter six gives a summary of the conclusions from each chapter and suggests some avenues for future research.

1.2 Choice of the Computer Model

With the vast array of computer software being developed in the last years one must field the question of why any particular method is chosen for a particular problem. Specifically, there is needed some argument for the credibility of the Vortex Lattice Method (VLM) as applied to the particular problems being considered. As indicated the VLM is used for this study. This VLM is basically a solution which uses a vortex lattice system but accounts for more of the aircraft geometry as is common with vortex panel methods. The computer code which was used for the study was developed entirely by the author. The VLM was chosen since it is a reliable technique and is always useful for comparison with more robust methods.

Other methods such as the Cloud in Cell (CIC) technique (as developed by Christiansen (1973) and Baker (1979)) are amongst the more efficient computationally. However the difficulty of developing the code and the corresponding input data in order to implement the boundary conditions may not prove beneficial (Sarpkaya (1989)), as compared to direct application of the Biot-Savart law. Sarpkaya (1989) also notes that "the time saved may be disappointingly small" as compared to directly applying the Biot-Savart law. Note that the VLM approach uses a direct application of the Biot-Savart law. As well, the use of the CIC method leads to solving a Poisson's equation, therefore only simple boundary conditions can be handled (Sarpkaya (1989)). The final result, therefore, is that even a simple winglet configuration is not feasible with the CIC method.

As stated by Sarpkaya (1989), "The ultimate objective of the simulation via vortex dynamics is the acquisition of new insights rather than accurate predictions. The flow simulated by the numerical model may not be physically realizable even under controlled laboratory conditions." However, sufficient accuracy is required of the particular vortex method being used to ensure that the results can provide the correct basis for the new insights which are acquired.

Sarpkaya (1989) pointed out that "the representation of a continuous distribution of vorticity by a finite number of discrete vortices is the major source of inaccuracy," then later he commented that "It is entirely possible that vorticity does not like to be discretized."

However, a good point made is that "As is often the case in computational vortex dynamics, the reasonableness of the results depends on the criteria of credibility." (Sarpkaya (1989) with regard to vortex sheet development which was reasonably predicted on the large scale, while at the same time there occurred the disorderly movement of individual vortices.)

Jones and Lasinski (1981) has commented that even lifting-line methods can produce results as good or better than those by vortex panel methods at least in the prediction of induced drag.

Rossow (1990) has developed other methods for determining loads during wing-vortex interaction and has stated that the vortex lattice method was used as a method with which to compare and verify the accuracy of the new analytical techniques. Apparently, the vortex lattice method was used for comparison since it was considered to be a sufficiently accurate tool in itself. There would be no point in comparing to another tool which was deficient.

These arguments and other verification within Chapter 3 concerning winglets show that the present VLM approach is sufficiently valid to produce believable results. This work does not pretend to be a final solution to each of the problems, however, in line with the sentiment expressed by Sarpkaya (1989) as quoted above, even the use of a relatively simple VLM model may provide some additional engineering information and useful insight.

REFERENCES

Baker, Gregory R. 1979. The "Cloud in Cell" Technique Applied to the Roll Up of Vortex Sheets. *Journal of Computational Physics* 31:76-95.

Christiansen, J.P. 1973. Numerical Simulation of Hydrodynamics by the Method of Point Vortices. *Journal of Computational Physics* 13:363-379.

George, M.F. 1985. *Tip Vortex Cavitation Research Literature Review.* Department of National Defence Canada. Defence Research Establishment Atlantic CR-85-409.

Jones, R.T. and T.A. Lasinski. 1981. *Effect of Winglets on the Induced Drag of Ideal Wing Shapes.* NASA-TM-81230.

Rossow, Vernon J. 1990. Estimate of loads during wing-vortex interactions by Munk's traverse-flow method. *Journal of Aircraft* 27(1):66-74.

Sarpkaya, Turgut. 1989. Computational Methods with Vortices -- The 1988 Freeman Scholar Lecture. Transactions of the ASME. *Journal of Fluids Engineering* 111:5-52. (esp. pp. 6, 16, 24, 30, 42)

CHAPTER 2

LITERATURE REVIEW of VORTEX SYSTEMS and WINGLETS

2.1 INTRODUCTION

2.1.1 Background and Literature Review

The purpose of this chapter is to survey the literature regarding the subjects of vortex methods for determining wing performance, vortex systems, and winglets. The performance of finite length wings can be calculated by numerous different vortex methods, some of which will be reviewed. Similar methods have been used for significant efforts to discover the nature of the trailing vortex wake, with one of the goals being to understand the velocity distribution through the evolving vortex core. Some of these numerical vortex methods as well as many experimental programs have been the source of much of the information which will be presented regarding winglet performance.

The use of vortex methods for aerodynamic performance calculations goes back at least as far as Munk (1921) and yet today continues to develop into a more precise science. The basics of the vortex lattice methods and vortex panel methods will be discussed. This work focuses on the low-speed, incompressible flow application of winglets. Thus, compressibility effects can be ignored, i.e. at speeds up to $M \approx 0.30$, which greatly simplifies computations.

The study of the trailing vortex wake development has been, currently is, and undoubtedly will continue to be the focus of much work in the next years. This focus will continue to dominate as the need to increase airport traffic without corresponding increase in capital expenditures. The BOEING 757 wake intensity during the 1993-4 year has been the focus of much attention by aerodynamicists following the crash of several small aircraft during wake vortex encounters. This is since the BOEING 757 (a medium jet) wake vortex appears to be much more intense than previously expected for that aircraft at the given loading and airspeed conditions.

Winglets are devices on the wing tip which are used to modify the tip flow. The main goals of winglets are to reduce the induced drag of a wing and to reduce the maximum tangential velocity of the vortex core. The redistribution of vorticity caused by winglets is the key to the reduction of the maximum tangential velocity in the vortex core, i.e. by the splitting of the circulation into more than one vortex.

The exact mechanism by which winglets work is not yet clearly understood. Several ideas have been put forth, but as yet the importance of each has not been confirmed. As well, it may be that the mechanisms suggested are only different manifestations of the same underlying phenomenon, or that the total is a combination of several effects. A review of the possible mechanisms and current design considerations will be given.

2.2 VORTEX METHODS and VORTEX SYSTEMS

2.2.1 General

A very thorough review of all aspects of vortex systems and the numerical simulation of many aspects of vortical flows including applications in aerodynamics was presented by Sarpkaya (1989), hence the reader is referred to that work for a comprehensive overview of vortex methods. Also, a good coverage of the material concerning vortex sheet roll-up and vortex systems (specifically relevant to trailing vortex cavitation) is given by George (1985) and hence the reader is referred to that work for more a detailed account of vortex roll-up. A survey of the literature will be given here with the concentration on areas not specifically covered by George (1985) and Sarpkaya (1989). Specifically covered are: numerical vortex models for wing loading, vortex core models and vortex sheet roll-up, multiple vortex systems, axial velocity deficit, and the persistence and decay of vortex systems.

2.2.2 Numerical Models for Wing Loading

A lifting wing generates lift by producing circulation such that the lift per unit span, ℓ, is given by:

$$\ell = \rho V_o \Gamma \tag{2.1}$$

where, ρ is the air density, V_o is the aircraft velocity. The total circulation generated by the wing, Γ_o, is obtained by an integration of the local value of circulation, Γ, across the span, b. Likewise, the total lift of a wing is obtained by integration of the local lift across the span. Circulation is defined as the line integral of the tangential velocity component, v_{tan}, around any closed circuit in a fluid (Houghton and Carruthers, 1982). If the closed circuit is taken around the vortex core, to enclose all of the vorticity, then the circulation is called the strength of the vortex.

Basically, a vortex is a line or chain of fluid particles spinning on a common axis and carrying around with them a swirl of fluid particles which flow around in circles (Houghton and Carruthers, 1982).

A vortex in inviscid incompressible fluid would demonstrate a tangential velocity, v_{tan}, versus radius, r, profile as shown in Figure 2.1, with

$$v_{tan} \propto \left(\frac{1}{r}\right) \tag{2.2}$$

Hence, merely increasing the distance from the vortex axis leads to decreased v_{tan}. For a vortex with total circulation, Γ_o,

$$\Gamma_o = 2\pi r v_{tan} \tag{2.3}$$

or,

$$v_{tan} = \left(\frac{\Gamma_o}{2\pi r}\right) \tag{2.4}$$

Beyond a certain distance from the axis, a vortex in a viscous fluid will behave as a vortex in inviscid fluid. However, the inner core is significantly affected by viscosity. A vortex in inviscid fluid has a singularity as $r \to 0$, which implies an infinite tangential velocity at the very center. Obviously this cannot be a realistic condition, and experimental measurements have confirmed this fact. The tangential velocity has been found to vary nearly linearly with the radius for the inner region of the viscous core, such that the core rotates like a solid body, then to round off to meet the curve of the potential vortex velocity profile, as shown in Figure 2.2. The exact extent of this viscous core, however, is not agreed upon entirely.

2.2.2.1 Vortex Lattice Methods

The vortex lattice method (VLM) involves replacing the wing and the trailing vortex sheet by a discrete number of horseshoe vortices. The finite bound vortex lies on the wing quarter chord position and the semi-infinite trailing vortices extend in the streamwise direction. For symmetrical loads the bound vortices may extend from the left semi-span to the right semi-span location. Alternately, the bound vortices may be discretized along the span. The location for each of the trailing vortices is determined by the method for discretizing the main wing in the spanwise direction. Typically, the vortex sheet is considered rigid, i.e. does not roll-up, for calculation of the wing loading. The Biot-Savart law is then used to determine the induced velocities at any point. The reader is referred to the next section concerning computational schemes for vortex sheet roll-up for references to the VLM. Also, a further explanation of the details of the VLM is given in Chapter 3.

2.2.2.2 Vortex Panel Methods

The vortex panel method (VPM) is such that the wing is partitioned into a discrete number of areas or panels which are oriented in the streamwise and spanwise directions. Once the wing is partitioned, a horseshoe vortex is attached to each panel. Generally, the bound vortex is placed at the quarter chord of each panel and the trailing vortices at the edge of the panel. The three quarter chord point of each panel is usually chosen as the location to ensure that the boundary condition of no normal flow. With some of these methods, the vorticity may be distributed across the panels according to some mathematical function. As well, for some of the VPM, the trailing vortex system is represented by a trailing vortex lattice system, just as for the VLM. For other types of the VPM the wake is partitioned using panels of vorticity. Which ever wake representation is used, the method may have a rigid wake or may allow the trailing vortex system to move with the local flow. The wing loading is calculated by solving for the spanwise and chordwise distribution of vorticity.

Generally, surface or panel methods do not consider wing thickness effects, hence, the thickness of wings must be accounted for in another fashion. As well, boundary layer development is not included, but could be added in another step. The reader is referred to the next section concerning computational schemes for vortex sheet roll-up for references to the VPM.

2.2.3 Fully Rolled-Up Vortex Core Models

Spreiter and Sacks (1951) were among the first to derive a value for the vortex core radius, r', of the fully rolled up trailing vortex behind a lifting wing. These authors derived a value for the vortex core radius based on equating the total kinetic energy (both inside and outside the core) per unit length of the vortex pair to the induced drag, D_i. (Note that D_i times distance travelled equals energy expended to overcome that induced drag.) They assumed a Rankine style vortex, as shown in Figure 2.3, such that the core rotated as a solid body and the fluid outside of the core conformed to potential flow.

Their calculations for an elliptically loaded wing gave $r' = 0.0775b$, where b is the wing span. Bilanin and Donaldson (1975) also used the $r' = 0.0775b$. Corsiglia, *et al.* (1973) used hot-wire anemometer surveys of the wing tip vortex to show that radius of the laminar core region is between $0.010b$ and $0.015b$.

Roberts (1983) has shown analytically that the laminar subcore radius, r', can be expressed as

$$r' = 0.175\ [(\frac{c}{2})\log(\frac{1}{c})]^{0.5}\ b \tag{2.5}$$

where $c = (40000/Re)$ and, for a lifting wing, $Re = (\rho\ V_o\ b/\mu\ A_R)$.

Based on a wing with elliptical spanwise loading and $Re = 10^7$, Roberts showed the laminar core radius, to be $0.018b$. This radius was the radial position of the maximum tangential velocity. Roberts (1983) then showed there to be a turbulent core region extending to $r = 0.175b$, which corresponded to the position at which the tangential velocity of the core region attained the same v_{tan} of the potential vortex. Roberts' view on the velocity profile of the core region is shown in Figure 2.2, and corresponds to the approximate currently accepted form for the velocity profile in the vortex core in viscous flow.

The exact extent of the viscous region is still a matter of debate. As well, there is uncertainty as to whether the core is mostly laminar or turbulent, and where v_{tan} for turbulent flow will match v_{tan} for potential flow. Also in question is the exact relationship between the tangential velocity and the radius of the core region. Roberts (1983), Donaldson *et al.* (1974), Bilanin and Donaldson (1975), Corsiglia *et al.* (1973), Brown (1973), and McCormick *et al.* (1968), all give good reviews and discussion of the velocity profile in the vortex core. Basically, all of these authors adhere to the idea that the core region velocity profile is similar to that already described, with the flow outside the core conforming to the potential flow field. The work of Brown (1973), however, differs from the rest in disputing the relationship of $v_{tan} \propto 1/r$. Instead, Brown (1973) proposed that the relationship should be $v_{tan} \propto 1/r^{0.5}$. This view apparently has not been supported elsewhere and, hence, is not pursued further at this time.

From the figures given by Roberts (1983) and Corsiglia *et al.* (1973), the maximum value of v_{tan} is seen to occur where $r' \cong 0.018b$. Also, from their figures, the value of the maximum v_{tan} of the viscous core is seen to be about the same as the value of v_{tan} for the potential vortex, provided that v_{tan} of the potential vortex is taken at $r \cong 2r'$, that is, twice the radius where the maximum v_{tan} occurs in a viscous core.

The core size of a vortex is determined largely from the roll up process, and hence can be shown to be significant to the induced velocities caused by the vortex. Staufenbiel (1984) noted that the Rankine vortex core model does not accurately represent the invariants of the vortex system during roll-up (i.e. the invariant the 2nd moment of vorticity), hence criticized the continued use of that core model.

Next, concerning the effect of wing loading, Donaldson *et al.* (1974) showed how "the exact behaviour of the load at the tip has a profound effect on the inviscid roll-up of a vortex. By changing the load distribution just slightly so as to reduce $d\Gamma/dy$ at the tip, the maximum velocities that can be achieved in roll-up can be reduced accordingly." (Γ is the local bound circulation, and y is the spanwise location.)

Ciffone and Orloff (1975) also show that by unloading the wingtips of a plain wing (which produces a single vortex) the maximum v_{tan} is reduced and the core radius is increased. As well, they found that the core size increases in the downstream direction as $(x/b)^{0.5}$ and the maximum v_{tan} decreases as $1/(x/b)^{0.5}$ hence the total circulation remains constant downstream.

The velocity field around a prescribed value of circulation was given by Lamb (1932). He showed that the effect of redistribution of vorticity in the region had no effect on the circulation contained in the region. However, Cone (1962) has shown that vorticity spreading and attenuation leads to reduced downwash, lower induced drag, and decreased kinetic energy in the vortex system. Staufenbiel (1984) also maintained that taking vorticity away from the core would increase the vortical dispersion and thus, in general, reduce the vortex energy. This may be a significant factor worthy of investigation.

2.2.4 Vortex Sheet Roll-Up Process

Lanchester (1907) was apparently the first to consider relating a finite span lifting wing to a vortex system. He attempted to explain the bound vortex and the streamwise vortices generated at the wing tip and their mode of roll-up, see Figure 2.4. Vorticity is first shed from the trailing edge of the wing as a vortex sheet, as proposed by Prandtl (1921). The vortex distribution shed from the trailing edge of the wing is determined largely by the planform and airfoil shape along the span (geometry of the wing) as shown by Spreiter and Sacks (1951), and others. For conditions of a smooth planform and no flap deflection, the vortex sheet rolls up, starting at the wing tips, into two discrete vortices trailing the wing. Figure 2.5 shows the scheme of roll up of the vortex sheet beginning at the wing tip.

Betz (1933) described the laws of conservation of vorticity. These show that a fully rolled up vortex sheet must produce a core region whose moments of vorticity are the same as that of the original vorticity distribution. Betz discussed how to relate the spanwise vorticity distribution to the radial distribution of vorticity in an evolving trailing vortex system.

Donaldson *et al.* (1974) refer to the Betz (1933) presentation of the vortex conservation theory and present the following equations (Equations 2.6 to 2.11) which summarize Betz' ideas. Figure 2.6 shows the Betz roll-up model as given by Donaldson *et al.* (1974). The spanwise circulation distribution is given by $\Gamma(y)$ or $\Gamma(\eta)$, and the radial distribution of circulation in an evolving trailing vortex system is given by $\Gamma'(r)$ or $\Gamma'(\rho)$. Γ_0 is the total circulation for the semi-span, and R is the radius for the fully developed vortex core within which all of the vorticity from each wing is contained.

For a fully rolled up vortex sheet from each wing semi-span, Equations 2.6 to 2.8 apply.

$$-\int_0^{b/2} \frac{d\Gamma(y)}{dy}\, dy = \int_0^R \frac{d\Gamma'(r)}{dr}\, dr = \Gamma_0 \tag{2.6}$$

$$-\int_0^{b/2} \frac{d\Gamma(y)}{dy}\, y\, dy = \Gamma_0\, \bar{y}_t \tag{2.7}$$

$$-\int_0^{b/2} \frac{d\Gamma(y)}{dy}\, (y-\bar{y}_t)^2\, dy = \int_0^R \frac{d\Gamma'(r)}{dr}\, r^2\, dr \tag{2.8}$$

For a partially rolled up vortex sheet along each wing semi-span, Equations 2.9 to 2.11 apply.

$$-\int_y^{b/2} \frac{d\Gamma(\eta)}{d\eta}\, d\eta = \int_0^r \frac{d\Gamma'(\rho)}{d\rho}\, d\rho = \Gamma(y) \tag{2.9}$$

$$\int_y^{b/2} \frac{d\Gamma(\eta)}{d\eta}\, \eta\, d\eta = \bar{y}(y) \int_y^{b/2} \frac{d\Gamma(\eta)}{d\eta}\, d\eta \tag{2.10}$$

$$-\int_y^{b/2} (\eta - \bar{y}(y))^2\, \frac{d\Gamma(\eta)}{d\eta}\, d\eta = \int_0^r \rho^2\, \frac{d\Gamma'(\rho)}{d\rho}\, d\rho \tag{2.11}$$

Equations 2.6 to 2.8 and 2.9 to 2.11 show the basic relationships for the conservation of circulation (0th moment) and the 1st and 2nd moments of vorticity, where η is the a dummy variable for y the semi-spanwise location measured outboard from the wing root towards the wing tip at $y=b/2$, $\bar{y}$ is the spanwise location of the centroid of vorticity shed by the wing outboard of the spanwise location y, $\bar{y}_t$ is the spanwise location of the centroid of vorticity for the semi-span, and ρ is dummy variable for the radial distance from the center of the evolving vortex core whose radius is indicated by r.

As Betz (1933) showed, the conservation laws require that the center of vorticity (the 1st invariant of vorticity, which is similar in nature to a center of gravity) will remain at a constant spanwise location during the roll up process, given that the aircraft is free of nearby boundaries. This will be the case even though the actual pattern of roll up will be influenced by the spanwise rate of change of loading of the wing ($d\Gamma/dy$). This topic is covered adequately by Spreiter and Sacks (1951), Brown (1973), Donaldson *et al.* (1974), Bilanin and Donaldson (1975), Roberts (1983), Yates (1974), and others. Yates (1974) gives an especially good discussion of vortex roll up considering the problem of multiple vortices, as would be the case from flap deflection.

"Roll up of a sheet asymptotically approaches the completely rolled up condition as distance to the wing approaches infinity," Spreiter and Sacks (1951). The actual time for the vortex sheet to roll up into discrete vortices incorporating essentially all of the vorticity, has been shown by Sprieter and Sacks (1951) to be dependent only on the aspect ratio, final vortex spacing (as determined by method of Betz), lift coefficient, and aircraft velocity. The calculations of Spreiter and Sacks (1951) were based on an elliptical wing loading and gave the following value for time to roll up:

$$t_{rup} = (\frac{0.36\, A_R\, b'}{C_L V_o}) \tag{2.12}$$

where, t_{rup} = time to roll up (s), A_R = aspect ratio of wing, b' = vortex spacing (m), C_L = lift coefficient, and V_o = aircraft velocity (m/s).

The distance to roll up, d_{rup}, then can be found:

$$d_{rup} = t_{rup} V_o = (\frac{0.36\, A_R\, b'}{C_L}) \tag{2.13}$$

For example, a typical fixed wing, single engine aircraft may have A_R = 5.5, C_L = 0.6, V_o = 45 m/s and b' = 0.82 b (where the span, b = 12 m), hence d_{rup} is determined to be 32.5 m and t_{rup} = 0.72 seconds.

The vortices will roll up even faster when more of the load (than for elliptical loading) is towards the wing tips as with subsonic rectangular wings (Spreiter and Sacks, 1951). Noting that winglets increase outboard spanwise loading, winglet vortices should tend to roll-up faster than those from a plain wingtip. However, since the vortex is split into several vortices of lesser intensity, the roll-up process may be delayed.

2.2.5 Vortex Behaviour Near the Ground and Vortex Bounce

In an unconfined region in the absence of crosswinds the movement of the fully rolled up trailing vortices from a lifting wing would be the same as two infinite line vortices. For two infinite line vortices at the same height, and of equal but opposite strength, Γ, their motion is vertically downwards. Their velocity of descent, v_{dec}, is given by

$$v_{dec} = \frac{\Gamma}{2\pi b'} \tag{2.14}$$

where b' is the lateral separation between the vortices.

The presence of a ground plane imposes a boundary condition such that there can be no airflow component perpendicular to the ground surface. This condition is adequately satisfied by the use of image vortices. The actual bound vortex and each of the trailing vortices are above the ground plane. The ground plane acts as a reflection plane such that the image vortices appear as reflections of the real vortices. Near a ground plane, actual trailing vortices, once rolled up, will be curved semi-infinite line vortices. This will occur because they stay connected with the wing vortex sheet as it moves away and, at any point, they move down and outwards laterally, depending on the ground plane proximity.

2.2.5.1 Vortex Roll-Up In Ground Effect

The influence of the ground plane will undoubtedly have an affect on the roll-up process and time for roll-up. This is one matter which does not seem to have received much attention in research as yet and, apparently, is not completely understood. In fact, it is likely that the vortex roll-up would not procede in the same fashion near the ground as would be the case in an unconfined region. Note that at distances far from a ground plane, the trailing vortices will roll-up such that their lateral spacing conserves the center of vorticity, as has been explained by Betz (1933). This is not the case with a wing which is in close proximity to a ground plane. When a wing is close to the ground the trailing vorticity is influenced by the ground plane or image vortex system. As a result of the vortex images, with a wing close to the ground plane, there will be considerable outward lateral movement of the trailing vortices during the vortex sheet roll-up process. The effect of the ground plane on the motion of the trailing vortices will be more dramatic the nearer to the ground the vortices originate or descend. Thus, the ground plane is a significant influence when considering both the vortex roll-up and the path taken by the trailing vortices after formation.

2.2.5.2 Ground Effect And Secondary Vortices

The formation of a secondary vortex at the ground level has been documented by Bilanin *et al.* (1978) and Harvey and Perry (1971). The trailing vortex descends near to the ground plane after some time and, at the same time, moves laterally outwards. The reason for the formation of this secondary vortex is linked with the viscosity of air and the scrubbing effects of the trailing vortex adjacent to the ground plane. Morris (1978) has suggested that the boundary layer below the descending trailing vortex grows and separates, resulting in the secondary vortex. The secondary vortex is of opposite sign to that of the descending trailing vortex. As the secondary vortex grows it will induce both upward and outward motion on the descending vortex, hence is termed 'vortex bounce'. This can be important when considering the movement of spray droplets in the aircraft wake, especially those droplets laterally inwards from the secondary vortex, will be affected by the same upwards and outwards induced flow. Harvey and Perry

(1971), using a wind tunnel with moving floor, were amongst the first to show that vortex bounce does occur and to explain the phenomenon in terms of the separation of the boundary layer. They suggested the formation of a 'bubble' of vorticity which separates from the boundary layer flow forming the secondary vortex. Bilanin *et al.* (1978) showed isopleths of vorticity for a vortex pair descending toward ground plane, and the vortex bounce caused by the secondary vortex, as shown in Figure 2.7.

Figure 2.8 shows the effect of the secondary vortex on the motion of the one of the trailing vortices, as compared to the movement under inviscid conditions. Dee and Nicholas (1969) were the first to actually measure the occurrence of vortex bounce using actual flight tests and commented on it. However, they made no effort to explain the phenomenon.

As shown in Figure 2.7, the formation of this secondary vortex will take a finite period of time, as indicated by the vortex flow time, t^*, a parameter which is a dimensionless measure of time in a vortex flow. Bilanin *et.al.* (1978) showed that

$$t^* = \frac{t\,\Gamma_o}{2\,\pi\,b'^2} \qquad \textbf{(2.15)}$$

An idea of the magnitude of t which corresponds to the particular values of t^* for standard small aircraft can be determined by substitution of the relevant parameters. Using the equation given by Houghton and Carruthers (1982) for a rectangularly loaded wing that $\Gamma_o = (b\ V_o\ C_L\ /\ 2\ A_R)$ with $b' = 0.82\ b = 0.82 \times 12.625$ m, $V_o = 50$ m/s, $C_L = 0.5$, and $A_R = 5.5$, gives $\Gamma_o \equiv 28.69\ \mathrm{m^2/s}$.

Now, subsitituting into equation 2.12, one gets $t^* = 0.043\ t$. Hence, for the value of $t^* = 8$ (from Figures 2.7 and 2.8), when the secondary vortex is starting to develop, $t = 188$ seconds. Since most drop movement for medium to large droplets takes only a few seconds, the secondary vortex will not be sufficiently developed to have any significant influence on these droplets. For finer sprays, the secondary vortex may have some affect, however, the exact magnitude is unknown at this time.

Drummond *et al.* (1991) show experimentally that vortex bounce does occur and should be included in any calculations for spray movement in the wake of an aircraft near the ground. Although some researchers are convinced of the importance of the secondary vortex, the model does not include the development of the secondary vortex in any case.

2.2.6 Computational Schemes for Vortex Sheet Roll-Up

The following section deals with the two most common methods of vortex sheet roll-up modelling: vortex lattice and vortex panel methods. A choice regarding the computational method may involve the cpu requirements of time and memory for a typical wake roll-up.

Some numerical modelling problems arise because of the uncertainty about whether the vortex sheet remains discrete long after roll-up or if viscous effects cause the core to develop immediately as the sheet deforms to some given curvature. In wind tunnel studies, O'Callaghan (1988) observed discrete spirals a short distance back from a wing. A single turn of the vortex sheet was indicated by the phenomenon of a discrete step increase in v_{tan} at a particular radius. As yet there still remains a significant question concerning how long the vortex sheet should remain discrete or when it should be combined into a viscous and/or turbulent core, when modelled by computer.

2.2.6.1 **Vortex Lattice (Filaments) Methods for Vortex Sheet Roll-Up**

The vortex lattice method (VLM) for modelling vortex sheet roll-up involves replacing the bound vortex system and the trailing vortex sheet by a discrete number of horseshoe vortices. These trailing vortices are then allowed to move with the local fluid flow. Rosenhead (1931) was amongst the first to study the rolling up vortex sheet using an array of discrete vortex filaments in the streamwise direction. Later, Westwater (1935) used 20 equal strength vortices to model the sheet roll-up with reasonable success. Numerical instabilities were observed in the core region, as evidenced by the erratic movement of the point vortices as the vortices rolled up and the core wound tighter.

Hackett and Evans (1971) also used discrete vortex lines and the Biot-Savart law for the induced velocities to model the vortex sheet roll-up. In addition, they mentioned an interesting method to show streamlines by the use of vortex lines of zero strength imbedded in the flow.

Moore (1974) used point vortex approximations with a 4th order Runge-Kutta integration scheme. That led to chaotic motion of the vortices, only worsening with increasing number of vortices. Moore developed his own method which he explains regarding spacing of vortices and the radius of spiral turns and when to combine vortices in the developing vortex core (see Moore (1974) pp.228-229). However, it should be noted that the decision as to how exactly to combine vortices into the core has been controversial (see Chorin & Bernard (1973), Clements & Maull (1973)). Moore noted that Euler integration leads to cumulative errors as previously noted by Crow (1965), i.e. a continuously increasing vortex separation, which contradicts potential theory and experimental observation.

2.2.6.2 **Vortex Panel Method for Vortex Sheet Roll-Up**

When the VPM is applied to the vortex sheet roll-up, the wake is partitioned using either vortex filaments or panels of vorticity which are allowed to move with the local flow.

Mokry and Rainbird (1975) used a first order panel method. They found that the use of discrete straight line vortex elements of constant strength over the element produced stable results without artificial viscosity (i.e. when to take the vortex element into the core).

Hoeijmaker and Vaatstra (1983) noted that numerical instabilities still occurred in the case of a wing with part span flaps when using the method of Mokry and Rainbird (1975). Therefore they developed a second order panel method, using a scheme to adapt the panels based on the curvature of the vortex sheet. As well, they used a concept for treating the highly rolled up portions of the vortex sheet. The method cut the rolled up and stretched vortex sheet when its angular extent exceeded a specified amount and dumped the cut portion into the core, which was then placed at the center of vorticity of the core and the cut off portion. The method gave accurate computation of the velocity field and, thus, allowed the vortex sheet motion to be followed in a reliable, smooth, and stable manner for long time periods.

Staufenbiel (1984) commented that discrete vortex approximations cannot be used to compute the maximum v_{tan} to agree with experiments. He points out some shortcomings of the Rankine vortex core model as to its inability to accurately represent the invariants of the vortex system during roll-up (i.e. the 2nd moment of vorticity). Staufenbiel was able to show that the same was the case for the Lamb and Betz core models.

Goldhammer (1976) used a lifting surface method with a continuous chordwise vorticity distribution. However, the method still retained a discontinuous spanwise vortex distribution. Goldhammer's method was found to give reasonably good correlation with experimental methods for nonplanar surfaces. Also of note was that Goldhammer used a rigid wake, hence the resulting induced velocity field would not accurately represent the real vortex sheet which rolls up. However, the exact shape of the wake will have a diminishing effect on the flow over the wing with increasing distance from the wing, hence for determining the airfoil characteristics a rigid wake may suffice, whilst saving considerable computational effort.

2.2.7 Axial Velocity Defect

The understanding of the axial velocity component, particularly its direction along the axis of the trailing vortex, still needs some research. Batchelor (1964) was one of the first to consider, in a purely theoretical sense, the problem of the axial flow in vortices but did not provide conclusive evidence to show what was really happening.

Roberts (1983) provided a very good discussion on the axial and radial flow in trailing vortices, and related that to the persistence and decay of the vortices. Roberts (1983) showed how the acceleration of flow along the axis of a vortex causes radial inflow countering radial diffusion, hence persistence of the vortex core. When the axial flow recovers to the free stream velocity, inflow ceases and the vortex starts to decay. (Possibly greater wing drag could cause larger axial defect thus causing the vortex to wind tighter and the maximum v_{tan} to increase, hence, the vortex to persist longer.)

Corsiglia *et al.* (1973) showed the axial velocity at the center of the core to be in the order of

0.2 V_o towards the wing. They found this value for both 10 and 31 span lengths downstream from the wing. This axial velocity is substantial from the view of the vortex life and energy considerations.

Figure 2.9 shows the vortex from a C-47 jet fly-by intercepting smoke emitted from a 31 foot smoke tower, from Olsen *et al.* (1971). The figure clearly shows the smoke in the vortex core drawn along towards the aircraft (which had flown by from right to left), hence indicating a strong axial flow in the vortex core.

Ciffone and Orloff (1975) were able to show the existence of a considerable axial velocity defect using a water channel. The defect was seen by air bubbles, which were entrained in the water along the axis of the vortex, moving towards a wing. They also measured the maximum v_{tan} through the vortex core with downstream distance. Of note from their work was that the maximum v_{tan} remained constant until about 30 spans downstream of the wing. Their work showed that the axial velocity defect was greatest (about 0.10 V_o) immediately behind the wing and decreased continuously, but at the greatest rate about 30 to 50 span lengths behind the wing. Thus some correlation between axial and tangential velocity is borne out.

Faery and Marchmann (1976) commented that a stronger axial velocity deficit leads to a greater reduction in maximum v_{tan}. They also note that with a Whitcomb winglet there would be a greater axial velocity deficit and a greater reduction of maximum v_{tan}. They noted that the upper winglet alone gave the greatest reduction of maximum v_{tan}. Of interest was their note that the upper winglet alone as well as the whole Whitcomb winglet produced 2 vortices, with a corresponding 64% reduction of maximum v_{tan}.

George (1985) suggested that the axial flow contribution to the minimum pressure in a vortex core may be under estimated. His suggestion was based on the work of Spreiter and Sacks (1951), who equated the rotational kinetic energy (i.e. that due to v_{tan} only) of the vortex to induced drag. George did not clearly explain his idea, but it can be shown that if both axial and tangential velocities were added when determining the kinetic energy of the trailing vortex core, then the radius of the core would be reduced. Hence, since the minimum pressure would be reduced (that occurring at the vortex center), cavitation would occur sooner (i.e. at a lower value of Γ).

2.2.8 Pressure Variation in a Rankine Vortex

For some studies the pressure variation through a vortex is relevant. The relationship for the pressure variation from the center of a Rankine style vortex can be shown to be as follows:

$$\begin{aligned} P &= P_o - \left(\frac{\rho\Gamma^2}{8\pi^2 a^2}\right)\left(2-\left(\frac{r}{a}\right)^2\right) && , r \le a \\ &= P_o - \left(\frac{\rho\Gamma^2}{8\pi^2 r^2}\right) && , r \ge a \end{aligned} \tag{2.16}$$

Where, ρ is the fluid density, and $\Gamma = 2\pi a v_{tan}$, with v_{tan} determined at the core edge, $r=a$. (Houghton and Carruthers, 1982). Observe that the minimum pressure which occurs at the center where $r=0$, is then a function of $(\Gamma/a)^2$. Any modification of a vortex, such that the value of Γ/a is smaller, will reduce the absolute value of the minimum pressure.

2.2.9 Multiple Vortex Systems

Multiple vortices rolling up off the trailing edge of a wing may be caused by discrete changes in lift distribution such as a wing with flap deflection, discrete changes in chord, winglets, etc. Such is the topic of this section.

Donaldson *et al.* (1974) used an inviscid model after the manner of Betz (1933) for multiple vortices. The Betz (1933) method replaced the rather difficult computation for the inviscid vortex sheet roll-up with a locally axisymmetric vorticity distribution. This vorticity distribution gave consideration to the invariants of the vortex system, i.e. conservation of vorticity and the first two moments of vorticity during the roll-up process. Donaldson *et al.* (1974) note that this method "does not give a complete description of an actual roll up" but does give a picture of the vortex system resulting from any initial spanwise loading.

Donaldson *et al.* (1974) compared the results from their model to flight tests and achieved sufficient agreement to suggest that the inviscid model was largely adequate. They showed the roll-up centroid to occur at the maximum value for the absolute value of ($d\Gamma/dy$), and that the roll-up occurs between points of minimum $d\Gamma/dy$. Also noted was that the flap and tip vortices spiral around each other until they finally merge into a single core.

Yates (1974) agreed with the findings of Donaldson *et al.* (1974) who stated that the "initial vorticity shed between the local minima of the curve abs($d\Gamma/dy$) vs $\bar{y}$ will roll up into a discrete vortex." Note that $\bar{y}$ is the spanwise location of the centroid of vorticity shed by the wing outboard of the spanwise location y. Rossow (1973) found that the roll up center occurred at the maxima of abs($d\Gamma/dy$) and that the shed sheet of vorticity roll up edges were at the minimum of sheet strength.

Cone (1962) found that vorticity spreading would decrease the maximum v_{tan} in the trailing vortex system. Similarly, O'Callaghan (1988) found that winglets effectively split the tip vortex and reduced substantially the maximum v_{tan}. Marsden (1988) also was able to show substantial reductions in the maximum v_{tan}.

Splitting of a vortex core by a winglet results in several vortex cores of lesser strength at different locations. The result is that the induced velocity at any given position is the combination of the induced velocities from each weaker vortex, such that the magnitude of the induced velocity, $\bar{v}_{ind}$, will be decreased.

$$\bar{v}_{ind} = |\bar{v}_{ind}| \leq \frac{1}{2\pi}(\frac{\Gamma_1}{r_1} + \frac{\Gamma_2}{r_2} + \frac{\Gamma_3}{r_3} + \ldots) \tag{2.17}$$

where $\Gamma_o = (\Gamma_1 + \Gamma_2 + \Gamma_3 + \ldots)$ and r_n is the distance to the axis of each core.

Note that the reduction in v_{tan} at any location will be marginal due to the mere rearrangement of the vortex cores, at least in potential flow. Since induced drag is related to the tilting of the lift vector due to the flow redirection, this change in v_{tan} is just a small part of the contribution to the reduced drag, but it will be a part of the answer. Also, since v_{tan} will be reduced in the core, the kinetic energy should be slightly lower with the vortex core split. (Note that Spreiter and Sacks (1951) showed that kinetic energy per unit length equals D_i; also, recall Cone (1962) on vorticity spreading.)

Also, simply increasing the spanwise displacement of the center of vorticity would lead to a lower v_{tan} at any spanwise location. This would be partly due to the reduced value of Γ_o because of the greater span, and partly due to the increased radius to each vortex core center, hence the resulting decreased induced drag again will be a definite part of the whole reduction. As will be shown later, winglets do in fact modify the spanwise loading so as to increase the outboard loading. This may be a significant factor in the overall effect of winglets.

2.2.10 Persistence And Decay Of Vortex Systems

Oseen (1927) and Lamb (1932) were among the first to consider vortex persistence, and derived expressions for the decay rate of the tangential velocity function of a vortex. They showed it to be an exponential function, as follows:

$$v_{tan}(r,t) = \frac{\Gamma_o}{2\pi r}(1 - \exp(\frac{-r^2}{4\nu t})) \tag{2.18}$$

where $\nu = \mu/\rho$ is the kinematic viscosity ($\nu_{air} \cong 1.5*10^{-5} m^2/s$). Hence, as can be seen by this equation, time must have a fairly large value for the decay of a vortex in air to be significant. Thus, vortex decay as a result of viscosity is inconsequential when determining the induced drag of an airfoil.

Crow (1970) was a major contributor to the knowledge about the instability of trailing vortex pairs. His most significant contribution, often called the Crow instability, concerned explaining a sinusoidal instability leading to the linking of the two trailing vortices to produce elongated vortex rings which appear to decay rapidly. He also commented on a core bursting phenomenon based on axial flow in the vortex core. However, both phenomena are most appropriate for longer time frames than of interest for induced drag reduction. Other researchers have elaborated on both the Crow instability and vortex core bursting. There does not yet appear to be an irrefutable explanation for the cause of core bursting.

Radial inflow, or tendency for such, will tend to cause increased persistence of a vortex, see Roberts (1983). The author speculates that the axial flow due to the wing profile drag will influence the radial inflow and the vortex life, such that if a wing has lower drag the mass defect behind the wing will be lower, hence the tendency for radial inflow will be reduced. This will result in less persistence of the vortex core and less concentration of it. This should then reduce the maximum v_{tan}. Lower drag should also give decreased axial flow toward the wing, therefore reduced time of persistence of the core.

There have been suggestions that injection into the core (blowing) would have a similar effect, i.e. to cause the vortex to diffuse more rapidly. Poppleton (1971) tried this, only to find that the necessary volume of air was a large amount of the flow through typical jet engines, hence too large a volume to be of practical interest. However, it should be noted that later work was done on the merit of wingtip mounted engines, for instance Dunham (1976), and Snyder and Zumwalt (1969) who used propellers mounted on the wingtips.

2.3 WINGLETS

2.3.1 General

The theory of induced drag has long been known. Munk (1921) showed for large aspect ratios, that a uniform downwash across the span, i.e. that generated by an elliptical loading, produced the minimum induced drag for a specified magnitude of lift. Hence, theory clearly demonstrates that for a planar lifting wing configuration generating a single vortex the minimum induced drag is obtained by an elliptical lift distribution across the span.

The theory is not so clear, however, for the generation of a multiple vortex wake, as would be the case for a nonplanar wing. Lanchester (1907) was probably the first to suggest the use of wing end plates to restrict the spanwise flow. Other early researchers such as Munk (1921), Mangler (1938), Nagel (1924), and Weber (1954) did investigate the nonplanar wing configurations (i.e. flat end plates) in potential flow and found them to be of limited benefit. Thus, even though some subsequent researchers did show that end plates could be useful, the application of winglets was not taken seriously prior to Whitcomb's work. However, serious work in the area was revived when Whitcomb (1976) investigated a winglet configuration which proved beneficial. Since that time the study of winglets has been alive and flourishing.

Winglets must produce a normal force in order to be effective, hence a vortex sheet is shed from their trailing edge. Since some spanwise vortices (i.e. bound vortices) will then extend along the winglet, the effective length of the bound vortex increases. Also, since $\ell = \rho V \Gamma$, more lift is produced further outboard due to the increased circulation outboard on the wing. This may help explain the increased local lift coefficient, C_ℓ, on outboard stations of the wing due to a winglet, and the possible link to the normal force coefficient of the winglet, C_N, i.e. as C_N of the winglet increases the C_ℓ of the wing outboard stations increases.

Vorticity spreading is accomplished by the addition of a winglet to a wing tip. As discussed earlier, any discontinuity of the spanwise circulation along a wing will result in initial vortex sheet roll-up at that location. Generally, the discontinuity of circulation produced by the junction between a wing tip and winglet root will provide a site for initial vortex sheet roll-up. Thus, a winglet on a wing tip will typically result in a double vortex core being formed in the wing tip region. As discussed by Cone (1962), this vorticity spreading may contribute to the benefits of winglet addition.

Investigations into winglet effectiveness must consider the thrust produced by a winglet, the vortex spreading and hence the possibly lower maximum v_{tan}, and the apparently increased outboard span loading caused by the addition of a winglet. All of these and more may be contributing factors and thus should be considered to fully explain the effectiveness of winglets.

The actual effectiveness of winglets for achieving drag reduction of lifting surfaces has generated significant discussion, hence, the literature will be reviewed and the significant points noted.

2.3.2 Mechanisms Of Induced Drag Reduction

The exact mechanism by which winglets work is not yet clearly understood. Several ideas have been put forth, but as yet the importance of each has not been confirmed. As well, it may be that the mechanisms suggested are only different manifestations of the same underlying phenomenon, or that some observed effects are just by-products of another, or that the total is a combination of several effects.

2.3.2.1 Forward Thrust Component of Winglet Normal Force

Some literature suggests that the forward thrust on a winglet due to the local flow angularity is a significant factor in the reduction of induced drag. As well, the significance of the forward thrust has been suggested by some preliminary wind tunnel tests by the author on a single and double winglet configuration at the University of Alberta. The local flow angles have been indicated by the use of wool tufts. As well, the normal force produced by a winglet has been demonstrated by observations of the surface flow (i.e. the position of the separation line on an airfoil), as indicated by a surface flow visualization technique. Since the local flow angle may be inclined to the mainstream, any thrust on the winglet which is perpendicular to the local flow may have a component in the mainstream direction, see Figure 2.10. To some degree this will offset some of the main wing drag, and is usually attributed to reducing the induced drag.

Flechner, Jacobs, and Whitcomb (1976) examined a Whitcomb style winglet on a jet transport semi-span model. They commented that the forward component of the side force vector produced by the winglet is the primary mechanism by which induced drag is reduced. Whitcomb (1976) also notes that significant side force (on a vertical winglet) is required for winglets to be effective, however at that time he made no comment concerning a forward thrust component.

Spillman (1987) gave a summary of a decade or so of work to that point, which has had him involved studying multiple winglet configurations (see section on multiple winglets). It should be noted that Spillman considered that the primary, if not only, effect of the winglet to be the forward thrust component; thus he appropriately labels his devices "sails." Spillman stated that "sails act like a fixed windmill in a rotating airflow, unwinding the flow and experiencing a thrust as a result." See Figure 2.10, Figure 2.18, and Figure 2.26 for a view of the thrust vector and Spillman's winglets.

Concerning the magnitude of this thrust, note should be taken of the area of winglets. Their area is generally rather small (i.e. 1/2 to 2 percent) compared to the whole wing area, indicating that ΔD_i contributions likely come from something additonal to the forward thrust component. Some rather hypothetical calculations given in Appendix 2.A for a typical aircraft provide an idea of the significance of this thrust component. It should be noted, for the sample calculations given, that the forward thrust of the winglet is shown to be a significant amount of the induced drag of the aircraft (but not enough to explain all of the possible drag reduction by winglets), hence should be considered in the overall analysis.

2.3.2.2 **Redistribution of Spanwise and Chordwise Loading**

Another significant effect of winglets is a redistribution of both the spanwise loading and chordwise loading at a given span location. Mangler (1938) was one of the first to show that in potential flow the use of an end plate would modify the circulation distribution over the entire wing. Since then many researchers have shown the same.

Ishimitsu and Zanton (1977) of Boeing have done a fairly comprehensive study of the retrofit of winglets to the KC-135 air transport. They used a potential, 3-D flow theory then strip theory of boundary layer growth (Boeing programs: TEA 230, 372, 200, and 242) and found good correlation of theoretical predictions with experimental results, see Figure 2.11. They found that the addition of winglets caused greater loading of the wing toward the outboard span locations, for an example of their results see Figure 2.12. They also found that the chordwise pressure distribution at about 90% span and greater was significantly affected by the winglet local pressure field, see Figure 2.13.

The significance of the change in spanwise loading lies in the fact that the minimum induced drag for a planar wing corresponds to elliptical spanwise loading. Thus, any increased outboard loading of an initially elliptical loading would cause increased induced drag for the same span of a planar wing. For the case of a nonplanar wing with winglets, any increased drag due to non-optimum loading along the main span must then be offset by the other benefits derived from the winglets, such as the forward thrust component or effective increases of span (or aspect ratio). Hence, the winglet thrust (or whatever the mechanism) really must be even more than just the apparent drag reduction compared to the basic configuration, but need also account for the change from the optimum configuration.

Horizontal winglets which have a narrow chord would not produce as much lift as a simple wing tip extension of the same length, therefore smaller increases in wing root bending moment could be expected. Likewise, the small chord of a winglet would not contribute to as much parasite drag as would a simple wing tip extension. Hence, a tip mounted winglet could act as a high aspect ratio wing (which inherently has low induced drag) attached to the wing. Also, increased cant angle (or dihedral) of a winglet would lead to decreased wing root bending since the moment arm would then be reduced. Note that, due to the orientation of the local flow and the cant angle of the winglet, the normal force of the winglet has a moment arm of less than the semi-span, $b/2$, (by a factor $\sim$sin(winglet cant angle) or $\sim$cos(winglet dihedral angle)), whereas the normal force on a wing tip extension would have a moment arm *equal* $b/2$ plus the distance to the center of pressure of the wing tip extension.

Heyson *et al.* (1977) undertook a parametric study of the relative advantages of winglets and wingtip extensions using a unified vortex lattice program from North American Rockwell (NARVUL). A single winglet with 30° leading edge sweep was used while varying the taper ratio, aspect ratio, and washout of the wing. The main result found was a 40% improvement in induced efficiency factor using winglets on an untapered, untwisted wing. A typical jet transport with $A_R=7$ gave $\sim 15\%$ drag reduction with winglet and $\sim 7.5\%$ with tip extension. They found that a winglet on an untwisted wing gave 2 to 5 times the benefit of a wing tip extension, whereas on a wing with twist the winglet was only 1.5 to 2 times as good as the tip extension. The reason considered for the winglet on the twisted wing performing more poorly was that the twisted wing reduced the outboard loading.

Heyson *et al.* (1977) commented that since winglets increase the wing loading at the tips, there is an increase in bending moment along the wing, the extent of which must be fully determined. This would be especially important for retrofit applications.

Flechner *et al.* (1976) have shown that the local pressure coefficient C_P increases on a wing from the span location $0.96b/2$ and greater, hence resulting in an increased wing root bending moment. Of note is that their work was for Mach numbers from $\cong 0.7$ to $\cong 0.8$. Flechner and Jacobs (1978) also showed, via transonic wind tunnel studies, that Whitcomb style winglets increased outboard loading of the wing.

2.3.2.3 Maximum v_{tan} Reduction due to Vorticity Redistribution

Vorticity redistribution by winglets has been shown to substantially reduce the maximum tangential velocity through a region of vorticity, v_{tan}, compared to that of the single trailing vortex from a plain tip, O'Callaghan (1988) and others.

O'Callaghan (1988) performed wind tunnel experiments using a wing tip configuration with as many as three winglets, and a total of sixteen different mounting configurations for the winglets. The winglet designs considered the combined velocity field over the wing and the chordwise pressure gradient, dP/dx, at the winglet root. O'Callaghan measured the mid-semispan lift on a wing via pressure taps, hence the lift curve slope could be determined. As well, a 0.195 inch diameter five hole probe downstream of the wing was used to measure the wake characteristics, including the vortex tangential velocity. O'Callaghan showed the maximum v_{tan} to be about 65% of freestream velocity, V_o, for a plain wing. The use of a single winglet was seen to reduce the maximum v_{tan} for each of the new vortex cores to 30% of V_o, or less. One could show that since a split vortex core reduces the maximum v_{tan}, the tilting of the lift vector would be reduced, at least locally in the region of the vortex core edge, hence resulting in slightly lower induced drag. Of note was that O'Callaghan did find an increase of lift curve slope, $dC_L/d\alpha$, due to winglet additions; as much as 26% lower induced drag was indicated.

2.3.2.4 Kinetic Energy Reduction due to Vorticity Redistribution

Rotational kinetic energy is dependent on the angular velocity of a rotating mass. Therefore, the redistribution of vorticity results in lower kinetic energy of the rotating air mass due to the lower maximum tangential velocities through the vortex core. Cone (1962) showed an energy reduction in the vortex system for multiple vortices, thus reduced induced drag, D_i, for the system as compared to a single core. As shown by Spreiter and Sacks (1951), the kinetic energy of the vortex core is directly related to the induced drag of the airfoil, hence the lower kinetic energy means lower induced drag. Cone (1962) showed this by integration for a single vortex core then with multiple cores of evenly distributed vorticity to determine the relative changes in total kinetic energy. Also seen in the section regarding multiple winglet configurations is Küppers' (1983) work relating the kinetic energy and the number of vortex cores. Küppers showed a decrease of the kinetic energy in the vortex system with increased number of vortex cores, for the same total vorticity (see section on multiple vortices, i.e. Figure 2.24).

2.3.2.5 **Delay of Tip Vortex Roll-Up**

Delay of roll-up of the tip vortex may be possible by the use of a winglet configuration (Ciffone & Orloff, 1975). This may explain the occurrence of lower v_{tan} at given downstream locations as compared to a plain wing. However, Faery and Marchman (1976) have shown the roll-up of a vortex sheet to occur within 20 chord lengths downstream for both a plain wingtip and winglet. Note that this appears to conflict with the idea that increased outboard loading (as caused by the attachment of one or more winglets to a wing) increases the rate of roll-up, as proposed by Spreiter and Sacks (1951). It may be that any difference in loading was not sufficient to be detected by the experimental work of Faery and Marchman (1976). However, anything beyond about 10 chord lengths behind the wing will likely have little effect on drag, although it may influence the persistence of a trailing vortex pair. This is entirely another topic for investigation.

2.3.3 Present Winglet Concept Design Considerations

Whitcomb (1976) pioneered work on optimized narrow chord winglets and formulated the general design considerations predominantly used to date. Others have also considered winglets of the Whitcomb style and done parametric studies on that general configuration. Hence, Whitcomb's work and that done by others will be reviewed.

Whitcomb (1976) investigated winglet configurations experimentally in the Langley 8 foot transonic wind tunnel. He used a semi-span model with the basic fuselage, wing, and engine nacelles representative of a typical first generation, narrow body jet transport. The C_L of the wing and winglet C_N were determined with chordwise pressure taps at various span locations along each.

Whitcomb (1976) contended that winglets must produce significant side force to reduce lift induced inflow above wing and outflow below the wing. He noted that the principle physical effect is a "vertical diffusion of the tip vortex flow at least just downstream of the tip." However, in that report he made no comment delineating the significance of a forward thrust component. Whitcomb winglets were for design $M \approx 0.78$, therefore they were swept back significantly and the airfoil was of necessity a supercritical design. See Figure 2.14 for a description of the Whitcomb winglet.

The performance benefits shown by Whitcomb (1977) showed a 9% increased maximum lift-drag ratio, $(L/D)_{max}$, due to the upper winglet alone and about 20% reduction of induced drag at $C_{L_{cruise}} = 0.44$. In comparison, a wingtip extension gave only about 4% improved $(L/D)_{max}$ for the same wing root bending moment increase, hence, note was made that the upper winglet alone was found to be approximately twice as effective as a simple wing tip extension. The addition of the lower winglet had little effect on the *L/D* at the design conditions, however, at higher lift coefficients adding the lower winglet gave significant improvements in the *L/D*. Whitcomb (1977) noted that the winglets were placed on a wing with nearly elliptical basic span loading, and that a winglet application on a wing with more inboard basic loading would result in less significant reductions in the induced drag (as suggested by Goldhammer, 1976).

2.3.3.1 **Wing Root Bending Moment**

Winglets appear to be a means of increasing the effective aspect ratio of a wing, hence, providing reductions of induced drag without the associated penalties accompanying an equivalent spanwise extension. Currently, the main objective is the reduction of induced drag, and this should be accomplished at the same wing root bending moment, especially when the winglets are designed for retrofit applications. The wing root bending moment is usually considered since it is a reasonable index of the structural weight of a wing. As will be shown, when considering winglet applications, a compromise must be made between the reduction of induced drag and the root bending moment.

It must be noted that the bending moment at all spanwise locations is also an important parameter for design considerations. For example, a plain wing will have no loading at the extreme tip. The addition of a winglet will create a finite load at the tip. Hence, the ratio, of bending moment at a plain wing tip to the bending moment at the tip with a winglet, will be *infinite*.

Mangler (1938) recognized that increased force on an upper end plate produced a proportionately greater increase in bending moment at the wing root. Also, Weber (1954) was able to show the increased loading of outboard span positions due to vertical plates at various spanwise locations; which would lead to greater bending moment.

Heyson *et al.* (1977) commented that since winglets increase the wing loading at the tips, there is an increase in bending moment along the wing, hence the extent of this effect must be determined.

Dahlin (1981) using a potential flow, lifting surface method calculated an induced efficiency factor, *e*, for a wing with given spanwise loading, with winglets or wing tip extensions, relative to an elliptically loaded wing. His findings (Figure 2.19) showed that the effectiveness of both winglets and wing tip extensions was sensitive to the spanwise loading. Of note was that Dahlin's work showed that for both cases of loading of the basic wing the winglet was superior to the wing tip extensions. Also seen was that increased wing loading gave better increases in the *e* for the winglets than for the wing tip extensions.

Dahlin (1981) examined the effect of winglet length on the root bending moment of a wing using lifting surface methods. His findings are shown in Figure 2.15, which shows that the root bending moment of the wing increased with increased length of winglet, for all cant angles (dihedral) of the winglet.

2.3.3.2 **Parasite Drag Considerations**

The attachment of a winglet or wing tip extension is intended to produce an induced drag reduction, however, whatever device is attached the increased surface area leads to increased parasite (skin friction) drag resulting in a penalty. According to Asai (1985) the inclusion of the parasite drag appears to be essential to determing the overall merits of any one tip configuration, and for the comparison with others.

Asai (1985) used a vortex-lattice representation of the Trefftz plane wake to show that if parasite drag is neglected and the perimeter length in the Trefftz plane is held constant then a planar wing is more efficient than a nonplanar wing from the view of induced drag even if the root bending moment is considered. That conclusion was based on a wing extension of the same chord as the main wing. Also, it is better to extend the wingspan and shift the load inboard to improve induced efficiency (according to Munk (1921) only the wake shape in the Trefftz plane and load distribution matter for induced drag). (Note: see Jones (1979) for comments about perimeter length in the Trefftz plane.)

Asai did go on to consider a winglet of chord equal to half of the tip chord of the main wing, this he did with a vortex-lattice program developed by Margason and Lamar (1971). For that he found that there was no real difference between the ability of the winglet or the extension to reduce the induced drag. However, for the planar versus the nonplanar, the highly nonplanar winglet or extension proved to be about twice as effective at reducing the induced drag at the same root bending moment as the planar. This was explained by the nonplanar being able to have a greater span than the planar to produce the same bending moment (note this was without the parasite drag added), see Figure 2.16. Asai comments "that the parasite drag consideration is indispensable to explain the relative advantages of a winglet and spanwise tip extension." This he adds, since the induced drag efficiency at a given wing root bending moment is insufficient to explain the advantage of a winglet over a wing tip extension. It should be noted that parasite (skin friction) drag is roughly proportional to the wetted area. A winglet has a smaller chord than an extension, hence lower parasite (skin friction) drag. When parasite drag is considered Figure 2.17 shows that for the same wing root bending moment narrow chord winglets are about twice as effective as simple spanwise extensions at all cant angles. Asai concludes that the primary reason (narrow chord) winglets are more effective than spanwise tip extensions is that the increase in parasite drag for the winglet is small compared to that of the extension, *not* due to winglet being nonplanar. Asai closes commenting that a short span planar winglet may be a promising alternative to a large span nonplanar winglet. Note that Asai (1985) did not include the interference drag at the winglet root.

2.3.3.3 **Winglet Length**

Weber (1954) was among the first to comment that induced drag reduction is approximately linear with height of winglet. Since then others have examined that approximate relation.

Taylor (1983) presented the final evaluation of winglet tests for the DC-10 flight test program. The winglets were of the Whitcomb style. Two upper winglet spans were considered, 3.22m and 2.13m, as well as a 0.76m lower winglet. Taylor noted a total drag reduction of 5.7% at $C_L=1.2$, and 2.5% at $C_L=0.47$ when using the long upper winglet, and 2% at $C_L=0.47$ using the short upper winglet. Hence, the improvement was proportionately less than the length increase, but nearly linear with C_L. The lower winglet enhanced performance such that its removal led to about 1% reduction in total drag coefficient gains (i.e. at $C_L=1.2$ removal of the lower winglet gave total drag reduction of 4.7%, as compared with 5.7% with upper and lower winglets installed). The improvements due to the winglet addition were not as significant as expected, but the performance shortfall was attributed to the high suction peaks noted on the outer span of the upper winglet.

Heyson *et al.* (1977) noted that the winglet efficiency did not increase as rapidly as length, but the root bending moment increased at a rate greater than the increase in efficiency. Specifically, for a wing of $A_R = 7$ and winglet lengths of $0.15b/2$ and $0.30b/2$, the longer winglet gave an induced efficiency 60% greater than the shorter one. However, the root bending moment of the longer winglet was 90% greater than that of the shorter winglet. Thus, Heyson et al. observed that the root bending moment increased at a faster rate than the induced efficiency. This implied that there would be an optimum length for a winglet, however, no specific length could be said to be optimum since that would be dependant on the allowable increase in bending moment.

Dahlin (1981) examined the effect of winglet length on the induced efficiency of a wing. His findings are shown in Figure 2.15. As can be seen the optimum efficiency factor of the wing increased with increased length of winglet, for all cant angles (dihedral) of the winglet.

Spillman (1978 and 1987) illustrated typical streamlines near the tip of a plain wing tip and gave an indication of the local flow angle as a function of distance from the tip, see Figure 2.10. The figure shows how the local flow angle decreases with distance from the tip. The figure also shows that the local flow velocity decreases with increased distance from the center of the rolling up vortex at the tip. Hence, the combination of these two effects would reduce the effectiveness of the sections of a winglet further from the wing tip (i.e. greater angle gives greater forward thrust or sail effect, and greater velocity gives greater dynamic pressure and thus greater normal force). This also would imply an optimum winglet/sail length.

Examination of Figure 2.16 and Figure 2.17, from Asai (1985), gives findings very similar to that of Heyson *et al.* (1977). The overall observation can be made that increasing the length of a winglet gives a decreasing marginal reduction of induced drag, thus implying an optimum winglet length. However, exactly what that length might be is not obvious.

2.3.3.4 **Winglet Chordwise Position**

Chordwise positioning of winglets is a significant consideration especially for control of pressure peaks on the upper surface of the wing. This may be most important for winglet applications at high subsonic conditions, as for most current generation transport aircraft. However, it will also be a consideration for low speed applications. Whitcomb (1976) suggested that "the leading edge of the root of a winglet should probably not be significantly ahead of the upper-surface crest of the wing-tip section." The combination of the chordwise pressure distributions of the wing and the winglet is the focus of the concern. Also, for multiple winglets of various sizes there is no consensus as to the optimum arrangement, i.e. are the larger winglets near the leading edge or trailing edge of the wing.

2.3.3.5 **Winglet Spanwise Load Distribution**

Note that many of the winglet characteristics (such as cant angle, toe-in angle, twist, taper, sweep angle, and airfoil shape) really relate to the spanwise variation of the normal force produced by the winglet. Hence, in the design of a winglet these would be dealt with all at the same time. The major issue would concern the spanwise load distribution along the winglet, however, each will be mentioned separately. The spanwise loading of a winglet was noted by Ishimitsu and Zanton (1977), but no recommendations were made concerning an optimum winglet load distribution and twist. The topic of optimizing the spanwise loading of the winglet itself has not yet been extensively studied (i.e. As suggested by Whitcomb (1976), should the normal force coefficient be constant along the winglet span?).

2.3.3.6 **Winglet Cant Angle**

The cant angle of a winglet is considered to be the angle from the vertical to the wing spar at the wing tip, where positive angles are usually taken to be outwards, such that the span of the wing is effectively increased. Sometimes the cant angle of the winglet is referred to as the winglet dihedral, with the 0° position being planar with the wing just like a simple extension. Note should be taken that winglet effectiveness will depend upon the winglet cant angle and the toe-in angle of the winglet, since the local winglet angle of attack is a function or combination of both values.

Spillman (1987) maintained that a winglet which is in the plane of the wing (i.e. 90° cant angle) results in the best improvement of induced drag. However, Spillman does not delineate the associated bending moment changes.

Heyson *et al.* (1977) noted that if the winglet cant angle were less than zero then induced efficiency would be significant with a corresponding low root bending moment. This would be a desirable situation. However, the acute angle between the winglet and the wing would cause increased interference which would likely offset the benefits derived from the induced efficiency improvements.

Dahlin (1981) examined the effect of winglet cant angle on the induced efficiency and root bending moment of a wing. His findings are shown in Figure 2.15. As can be seen the root bending moment and optimum efficiency factor of the wing increased with cant angles (dihedral) of the winglet, approaching 90° (or 0°), i.e. approaching planar extensions of the wing.

Whitcomb (1976), based on the work of Lundry (1968), suggested a small outward cant angle based on the trade off between induced drag reduction, skin friction, and bending moment increases; and confirmed experimentally that positive cant angles were best.

As can be seen there is little agreement as to the correct or optimum winglet cant angle, however, winglet effectiveness generally increases with greater cant angle although this increase is accompanied by even greater percentage increases of wing root bending moment.

2.3.3.7 **Winglet Toe-In Angle**

The toe-in angle of a winglet is defined by the angle the winglet chord makes with the free stream direction. For a winglet design, the winglet toe-in angle will be directly related to the cant angle of the winglet since the local angle of attack, and hence the normal force of the winglet, is a function of both values.

Cary (1976) used a nonplanar lifting surface theory (the method of Goldhammer, 1976), hence no assumptions of small perturbations, to study winglet effects on a Boeing BAC 311 wing (design M = 0.78) with a taper ratio of 1/3. The single upper winglet was mounted at the rear top of the wing tip as per Whitcomb (1976). Of note is that the method used considered only inviscid, irrotational, uniform flow; hence, the model had no consideration given to viscosity and thus skin friction drag, or to interference between the winglet and wing. Cary managed to achieve from 15% to 27.5% reductions of induced drag for the range of wing dihedral, aspect ratio, and sweep angles studied. The best reduction of induced drag achieved was 27.5% for a wing with 45° sweep and $A_R=7$ (note that the range of A_R from 4 to 7 was studied). Cary noted the best *percentage* reduction of induced drag occurred for the highest wing aspect ratios, but best absolute *magnitude* of decrease was achieved for low aspect ratios.

Cary (1976) examined winglet toe-in angle and found that a small inward angle to be the best. At $C_L=0.6$ Cary found that an angle of +10° gave $\Delta C_{Di} \cong 0.0032$, and -10° gave $\Delta C_{Di} \cong 0.0030$ (where, C_{Di} is the coefficient of induced drag). Hence, toe-in angle was seen to affect the ΔC_{Di}, but not to be a really significant factor in itself. Note that Cary (1976) found that at $C_L=0.5$ and toe-in angle equal -10°, the $\Delta C_{Di} \cong 0.0021$; hence, C_L was significantly more important than toe-in angle. Also refer to section 2.3.3.18 for the effects of main wing C_L on ΔC_{Di} due to winglets.

2.3.3.8 **Winglet Twist**

Spillman (1978 and 1987) suggested that the twist, as shown in Figure 2.18, is necessary for wing sails to work and to avoid separation from the root to the tip of the sail. Spillman's figure of streamlines around the tip of a plain wing tip (Figure 2.10) show significant change in flow angle with radius from the tip, but the imposition of the winglet in the flow would straighten the flow somewhat. Some work by Marsden (1988) has determined that the flow angle after installation of a winglet is vastly different from that around a basic wing tip, thus the winglet twist can not be determined by the flow around a plain wing tip. Recall that winglet twist would be integrally related to winglet spanwise loading.

2.3.3.9 Winglet Sweep Angle

Heyson et al. (1977) maintained that sweep of a winglet would help to reduce junction drag (interference drag). Forward sweep would lead to aeroelastic problems, therefore backward sweep is the only practical alternative. This conforms to the general recommendations of Whitcomb (1976).

2.3.3.10 Winglet Taper

According to Whitcomb (1976), winglet taper is desirable so as to optimize the spanwise loading of the winglet itself, i.e. such that the normal force coefficient is constant along the winglet span. This is another topic not yet extensively studied, and perhaps should be.

2.3.3.11 Winglet Airfoil Shape

The efficient production of the normal force by the winglet necessitates consideration of an airfoil which will operate adequately over the range of Reynold's numbers and Mach numbers expected. As well, the C_N of the winglet should be kept nearly equal to the C_L of the wing, so as to avoid severe separation problems on the winglet, and thus any adverse drag rises.

A related concern deals with the pressure distribution over the winglet surface. A winglet or tip modification must produce some effect on the flow about it, hence, the force generated and the range of necessary normal force coefficients needed will determine the type of flow regime. Also, of concern is the combination of flow fields produced by the winglet and that produced by the wing in the tip region.

2.3.3.12 Winglet Fairing to Wing

Another topic apparently neglected, or at least not emphasized, by most researchers to date, concerns the precise nature of the winglet fairing to the wing. Winglet designs should consider the combined velocity field over the wing and the chordwise pressure gradient, dP/dx, at the winglet root. The importance of this cannot be neglected since flow separation at the root of the winglet would lead to significantly greater drag.

2.3.3.13 Effects of Spanwise Loading of the Wing

Weber (1954), Lundry (1968), and Goldhammer (1976) all indicate that in order for winglets to work well the outboard regions of the main wing need significantly increased loading. The same comment, that increased outboard loading increases winglet effectiveness, is made by many other researchers. Hence, second generation aircraft, which tend to have lower tip loading than the elliptically loaded first generation aircraft, stand to benefit less from the retrofit of winglets (Taylor, 1983).

Webber and Dansby (1983) showed, via analytical methods of the Lockheed-Georgia Co., Canada, that increased outboard wing loading provides greater benefit from winglets. They offered the explanation that greater tip loading gives greater vorticity shed at the tip, thus greater induced velocity at the wing tip therefore greater thrust on the winglet.

Heyson *et al.* (1977) found that a winglet on an untwisted wing gave 2 to 5 times the benefit of a wing tip extension, whereas on a wing with twist the winglet was only 1.5 to 2 times as good as the tip extension. The reason considered for the winglet on the twisted wing performing more poorly was that the twisted wing reduced the outboard loading.

Dahlin (1981) showed that the effectiveness of both winglets and wing tip extensions was sensitive to the spanwise loading, as shown in Figure 2.19. Dahlin also noted that increased wing loading gave better increases in the induced efficiency factor, e, for the winglets than for the wing tip extensions.

Flechner and Jacobs (1978) carried out transonic wind tunnel investigations of four representative large jet transport aircraft. Their results showed an 8% improvement in the L/D for the KC-135, 4% for the DC10 and L1011, and 6.5% for a future aircraft of $A_R = 9.8$, with the same winglet configuration. The significance was that the KC-135 has the highest outboard wing loading of the four aircraft studied, supporting the contentions of other researchers.

2.3.3.14 Effects of Spanwise Twist of the Wing

Spanwise twist or washout of a wing is basically a means to modify the spanwise loading of a wing. The use of washout on a wing results in unloading of wing tips and increased loading of the inboard regions of the wing, hence the bending moment along the wing is decreased at the sacrifice of induced efficiency. Heyson *et al.* (1977) showed the effects of spanwise twist or washout of a wing on the effectiveness of winglets. Figure 2.20 through 2.22 (Figures 15,18, and 21 from Heyson *et al.* (1977)) show that the ratio of induced efficiency with winglets to that without winglets decreases with increasing amount of washout for both high and low lift coefficients. This is basically the result found by others, i.e. that increased outboard span loading improves the effects of winglets.

2.3.3.15 Effects of Main Wing Aspect Ratio

Cary (1976) found the greatest reduction of induced drag achieved was 27.5% for a wing with 45° sweep and $A_R=7$ (note that the range of A_R from 4 to 7 was studied). Cary noted the best *percentage* reduction of induced drag occurred for the highest wing aspect ratios, but best absolute *magnitude* of decrease was achieved for low aspect ratios. The reason for such a trend was not discussed.

2.3.3.16 Effects of Main Wing Sweep Angle

Cary (1976) investigated the effect of wing sweep on the effectiveness of winglets. He found that reductions of C_{Di} were greater in both magnitude and percentage with increased sweep of the wing. The range of wing sweep angles was from 15° to 45°. Again he found the greatest reduction of induced drag achieved was 27.5% for a wing with 45° sweep and $A_R=7$. He also noted that the ΔC_{Di} was just better than linear with the sweep angle, however no rationale was offered. To reiterate, winglet effectiveness was better for greater sweep angles of the main wing.

2.3.3.17 Multiple Winglets Configurations

Küppers (1983) considered the wing tip feather concept seen in nature on soaring birds. To model the bird feathers he developed a multiple winglet configuration employing five winglets which were mounted using a ball and socket joint to provide complete flexibility of position, see Figure 2.23. However, the root of each winglet could not have been faired into the wing tip very well for all positions. Another of the significant drawbacks of his work was the low *Re* ($\approx 10^5$) at which the testing took place, especially when comparing his results to aircraft with typical *Re* $\approx 10^6$ to 10^7.

Note that Küppers developed a method to calculate the induced drag kinetic energy loss due to one or more Rankine style vortices. He assumed that the radius to the maximum v_{tan} was inversely related to the number of vortices, and that the circulation contained in each vortex was likewise inversely related to the number of vortices. i.e.

$$r_i = \frac{r}{n} \tag{2.19}$$

$$\Gamma_i = \frac{\Gamma}{n} \tag{2.20}$$

Recall that $\Gamma = 2\,\pi\, r\, v_{tan}$. Küppers showed the relationship between energy in the multiple vortex system and the number of vortices, n, (or number of winglets plus one). The relationship appears nearly as $1/n^2$ see Figure 2.24.

Here it should be noted that Küppers' assumptions imply that the maximum $v_{t\infty}$ for each of the smaller vortices is still the same as that of a single large vortex. This has been shown not to be the case. For instance, O'Callaghan (1988) showed that the maximum $v_{t\infty}$ for each of two smaller vortices shed from a winglet was about half of that of a single large vortex. Hence, Küppers' assumptions about either circulation in or radius of split vortices appear to be in error.

Küppers then showed the combination of energy in the vortex system plus that lost due to the increased parasite drag. The result was that there is an optimum number of winglets which will give a minimum drag, see Figure 2.25. Note that the parasite drag is related to the wetted area of the winglets, hence, parasite drag is approximately linear with the number of winglets.

O'Callaghan (1988) (and Marsden, 1988) considered various winglet configurations in experimental measurements, for example a double winglet with the top winglet ahead of a lower one. His wind tunnel investigations revealed potential for induced drag reductions in the order of 26% for a double winglet, even without optimization of the configurations. O'Callaghan, in agreement with Küppers (1983) and Spillman (1978) found a decreasing benefit from each additional winglet, hence, indicating an optimum number of winglets.

Spillman (1987) achieved approximately 12% and 28% induced drag reductions for the single and triple winglet configurations (for example, see Figure 2.26), respectively, but gave no clear indication as to the change in root bending moment associated with these. Also, using a Paris aircraft (a light jet) at $C_L=0.5$, Spillman (1978) measured an *L/D* increase from 12.5 in standard configuration to 15.6 with 3 sails. Of note is that Spillman (1987) maintained that a winglet which is in the plane of the wing (i.e. 90° cant angle) results in the best improvement of induced drag.

Spillman (1978) found that with 3 or 4 wing sails, a spiral angle of ~15° to ~20° between each sail was the best. He found that greater spiral angles reduced the overall effectiveness of the sail group.

2.3.3.18 Effects of Main Wing C_L on ΔC_{Di} due to Winglets

From the considerations of winglet effectiveness thus far, the effect of the overall aircraft wing C_L has been acknowledged. However, to be specific, the consensus has been that winglets generally provide greater reductions of induced drag at greater values of C_L. Cary (1976), Flechner *et al.* (1976), Montoya *et al.* (1977), Spillman (1987), Webber and Dansby (1983), Whitcomb (1976), and most others will agree with this result. The reason as suggested by Cary (1976) is that the increased angle of attack associated with increased C_L leads to greater flow around the tip. This greater flow around the wing tip increases the thrust of the winglet, therefore the forward thrust component is greater to offset the induced drag of the aircraft. Note that this is virtually the same argument provided by Webber and Dansby (1983) concerning the increased effectiveness of winglets at greater outboard span loading.

Cary (1976) also noted that ΔC_{Di} is almost linear with C_L. This observation could be confirmed by the work of Taylor (1983) who found $\Delta C_{Di}=5.7\%$ at $C_L=1.2$ and $\Delta C_{Di}=2.5\%$ at $C_L=0.47$. Ishimistu and Zanton (1977) also show a nearly linear relation between ΔC_{Di} and C_L for their winglet styles (only one typical example given here), using both analytical and experimental methods, see Figure 2.27. However, notice that these do not consider low values of C_L.

Similarly, this basic result was found by O'Callaghan (1988) and Marsden (1988) by analyzing the effect of winglets on the lift curve slope of an airfoil. O'Callaghan (1988) showed that an increase in the lift curve slope, $dC_L/d\alpha$, was related to induced drag reduction for modified wingtips, and that the curve remained basically linear up until stall. Thus, winglets provide the best percentage improvement at low speeds mostly because the induced drag becomes a greater portion of the total drag of an aircraft at low speed (high C_L) than at high speed (low C_L).

The relation between C_L and twist of a wing should also be noted. Heyson *et al.* (1977) and Montoya *et al.* (1977) noted improved effectiveness of winglets on wings with washout as the C_L increased. The reason for this stems from the basic and additional loading of the wing, due to C_L. The argument is as follows. At low C_L (i.e. as $C_L \rightarrow 0$) the inboard sections of the wing take most of the loading, while the outboard sections may not be loaded at all, or may even have negative loading. At high C_L, the load increases near uniformly across the span, hence, the tip loading increases the greatest percentage. The result is that the winglet normal force, and hence effectiveness, increases with increasing C_L.

Dahlin (1981) also noted that increased wing loading gave better increases in the induced efficiency factor, e, for the winglets than for the wing tip extensions.

2.3.3.19 **Various Other Considerations**

Winglet effects on aileron effectiveness has been noted by Flechner and Jacobs (1978). For transonic wind tunnel investigations of the KC-135 they found that the installation of winglets increased aileron effectiveness.

2.3.3.20 **Economic Considerations**

Boeing (1983) considered the overall benefit-cost analysis for winglet or wing tip extension retrofit to the Boeing 747 derivatives. Their concerns included weight, performance improvement potential, initial cost and complexity of construction, capital recovery, time to recover 100%, etc. Their work was based on the Whitcomb style winglet which they found could provide ~3.2% improvement of $(L/D)_{max}$. Operationally, the winglets were superior with regard to reducing drag and thus fuel consumption. However, the winglet initial costs were higher, i.e. the production costs for the winglet retrofit was three times that for the extensions (~\$100000 vs ~\$30000 respectively). The overall result was that for the needed return on investment of 15% only the extension was acceptable.

It should be pointed out that since the Boeing (1983) study was done, the Boeing Aircraft Co. has produced the 747-400 which does employ winglets. As well, the Boeing 7J7 which was studied and was scheduled for production in the 1990's was proposed to employ winglets. These developments imply that the relative merit of winglets versus tip extensions must have improved since their 1983 study.

The small margin of improvement and the high production cost for the Boeing winglet should be noted. Most probably, the cost for the production of winglets for smaller aircraft together with a greater potential drag reduction would favour the application of winglets.

2.3.4 Winglets Applied To Propellers

The application of winglets to propellers has been the focus of a limited number of studies. Goodman and Breslin (1980) performed a case study concerning winglets on marine propellers. However, their work lacks credibility due to rather poor experimental design. For instance, they used flat plate winglets and no real consideration was given to the details of mounting the winglets to the propeller blades. Not surprisingly they found that winglets on the propeller gave no performance increase, and in fact decreased the propeller efficiency.

Chang (1980) analyzed winglets on aircraft propellers using a vortex lattice method and noted a small performance improvement, in the order of 1 to 3 percent.

2.3.5 Other Wingtip Modifications

The idea of wing tip modifications has received considerable attention over the years. Modifications have ranged from changes of the tip geometry in the plane of the wing, to nonplanar modifications (e.g. end plates and winglets), to active tip flow control devices (e.g. blown wingtip jets). A couple will be discussed merely for demonstration of the diversity of ideas for induced drag reduction.

Zimmer (1987) discussed a triangular tip, i.e. one for which there is simply a discrete change in leading edge sweep near the wingtip, which shows some success. Perhaps such a tip produces the same phenomenon as appears from winglets, that of splitting the tip vortex core.

Wu *et al.* (1982) have investigated the use of wingtip jets to replace winglets. They used an adjustable jet of air blown in the desired direction to attempt to achieve the same end result.

2.4 LITERATURE REVIEW CONCLUSION

This chapter surveyed the literature concerning vortex systems of a lifting wing and winglets applied to aircraft wing tips. The subject of winglets received the greatest attention, since they are a means of reducing the induced drag of finite span wings through the modification of the trailing vortex system.

An overview of vortex systems has been given as pertains to lifting wings of moderate aspect ratio. A lifting wing generates vorticity in the three dimensions of the wing, but the most significant is the spanwise distribution. The review of vortex methods showed that vortex techniques have proven satisfactory for the calculation of aircraft wing loadings since the time of Munk (1921) and Prandtl (1921). The requirements for engineering design and aerodynamic improvement can be done even with relatively simple vortex methods. The vortex lattice method is one of these methods which can provide useful information when analyzing aircraft aerodynamics. As with any model there is some difficulty in exact replicaton of real flows. However, even the vortex lattice method is a useful tool and has success in showing trends and the development of the aircraft trailing vortex wake.

The application of winglets to aircraft wings was reviewed, since they appear to be an effective means of drag reduction. As stated by Webber and Dansby (1983), "it is clear that a tip device is not a universal panacea that will in all cases confer drag savings for little or no penalty in other areas." Winglet application will inevitably result in increased bending moment both at the root and at all spanwise locations.

This review has shown that properly designed winglets can effectively reduce drag during all phases of flight. However, winglets have been shown to be most effective during high C_L phases of flight, i.e. takeoff and climbout, hence providing greater reduction in induced drag thus less power is required and less noise generated during that phase (Heyson *et al.*, 1977). The reason for improved winglet effectiveness at low speeds was discussed. Some researchers have shown that, for a limited range of C_L, the reduction of induced drag varies *linearly* with C_L (i.e. a constant fraction of C_L). Therefore, the reason that winglets work best at low speeds is due to the induced drag becoming a greater portion of the total drag of an aircraft at low speed (high C_L) than at high speed (low C_L).

The assertion that the forward component of the side force vector produced by the winglet is the primary mechanism by which D_i is reduced must be investigated. The level of uncertainty about the importance of the forward thrust is sufficient motivation for further research into the induced drag reduction mechanism of winglets.

Winglets operate to split the vortex into more than one vortex with a resulting change in core sizes and maximum v_{tan}. The recombination of the multiple cores then would follow, finally producing a single vortex core with a velocity distribution different from that which would be produced by the simple wingtip. The hope is that by tailoring the winglet configuration properly the maximum v_{tan} can be reduced in the final rolled up single vortex per semi-span. However, the maximum v_{tan} downstream may not be as important for drag as it may be for trailing vortex persistence. Also, the decreased magnitude of v_{tan} may merely be a manifestation of the effects of winglets. This concept and the nature of dependency should receive some consideration in order to determine more precisely if there is any link to the winglet normal force.

The relationship between the induced drag and the kinetic energy of a vortex system was discussed. As could be shown, a trailing vortex system composed of multiple vortices would have lower kinetic energy than a single large vortex of equal circulation. This problem appears to be of sufficient significance that investigation of a vortex system with minimum kinetic energy as well as a winglet configuration to produce such a system should be considered.

The spanwise loading of the wing has been shown to be a significant factor when considering the potential for reduction of induced drag by a winglet, hence should be the subject of further study. Winglets have been seen to give greater reductions of induced drag, and hence total drag, for applications on wings with greater outboard spanwise loading. The connection between spanwise loading and the twist or washout of a wing has been discussed. The amount of washout has been shown to be directly related to the increased benefit of winglets at high lift coefficients with increasing washout. Heyson *et al.* (1977) commented that for an untwisted wing "it would be difficult to design a winglet so poorly that it would not obtain a greater gain in induced efficiency (at the same cost in root moment) than a tip extension."

As well, for retrofit applications, the modification of the spanwise loading of the wing upon addition of a winglet has been shown to be significant enough to warrant investigation. The reason is two fold. First a modified spanwise loading such that the center of vorticity is further outboard (due to increased effective aspect ratio) leads to reduced total circulation Γ_o, hence, lower values for v_{tan} and induced drag. The second reason stems largely from the modification of the bending moment at the root of the wing and at spanwise locations, especially near to the tip. This concern would be most important when considering the application of winglets for aircraft with optimized structural designs. Whereas most light aircraft likely have sufficiently over designed wing sections near the tip (i.e. those with rectangular planform and uniform spar) that bending moment increases, especially near the wing tip, would probably be of little significance.

The delay of trailing vortex roll-up was considered. This would have some effect on the induced velocities at the wing, but mostly the roll-up delay would affect the vortex persistence and decay.

Winglet physical parameters were discussed. An optimum length for winglets could not be predetermined without considerations of the allowable increases in bending moment over the span of a wing. As well, the observation was made that increasing the length of a winglet gave a decreasing marginal reduction of induced drag, hence implying an optimum winglet length (although it was not obvious what that length might be). As well, the cant angle of a winglet, or winglet group, cannot be determined exclusively on its own. Considerations of a specific winglet (or winglet group) design such as cant angle, toe-in angle, sweepback, twist, taper ratio, airfoil type, chordwise positioning, must be dealt with simultaneously. All of these parameters of the winglet will have an effect on the spanwise load distribution of the winglet (or winglet group), and how the wing spanwise loading is effected, especially in the tip region. Without a doubt, winglet effectiveness will have a direct link with the spanwise loading of the winglet.

The importance of the inclusion of parasite drag has been discussed. In order to determine the merits of a specific winglet over other tip modifications, no doubt the parasite drag will have to be considered.

The problem of winglet effectiveness has been argued. It should be noted that much of the literature examined dealt with one very similar wing scenario and winglet type - the Whitcomb winglet. This has occurred because Whitcomb's research published in 1976 was led a significant revival into winglet research. The general results and ideas are expected to be applicable for most winglet configurations, however, the improvements expected may be significantly different from those derived thus far. Also, the variety of current aircraft with the diversity of their wing types and spanwise loadings currently used as yet appears to leave the design of winglets to be very specific for each aircraft.

REFERENCES

Asai, K. 1985. Theoretical Considerations in the Aerodynamic Effectiveness of Winglets. *Journal of Aircraft* 22(7):635-637.

Batchelor, G.K. 1964. Axial Flow in Trailing Line Vortices. *Journal of Fluid Mechanics* 20(4):645-658.

Betz, A. 1933. *Behaviour of Vortex Systems*. National Advisory Committee for Aeronautics, Technical Memorandum, NACA-TM-713.

Bilanin, A.J. and C.duP. Donaldson. 1975. Estimation of Velocities and Roll-up in Aircraft Vortex Wakes. *Journal of Aircraft* 12(7):578-585.

Bilanin, A.J., M.E. Teske, and J.E. Hirsh. 1978. Neutral atmospheric effects on the dissipation of aircraft vortex wakes. *AIAA Journal* 16(9):956-961.

Boeing. 1983. *Selected Advanced Aerodynamics and Active Controls Technology Concepts Development on a Derivative B-747 Aircraft*. Boeing Commercial Aircraft Company. NASA CR-3295.

Brown, C.E. 1973. Aerodynamics of Wake Vortices. *AIAA Journal* 11(4):531-536.

Cary, M.D. 1976. *A Parametric Analysis of Winglet Effects*. M.Sc. Thesis. Air Force Institute of Technology, Wright-Patterson A.F.B., Ohio.

Chang, Li Ko. 1980. *The Theoretical Performance of High Efficiency Propellers*. Ph.D. Thesis, Purdue University.

Chorin, A.J. and P.S. Bernard. 1973. Discretization of a Vortex Sheet, with an Example of Roll-up. *Journal of Computational Physics* 13:423-429.

Ciffone, D.L. and K.L. Orloff. 1975. Far-Field Wake-Vortex Characteristics of Wings. *Journal of Aircraft* 12(5):464-470.

Clements, R.R. and D.J. Maull. 1973. The Rolling up of a Trailing Vortex Sheet. *Aeronautical Journal* 77(46).

Cone, C.D. 1962. *The Theory of Induced Lift and Minimum Induced Drag of Nonplanar Lifting Surfaces*. NASA Technical Report R-139.

Corsiglia, V.R., N.A. Chigier, and R.G. Schwind. 1973. Rapid Scanning, Three Dimensional Hot-Wire Anemometer Surveys of Wing-Tip Vortices. *Journal of Aircraft* 10(12):752-757.

Crow, S.C. 1965. Ph.D. Thesis. California Institute of Technology.

Crow, S.C. 1970. Stability Theory for a Pair of Trailing Vortices. *AIAA Journal* 8(12):2172-2179.

Dahlin, J.A. 1981. *Aerodynamic Evaluation of Winglets for Transport Aircraft*, Douglas Aircraft Co. AIAA Paper No. 81-1215.

Dee, F.W. and O.P. Nicholas. 1969. *Flight Measurements of Wing-Tip Vortex Motion near the Ground*. Aeronautical Research Council. Current Papers CP-1065. London, England.

Donaldson, C. duP., R.S. Snedeker, and R.D. Sullivan. 1974. Calculation of Aircraft Wake Velocity Profiles and Comparison with Experimental Measurements. *Journal of Aircraft* 11(9):547-555.

Drummond, A.M., R. Onno, and B. Panneton. Dec 1991. *Trajectories and Stability of Trailing Vortices Very Near the Ground.* NRC (Canada) Aeronautical Note lar-AN-74.

Dunham, R.E. Jr. 1976. *Unsuccessful Concepts for Aircraft Wake Vortex Minimization. Wake Vortex Minimization.* NASA-SP-409.

Faery, H.F.Jr. and J.F. Marchmann III. 1976. Effect of Whitcomb Winglets and Other Wingtip Modifications on Wake Vortices. :207-216.

Flechner, S.G. and P.F. Jacobs. 1978. *Experimental Results of Winglets on First, Second, and Third Generation Jet Transports.* NASA-TM-72674.

Flechner, S.G., P.F. Jacobs, and R.T. Whitcomb. 1976. *A High Subsonic Speed Wind-Tunnel Investigation of Winglets on a Representative Second-Generation Jet Transport Wing.* NASA-TN-D-8264.

George, M.F. 1985. *Tip Vortex Cavitation Research Literature Review.* Department of National Defence Canada. Defence Research Establishment Atlantic CR-85-409.

Goldhammer, M.I. 1976. *A Lifting Surface Theory for the Analysis of Nonplanar Lifting Systems.* AIAA Paper No. 76-16.

Goodman, T.R. and Breslin. 1980. *Feasibility Study of the Effectiveness of Tip Sails on Propeller Performance, Final Report.* Stevens Institute of Technology. MA-RD-940-81006.

Hackett, J.E. and M.R. Evans. 1971. Vortex Wakes Behind High-Lift Wings. *Journal of Aircraft* 8(5):334-340.

Harvey, J.K. and F.J. Perry. 1971. Flowfield produced by trailing vorticies in the vicinity of the ground. *AIAA Journal* 9(8):1659-1660.

Heyson, H.H., G.D. Riebe, and C.L. Fulton. 1977. *Theoretical Parametric Study of the Relative Advantages of Winglets and Wing-Tip Extensions.* NASA TP-1020.

Hoeijmaker, H.W.M. and W. Vaatstra. 1983. A Higher Order Panel Method Applied to Vortex Sheet Roll-Up. *AIAA Journal* 21(4):516-523.

Houghton, E.L. and N.B. Carruthers. 1982. *Aerodynamics for Engineering Students, 3rd Edition.* p256. Edward Arnold Pub. Ltd. London.

Ishimitsu, K.K. and D.F. Zanton. 1977. *Design and Analysis of Winglets for Military Aircraft, Phase II.* Boeing Commercial Aircraft Company. AFFDL-TR-77-23.

Jones, R.T. 1979. Minimizing Induced Drag. *Soaring* pp.26-29.

Küppers, U. 1983. Vortex Separation by Slotted Wing Tips, Energy Conservation According to Biological Model. Fortschritt-Berichte Der VDI Zeitchriften No. 81(Reihe 7). ("Randwirbelteilung durch aufgefacherte Flugelenden, Energiesparen nach biologischem Vorbild")

Lamb, H. 1932. *Hydrodynamics, 6th Ed.* pp220-224. Dover Publications, New York.

Lanchester, F.W. 1907. *Aerodynamics.* Constable & Co., Ltd. London.

Lundry, J.L. 1968. *Numerical Solution for the Minimum Induced Drag, and the Corresponding Loading, of Nonplanar Wings.* NASA CR-1218

Mangler, W. 1938. *The Lift Distribution of Wings with End Plates.* National Advisory Committee for

Aeronautics. Technical Memorandum No. 856.

Margason, R.J. and J.E. Lamar. 1971. *Vortex-Lattice Fortran Program for Estimating Subsonic Aerodynamic Characteristics of Complex Planforms*. NASA-TN-D-6142.

Marsden, D.J. 1988. Personal Communication. Department of Mechanical Engineering, University of Alberta.

McCormick, B.W., J.L. Tangler, and H.E. Sherrieb. 1968. Structure of Trailing Vortices. *Journal of Aircraft* 5(3):260-267.

Mokry, M. and W.J. Rainbird. 1975. Calculation of Vortex Sheet Roll-up in a Rectangular Wind Tunnel. *Journal of Aircraft* 12(9):750-752.

Montoya, L.C., S.G. Flechner, P.F. Jacobs. 1977. *Effect of Winglets on a First Generation Jet Transport Wing; 3: Pressure and Spanwise Load Distributions for a Semispan Model at Mach 0.30*. NASA-TN-D-8478.

Moore, D.W. 1974. A Numerical Study of the Roll-up of a Finite Vortex Sheet. *Journal of Fluid Mechanics* 63(2):225-235.

Morris, D.J. 1978. *Analytical Prediction of Agricultural Aircraft Wakes*. ASAE Paper No. 78-1506. Am. Soc. Ag. Eng., St. Joseph, Michigan 49085.

Munk, M. M. 1921. *The Minimum Induced Drag of Aerofoils*. N.A.C.A. Report No. 121.

Nagel, F. 1924. *Wings With End Plates*, Memo Rep 130. Eng. Div., McCook Field.

O'Callaghan, W.J. 1988. *The Induced Drag Reduction Mechanism of Wingtip Surfaces from Studies of the Lift Curve and Vortex Wake*. M.Sc. Thesis, University of Alberta.

Olsen, J.H., A. Goldburg and M. R[illegible]er (editors). 1971. *Aircraft Wake Turbulence and its Detection*. Plenum Press, New York. p121, 279 .

Oseen, C.W. 1927. *Hydromechanik*. Leipzig. p.82.

Poppleton, E.D. 1971. Effect of Air Injection into the Core of a Trailing Vortex. *Journal of Aircraft* 8(8):672-673.

Prandtl, L. 1921. *Applications of Modern Hydrodynamics to Aeronautics*. NACA Report No. 116.

Roberts, L. 1983. *On the Structure of the Turbulent Vortex*. AGARD CP 342. Aerodynamics of Vortical Type Flows in Three Dimensions. Advisory Group for Aeronautical Research and Development, NATO, France.

Rosenhead, L. 1931. The Formation of Vortices from a Surface of Discontinuity. *Proceedings of the Royal Society of London*, Series A, Vol. 134, pp.170-192.

Rossow, V.J. 1973. On the Inviscid Rolled Up Structure of Lift Generated Vortices. *Journal of Aircraft* 10(11):647-650.

Sarpkaya, Turgut. 1989. Computational Methods with Vortices -- The 1988 Freeman Scholar Lecture. Transactions of the ASME. *Journal of Fluids Engineering* 111:5-52. (esp. pp. 6, 16, 24, 30, 42)

Snyder, M.H. Jr. and G.W. Zumwalt. 1969. Effects of Wing-Tip Mounted Propellers on Wing Lift and Induced Drag. *Journal of Aircraft* 6(5):392-397.

Spillman, J.J. 1978. The Use of Wing Tip Sails to Reduce Vortex Drag. *Aeronautical Journal* 82(9):387-395.

Spillman, J.J. 1987. Wing Tip Sails; Progress to Date and Future Developments. *Aeronautical Journal* 91(12):445-453.

Spreiter, J.R. and A.J. Sacks. 1951. The Rolling up of the Trailing Vortex Sheet and its Effect on the Downwash Behind Wings. *Journal of the Aeronautical Sciences* 18(1):21-23.

Staufenbiel, R.W. 1984. Structure of Lift-Generated Rolled-Up Vortices. *Journal of Aircraft* 21(10).

Taylor, A.B. 1983. *DC-10 Flight Evaluation (Summary Report).* McDonnell-Douglas Corporation. NASA CR-3748.

Webber, G.W. and T. Dansby. 1983. Wing-Tip Devices for Energy Conservation and other Purposes - Experimental and Analytical Work in Progress at the Lockheed-Georgia Company. *Canadian Aeronautics and Space Journal* 29(2):105-120.

Weber, J. 1954. *Theoretical Load Distribution on a Wing with Vertical Plates.* R.A.E. Reports and Memoranda No. 2960.

Westwater, F.L. 1935. *The Rolling Up of the Surface of Discontinuity Behind an Aerofoil of Finite Span.* R & M 1692, Aeronautical Research Council, Great Britain.

Whitcomb, R.T. 1976. *A Design Approach and Selected Wind-Tunnel Results at High Subsonic Speeds for Wing-Tip Mounted Winglets.* NASA TN D-8260.

Whitcomb, R.T. 1977. *Methods for Reducing Subsonic Drag Due to Lift.* AGARD Report No. 654. Advisory Group for Aeronautical Research and Development, NATO, France.

Wu, J.M., A. Vakili, and Z.L. Chen. 1982. Wing-Tip Jets Aerodynamic Performance. *ICAS Proceedings 1982; 13th Congress of the International Council of the Aeronautical Sciences.*

Yates, J.E. 1974. Calculation of Initial Vortex Roll up in Aircraft Wakes. *Journal of Aircraft* 11(7): 397-400.

Zimmer, H. 1987. *The Aerodynamic Optimization of Wings at Subsonic Speeds and the Influence of Wing Tip Design.* NASA-TM-88534. (Translation of German Thesis from 1977)

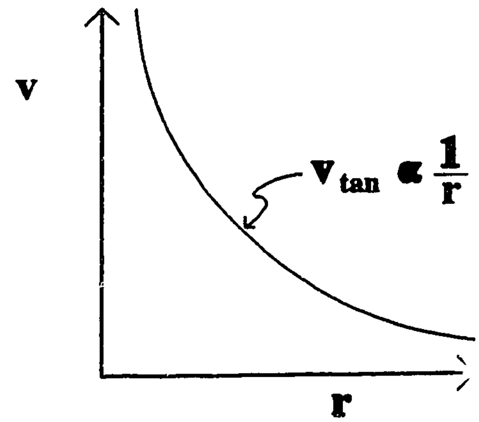

Figure 2.1 Vortex in Inviscid Incompressible Flow.

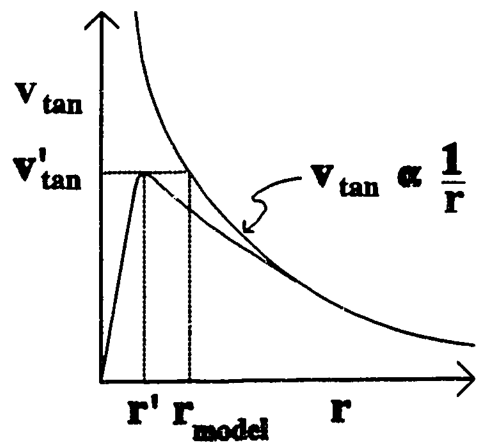

Figure 2.2 Vortex with Viscous Core Region.

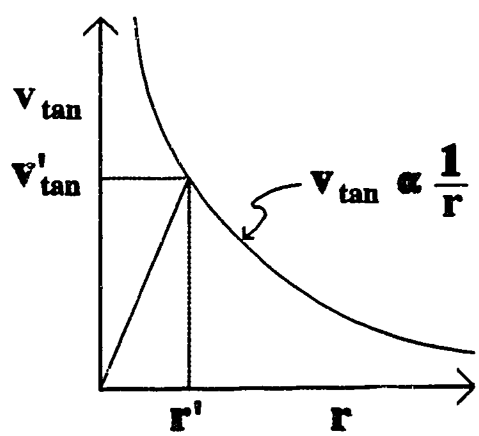

Figure 2.3 Vortex with Rankine Core.

Figure has been removed due to copyright restrictions

Figure 2.4 Lanchester's drawing of vortex system behind a wing, adapted from Lanchester (' '07).

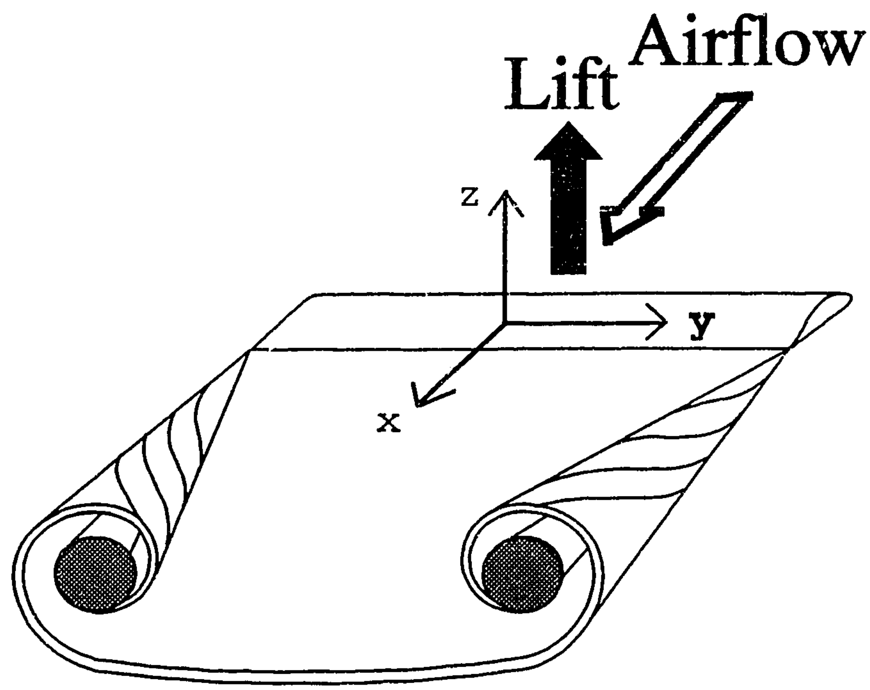

Figure 2.5 Vortex Roll Up Behind a Lifting Wing.

Figure has been removed due to copyright restrictions

Figure 2.6 Betz vortex roll-up model, adap[illegible] from Donaldson *et al.* (1974).

Figure has been removed due to copyright restrictions

Figure 2.7 Isopleths of Vorticity for a Vortex Pair Descending near Ground Plane, adapted from Bilanin *et al.* (1978).

Figure has been removed due to copyright restrictions

Figure 2.8 Effect of Secondary Vortex on Trailing Vortex Motion

Figure has been removed due to copyright restrictions

Figure 2.9 Vortex Core Visualization by Tower Fly By, adapted from Olsen *et al.* (1971).

Figure has been removed due to copyright restrictions

Figure 2.10 Flow Streamlines, Tip Flow Angle, and Forward Thrust Component, adapted from Spillman (1987).

Figure has been removed due to copyright restrictions

Figure 2.11 Comparison of Analytical and Experimental Winglet Pressure Distributions, adapted from Ishimitsu and Zanton (1977).

Figure has been removed due to copyright restrictions

Figure 2.12 Winglet Effects on Spanwise Pressure Distributions, adapted from Ishimitsu and Zanton (1977).

Figure has been removed due to copyright restrictions

Figure 2.13 Winglet Effects on Chordwise Pressure Distributions, adapted from Ishimitsu and Zanton (1977).

Figure has been removed due to copyright restrictions

Figure 2.14 Whitcomb Winglet, adapted from O'Callaghan (1988)

Figure has been removed due to copyright restrictions

Figure 2.15 Induced Efficiency and Wing Root Bending versus Winglet Length and Cant Angle, adapted from Dahlin (1981).

Figure has been removed due to copyright restrictions

Figure 2.16 Induced Drag versus Percentage Change in Root Bending Moment, adapted from Asai (1985).

Figure has been removed due to copyright restrictions

Figure 2.17 Induced Plus Parasite Drag versus Percentage Change in Root Bending Moment, adapted from Asai (1985).

Figure has been removed due to copyright restrictions

Figure 2.18 Winglet Twist, adapted from Spillman (1978 and 1987).

Figure has been removed due to copyright restrictions

Figure 2.19 Induced Efficiency Factor for ... versus Wing Tip Extensions for Two Span Loadings, adapted from Dahlin (1981).

..gure has been removed due to copyright restrictions

Figure 2.20 Ratio of Induced Efficiency Factors for Winglets versus Plain Wing Tip with Washout = 0°, adapted from Heyson *et al.* (1977).

Figure has been removed due to copyright restrictions

Figure 2.21 Ratio of Induced Efficiency Factors for Winglets versus Plain Wing Tip with Washout = 5°, adapted from Heyson *et al.* (1977).

Figure has been removed due to copyright restrictions

Figure 2.22 Ratio of Induced Efficiency Factors for Winglets versus Plain Wing Tip with Washout = 10°, adapted from Heyson *et al.* (1977).

Figure has been removed due to copyright restrictions

Figure 2.23 Winglet Configuration of Küppers (adapted from Küppers, 1983).

Figure has been removed due to copyright restrictions

Figure 2.24 Energy in Multiple Vortices, adapted from Küppers (1983).

Figure has been removed due to copyright restrictions

Figure 2.25 Induced and Skin Friction Drag for Multiple Vortices, adapted from Küppers (1983).

Figure has been removed due to copyright restrictions

Figure 2.26 Wingtip Sails, adapted from Spillman (1987).

Figure has been removed due to copyright restrictions

Figure 2.27 Relation between ΔC_{Di} and C_L with Winglets, adapted from Ishim a and Zanton (1977).

APPENDIX 2.A. SAMPLE CALCULATIONS FOR THE FORWARD THRUST COMPONENT OF A WINGLET NORMAL FORCE VECTOR

The following is a sample calculation to demonstrate the magnitude of the forward thrust component of the winglet normal force vector. This forward thrust component directly counters the drag of the aircraft, and generally is considered as a reduction of induced drag.

Assume that the winglet operates at the same C_L as the wing, and that the forward thrust component is $\sim(1/5)$ of the normal force of the winglet (i.e. 11.5° local cross flow angle), and that the winglet area is 1% of the wing area.

Now,

$$L/D = (C_L/C_D) = \text{Lift-Drag ratio of aircraft}$$

Now assume that $L/D = 50$ (or $D = L/50$).

Also, the forward thrust component, F_T, is

$$F_T = (1/5)\,(0.01)\,L = (L/500).$$

But we have $D = (L/50)$, thus,

$$(F_T/D) = [(L/500)/(L/50)] = (1/10)$$

Hence, the forward thrust component is 10% of the *total* drag of the aircraft wing.

Similarly, if $L/D = 20$, then $(F_T/D) = (1/25) = 4\%$, which is still a significant amount.

Note that these values do not account for the total induced drag reduction possible by the use of winglets, therefore this forward thrust is only one part of the drag reduction mechanism by winglets.

CHAPTER 3

WINGLET FORWARD THRUST QUANTIFIED and the MECHANISM of INDUCED DRAG REDUCTION[1]

3.1 INTRODUCTION

What are winglets? What are they supposed to do, and do they actually help? These are some frequently asked questions about winglets. Winglets are a passive drag reduction device aimed at reducing the induced or trailing vortex drag of a wing. They are typically reduced chord tip extensions, which are usually oriented vertically. Basically, the winglet is a smaller wing attached to the tip of the main wing. By observing the aircraft that are currently on the market, one quickly notes that winglets are on many aircraft today. For instance, the Gates LearJet 28L Longhorn, BOEING 747-400, Airbus A320, and the Canadair 601 and RJ, to name just a few.

Winglets are designed to reduce the induced drag (also called the trailing vortex drag) of a finite wing. The induced drag is the drag of a finite wing due to the trailing vortex system. The trailing vortex system induces a downwash at the wing and tilts the lift vector into the downstream direction. The result is that there is a component of the lift in the downstream direction which is then considered to be the induced drag or trailing vortex drag, as shown in Figure 3.1.

The structure of the trailing vortex system (or trailing vortex wake) is dependent on the spanwise loading of the wing generating the wake. The optimum spanwise loading of a wing is elliptical, as every good student of aerodynamics will remember. With respect to induced drag the elliptical loading has been "known" to be the most efficient ever since that was proven by Munk (1921). However, as will be shown in this study, with tip modifications such as winglets, one still can produce some reduction of the induced and total drag, for a given wing span, even with an initially elliptical wing loading. The explanation for this apparent incongruity lies with the assumptions leading to the result that the optimum spanwise loading

---

[1] A version of this chapter was presented at the 5th CASI Aerodynamics Symposium, Canadian Aeronautics and Space Institute 42nd Annual Conference, Montreal, Quebec. May 08-10, 1995.

is elliptical for a given wing span. These assumptions are: 1) a planar wing, 2) uniform downwash at the wing, 3) small induced velocities (due to a low average lift coefficient of the wing), and thus, 4) the rigid wake. Note that under these assumptions the elliptical loading can be accomplished by an elliptical planform. The planar wing assumption is a key assumption to explaining why and how winglets work. Note that non-planar wings are very different. Therefore, this paper will comment on ***dispelling the myth that the elliptical spanwise loading is optimum.***

Precisely what is the mechanism of drag reduction by a winglet? There has always been debate about how winglets work, or even if they can produce an induced and total drag reduction on any given wing. Some researchers suggest that winglets produce a forward thrust, but they don't know or state the quantity of that thrust (Spillman, 1978 and 1987). Others say that winglets operate by splitting the vorticity and thus reduce the kinetic energy in the wake (Küppers, 1983). (The matter of kinetic energy reduction in the wake is really just a manifestation, in the wake of the wing, of the winglet influence at the wing itself.) A few have suggested that the main reason is a reduction of induced drag all along the span. The latter has been demonstrated by the experimental technique of measuring the change in mid-span lift coefficient to determine the magnitude of the drag reduction due to winglets (O'Callaghan, 1988). This paper will help to show clearly the nature of the mechanism by which winglets produce the drag reduction.

The main focus of this paper will be to explain the mechanism of the induced drag reduction produced by winglets and to show the relative importance of the forward thrust due to the winglet compared to the reduction of induced drag along the span of the main wing. The forward thrust of a winglet is basically a *negative induced drag*. This is sketched in Figure 3.2 for the cases of a reduced chord vertical and a horizontal winglet (i.e. winglet root chord is substantially less than the tip chord). As seen in the figure, in both cases the induced flow field at the wing tip where the winglet is attached [illegible]ses there to be a negative induced drag or forward thrust by a winglet. As will be shown, the other m[illegible]n by which winglets reduce drag is by the reduction of the downwash along the entire span of the [illegible] Figure 3.3 shows a sample of this downwash reduction for a small winglet on an elliptical wi[illegible] that the figure clearly shows that this downwash reduction is along the entire wing span, hence leads [illegible] reduction of induced drag all along the span of the main wing. This downwash reduction is due in part to the vorticity redistribution at the tip of the wing and also to the change in spanwise loading of a wing with a winglet attached.

The explanation of how winglets work will proceed as follows. The general winglet design and the parameters involved will be discussed. Then the necessary background theory will be discussed, followed by the computer model which was employed. The results of the studies will be given and finally some conclusions will be drawn.

3.1.1 The General Winglet Design Problem

Winglets are wing tip modifications which are different from a simple wing extension in that the wing extension would have the same chord as the wing at the junction with the wing. In contrast, winglets are extensions to the wing which have a marked reduction of chord at the junction with the main wing. This feature allows the (single) winglet to produce a trailing vortex system which has a double vortex core structure, giving a broader distribution of the vorticity in the core region. This vorticity redistribution leads to the effective induced drag reduction attributed to the winglet, due to both the reduction of downwash along the span and the forward thrust of the winglet itself.

The design of a specific winglet involves numerous parameters. These include: the winglet airfoil, the winglet span, the winglet root chord and tip chord (hence the winglet taper ratio), the winglet dihedral angle, the winglet root toe-in and the winglet tip toe-in (hence the winglet twist), the winglet sweep angle, the placement and design details of the wing-winglet junction, and the winglet tip shape. These were chosen since these parameters are sufficient to completely specify the requirements for the design of a particular winglet. In general, aside from the operational or performance related parameters, some consideration is often given to aesthetics of a particular winglet design.

3.1.1.1 The Winglet Airfoil

The winglet airfoil used for this study is designated by UA(2)-180, a good low Reynolds number airfoil developed at the University of Alberta by Dr. D.J. Marsden (1988). The UA(2)-180 airfoil is a 18% thick airfoil with a convex upper and lower surface. The absence of concave surfaces allows easy construction of the airfoil shape.

Optimizing a winglet design for a particular wing involves matching the winglet airfoil characteristics to the desired operating conditions. The importance of the winglet airfoil is related to the amount of the reduction of induced drag and at the same time the increase in profile drag of the winglet. There will also be a need to strike a balance between the potential improvements at the different operating conditions to be encountered. Specifically, it is important to use an airfoil with a low drag region ("drag bucket") which covers the range of lift coefficients at which the winglet is operating. If the range of operating lift coefficients is outside of the "drag bucket" then the decision must be made as to where the greatest penalty will occur. The UA(2)-180 was chosen since the range of low drag lift coefficients corresponds well to the range of desired winglet lift coefficients (roughly 0.6 to 1.2), and the off design profile drag penalty is not severe.

3.1.1.2 The Winglet Span and the Winglet Size

The winglet span (or length of the winglet) is one of the most obvious variables. However, what is not so clear is exactly how to relate that to the other parameters. For this study, the winglet span is used to define each winglet size. This is done by using a paricular typical winglet "family." This winglet family is defined by a set of winglets all possessing the same general qualities. Specifically, the winglet root chord is one half of the winglet length, and the winglet tip chord is one quarter of the winglet length. This gives a set of winglets all having a taper ratio equal 0.5, and the winglet aspect ratio is 5.33 when the winglet semi-span is considered to be the winglet length from root to tip. The end result is that each member of this winglet "family" looks just like a scale version of any other in the same family. Also, note that with this "family" of winglets, the winglet area equals (3/8)x(winglet span)^2.

3.1.1.3 The Winglet Root Chord, Root Toe-in, Taper Ratio, and Twist

Once the winglet airfoil has been chosen, the winglet root chord and root toe-in controls the amount of circulation moved onto the winglet, and hence governs the maximum normal force that the winglet may produce. The taper ratio along with the winglet twist determines the spanwise loading of the winglet itself, thus controlling the location of the centroid of vorticity for the winglet. (The reader is referred to Chapter 2, section 2.2.4 for the discussion of vortex sheet roll-up.) Also, notice that the winglet toe-in and twist affect the winglet local C_l and hence the profile drag of the winglet

3.1.1.4 The Winglet Sweep Angle

The sweep angle of a wing is usually defined in terms of either the leading edge sweep or the sweep of the quarter chord line. The latter definition is used here. The sweep angle may be chosen to minimize Mach number effects, however very often the sweep is chosen more on the basis of aesthetics. Since this study is for incompressible flow, all winglets examined have zero quarter chord sweep.

3.1.1.5 The Winglet Dihedral Angle

The dihedral of the winglet has a significant effect on the bending moment at the root of the wing and along the wing. According to the definition for this study, the dihedral is defined with respect to the horizontal plane, such that a horizontal winglet would have 0° dihedral angle. Thus, the winglets which are modelled all have a diheral angle of 90° which produces a straight vertical winglet, with no resulting increase of wing span.

3.1.1.6 The Wing-Winglet Junction

The design of the geometry of the wing-winglet junction is a significant challenge. The actual final shape is very difficult to optimize, hence is usually done with wind tunnel experiments to ensure attached flow in the wing-winglet junction region. Basically, the winglet root region must be faired into the wing at the tip. The radius of the faired region should increase towards the trailing edge of the wing so as to reduce the adverse pressure gradient within the junction region as the air flows chordwise from the leading edge to the trailing edge.

The location of the winglet fore and aft on the wing tip is also a design parameter. For the study

2

PM-1 3½"x4" PHOTOGRAPHIC MICROCOPY TARGET
NBS 1010a ANSI/ISO #2 EQUIVALENT

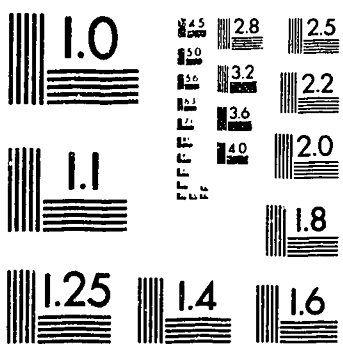

PRECISION℠ RESOLUTION TARGETS

at hand the quarter chord line of the winglet is aligned with the quarter chord of the wing at the tip. The merit in the particular location depends on the flight velocity and Mach number expected for the wing, as well as structural dynamic considerations.

3.1.1.7 The Winglet Tip Shape

Just as the main wing tip shape determines the wing induced drag, the winglet tip shape determines to some degree the induced drag of the winglet. However, it is clear that the size of the winglet is much less than the main wing, therefore the benefits gained by optimizing the winglet tip shape are very small. Realistically there is a trade-off made between the efficiency gain possible, the increased cost of construction, and aesthetics. For simplicity of construction the recommended winglet would have an efficient wing tip shape such as the Hoerner tip, which many consider to be aesthetically pleasing.

3.2 THEORY and METHOD

3.2.1 Theory for the Wing Loading and the Trailing Vortex Wake

A lifting body produces its lift by generating vorticity. For an aircraft wing producing lift, this vorticity is distributed in the three dimensions of the wing and is considered bound to the wing itself. The bound vorticity distribution is dependent on the geometry of the wing in three dimensions, but most significant is the spanwise distribution of that bound vorticity. The significance is due to the fact that the spanwise loading of the wing is determined by the spanwise distribution of bound vorticity. The orientation of the bound vorticity vector is generally considered to be along the spanwise direction of the wing. Since vorticity or vortex filaments cannot simply terminate within a fluid, the vorticity trails off the wing in the downstream direction. The trailing region of the wing sheds the vorticity as a three dimensional vortex sheet while the aircraft moves longitudinally. The result is the aircraft wake which is a three dimensional region of vorticity which induces a flow field. That induced flow field combined with the ambient air movement, and the aircraft velocity (hence, the location of the bound vortex system), all contribute to the way in which the trailing vorticity itself moves.

3.2.1.1 Quantifying Vorticity and the Circulation Generated by a Lifting Wing

The general case of the induced velocity field and the aerodynamic forces for a finite wing is given by Cone (1962). Cone presents a formula which clearly shows the air velocities involved in calculating wing loading. Using the notation of Cone (1962) for Equations 3.1 and 3.2, the total velocity is $\bar{q}(s)$, at a point along the arc of the wing, s, where r is the distance vector from the vortex element to the point on the arc. $\bar{q}(s)$ is given by the sum of the velocity at a point due to the freestream, $\bar{V}$, the induced velocity, $\bar{q}_\Sigma$, due to the semi-infinite vortex sheet which has the vorticity intensity vector given by $\bar{\Omega}_\Sigma$ at the elemental area of the vortex sheet dS, and the induced velocity due to the bound vorticity of the wing, $\bar{q}_s$, where $\bar{t}$ is the unit tangent vector along the arc giving the orientation of the bound vorticity, $\Gamma(s)$.

$$\bar{q}(s) = \bar{V} + \overline{q_\Sigma} + \overline{q_s} = \bar{V} + \frac{1}{4\pi}\iint^{\Sigma} \bar{\Omega}_\Sigma \times \frac{\bar{r}}{r^3}\,dS + \frac{1}{4\pi}\int^{s} \Gamma(s)\,\bar{t} \times \frac{\bar{r}}{r^3}\,ds \tag{3.1}$$

Thus, the for that spanwise location on the wing, the aerodynamic force per unit length, $\bar{F}$, is a sum of the lift, $\bar{L}$, the induced drag, $\bar{D}_i$, and the self induced force, $\bar{F}_i$.

$$\bar{F} = \rho\,\bar{q}(s) \times \Gamma(s)\bar{t} = \rho\,(\bar{V} + \overline{q_\Sigma} + \overline{q_s}) \times \Gamma(s)\bar{t} = \bar{L} + \overline{D_i} + \overline{F_i} \tag{3.2}$$

Note that the self induced force is negligible for a near planar wing (where the bound vortices are nearly parallel, giving $\Gamma(s)\bar{t} \times \bar{r} \approx 0$), hence for this reason is generally neglected. However in this study of nonplanar wings the self induced force must be and is included. (The computer model used for this work includes all of the components of the aerodynamic force and stores them separately to facilitate analysis of the results.)

As noted, a lifting body or wing produces lift by generating vorticity. This vorticity can be quantified by the *circulation*, Γ, which is a measure of ω, the component of the vorticity, $\bar{\omega}$, normal to the area, $\bar{A}$.

$$\Gamma = \iint \omega \, dA = \iint \bar{\omega} \cdot d\bar{A} \tag{3.3}$$

Alternately, circulation can be given as the line integral of the tangential vel... component around any closed circuit in a fluid. If the closed circuit is taken around the center of a vortex, then the circulation is called the strength of the vortex. (Basically, a line vortex is a line or chain of fluid particles spinning on a common axis and carrying around with them a swirl of fluid particles which flow around in circles (Houghton and Carruthers, 1982).)

$$\Gamma = \oint \bar{v}_{tan} \cdot d\bar{s} \tag{3.4}$$

where, v_{tan} is the tangential velocity and ds is an element of the arc length around the closed circuit.

For a circular contour of radius, r, this becomes:

$$\Gamma = 2 \, \pi \, r \, v_{tan} \tag{3.5}$$

The total circulation generated by the wing, Γ_o, is the local change in the circulation, $d\Gamma(y)/dy$, integrated across the semi-span, $b/2$.

$$\Gamma_o = -\int_o^{b/2} \frac{d\Gamma(y)}{dy} \, dy \tag{3.6}$$

Notice that the total value, Γ_o, corresponds to the circulation of the wing in the plane of symmetry which is at the centerline.

As shown by McCormick (1979), the circulation at each spanwise location, y, can be given by:

$$\Gamma(y) = \frac{1}{2} \, c(y) \, C_\ell(y) \, V(y) \tag{3.7}$$

where,

$$C_\ell(y) = C_{\ell o}(y) + C_{\ell \alpha}(y) \, \alpha(y) \tag{3.8}$$

and,

$$\alpha(y) = \alpha_{init}(y) - \frac{v_{normal}(y)}{V(y)} \tag{3.9}$$

where, $c(y)$ is the local chord, $C_\ell(y)$ is the local lift coefficient, $V(y)$ is the local streamwise air velocity, $C_{\ell o}(y)$ is the local lift coefficient at $\alpha = 0°$, $C_{\ell\alpha}(y) = dC_\ell(y)/d\alpha$ is the local lift curve slope, $\alpha(y)$ is the local angle of attack, $\alpha_{init}(y)$ is the angle of attack due to the initial wing incidence and air velocity without the downwash considered, $v_{normal}(y)$ is the induced velocity component normal to the local wing section at y. The rate that circulation is shed at any spanwise location can be determined by the spanwise rate of change of circulation of the wing, $d\Gamma(y)/dy$.

As given by Houghton and Carruthers (1982), the distribution of the load on a wing is related to the bound circulation distribution (where $\Gamma(y)$ can be determined from Equation 3.7) since the circulation generates the lift per unit span at any spanwise location equivalent to $l(y)$.

$$l(y) = \rho V(y) \Gamma(y) \tag{3.10}$$

Where, ρ is the air density, and $V(y)$ the local streamwise air velocity. Hence, the total lift of the wing is given by:

$$L = \int_{-b/2}^{b/2} l(y)\, dy \tag{3.11}$$

3.2.1.2 **Vortex Sheet Roll-Up**

For an actual wing, vorticity is first shed from the trailing edge region of the wing as a vortex sheet. The circulation distribution, $\Gamma(y)$, on a three dimensional wing is determined largely by the planform, airfoil shape, wing twist, and flap deflection along the span. Hence, those parameters of the wing determine $d\Gamma(y)/dy$, also. As was noted by Bilanin and Donaldson (1975) the vortex sheet starts to roll up at local maximums of $d\Gamma(y)/dy$. For conditions of a smooth planform and no flap deflection, the vortex sheet rolls up, starting at the wing tips, into two discrete vortices trailing the wing. When a wing with winglets is considered, there is more than one location for roll-up in the near wake. The shed vortex sheet rolls up into discrete trailing vortex cores. This roll-up starts at the positions of the local maximum $d\Gamma(y)/dy$, specifically at the tips of the main wing and at the tips of the winglets. These later amalgamate into a trailing vortex from each semi-span, giving the more familiar pair of counter rotating tip vortices, one from each semi-span. Figure 3.4 shows a general idea of the vortex sheet roll-up for the conditions of a smooth planform and no flap deflection.

A wing with winglets will produce a multiple core vortex system, in the early stages. In these early stages of the wake development, the local centers of vorticity determine the local vortex core development. These vortex cores will wrap or rotate around each other in the wake. Later in the wake development downstream, the center of vorticity (where the center of vorticity is much like a center of gravity) of the wing semi-span as a whole is dominant, and the multiple vortex cores merge to become a single vortex core per semi-span.

For the purposes of this study, the vortex sheet is considered to be "rigid." This "*rigid wake*" *does not roll up*. However, the actual initial location of the shed vortex sheet is dependent on the geometry of the wing which is modelled. Therefore note that winglets will cause the shed vortex sheet to be nonplanar even without the wake roll-up.

3.2.1.3 **The Induced Velocity of a Vortex**

A lifting wing sheds a vortex sheet which is dependent on the spanwise loading of that wing (more accurately, the arc-wise loading). The shed vortex sheet itself has a dominant influence on the load distribution of that wing. This occurs since the downwash distribution is determined largely by the induced velocity field of that vortex wake. As will be discussed later, the vortex wake is discretized into trailing vortex filaments which are modelled as semi-infinite line vortices, parallel to the longitudinal axis of the aircraft, with a Rankine core. The bound vortices are modelled as finite vortex elements. As given by Houghton and Carruthers (1982), Figure 3.5 shows that for a finite vortex element the induced velocity, v_{tan}, is given by:

$$v_{tan} = \frac{\Gamma}{4\pi r}(\cos\beta_1 + \cos\beta_2) \tag{3.12}$$

where, r is the perpendicular radius from the axis of the vortex element, and β_1 and β_2 are the included angles to the respective ends of the finite vortex element. For a semi-infinite vortex (i.e. a vortex with one finite end location, such that $\beta_2 \neq 0$), the angle to the second end of the vortex is zero, $\beta_1 = 0$, hence the induced velocity, v_{tan}, is given by:

$$v_{tan} = \frac{\Gamma}{4\pi r}(1 + \cos\beta_2) \tag{3.13}$$

In order to avoid singularities when exactly on a vortex axis, the modelled vortices use a Rankine vortex core. For a Rankine vortex the induced velocity is the same as that given above while *outside* of the core radius, $r > r'$. However, *within* the core of a Rankine vortex, $r \leq r'$, the induced velocity is given by:

$$v_{tan} = \frac{\Gamma\, r}{4\pi(r')^2}(\cos\beta_1 + \cos\beta_2) \tag{3.14}$$

To determine the induced velocity for a semi-infinite trailing vortex filament parallel to the positive x-axis simply let $\beta_1 \to 0$ and $\beta_2 \neq 0$.

Thus we can get the induced velocity components in an xyz Cartesian coordinate system at point P at (x_p, y_p, z_p). The Cartesian coordinate system which is used for this work is shown in Figure 3.4. The vortex location is given by (x_v, y_v, z_v). Now with the circulation positive (according to the right hand rule: right hand thumb along the axis) we get the following velocity components:

$$v_y = -v_{tan}\left(\frac{\Delta z}{r}\right) \tag{3.15}$$

$$v_z = v_{tan}\left(\frac{\Delta y}{r}\right) \tag{3.16}$$

where, $\Delta x = x_p - x_v$, $\Delta y = y_p - y_v$, and $\Delta z = z_p - z_v$. Now for a bound vortex element parallel to the positive y-axis (note typically: $\beta_1 \neq 0$ and $\beta_2 \neq 0$) with positive circulation, we get:

$$v_x = v_{tan}\left(\frac{\Delta z}{r}\right) \tag{3.17}$$

$$v_z = -v_{tan}\left(\frac{\Delta x}{r}\right) \tag{3.18}$$

3.3 THE COMPUTER MODELS

The research involved the computer simulation of a winglet attached to a wing. The main task was that of determining the spanwise loading and drag for each wing with and without winglets. As mentioned, the wake is assumed to be rigid.

3.3.1 The Computer Model for the Aircraft Wing Loading and the Wake

The aircraft wing loading and vortex wake is modelled using a simplified vortex lattice method (VLM). The VLM involves replacing the wing and the trailing vortex sheet by a discrete number of horseshoe vortices. The finite bound vortex lies on the wing quarter chord position and the semi-infinite trailing vortices extend in the streamwise direction. The current model allows most of the wing geometry to be included, although the effects of wing thickness and chordwise variation effects are not considered. This model is based on the equations by Cone (1962). The VLM computer model solves for the spanwise circulation distribution, $\Gamma(y)$, considering the velocity field from trailing vortex filaments, and the velocity field from the bound vortex elements with the 3-D effects of the non-planar wing included.

Note that the airfoil characteristics at each wing section are incorporated in the model. The airfoil lift curve is represented as a linear function which is capped at the maximum lift coefficient, $C_{l\max}$, as shown in Figure 3.6, and given in Equation 3.19. The fluid viscous effects are included by determining the profile drag of each wing section. This is is accomplished by employing a parabolic function for the C_D-C_l from the airfoil drag polar as shown in Figure 3.7, and given in Equation 3.20. These allow reasonable approximation for the lift and drag characteristics of any airfoil used for a wing.

$$\begin{aligned} C_l(y) &= C_{l_o}(y) + C_{l_\alpha}(y)\ \alpha(y) \quad , && \leq C_{l\max} \\ &= C_{l\max} \quad , && > C_{l\max} \end{aligned} \tag{3.19}$$

$$C_D(y) = C_{d_{min}}(y) + C_{d_{fac}}(y)\ (C_L(y) - C_{lCd_{min}})^2 \tag{3.20}$$

As given in Figure 3.7 $C_{d_{min}}$ is the minimum C_d, $C_{lCd_{min}}$ is the C_l at which $C_{d_{min}}$ occurs, and $C_{d_{fac}}$ is the parabolic shape function.

The simplified vortex lattice method is used to study the individual components of the total drag of a lifting wing. The profile drag and the induced drag are examined separately along the main wing and winglet span. This model gives a good first estimate of the change of the coefficients of induced drag, ΔC_{Di}, and total drag, ΔC_{DTotal}, due to a winglet application on a wing. Hence, the actual mechanism for winglet effectiveness in producing a drag reduction is shown clearly. When considering the total drag reduction attributable to winglets one must consider the additional profile drag produced (Asai, 1985). This includes both the increased profile drag due to the winglet itself and the change in profile drag of the main wing especially in the tip region.

A winglet will be shown to produce significant induced drag reduction all along the span of a wing, as well as providing a *forward thrust* (or negative induced drag) component on the winglet itself, hence, reduction of the total drag of a wing. The wing bending moment has been calculated for the wings considered in this study.

The model used for determining the aircraft wing loading is a simplified vortex lattice model with a rigid wake. By the term "rigid wake" it is meant that the trailing vortex filaments are semi-infinite line vortices which remain in their initial positions attached to the wing and trail off to infinity. Hence, the induced velocity field used in determining the wing loading is that due to those trailing vortices while attached to the wing. Figure 3.8 shows the main set up of the vortex lattice system on the wing. The wing spanwise circulation distribution and loading is determined by simultaneous solution of the equations for $l(y) = \rho V(y)\Gamma(y)$; where $\Gamma(y)$ is dependent on $C_l(y)$ which is dependent on the induced velocity at y, which is itself dependent on $\Gamma(y)$. The total circulation contained in the system of trailing vortex filaments from each wing is equal to the total circulation generated by the wing. The local circulation at any spanwise location of the wing is considered to be produced by the bound vortex element, which is a vortex element located at 25 percent chord and at the center of that spanwise element. The spanwise extent of each bound vortex element is determined by the initial spanwise separation of the two trailing vortex filaments. One vortex filament trails off the inboard side of the spanwise element, while the other vortex filament trails off the outboard side of the spanwise element. These trailing vortex filaments are attached to the wing at 25 percent local chord so as be continuous with the bound vortex elements.

The aircraft wake model is based on a free flight condition, meaning that the aircraft is clear of the ground or any other boundaries. The spanwise loading is determined by the spanwise circulation distribution. Appendix 3.A gives the development of the equations from which the model is programmed, and the method used to arrive at the solution.

For the current study the computer model limitations led to the following. The interference effects of the winglet and wing at the tip can not be determined. The problem of the winglet root junction to the main wing is not trivial, and generally extensive wind tunnel testing is required to develop a fully attached flow regime within the region. An assumption made for this model is that attached flow is achieved on both the wing and winglet (no flow separations), and that the 2-D airfoil properties on the winglet and those of the main wing near the tip are not substantially altered due to interference effects.

3.3.2 Computer Model Verification

The computer model verification was done to ensure accuracy of the calculations. These tests included comparisons with known wings for the spanwise distribution of circulation and lift coefficient. Also, the induced drag component was verified by examining various known taper ratios. Also, included is a demonstration that the vortex sheet discretization was sufficient.

A necessary first step in using the computer model was the confirmation of the computer model's ability to accurately perform circulation and lift calculations. This was done by calculation of the circulation distribution and lift coefficient variation along the span for the four wing types to be used and comparing them with the known lift distributions for these wing shapes. These were the elliptical wing, and linearly tapered wings with taper ratios 0.4, 0.6, and 1.0. The computer model calculations of the circulation distribution for wings of aspect ratio 12.7 are show in Figures 3.9. (The wing modelled here had 15 m span, and was at C_L = 1.13.) Note that the shape of the curves are the important feature, and that the particular values for the circulation distributions are for specific conditions and can be scaled by any valued desired. The results can be compared with information shown in Figure 3.10 from McCormick (1979) for A_R = 6.0. These figures can be compared examining the circulation at the centerline (where y/b = 0) for the elliptical and rectangular wings, giving $\Gamma_{0\,ell}$ and $\Gamma_{0\,rec}$ respectively. For this VLM model, $\Gamma_{0\,ell} / \Gamma_{0\,rec} = 24.0 / 20.7 = 1.16$, and McCormick's shows $\Gamma_{0\,ell} / \Gamma_{0\,rec} = 0.180 / 0.152 = 1.18$. Thus, this VLM model is within 2.1% of that of McCormick. These calculated circulation distributions compare with acceptable accuracy with those numerical results by McCormick which were calculated using a vortex lattice method.

The VLM computer model calculations for the normalized lift coefficient (C_ℓ/C_L) for the same four wings as above are given in Figure 3.11. Note that the curve for the elliptical wing should show the value of C_ℓ/C_L = 1.0 across the entire span. The calculations show this to be the case for most of the span, but that near the tip region the value increases to greater than 1.0. This is due to the upwash at the tip region, as a result of the vortex sheet discretization. Notice that this effect was also seen in Figure 3.3 showing the downwash comparisons for a sample winglet and for the case of no winglet on an elliptical wing. This effect is well known for vortex sheet discretizations using the same sign of vorticity (Rossow, 1992) which causes the last two vortices near the wing tip to experience an upwash at the start of roll-up. Note that the Figure 3.11 compares favorably with that given by McCormick (1979) shown in Figure 3.12, and that McCormick's figure shows the same phenomenon of increased C_ℓ/C_L near the tip. The comparisons of the calculations for the normalized lift coefficient (C_ℓ/C_L) by this VLM model are seen to be within 2.5% of those given by McCormick (1979), when comparing the centerline values.

The induced drag calculations will form the most important information to be determined by this study. Therefore, for a comparison of induced drag calculations, the computer model is used to provide curves of Effective Aspect Ratio Factor versus Taper Ratio for untwisted, linearly tapered wings. The effective aspect ratio factor, e, is given by $C_{Di} = C_L^2 / (\pi\, e\, A_R)$. This information is presented in Figure 3.13 for the aspect ratios 8.0, 10.0, 12.7, 15.0, 20.0. Similar curves are given by Abbott and von Doenhoff (1959) and McCormick (1979), which are shown in Figures 3.14 and 3.15, respectively. Note that both of these other figures are in slightly different format, however can be used for comparison. Again, the comparisons of the calculations for the effective aspect ratio factor by this VLM model are seen to be in excellent agreement with others. These results are within 1.5% of those given by Abbott and von Doenhoff (1959). Also, these are within 3% of those given by McCormick (1979). Notice that McCormick uses the form $C_{Di} = C_L^2\,(1 + \delta) / (\pi\, A_R)$, such that $e = 1 / (1 + \delta)$.

For the simulations performed, there were 59 bound vortex elements and 59 vortex filaments used to model each semi-span of each planar wing, and an additional 10 of each were used when a winglet was considered. This number proved to be sufficient to give reasonable results which could be done even on an IBM 386 desktop computer, and kept the computational time required very reasonable at about 40 seconds per run. (The odd numbers are due to the effect of the aircraft centerline with the method used for discretizing the wing span.) Figure 3.16 shows the relation between the Effective Aspect Ratio Factor and the number of vortices per semi-span for the case of an elliptical wing with A_R = 12.73 (the figure shows points for discrete numbers of vortices from 9 + 10n to 99, and from 99 + 100n to 999, where n = 1, 2,...9). Note that the value of the effective aspect ratio for the elliptical wing should be 1.0. Noting the verical scale, as the figure shows, even a small number of vortices (as few as 19 per semi-span) proved to be adequate to give accurate results (i.e. 19 vortices gave e >0.993, and 59 vortices gave e >0.999). The calculations for this work were done with 59 vortices on the main wing, since the use of a greater number only increased computation time without any substantial increase in accuracy. Note that Figure 3.16 shows the value of e slightly > 1.0 for greater than 79 vortices. This happens due to the vortex sheet discretization process, which as mentioned by Rossow (1992) causes an upwash at the outer 2 vortices. This upwash tends to increase the apparent efficiency of the wing by a very small amount. There is no real concern with this since the same phenomenon happens for each wing, thus the relative merits of different cases will still be correct. As shown, this VLM method gives the effective aspect ratio factor accurate to within 0.1% of the correct value for an elliptical wing.

These favourable comparisons of the results of this model for planar wings with those from other researchs gives confidence that this VLM model may be used to provide at least relative comparisons between different wing configurations, even when extrapolated to the case of a nonplanar wing.

The comparisons thus far have been for the conditions of planar wings only. The verification of the model for non-planar wings was less straight forward since the available data for comparison was more limited.

Recall from Chapter 2, Ishimitsu and Zanton (1977) of Boeing have done a fairly comprehensive study of the retrofit of winglets to the KC-135 air transport. They used a potential, 3-D flow theory then strip theory of boundary layer growth (Boeing programs: TEA 230, 372, 200, and 242) and found good correlation of theoretical predictions with experimental results (see Chapter 2, Figure 2.8). They found that the addition of winglets caused greater loading of the wing toward the outboard span locations (for an example of their results see Chapter 2, Figure 2.9). They also found that the chordwise pressure distribution at about 90% span and greater was significantly effected by the winglet local pressure field (see Chapter 2, Figure 2.10).

The specific information about the winglet design from other studies, was not available to allow modelling of the same case. However, using the VLM for the wings of this study a similar increase in loading near the wing tip was determined. This similarity adds credibility to the usefulness of this model for non-planar cases.

Figures 3.17 and 3.18 showing the span loading (or circulation) for a wing with a winglet addition on an elliptical wing and on a wing with taper ratio 0.4. These figures show increased circulation on the outboard portion of the wing with a winglet. This is qualitatively consistent with the experimental work of Ishimitsu and Zanton (1977).

Later the results section presents predictions of percentage change in L/D for various wing and winglet combinations. As well, some of the results presented show the percentage $\Delta L/D$ versus the main wing C_L. This model predicts $\sim 3\%$ $\Delta L/D$ at $C_L \approx 0.4$ and $\sim 15\%$ $\Delta L/D$ at $C_L \approx 1.1$ depending on the wing and winglet combination. These values are similar to the findings of Ishimitsu and Zanton (1977), Spillman (1987) and others. The reader is referred to the literature review of winglets for a summary of the findings of others to note the similarity of these findings with other research.

The fact that other researchers such as Asai (1985) and Heyson *et al.* (1977) and others have used vortex lattice methods for determining winglet performance gives some confidence that the VLM is sufficient to give believable results. The accuracy of the model may not be perfect but the results are expected to be within about 15% of actual $\Delta L/D$ for the wing and winglet combinations examined. As well, since the model is based on a rigid wake the results for $\Delta L/D$ are expect to be slightly higher for the actual case including wake roll-up.

The credibility of these results for the predictions of percentage change in L/D gives confidence that the drag reduction mechanism determined is sufficiently accurate to predict the trends which show the importance of the forward thrust of the winglet and the induced drag reduction along the main wing span.

The comparison made here is of a more qualitative nature than those for the planar wings, however gives some assurance that the model can be used with reasonable confidence for the current study.

3.4 CONDITIONS MODELLED

The main variables considered are the main wing shape and the significant winglet parameters. Four different spanwise wing load distributions are considered. As well, a particular "winglet family" is modelled. However, the results from this family will help to show trends that will occur with other particular winglets.

3.4.1 Main Wing Types Modelled

There are four different main wing types modelled which are considered to represent a wide range of spanwise load functions. These are the elliptical wing, and three wings wings each with a linear taper. The taper ratios used are 0.4, 0.6, and 1.0. The value 0.4 is used since it is nearly what is considered to be the most efficient linearly tapered wing. (Note that untwisted wings with linear taper = 0.4 are not usually used due to their undesirable stall characteristics.) The taper of 1.0 corresponds to a rectangular planform wing which is commonly in use in general aviation, due to the ease of construction associated with that shape. All of the main wings that are examined are simple wings in that there are no discontinuities of the surface. Specifically, there are no flaps or ailerons, and the wings considered have no twist along the span. The main wing airfoil used is the NACA 64_3-618. Also, the airfoil section is unchanged for the entire span of the main wing of each test, although the characteristics of the main wing airfoil do have an affect on the results as shown later. The main wings are planar (i.e. zero dihedral) and have zero sweep of the quarter chord line. Also, the performance of the wing alone is determined with no consideration given to the fuselage or tail. Table 3.B.1 of Appendix 3.B gives the wing spans used at each A_R (for all taper ratios).

3.4.2 The Winglet "Family" Modelled

One of the comparisons is to be between a simple elliptical wing and one with a winglet attached. However, an elliptical wing has a zero tip chord which makes attachment of a finite chord winglet somewhat difficult. Therefore the elliptical wing has been modified to produce a finite tip chord. Figure 3.19 shows the method of extrapolating to a finite tip on an elliptical wing. In order to produce the modified elliptical wing, the elliptical wing used is one with a linear trailing edge and elliptically curved leading edge. As explained in Appendix 3.B, the modification was such that there was a tangent taken to the elliptical curve at some designated spanwise location. Then that tangent line was used to extrapolate to the same span as the original elliptical wing. Of course, since the total wing area would have been increased due to the increased tip area, the wing chord was adjusted all along the span to produce the same wing area as the basic elliptical wing. This chord adjustment produced a final wing with winglet with the same area and aspect ratio as the basic elliptical wing, hence comparisons are made correctly between resulting wings. This method of modifying the elliptical wing was used to produce three different winglet sizes, based on the linear taper of the elliptical wing from three semi-span locations $(y/(b/2)) = 0.7, 0.8$, and 0.9. For these, Winglet1 corresponds to the taper from $(y/(b/2)) = 0.7$, Winglet2 corresponds to the taper from $(y/(b/2)) = 0.8$, and Winglet3 corresponds to the taper from $(y/(b/2)) = 0.9$. This produces the three winglets in order of size such that: Winglet1 > Winglet2 > Winglet3. These three sizes of winglets were then attached to the four wings used in the study. Note that when the winglets were on the modified elliptical wings the winglet spans were always equal to the modified wing tip chord. However, when those same winglets were on the tapered wings they had three different ratios of winglet span to wing tip chord. The winglet sizes for two particular aspect ratios are given to provide an idea of the actual size of the winglets used. For a wing span 15 m and $A_R = 12.73$: Winglet 1 span = 0.61 m; Winglet 2 span = 0.45 m; Winglet 3 span = 0.34 m. For a wing span 11.89 m and $A_R = 8.0$: Winglet 1 span = 0.77 m; Winglet 2 span = 0.62 m; Winglet 3 span = 0.43 m. (Table 3.B.1 given in Appendix 3.B presents the wing and winglet geometry information for all of those used in the study.)

Also, note that the exact same *size* of winglet is used on each of the four wing types when they are compared at the same A_R. This means that two different wing shapes, at the same aspect ratio and wing span, will have the exact same winglet attached. Hence, comparisons between different planform wing shapes of the same aspect ratio and span can be made and still be meaningful. However, note that for wings of different aspect ratio, the winglet is actually a different physical size. This is since the winglet span is based on the wing tip chord of the modified elliptical wing. This produces larger winglets for low aspect ratios than for high aspect ratios. Note that since the winglets are scale versions of one another, the area of say winglet 1 on a wing of A_R1 is inversely proportional to the area of winglet 1 on a wing of A_R2, such that: $(Area_{Winglet1} / Area_{Winglet2}) = (A_R2 / A_R1)$. Also, note that with this "family" of winglets, the winglet area equals $(3/8)\times(\text{winglet span})^2$. Note that $(Area_{Winglet1} \approx 3 \times Area_{Winglet3})$ and that $(Area_{Winglet2} \approx 2 \times Area_{Winglet3})$.

For the winglet family used the other defining characteristics were as follows: The winglet span is equal to 1.0 times the modified elliptical wing tip chord, i.e. the tip chord which was produced by the linear extrapolation from the designated spanwise location on the elliptical wing. All of the winglets examined were vertical winglets (winglet cant angle = 90°). The winglets have no sweep of their quarter chord line. The winglet root chord equals the one half of that winglet span. The winglet root is set at a zero toe-in angle with respect to the freestream direction. The winglet tip chord equals one quarter of that winglet span. Hence, the winglet has 0.5 taper ratio and the winglet $A_R = 5.3$. At the winglet tip, the toe-in is set at 3° (unless stated otherwise), such that the winglet is twisted inboard at the leading edge. The quarter chord line of the winglet at the winglet root is aligned with the quarter chord line of the main wing at the main wing tip. Figure 3.20 shows a sketch of a typical winglet. For most comparisions the winglet airfoil is the UA(2)-180 (Marsden, 1988), although a few cases done to examine the effects of C_L use the NACA 64_3-618 airfoil. Note that the UA(2)-180 airfoil is used for the winglet unless explicitly stated otherwise.

3.5 RESULTS

The results here apply specifically to the analysis done on this particular winglet family. However, the trends which are shown will be applicable to other winglet designs. The following are some of the most significant of the results which can be shown by the use of this non-planar vortex model to examine winglets.

The terms "forward thrust" and "forward thrust component", as used for this study, warrant some explanation. In the interest of brevity, so far in the chapter the term "forward thrust" has referred to the negative induced drag of a winglet. The forward thrust is actually the sum of the induced drag force plus the profile drag of the winglet. (Recall that this VLM model does calculate both the induced drag and the profile drag of the wing and winglet.) Thus, the forward thrust produced by a winglet effectively considers the profile drag of the winglet. This is done by using the drag polar for the airfoil and the local lift coefficient to determine the profile drag.

Note that the wing and winglet profile drag is always in the streamwise direction. However, if induced velocities cause the induced drag to be negative that means that the induced drag is actually in the opposite direction to the streamwise direction and the induced drag and is labelled a "thrust."

If the sum of the induced drag and the profile drag is in the opposite direction to the freestream, then there is a resultant forward thrust due to the winglet. However, if the sum of the winglet induced drag and the winglet profile drag is in the same direction as the freestream, then there is a negative resultant forward thrust (which is the same a drag in the typical sense). Note that irrespective of the direction, this study uses the term "forward thrust" to account for the sum of both the induced drag and the profile drag along the span of the winglet.

The "forward thrust component" is simply the ratio of the forward thrust to the total drag reduction produced by the winglet. Note that this ratio may be positive or negative. This total drag reduction is the total drag of the basic wing alone minus the total drag of the given wing and winglet combination.

For overall performance of a finite wing the change of Lift/Drag ratio, $\Delta L/D$, is used. Clearly, the $\Delta L/D$ takes into account the induced drag of the finite wing as well as the profile drag which is a function of the airfoil C_D-C_L characteristics.

3.5.1 Spanwise Drag Distribution of a Wing

The Figures 3.21 to 3.24 present the chord adjusted drag coefficient along the arc length of the wing, as opposed to the more conventional method of showing the typical drag coefficient. The chord adjusted drag coefficient is a significant parameter used for this study, since this is the parameter which most clearly shows the actual mechanism of the drag reduction along the span of a wing due to winglets. The chord adjusted drag coefficient is determined by simply multiplying the local drag coefficient by the local chord and dividing by the mean chord, this provides a more informative scaling of the drag of that particular local wing section. For comparisons, the results are presented for the wings under study without winglets and with winglets 1 to 3. Thus, by using the chord adjusted drag coefficient, a winglet is shown to produce a significant induced drag reduction all along the span of a wing, as well as providing a *forward thrust* (or negative induced drag) component. The cases presented are for the elliptical wing and the three linearly tapered wings (0.4 to 1.0) with $A_R = 8.0$, at a wing $C_L = 1.13$.

Figures 3.21 to 3.24 for these four wing shapes all show that much of the span of the main wing experiences a reduction of induced drag by a constant amount, regardless of the wing shape (i.e. the wing loading).

Again referring to Figures 3.21 to 3.24, observe that the case of the elliptical wing shows a winglet producing an increased drag in the tip region on the main wing, then a negative drag on much of the winglet. The case of the tapered wings are much different, showing a winglet producing a *decreased* drag in the tip region on the main wing, then a *negative drag* on much of the winglet. As well, the tapered wings show that the winglet affects the main wing all along the span, and an even greater amount for about one winglet span in from the tip. The results shown for $C_L = 1.13$ show a forward thrust on most of the winglet, whereas the extreme tip region of the winglet produces drag in the streamwise direction.

The results of the total and component drag along the wing span are shown in Figures 3.25 and 3.26 for a tapered wing ($c_t/c_r = 0.4$), $A_R = 8.0$, with winglet 1. These sample figures clearly show that the induced drag provides the major contribution to the total drag at high lift coefficients, i.e. $C_L = 1.13$, whereas at lower lift coefficient values, i.e. $C_L = 0.45$, the profile drag begins to dominate.

The drag may be integrated along the span to provide insight into the relative magnitude of the drag components. Table 3.1 shows results of comparisons of such a summation of the drag reductions. (Note that this table is for a wing span of 15m and Aspect Ratio 12.73 with a UA(2)-180 airfoil (Marsden, 1988) at $C_L=1.13$, and winglet twist $= 6°$.) Note that the comparison is made with the drag due to each wing without a winglet. (The winglets on the elliptic wing are compared to the basic elliptic wing, and the winglets on the 0.4 tapered wing are compared to the basic 0.4 tapered wing.) The changes are shown as a percentage of the total drag of each basic wing. The change in total drag up to the tip of the main wing is shown first, which indicates the total (mostly induced) drag reduction along the main wing span. Then the additional change in total drag due to the winglet itself is given, which indicates the magnitude of the forward thrust (which includes the negative induced drag plus the winglet profile drag). Equations 3.21 and 3.22 show the drag integration method.

$$\begin{aligned} D_{Total} &= \int_{-s/2}^{s/2} D(s)\, ds \\ &= \int_{-s/2}^{-b/2} D(s)\, ds + \int_{-b/2}^{b/2} D(s)\, ds + \int_{b/2}^{s/2} D(s)\, ds \end{aligned} \tag{3.21}$$

where, $D(s)$ is the drag at the arc-wise location, s, from the wing root along the semi-span, $b/2$, and the total length of the semi-span arc is given by $s/2$. Since a symmetric wing is being studied,

$$\begin{aligned} D_{Total} &= 2 \int_0^{s/2} D(s)\, ds \\ &= 2 \int_0^{b/2} D(s)\, ds + 2 \int_{b/2}^{s/2} D(s)\, ds \end{aligned} \tag{3.22}$$

Notice that the *forward thrust component is easily quantified* by the area of the negative drag on the winglet. Clearly, the drag reduction along the span is a significant component, although the winglet thrust must also be recognized as significant. Recall that for an elliptical wing the induced drag coefficient is $C_{Di} = C_L^2 / (\pi A_R)$. Hence, for any other wing the effective aspect ratio factor, e, is given by $C_{Di} = C_L^2 / (\pi\, e\, A_R)$. These results show that both the drag reduction along the span of a wing *and* the forward thrust of a winglet contribute to drag reduction. Table 3.1 also includes the change of wing root bending moment since it is an important structural design parameter.

3.5.2 Change in Lift/Drag Ratio vs. Aspect Ratio

The percent change in Lift/Drag ratio is a good indicator of the performance of a finite wing. Figures 3.27 to 3.30 show the percent change in Lift/Drag ratio versus aspect ratio, all at a wing C_l = 1.13. The wings examined are the elliptical and tapered with taper ratios = 0.4 to 1.0. Notice that winglets are shown to help even the elliptical wing. The elliptical wing shows up to 16% increase in Lift/Drag ratio at A_R = 6.0, when fitted with winglet 1. Even at A_R = 20.0 the elliptical wing shows more than 5% increase in Lift/Drag ratio when fitted with winglet 1. The wing with linear taper = 0.4 shows improvements similar to the elliptical, whereas the less tapered wings show more improvement with winglet addition. When fitted with winglet 1, the rectangular wing shows a 19% increase in Lift/Drag ratio at A_R = 6.0, and at A_R = 20.0 the rectangular wing shows about 8% increase in Lift/Drag ratio.

In all cases the much smaller winglet 3 produces an increase in Lift/Drag ratio which is more than half of that shown by the winglet 1. Qualitatively, this shows a decreasing benefit from increasing the winglet size. Recall that ($\text{Area}_{\text{Winglet1}} \approx 3 \times \text{Area}_{\text{Winglet3}}$). Notice that for these figures the winglets are those determined by the modified elliptical wing hence the sizes are dependent on the wing aspect ratio.

Note another feature which these figures show. Examining Table 3.B.1 shows that Winglet 1 at A_R = 20.0 has about the same area as Winglet 2 at A_R = 12.73 and Winglet 3 at A_R = 6.0. Also, Winglet 2 at A_R = 20.0 has about the same area as Winglet 3 at A_R = 10.0. Examining the points for these winglets on each of Figures 3.27 to 3.30 shows that, for a given wing type, the percent change in Lift/Drag ratio is nearly constant for a given winglet area, regardless of the wing aspect ratio.

3.5.3 Forward Thrust/Total Drag Reduction vs Winglet Length (Size)

Figure 3.31 shows the forward thrust/total drag reduction versus winglet length (size) for a wing with taper = 0.4, at C_L = 1.13. The wing is shown at A_R = 6 to 20. This figure shows the interesting trend that larger winglets produce about 20% of the total drag reduction via the forward thrust component. This leaves the most significant portion of about 80% of the total drag reduction due to the induced drag reduction along the span of the main wing. This value is somewhat dependent on the aspect ratio, however the aspect ratio is not a dominant factor.

Figure 3.32 shows similar information, except now the different wing shapes (elliptical and taper = 0.4 to 1.0) are compared. These wings of A_R = 12.7 are operating at C_L = 1.13. This figure shows a very interesting trend that even though the wings have very different spanwise load functions, the forward thrust/total drag reduction ratios are very much similar. Also, notice that winglets which are of practical sizes are about 0.25 to 1.0 times the tip chord. Thus, the practical range of winglet sizes produce about 50% to 20%, respectively, of the drag reduction by a forward thrust at this C_L.

3.5.4 Forward Thrust/Total Drag Reduction variation with C_L

The forward thrust component (or forward thrust/total drag reduction) variation with C_L is shown in Figure 3.33. Now note that two wings are shown, taper ratio = 0.4 and 1.0. Both wings are at A_R = 12.7, and show the results with winglets 1 and 2 attached. This figure shows a key relationship between the forward thrust component of the total drag reduction and the wing C_L. Clearly, the forward thrust component is seen to decrease to the point of being negligible or even negative (i.e. a drag in the typical sense), with decreasing C_L. Near C_L = 1.13 the forward thrust component is about 30% of the total drag reduction. Also of interest is that the curves seem to show an asymptotic behaviour at high C_L indicating that with increasing C_L above that shown the forward thrust component does not become any more dominant. However, the significance of the C_L is shown, since when the $C_L \approx 0.5$ the forward thrust component is zero, and for $C_L < 0.5$ the forward thrust component is actually negative.

There is some dependence of the results on the wing taper. The rectangular wing with a greater outboard wing loading shows a greater forward thrust component for both winglets, than does the wing with taper = 0.4. Also, again note that the smaller of the winglets (Winglet 2) produces a greater forward thrust component than the larger Winglet 1 for both wings at all C_L. Note that Figures 3.32 and 3.33 show an "apparent" contradiction of results for different winglet sizes. However, such is not the case. Note that Figure 3.32 gives (winglet size / tip chord). Therefore since the rectangular wing has a larger tip chord, for a given winglet the ratio of (winglet size / tip chord) will be significantly smaller than for the wing taper 0.4.

This influence of the C_L of the wing could easily explain why many researchers find different results regarding the forward thrust of winglets. The findings regarding the importance of the forward thrust are highly dependent on the C_L of the wing.

3.5.5 Change in Lift/Drag Ratio variation with C_L

The Figure 3.34 shows the specific cases of two wings with taper = 0.4 and 1.0, with A_R = 12.7, and with the winglets 1 and 2. Clearly there is greatest positive change in Lift/Drag ratio at high values of wing C_L. Also, there appears to be a decreasing rate of improvement at higher lift coefficients. As well, at low C_L there is no real benefit with winglets in terms of increase in Lift/Drag ratio. However, for most practical C_L values (say, 0.3 to 1.2) there is some increase in Lift/Drag ratio to be obtained.

The same figure shows the comparison of the two winglet sizes on the two different wing taper ratios at the same aspect ratio. Note that because the wings are the same aspect ratio, winget 1 is the same physical size, independent of the wing to which it is attached. Likewise, winglet 2 is the same physical size independent of the wing. With that in mind, observe that the same winglet (say #1) produces more improvement on the wing with taper 1.0, than the wing of taper 0.4. Also, notice that the larger winglet 1 gives more increase in Lift/Drag ratio than winglet 2, for both wings at the high C_L values. Also, for both wings the smaller winglet 2 gives slightly greater improvement at the low C_L values. This means that when considering winglets for a particular wing, some performance trade off will be made depending on the typical operating scenerio of the given aircraft.

3.5.5.1 Effect of the Main Wing Airfoil

A very subtle but important affect on the apparent performance of a winglet is due to the airfoil C_D-C_L characteristics of the *main wing*. The influence is not immediately obvious, but can have an impact on the percentage improvements shown in the Lift/Drag ratio. Take for instance two wings identical in every way except that of the airfoil, let wing #1 have C_D-C_L values greater than wing #2 (i.e. at the same C_L the C_D for wing #1 is higher than the C_D for wing #2). Now attach an identical winglet to each wing. Observe, even though magnitudes of drag reduction may be the same for two wings, now the percentage of drag reduction for wing #2 will be greater than the percentage drag reduction for wing #1. Since percentage improvement is often the criterion used for winglet performance evaluation, this subtle effect may explain why different researchers find such different results.

A similar effect is noticable depending on the low drag region for the airfoil. (The information for the NACA airfoil presented in this section is taken from Abbott and von Doenhoff (1959).) Take for instance the two similar low drag, laminar flow airfoils, the NACA 64_3-018 and the NACA 64_3-618. Both airfoils have a wide drag bucket, with a low drag coefficient ($\approx$ 0.0055). However, the former has the low drag range for $C_L \approx 0.0 \pm 0.3$, whilst the latter operates in the low drag region at a moderately high $C_L \approx 0.6 \pm 0.3$. Now consider the NACA 64_3-018 at $C_L = 0.5$, the $C_D \approx 0.007$, whereas the NACA 64_3-618 $C_D \approx 0.0055$. Next examine the NACA 64_3-018 at $C_L = 1.0$, the $C_D > \approx 0.011$, whereas the

NACA 64_3-618 $C_D \approx 0.006$. This may have a significant influence on the apparent performance of a particular winglet on a given wing.

For this study, the main wing airfoil is maintained as one of two standard airfoils. The ones chosen are low drag, laminar flow airfoils, the UA(2)-180 and the NACA 64_3-618. The UA(2)-180 has a wide drag bucket, with a low drag coefficient ($C_D \approx 0.0063$) while operating at a high C_L ($\approx 1.0 \pm 0.3$). The NACA 64_3-618 airfoil has a wide drag bucket, with a low drag coefficient (≈ 0.0055) while operating at a moderately high C_L ($\approx 0.6 \pm 0.3$). For most of the study when examining winglet effects at a high $C_L \approx 1.13$ the UA(2)-180 airfoil is used. For the part of the study when examining winglet effects at a varying or low C_L the NACA 64_3-618 airfoil is used. This should be kept in mind when scrutinizing the results and comparing with results from other studies. The relative merits shown by different winglets will still be valid, however the absolute magnitudes may vary according to the main wing airfoil selected.

Figure 3.35 shows a comparison of the percentage change in L/D versus C_L for the same winglet (winglet 2) applied to main wing with taper ratio 0.4, but using three different airfoils. These airfoils are: the UA(2)-180, NACA 64_3-618, and NACA 2412. The first two are described above. The NACA 2412 is a common general aviation airfoil (see Abbott and von Doenhoff, 1959). Although, the NACA 2412 does not have a drag bucket as the other two, it does have its lowest drag $C_D \approx 0.0065$ in the region of $C_L \approx 0.2$-0.25. Notice that the figure shows the UA(2)-180 airfoil producing the greatest $\Delta L/D$ at the high $C_L \approx 1.1$, with the NACA 64_3-618 showing similar performance. However, note that at the high $C_L \approx 1.1$, the NACA 2412 main wing leads to poorer apparent performance of the winglet. Similarly, at low $C_L \approx 0.4$, the main wings with the NACA 64_3-618 and NACA 2412 (which have their low drag regions at low C_L) show greater $\Delta L/D$ due to the winglet, than the wing with the UA(2)-180, because the UA(2)-180 has its low drag region at high C_L. Generally, the trend is that the main wing using the airfoil with lower profile drag for a given C_L will produce a greater apparent change in L/D at that particular C_L.

Recall that the addition of a winglet to a wing produces a downwash reduction along the main wing span, especially near the tip. This leads to another subtle effect which should be noted. The downwash reduction at any spanwise location changes the local angle of attack, which results in a different local lift coefficient. This will produce a change in the profile drag of that section. Depending on the main wing airfoil C_D-C_L characteristics and the local C_ℓ this may produce a decrease in the local profile drag of the main wing. For an aircraft in flight, a reduction of downwash along the span will require an increase in wing incidence to maintain the same aircraft C_L. The over all result of a downwash reduction can be important and is accounted for in this model.

3.5.6 The Lift/Drag Ratio versus Wing Root Bending Moment

Many researchers consider the wing root bending moment to be a reasonable measure of the structural requirements of a wing. With the addition of a winglet the change in wing root bending moment can be directly related to the structural modifications required for the winglet addition to the wing.

Figures 3.36 to 3.39 show that for a given wing root bending moment winglets can give some increase in the Lift/Drag ratio. Another way of viewing the results is that for a given Lift/Drag ratio the wing root bending moment can be decreased by adding winglets to a wing. The figures show that the greatest benefit is obtained by attachment of the winglet to a wing with less taper. Specifically, the rectangular wing demonstrates the greatest potential for improvement with winglets. However, for all taper ratios examined (0.4, 0.6, and 1.0) there is some increase of Lift/Drag ratio for all aspect ratios. Notice that these figures, which show groups of 4 points which represent the wing and 3 winglets, also show that when retrofitting a winglet on a given wing, there is an increase in the Lift/Drag ratio *and* the wing root bending moment.

Another significant feature shown in these figures is that the lines are virtually parallel. This shows that the magnitude of improvement is virtually constant for the addition of the winglet of a particular family to a given wing. However, the same observation shows that the percentage improvement at low aspect ratios is greater than at higher aspect ratios.

These comparisons are for winglets 1 to 3, and none. Note that increased winglet length (size) gives decreased benefit in terms of Lift/Drag ratio at a given wing root bending moment (at C_l = 1.13).

Figure 3.40 shows all of these results, from these previous four figures, for the Lift/Drag ratio versus wing root bending moment (at C_L = 1.13) plotted onto one figure. This figure provides a convenient means to compare the final result of each of the winglets on each wing type being studied. Notice that there are 6 clumps of 16 data points each, which correspond to the 6 aspect ratios examined. The 16 data points within each clump are for the 4 wings and 4 winglet cases on each wing (no winglet, and winglets 1 to 3). Note that the data points at the top of each of the 6 clumps correspond to Winglet1 and the points at the bottom of each clump correspond to the no winglet case. (Recall that the larger winglets for each wing produce greater improvements in the *L/D*.)

Figure 3.40 shows that linearly tapered wings with winglets can produce *L/D* values greater than for the planar elliptical wing without a winglet. Specifically, the data clump for the wings with A_R = 6.0 (the clump at the lower left side) shows the Winglet 1 on the 1.0 tapered wing has *L/D* = 17.56, while the elliptical wing without a winglet only has *L/D* = 15.25. This is an improvement of 15% for the rectangular wing and winglet compared to the planar elliptical wing. Note that for all cases $A_R \leq 15.0$ the wings with winglets could perform equal to or better than the planar elliptical wing. Remember that this is at C_L = 1.13, and a lower C_L will not give as great an improvement.

Another feature becomes apparent when comparing the *L/D* for each winglet size within each aspect ratio clump of Figure 3.40. Recall that the winglets used are exactly the same size of winglet for each of the 4 wing types at that particular aspect ratio. The figure shows that at A_R = 6.0 the rectangular wings (1.0 taper) with winglets can produce L/D values nearly equal to those by the other tapered wings with the exact same winglets attached, at this C_L. Even at the moderate aspect ratios the rectangular wing with winglets produce L/D values comparable to the other wings. As well, the figure indicates that the L/D is not significantly different when using a winglet on a wing with taper 0.4 or 0.6 or on an elliptical wing. Also, the 1.0 tapered wing produces a greater wing root bending moment for a given value of L/D, than the 0.6 and 0.4 tapered wing and the elliptical wing. These features can be important when considering the trade-off between the construction difficulty and cost of a wing versus the aerodynamic performance.

The effect of C_L on the L/D versus wing root bending moment is shown in Figure 3.41. This figure shows the 0.4 tapered wing at A_R = 12.73 with no winglet and various sizes of winglets. For each of C_L = 0.282, 0.447, and 1.13 there are 8 points given. The left-most point of each set is the no winglet case, then the next points give winglets of increasing size. The figure shows winglet lengths such that (winglet length/wing tip chord) = 0.00 (no winglet), 0.509 (winglet 3), 0.732 (winglet 2), 0.910 (winglet 1), 1.40, 1.60, 1.80, and 2.00. This figure accentuates the observation that larger winglets are best suited to high C_L and smaller winglets to low C_L flight regimes. This type of figure would help the winglet designer pick the optimum size of winglet for the range of flight conditions expected for a particular aircraft.

3.6 CONCLUSIONS

The mechanism by which a winglet reduces wing drag has been shown. A winglet has been shown to produce a significant induced drag reduction all along the span of a wing, as well as providing a *forward thrust* (or negative induced drag) component by the winglet itself. This forward thrust has been quantified and shown to be significant, although for most practical winglet sizes the dominant drag reduction mechanism is the induced drag along the main wing. Specifically, the following results have been shown.

Winglets *can* reduce the total drag of an elliptical wing. Also, tapered wings with winglets have been shown to have a greater *L/D* at high C_L than a planar elliptical wing. This is significant since the elliptical shape is "known" to be the most efficient shape for the case of a planar wing. This shows that a winglet can improve upon even the most efficient planar wing.

For the wings considered in this study, the winglet forward thrust component has been quantified. The forward thrust component has been shown to be about 20% to 50% of the total drag reduction due to winglets at high C_L, for most practical winglet sizes. This means that even for a wing operating at high C_L, the induced drag reduction along the main wing span accounts for 50% to 80% of the total drag reduction, therefore is the dominant mechanism.

The forward thrust component due to a winglet was found to be relatively insensitive to the wing spanwise loading. Although, the actual change in Lift/Drag ratio is dependent on the spanwise loading of a wing.

The relationship has been shown between the forward thrust component of the total drag reduction and the wing C_L. Specifically, the forward thrust component has been shown to decrease to the point of being negligible or even negative (i.e. a drag in the typical sense), with decreasing C_L.

Another significant result is the change in Lift/Drag ratio versus C_L. The results show that a winglet can produce a significant increase in the Lift/Drag Ratio at high C_L, and a winglet can produce some increase in the Lift/Drag ratio even at low C_L. This result taken together with the relation between the forward thrust component and C_L highlights the important result, that the induced drag reduction along the main span due to winglets is the most important mechanism for drag reduction due to winglets, especially at low C_L.

Notice that the change in L/D is *not* linear with C_L as noted by other researchers in the literature review of Chapter 2. (Note that the change in L/D is the reciprocal to the change in C_D at a given total lift.) However, there can be an erroneous appearance that the relationship is linear if limited data is selected only at high C_L values. (This appears to the the case for Ishimitsu and Zanton (1977). See Chapter 2, Figure 2.24.)

The vortex lattice method has been utilized to show that winglets can help improve the efficiency of most planar wings. However, the dominant operating scenario of a particular aircraft will dictate the specific geometry for winglets employed to give the optimum improvement. Generally, the operation of aircraft at high C_L values will favour the choice of large winglets, whereas operation at low C_L values will favour the choice of small winglets. In all cases, the winglet airfoil should have low drag for the range of lift coefficients of the winglet itself.

As a final note, the wing root bending was examined. For a winglet retrofit on a given wing the wing root bending moment will increase. However, The main finding was that for a given wing root bending moment winglets can produce some increase in the Lift/Drag ratio.

RECOMMENDATIONS for FUTURE RESEARCH

The implications of the rigid wake should be considered. The author intends to include the wake roll-up feature in this VLM computer model in order to investigate the change of winglet effectiveness with the vortex roll-up included.

REFERENCES

Abbott, Ira H. and Albert E. von Doenhoff. 1959. *THE THEORY OF WING SECTIONS - including a summary of airfoil data.* Dover. pp. 17, 580-581, 586-587.

Asai, K. 1985. Theoretical Considerations in the Aerodynamic Effectiveness of Winglets. *Journal of Aircraft* 22(7):635-637.

Bilanin, A.J. and C.duP. Donaldson. 1975. Estimation of Velocities and Roll-up in Aircraft Vortex Wakes. *Journal of Aircraft* 12(7):578-585.

Cone Jr., C.D. 1962. *The Theory of Induced Lift and Minimum Induced Drag of Nonplanar Lifting Surfaces.* NASA-TR-R-139.

Heyson, H.H., G.D. Riebe, and C.L. Fulton. 1977. *Theoretical Parametric Study of the Relative Advantages of Winglets and Wing-Tip Extensions.* NASA TP-1020.

Houghton, E.L. and N.B. Carruthers. 1982. *AERODYNAMICS FOR ENGINEERING STUDENTS., 3rd Ed.* Arnold. pp. 198-199, 254-255.

Ishimitsu, K.K. and D.F. Zanton. 1977. *Design and Analysis of Winglets for Military Aircraft, Phase II.* Boeing Commercial Aircraft Company. AFFDL-TR-77-23.

Küppers, U. 1983. *Vortex Separation by Slotted Wing Tips, Energy Conservation According to Biological Model.* Fortschritt-Berichte Der VDI Zeitchriften No. 81(Reihe 7). ("Randwirbelteilung durch aufgefacherte Flugelenden, Energiesparen nach biologischem Vorbild")

Marsden, D.J. 1988. A High-Lift Wing Section for Light Aircraft. *Canadian Aeronautics and Space Journal* 34(1):55-61.

McCormick Jr., Barnes Warnock. 1979. *AERODYNAMICS, AERONAUTICS, AND FLIGHT MECHANICS.* John Wiley & Sons, Inc. pp. 191-193.

Munk, M. M. 1921. *The Minimum Induced Drag Of Aerofoils.* N.A.C.A. Report No. 121.

O'Callaghan, W.J. 1988. *The Induced Drag Reduction Mechanism of Wingtip Surfaces from Studies of the Lift Curve and Vortex Wake.* M.Sc. Thesis, University of Alberta. (under the supervision of D.J. Marsden)

Rossow, V.J. 1992. Prospects For Alleviation of Hazard Posed by Lift-Generated Wakes. *Proceedings of the AIRCRAFT WAKE VORTICES CONFERENCE - Vol. 1.* Washington, D.C., October 29-31, 1991. p.22-11. (Senior Scientist, Fixed Wing Aerodynamics Branch, NASA Ames Research Center, Moffett Field, Calif.).

Spillman, J.J. 1978. The Use of Wing Tip Sails to Reduce Vortex Drag. *Aeronautical Journal* 82(9):387-395.

Spillman, J.J. 1987. Wing Tip Sails; Progress to Date and Future Developments. *Aeronautical Journal* 91(12):445-453.

Table 3.1. Results from Wing-Winglet combinations on an Elliptical and a 0.4 Tapered wing at $C_L = 1.13$.

Wing-Winglet combination	Δ**Total Drag** % on the main wing	Δ**Total Drag** % additional along winglet	*e* Effective A_R factor	% $\Delta L/D$	% ΔBM at root
Elliptical (No Winglet)	0	0	1.00	0	0
Elliptical & Winglet 1	-6.0	-1.5	1.10	+8.1	+3.7
Elliptical & Winglet 2	-4.9	-1.3	1.08	+6.6	+2.4
Elliptical & Winglet 3	-3.4	-0.9	1.05	+4.4	+1.3
0.4 Tapered (No Winglet)	0	0	0.99	0	0
0.4 Tapered & Winglet 1	-5.6	-1.6	1.09	+7.8	+1.5
0.4 Tapered & Winglet 2	-4.5	-1.6	1.07	+6.4	+1.2
0.4 Tapered & Winglet 3	-3.0	-1.5	1.05	+4.7	+0.8

Note that except for the value of *e* , the comparisons of the elliptical plus winglets are to the basic elliptical wing and the tapered plus winglet are compared to the basic tapered wing.

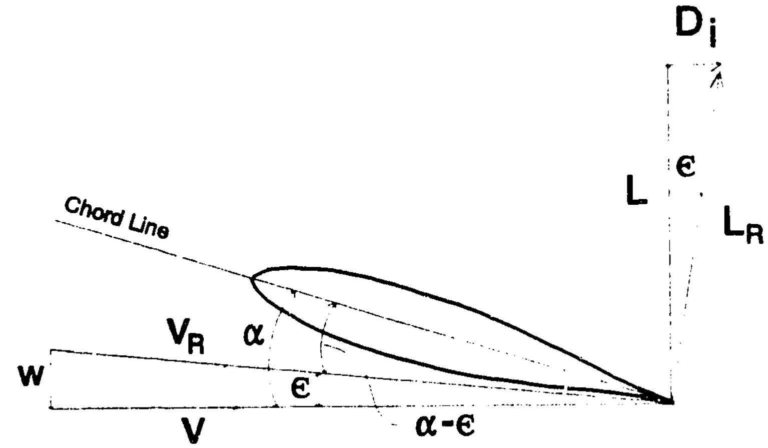

Figure 3.1 Trailing Vortex Drag or Induced Drag shown as caused by the tilting of Lift vector.

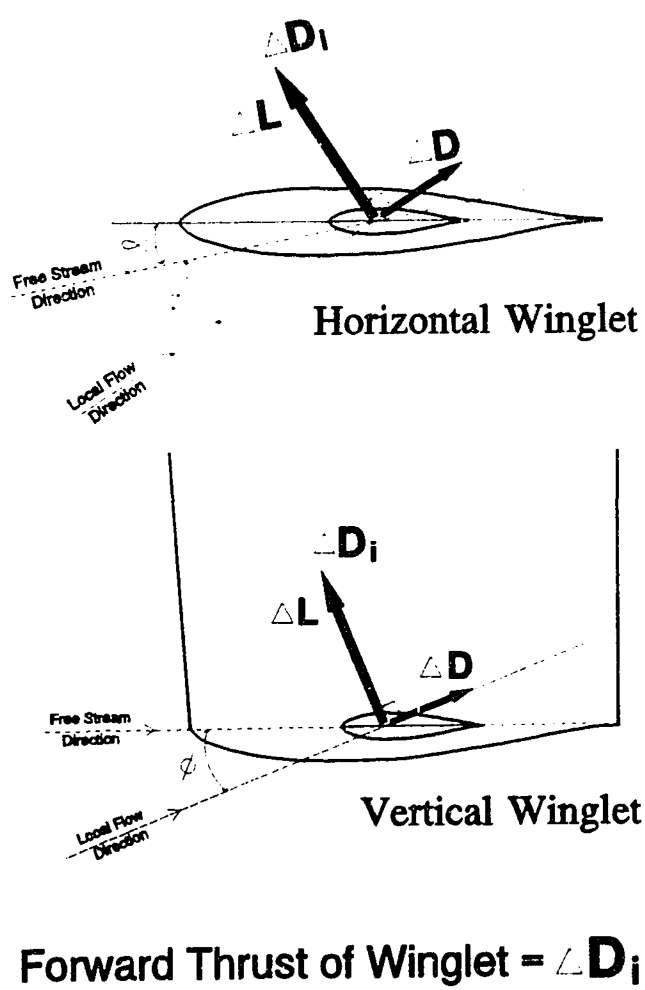

Figure 3.2 Forward Thrust of vertical or horizontal Winglet.

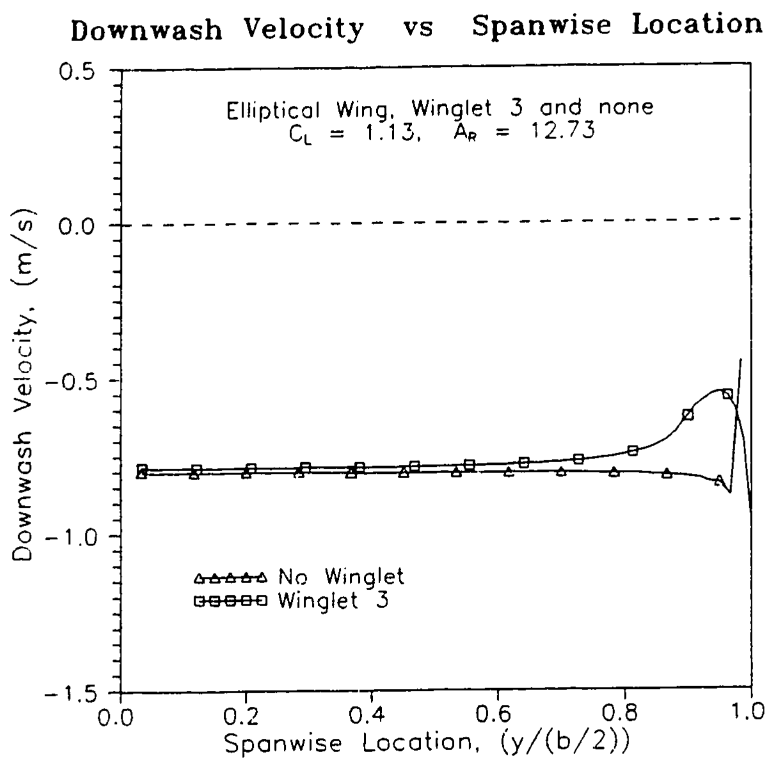

Figure 3.3 Downwash Velocity vs Spanwise Location for an Elliptical wing with Winglet 3 and without a winglet (wing span = 15.0 m, A_R = 12.7, C_L = 1.13).

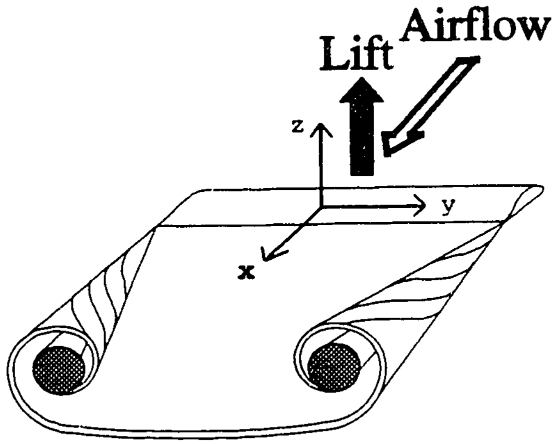

Figure 3.4 Vortex Sheet Roll-Up.

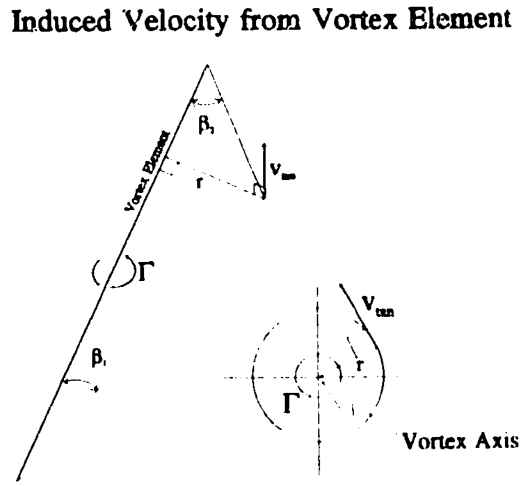

Figure 3.5 Induced Velocity by a Vortex.

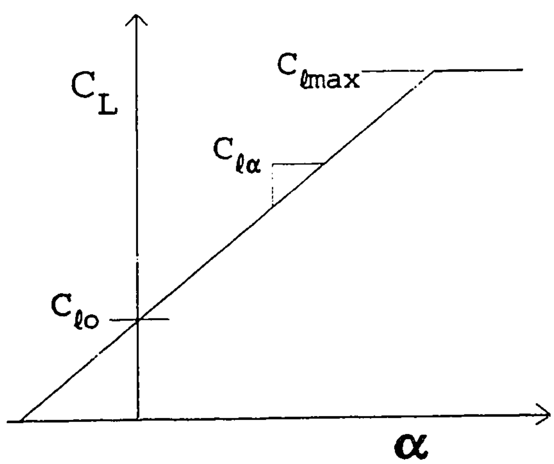

Figure 3.6 Lift curve parameters.

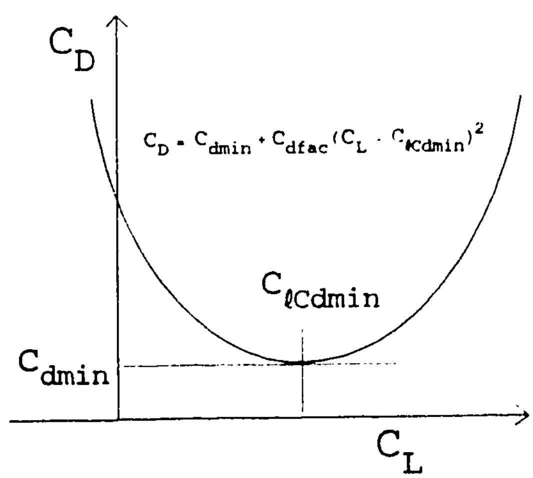

Figure 3.7 C_D - C_L curve parameters.

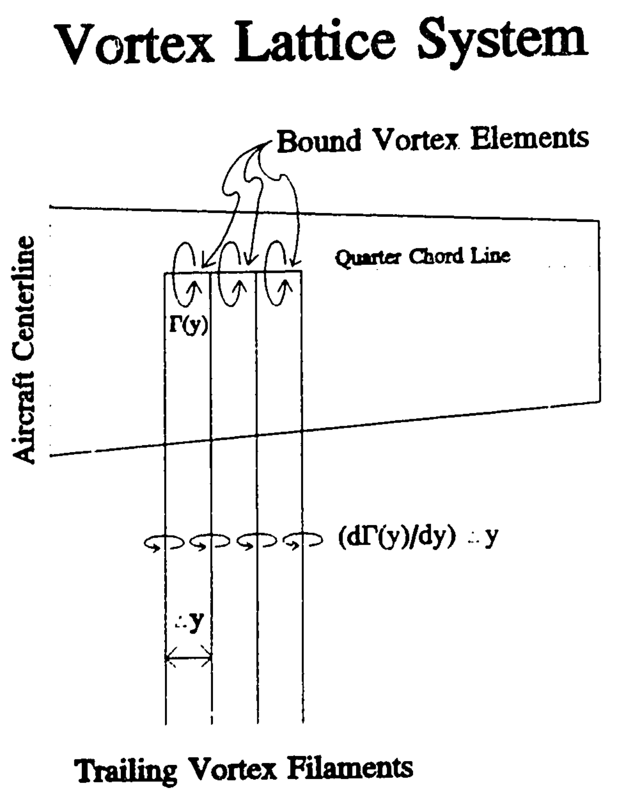

Figure 3.8 Simplified Vortex Lattice for Simple Unswept Tapered Wing.

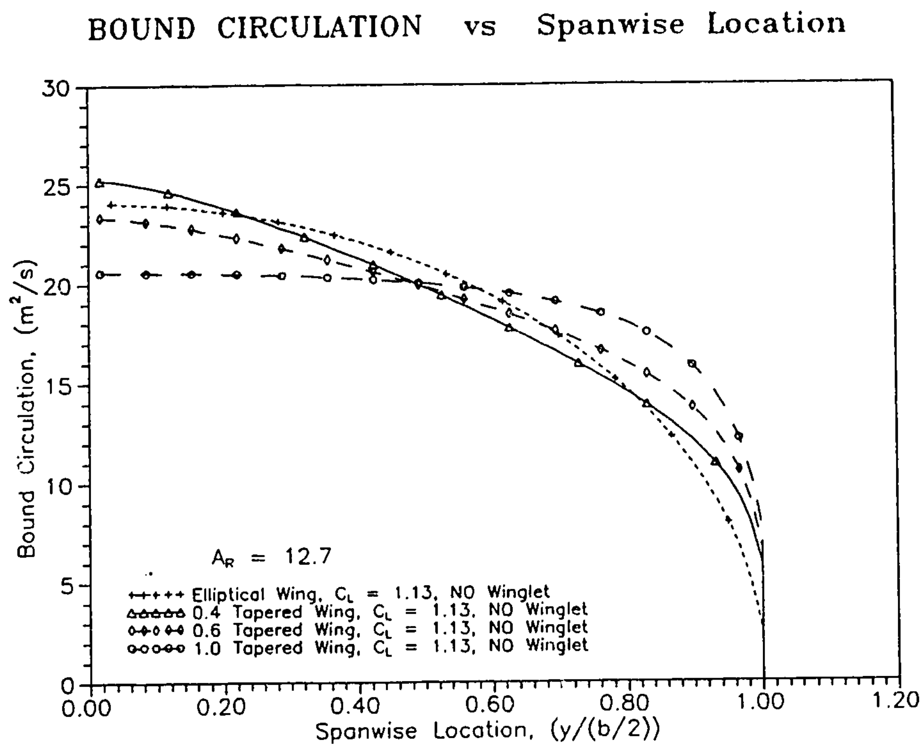

Figure 3.9 Circulation distribution for the four wing types used.

Figure has been removed due to copyright restrictions

Figure 3.10 Spanwise bound circulation distribution, adapted from McCormick (1979).

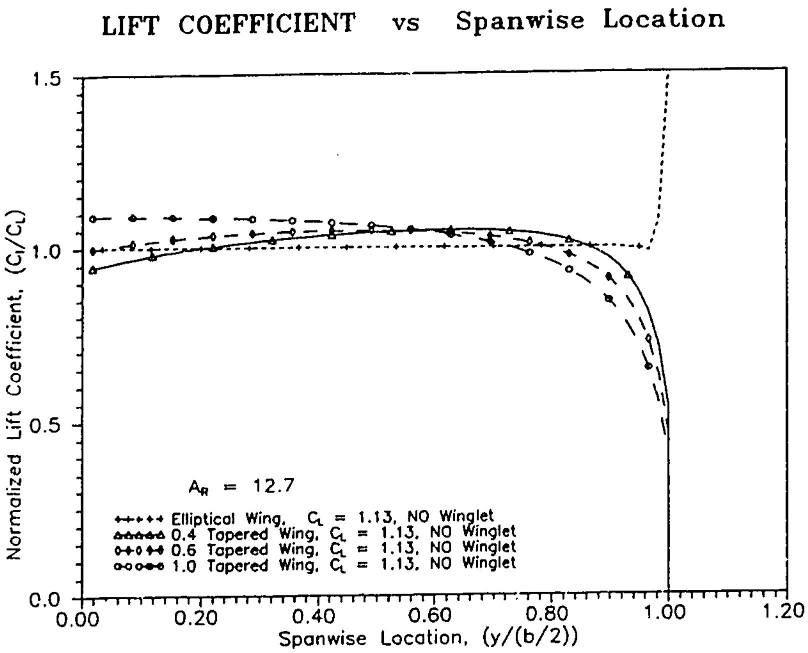

Figure 3.11 Normalized Lift Coefficient distribution for the four wing types, $A_R = 12.73$.

Figure has been removed due to copyright restrictions

Figure 3.12 Spanwise C_ℓ distribution, adapted from McCormick (1979).

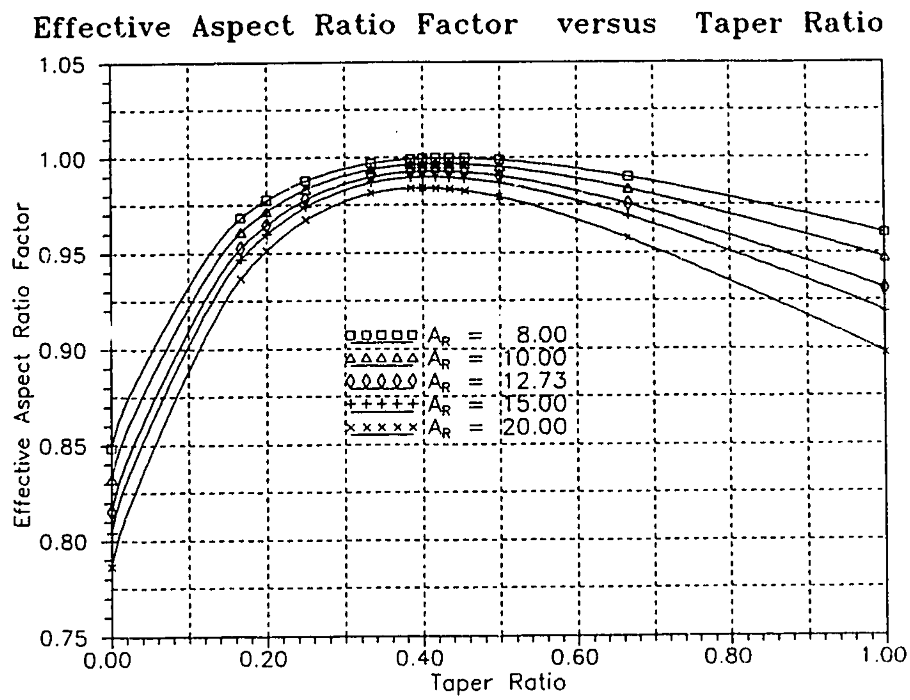

Figure 3.13 Effective Aspect Ratio Factor versus Taper Ratio, A_R = 8.0, 10.0, 12.73, 15.0, 20.0.

Figure has been removed due to copyright restrictions

Figure 3.14 Induced drag factor versus taper ratio, adapted from Abbott and Von Doenhoff (1959).

Figure has been removed due to copyright restrictions

Figure 3.14 continued...

Figure has been removed due to copyright restrictions

Figure 3.15 Induced drag factor for unswept linearly tapered wings, adapted from McCormick (1979).

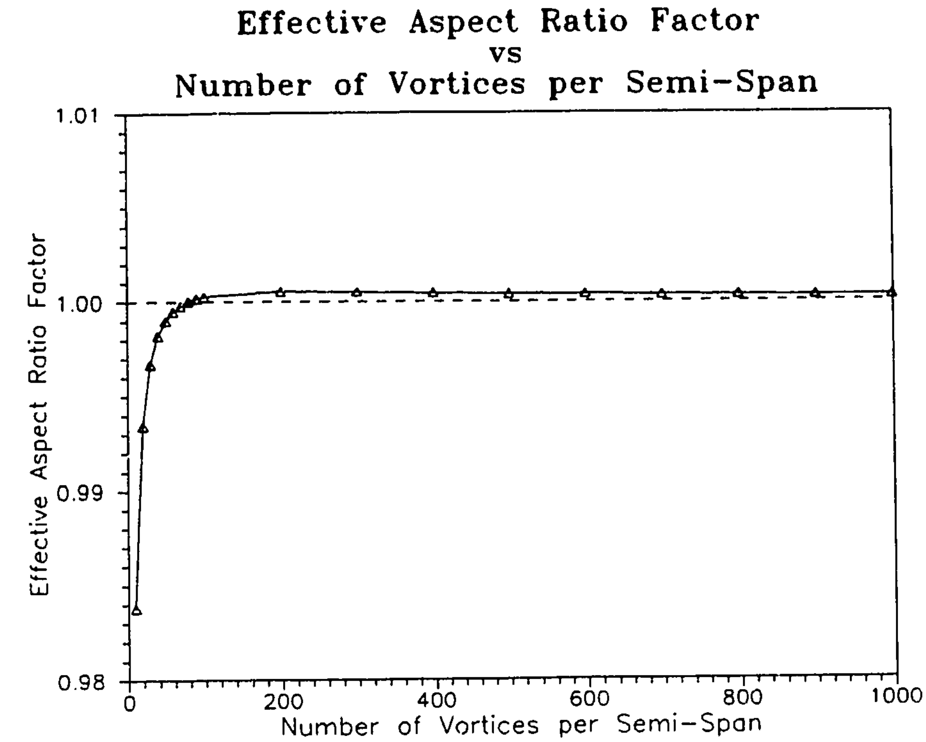

Figure 3.16 Effective Aspect Ratio Factor versus Number of Vortices per Semi-Span, elliptical wing, A_R = 12.73, and Elliptical Wing.

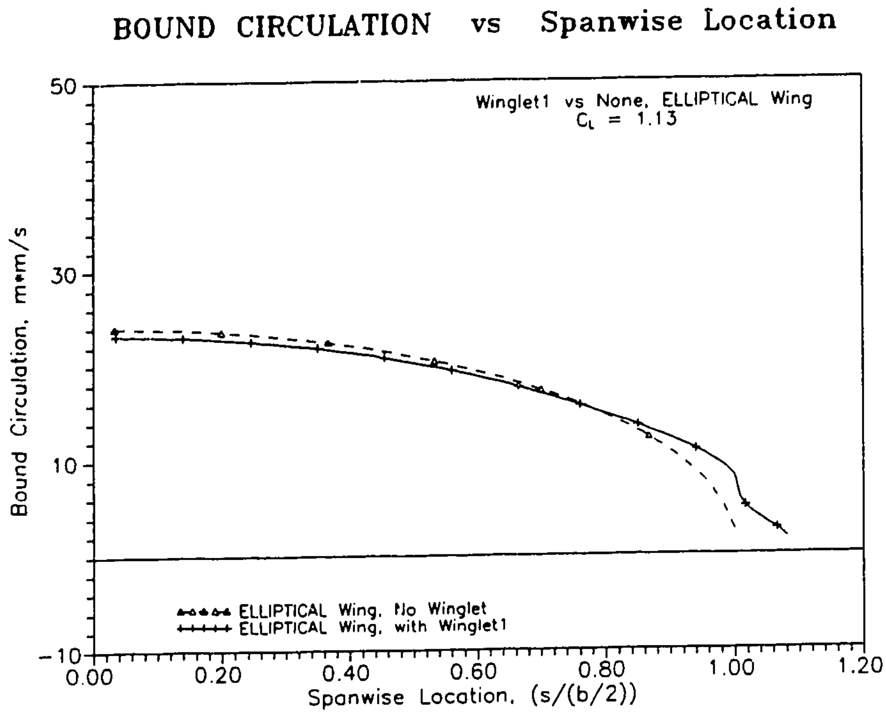

Figure 3.17 Spanloading of elliptical wing, with and without a winglet, A_R = 12.73, at C_L = 1.13.

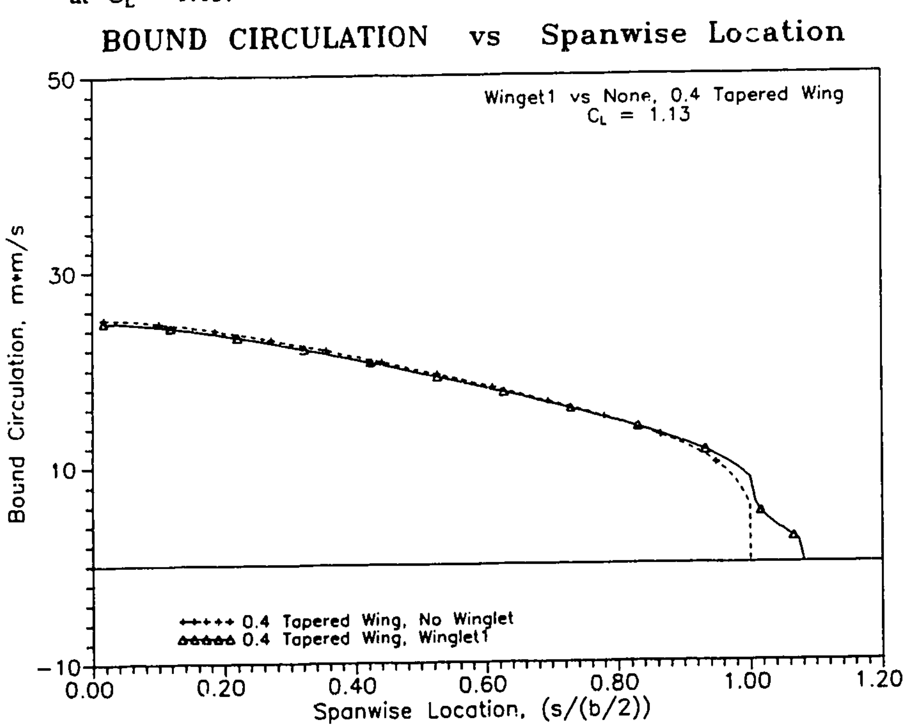

Figure 3.18 Spanloading of a 0.4 taper wing, with and without a winglet, A_R = 12.73, at C_L = 1.13.

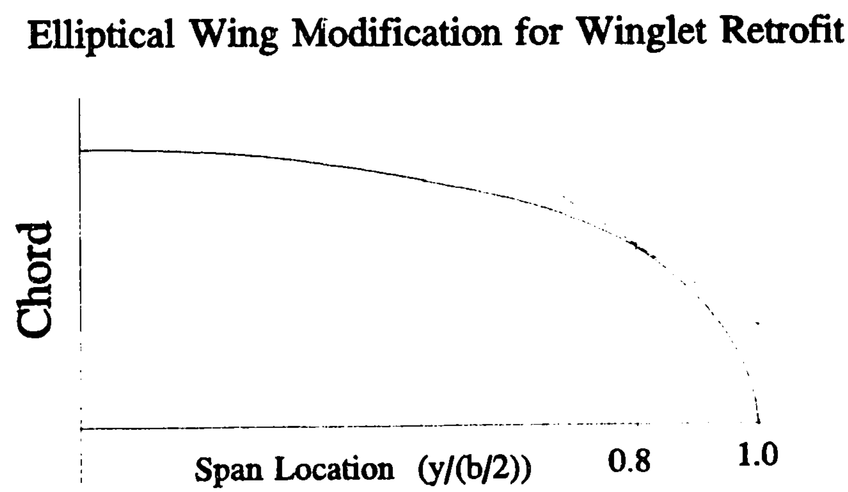

Figure 3.19 Elliptical wing modified to produce a finite tip for a winglet attachment.

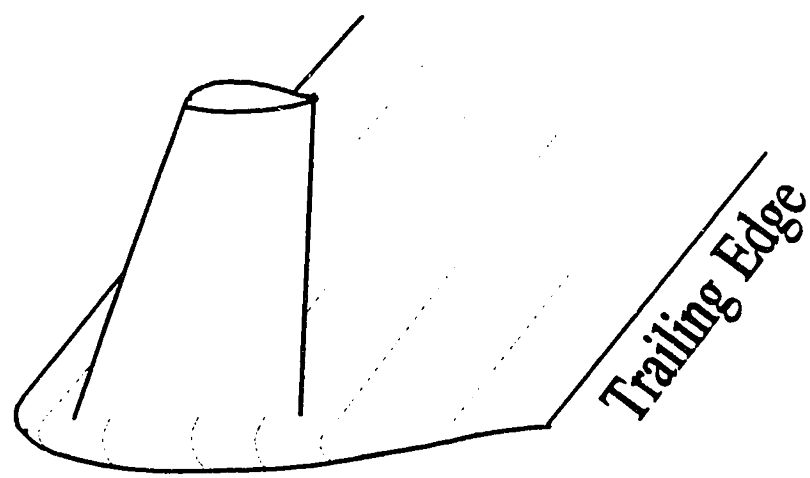

Figure 3.20 Typical member of winglet "family" in the study.

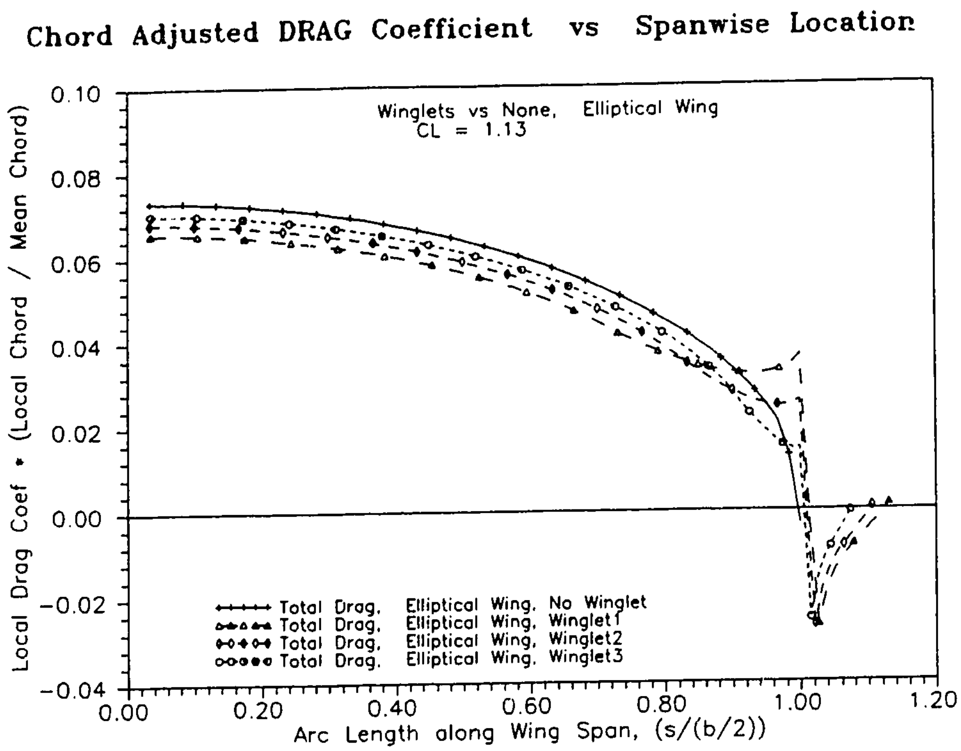

Figure 3.21 Total Drag for an Elliptical Wing with and without Winglets, A_R = 8.0.

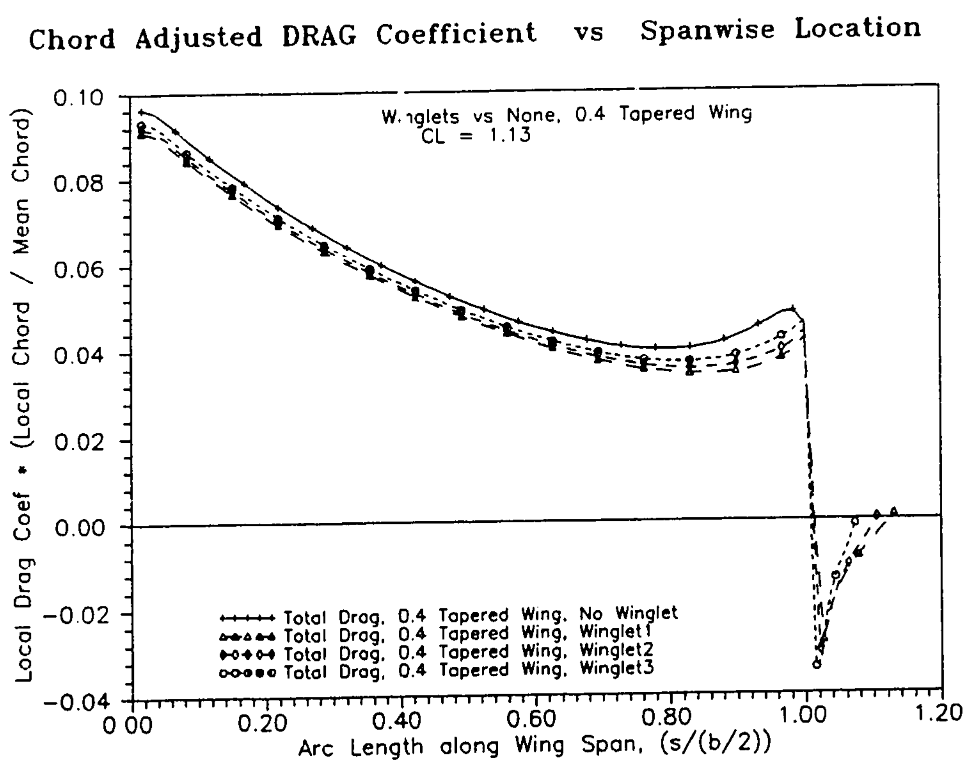

Figure 3.22 Total Drag for 0.4 Tapered Wing with and without Winglets, A_R = 8.0.

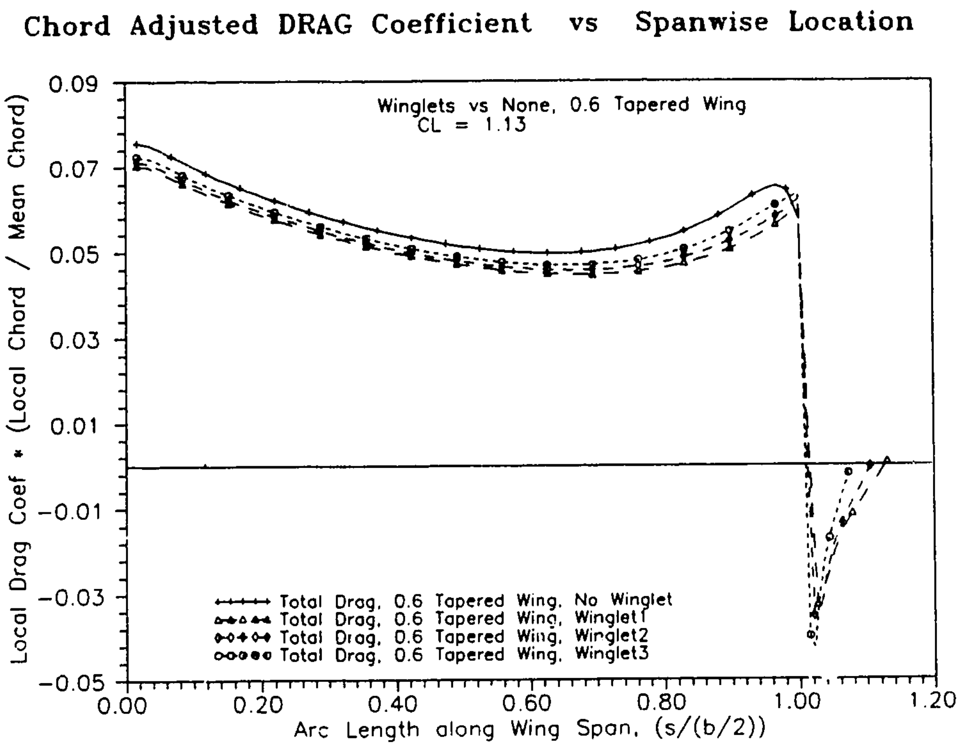

Figure 3.23 Total Drag for 0.6 Tapered Wing with and without Winglets, $A_R = 8.0$.

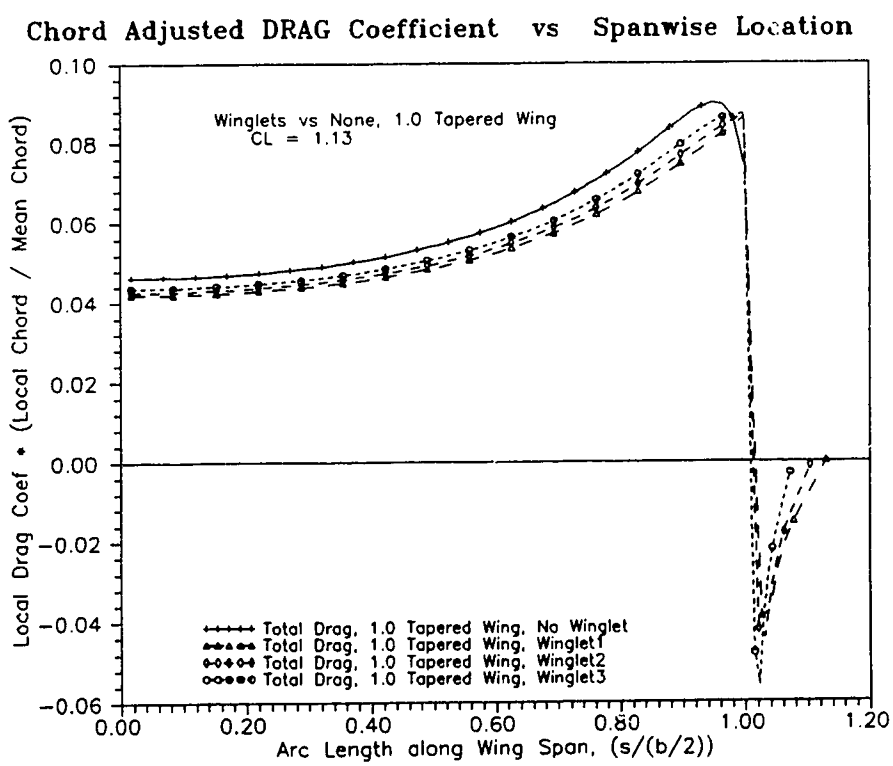

Figure 3.24 Total Drag for 1.0 Tapered Wing with and without Winglets, $A_R = 8.0$.

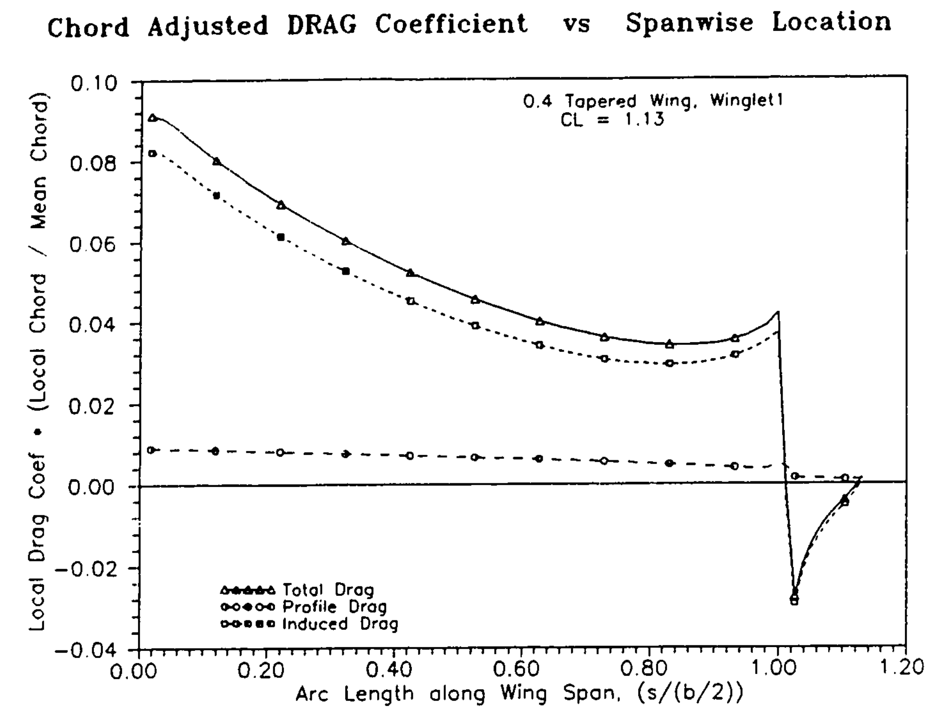

Figure 3.25 Components of the Drag Coefficient for 0.4 Tapered Wing with Winglet 1, $A_R = 8.0$, at $C_L = 1.13$.

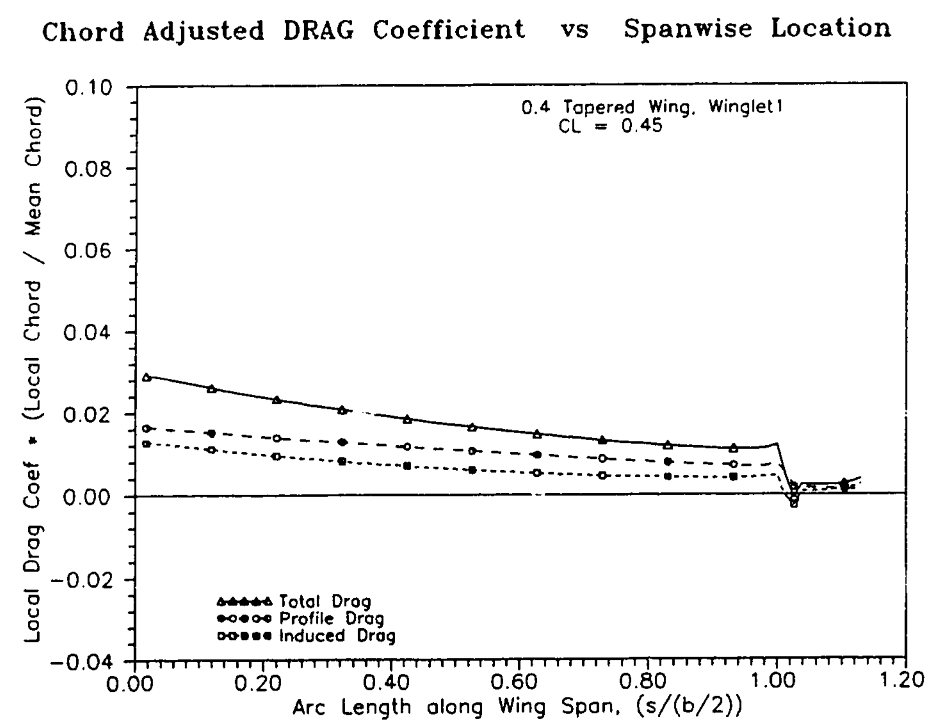

Figure 3.26 Components of the Drag Coefficient for 0.4 Tapered Wing with Winglet 1, $A_R = 8.0$, at $C_L = 0.45$.

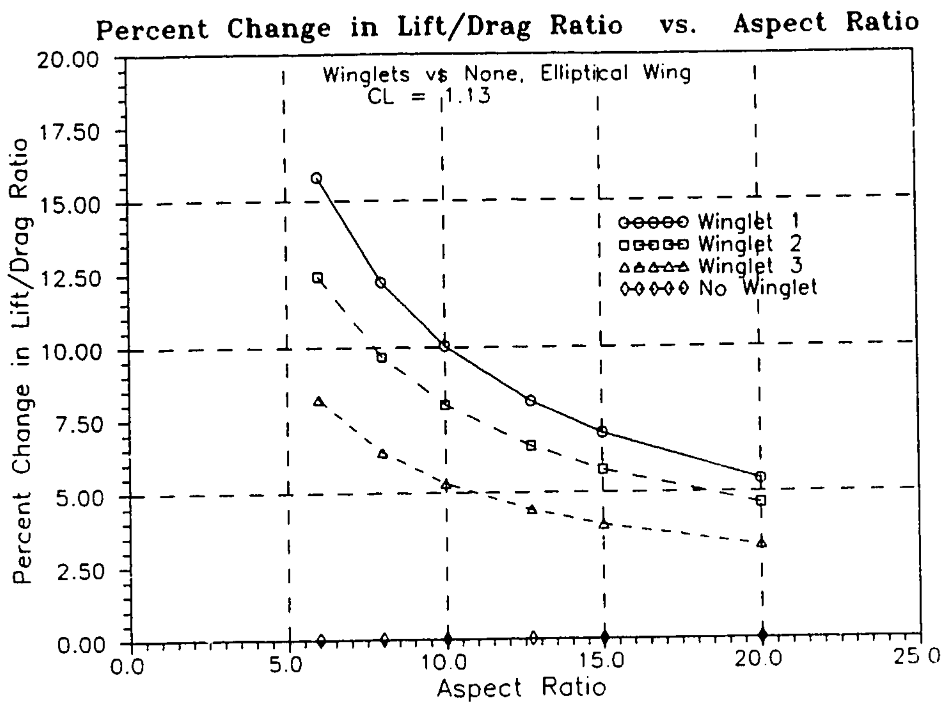

Figure 3.27 Percent Change in Lift/Drag Ratio vs Aspect Ratio for an Elliptical Wing with and without Winglets, A_R = 12.73.

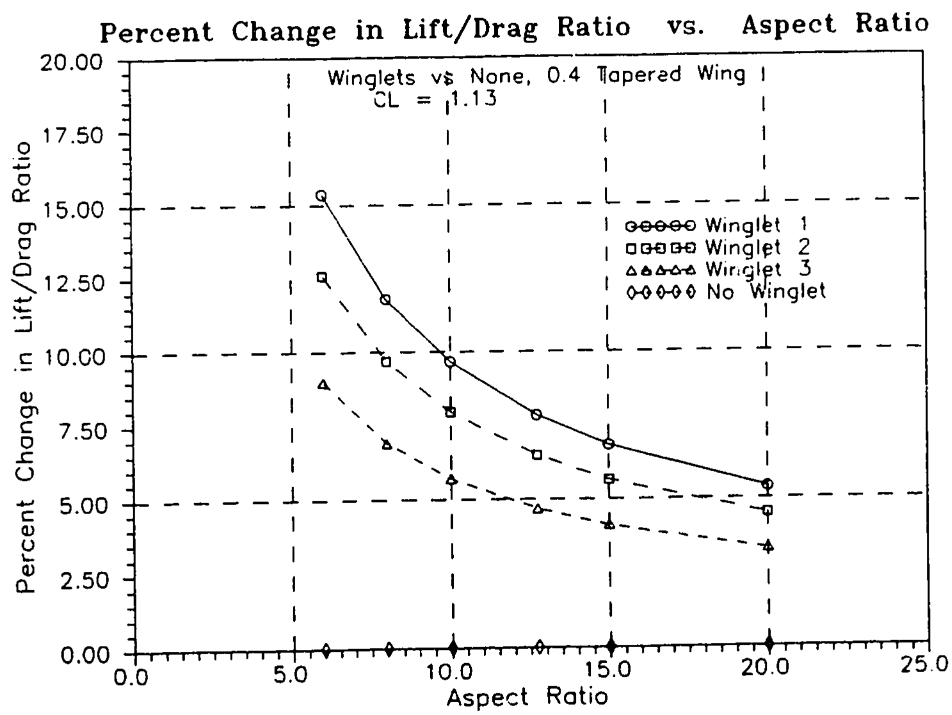

Figure 3.28 Percent Change in Lift/Drag Ratio vs Aspect Ratio for a 0.4 Tapered Wing with and without Winglets, A_R = 12.73.

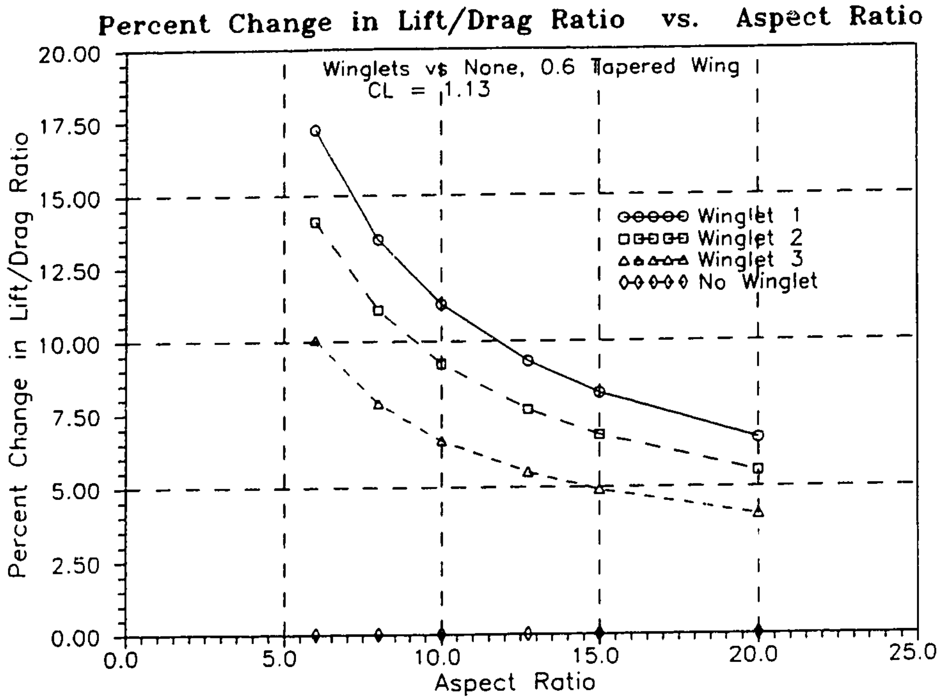

Figure 3.29 Percent Change in Lift/Drag Ratio vs Aspect Ratio for 0.6 Tapered Wing with and without Winglets, A_R = 12.73.

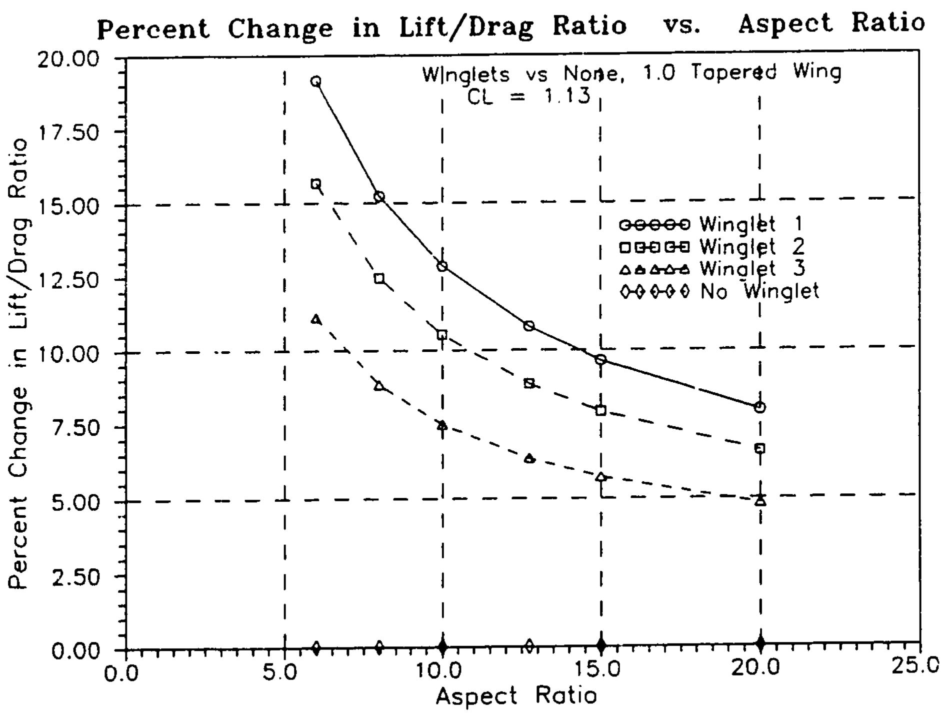

Figure 3.30 Percent Change in Lift/Drag Ratio vs Aspect Ratio for a 1.0 Tapered Wing with and without Winglets, A_R = 12.73.

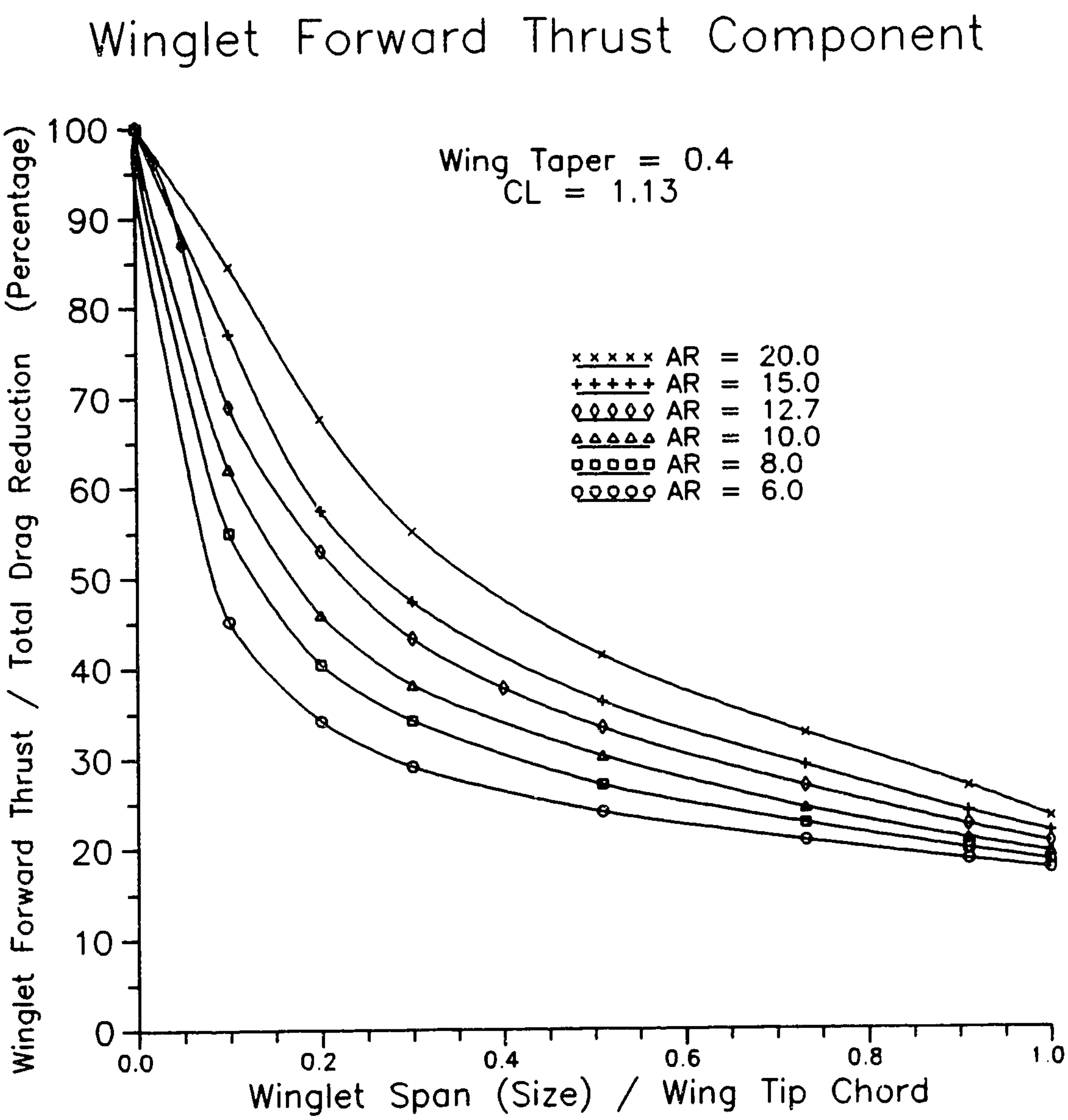

Figure 3.31 Winglet Forward Thrust Component versus (Winglet Span / Wing Tip Chord).

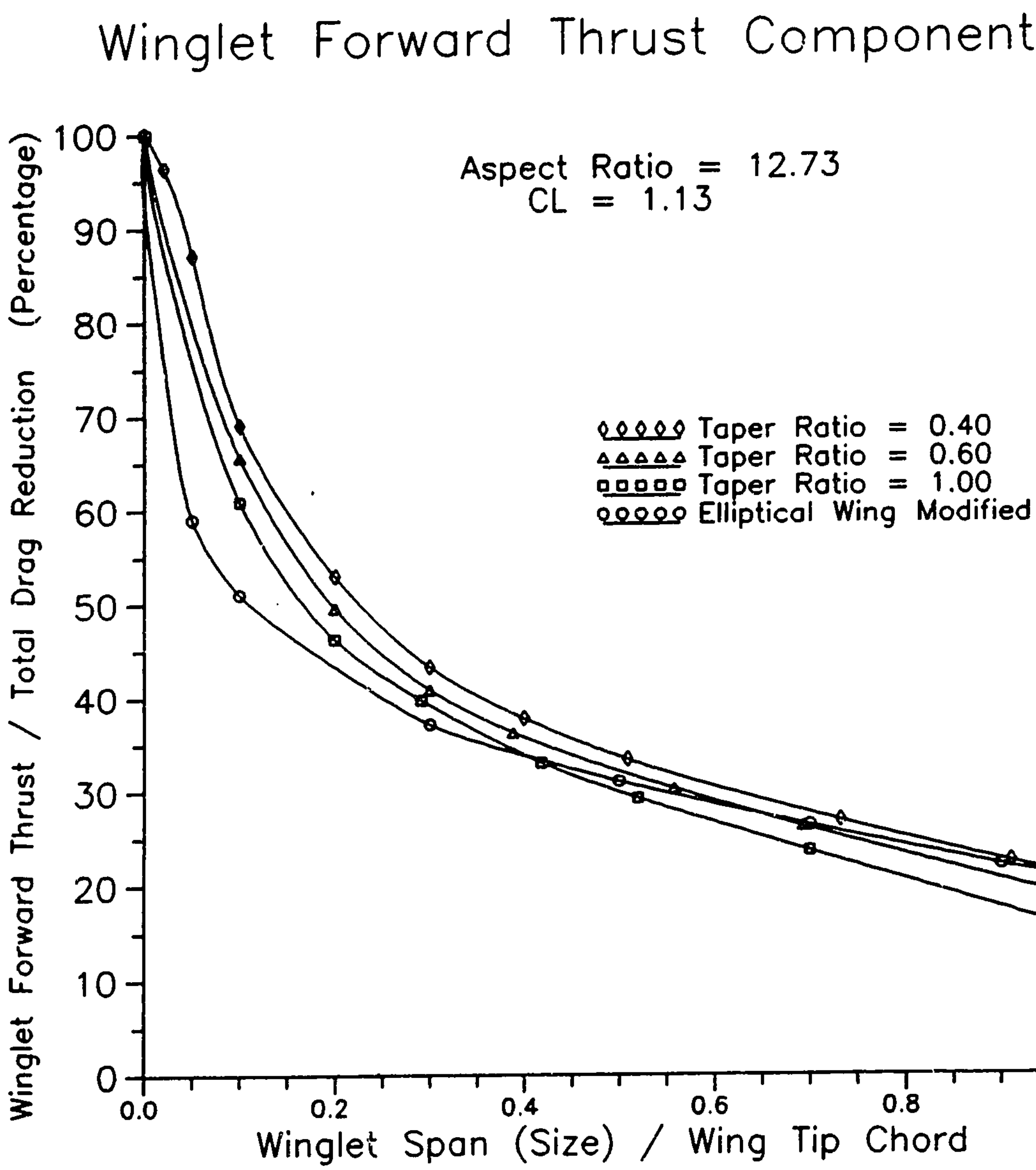

Figure 3.32 Winglet Forward Thrust Component versus (Winglet Span / Wing Tip Chord).

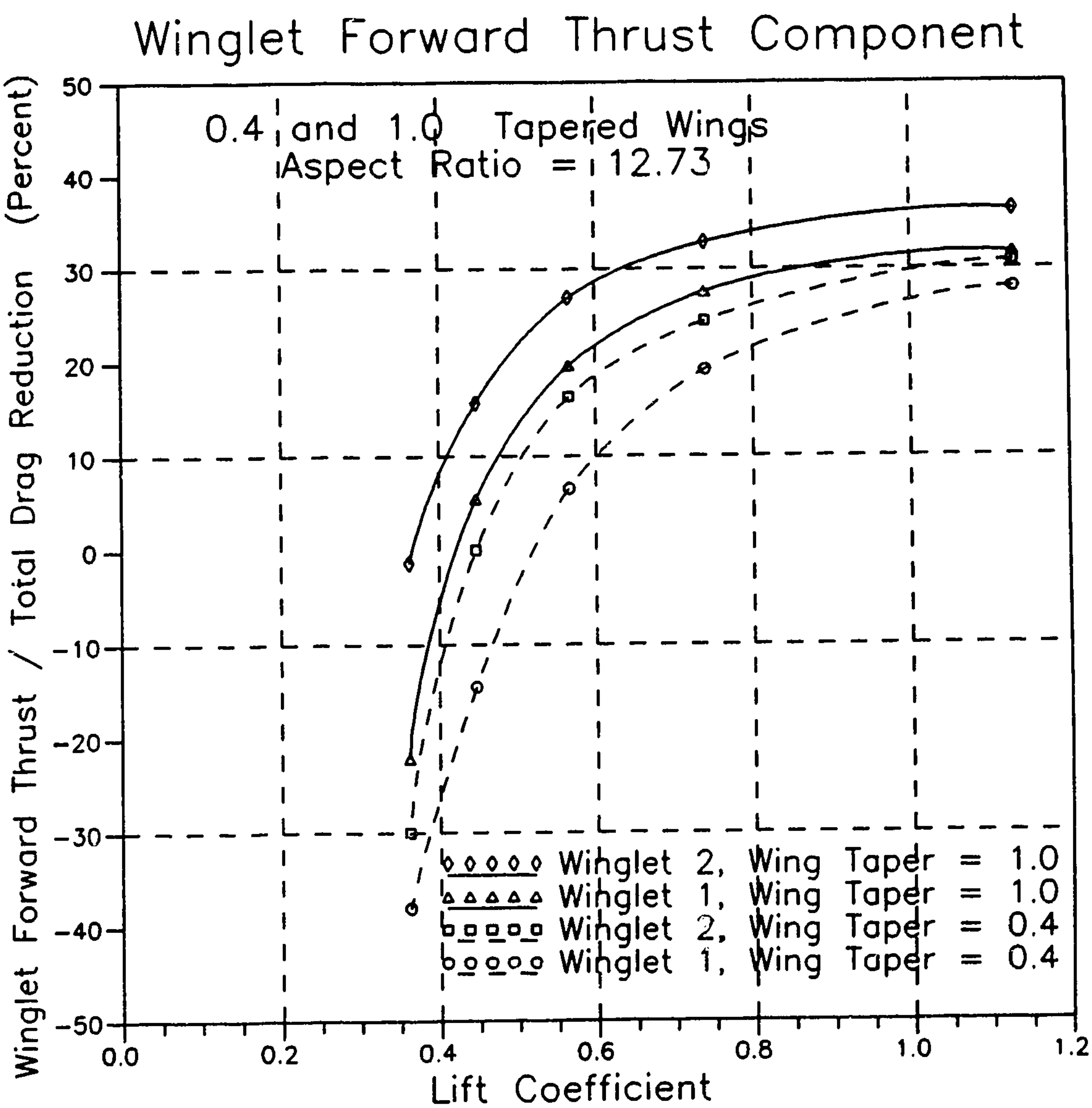

Figure 3.33 Forward Thrust Component vs Lift Coefficient for 0.4 and 1.0 Tapered Wings with and without Winglets, A_R = 12.73.

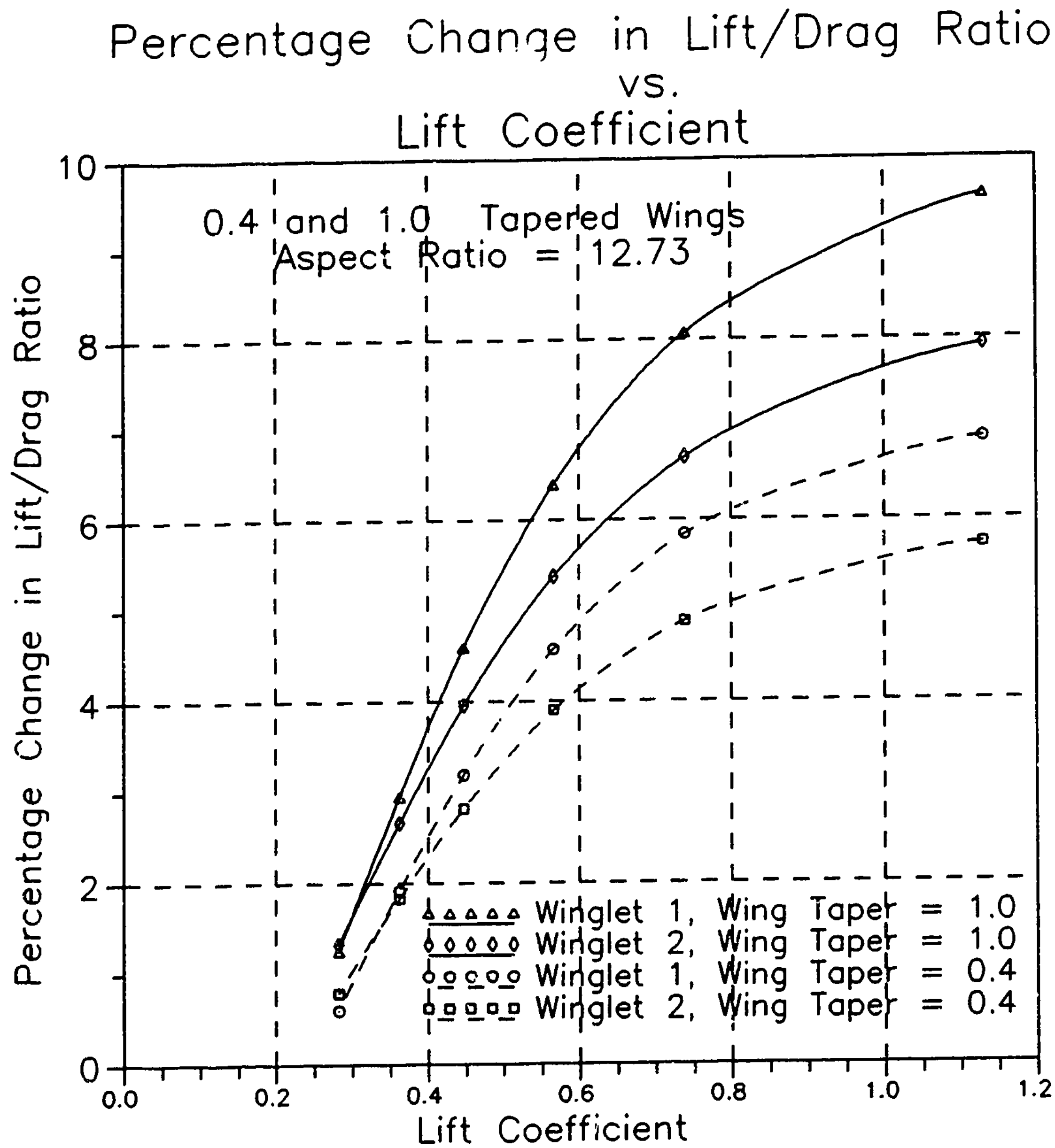

Figure 3.34 Percentage Change in Lift/Drag Ratio vs Lift Coefficient for 0.4 and 1.0 Tapered Wings with and without Winglets, A_R = 12.73.

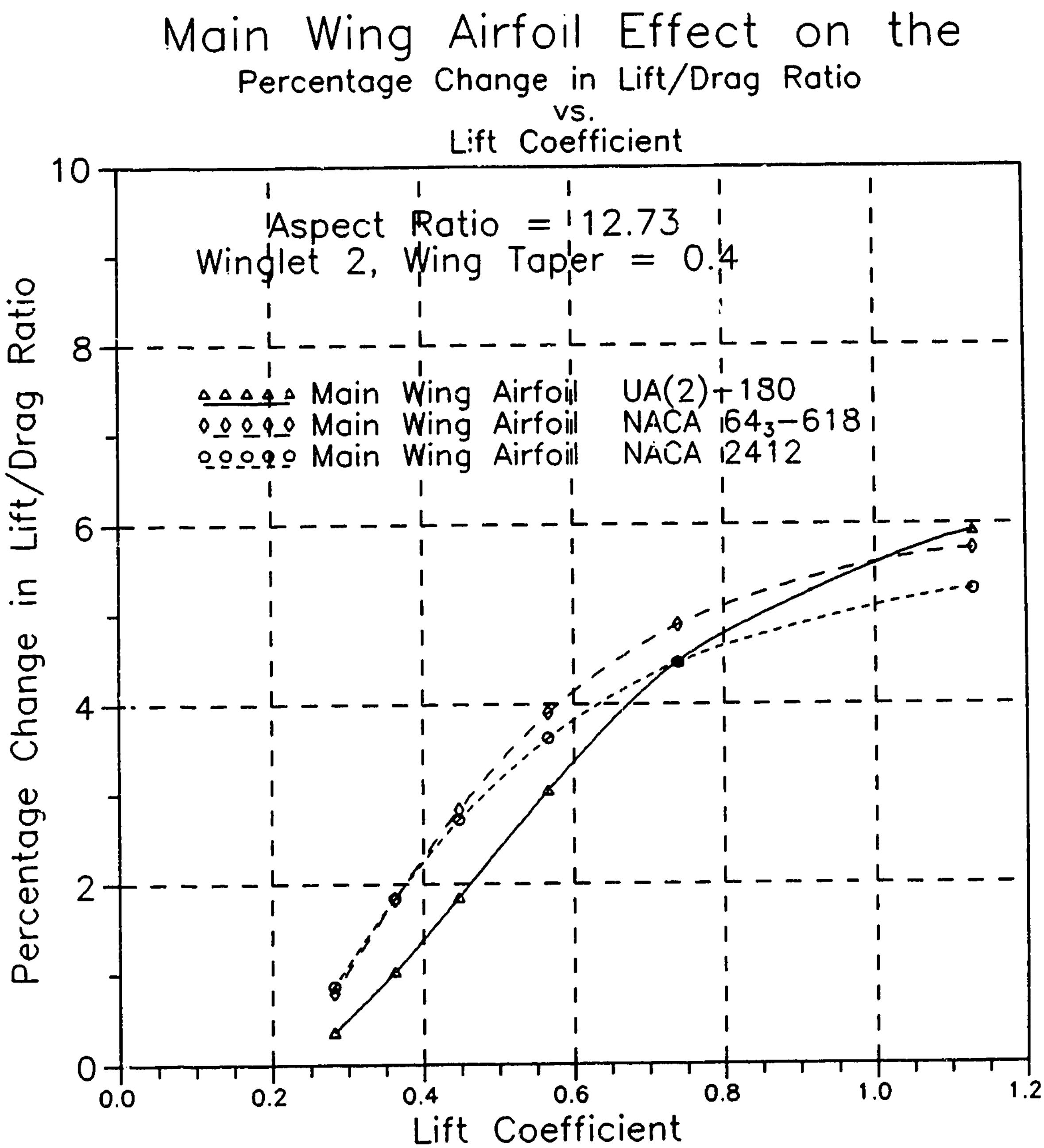

Figure 3.35 Main Wing Airfoil Effect on the Percentage Change in Lift/Drag Ratio vs Lift Coefficient for 0.4 Tapered Wings with Winglet 2, A_R = 12.73.

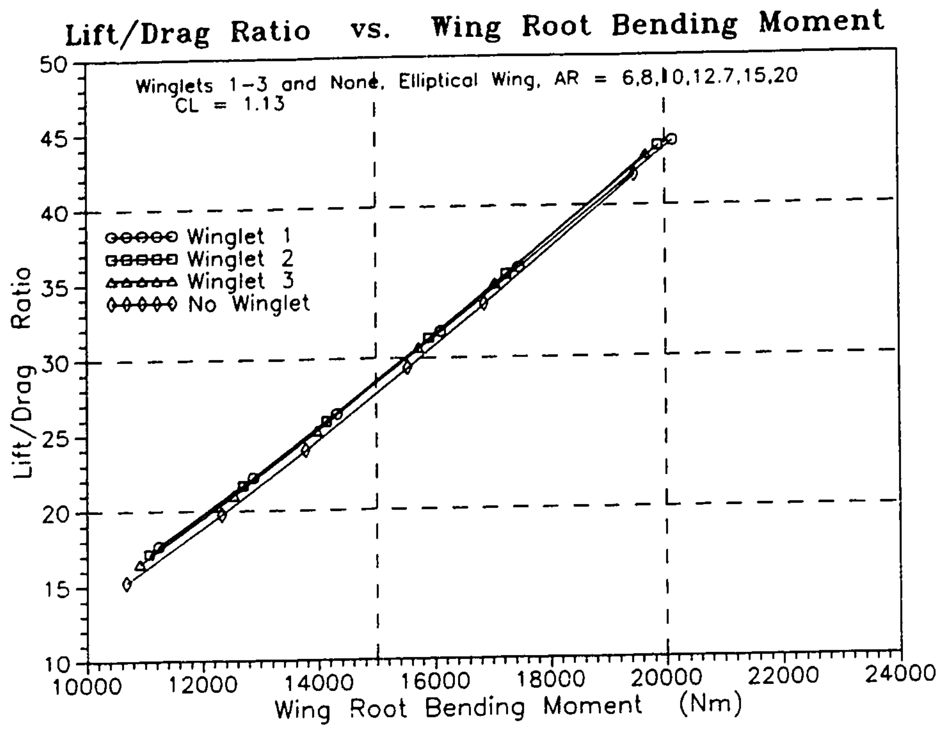

Figure 3.36 Lift/Drag Ratio vs wing root Bending Moment for an Elliptical Wing with and without Winglets.

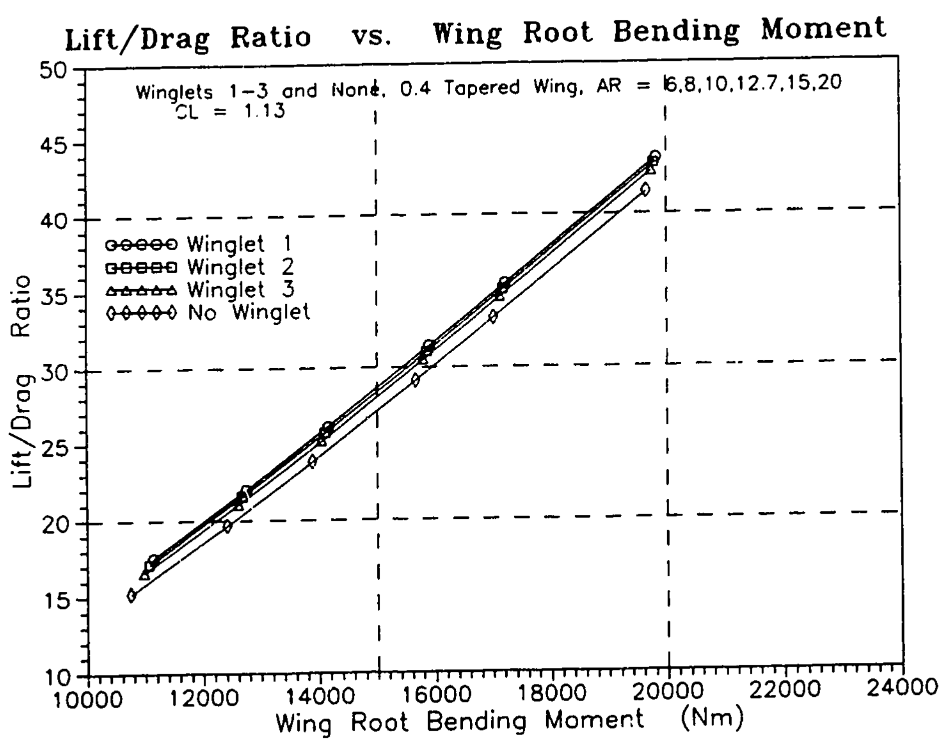

Figure 3.37 Lift/Drag Ratio vs wing root Bending Moment for a 0.4 Tapered Wing with and without Winglets.

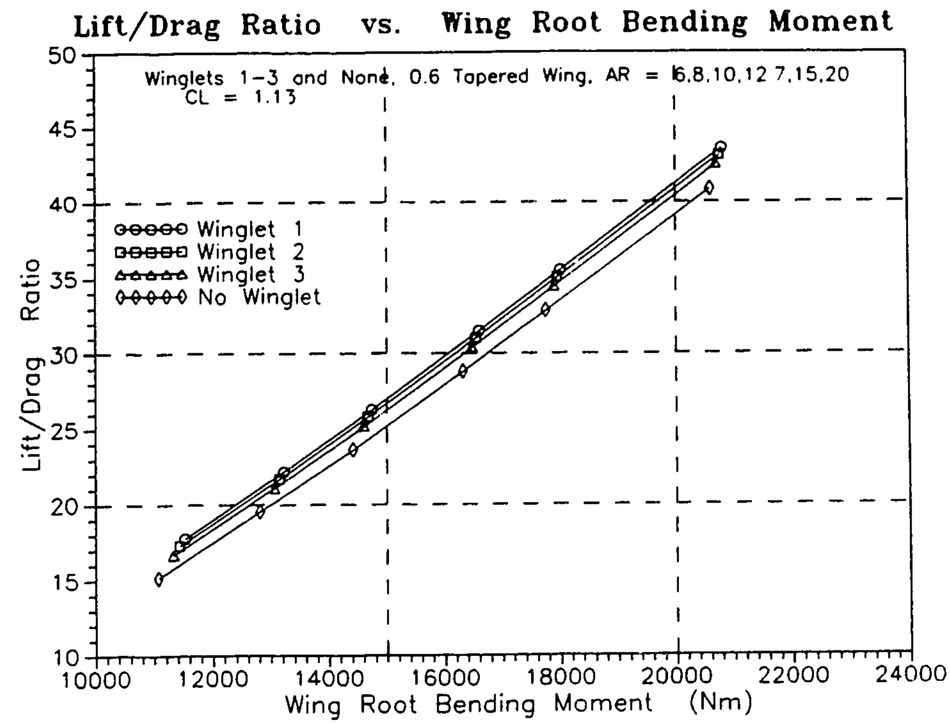

Figure 3.38 Lift/Drag Ratio vs wing Root Bending Moment for 0.6 Tapered Wing with and without Winglets.

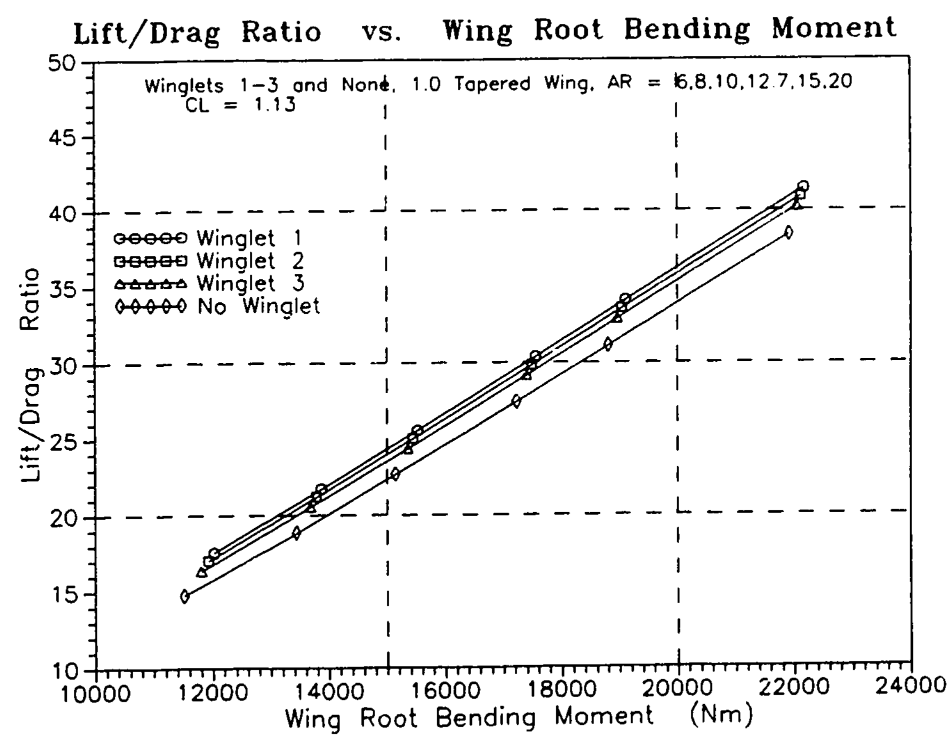

Figure 3.39 Lift/Drag Ratio vs wing root Bending Moment for a 1.0 Tapered Wing with and without Winglets.

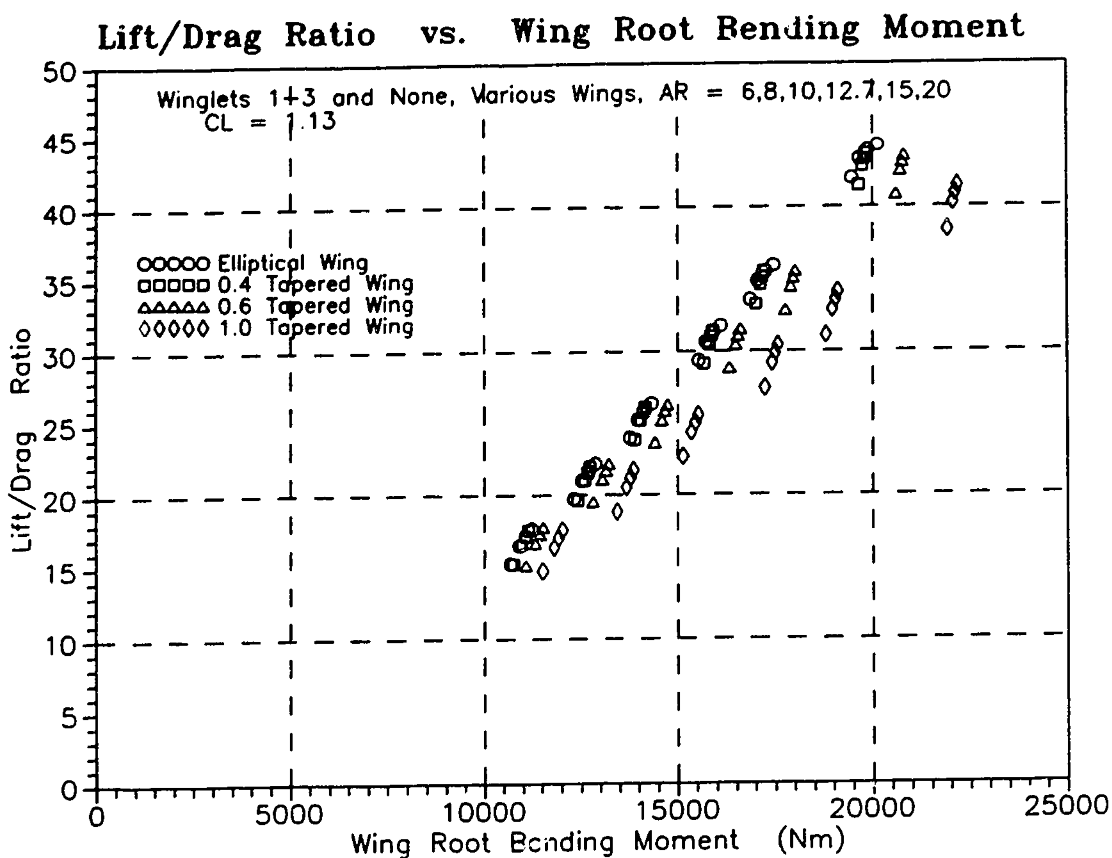

Figure 3.40 Lift/Drag Ratio vs wing root Bending Moment for a 0.4, 0.6, 1.0 Tapered and an Elliptical Wing with and without Winglets.

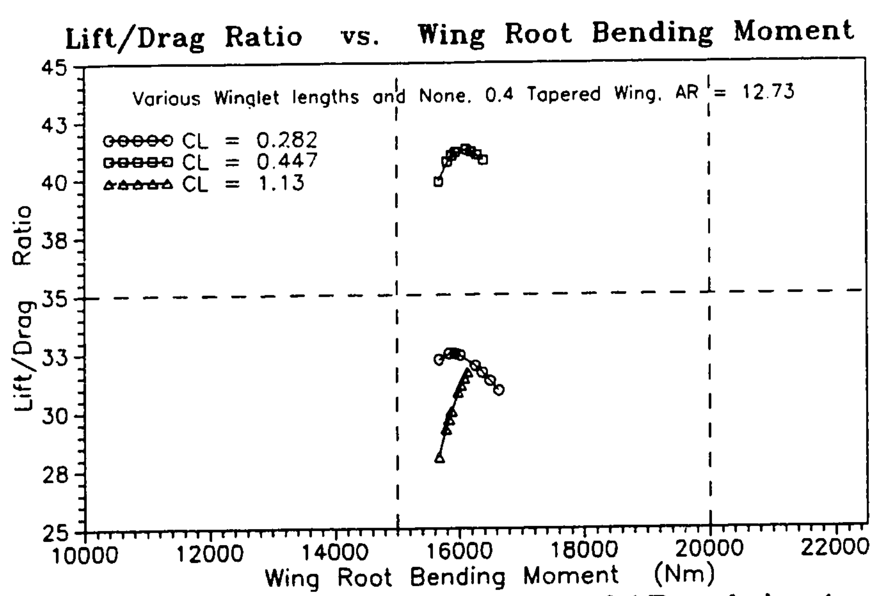

Figure 3.41 Lift/Drag Ratio vs wing root Bending Moment for a 0.4 Tapered wing, A_R = 12.73, with and without winglets, at C_L = 0.282, 0.447, and 1.13.

APPENDIX 3.A

The Simplified Vortex Lattice Method (VLM)

This section gives the approach used for the solution for the spanwise loading of a non-planar wing using this simplified vortex lattice method. Note that this solution also includes the geometry for a finite wing with varying chord, twist, and airfoil.

The distribution of the load on a wing is related to the bound circulation distribution since the circulation generates the lift for a unit span at any spanwise location equivalent to, $l(y)$.

$$l(y) = \rho\, V(y)\, \Gamma(y) \tag{3.A.1}$$

Where, ρ is the air density, and $V(y)$ the local resultant air velocity. Hence, the total lift of the wing is given by:

$$L = \int_{-b/2}^{b/2} l(y)\, dy \tag{3.A.2}$$

Note also that per unit span the lift, $l(y)$, can be given by,

$$l(y) = \frac{1}{2}\, \rho\, C_l(y)\, c(y)\, V(y)^2 \tag{3.A.3}$$

with,

$$\begin{aligned} C_l(y) &= C_{l_o}(y) + \frac{dC_l}{d\alpha}(\alpha(y)) \\ &= C_{l_o}(y) + dC_{l_\alpha}\,(\alpha(y)) \end{aligned} \tag{3.A.4}$$

where, $c(y)$ is the local chord of the airfoil, $C_l(y)$ is the local lift coefficient, $C_{l_o}(y)$ is the local lift coefficient of the airfoil at $\alpha = 0°$, and $C_{l_\alpha} = dC_l(y)/d\alpha$ is the local airfoil lift curve slope. Also, $\alpha(y)$ is the local angle of attack, which is given by:

$$\alpha(y) = \alpha_{init}(y) - \frac{v_{normal}(y)}{V(y)} \tag{3.A.5}$$

where, $V(y)$ is the resultant air velocity, and $v_{normal}(y)$ is the induced air velocity component normal to the wing section at the spanwise location y.

$$\alpha_{init}(y) = \alpha_o + \alpha_{twist}(y) \tag{3.A.6}$$

Also, $\alpha_{init}(y)$ is the angle of attack due to the initial wing incidence and the direction of the freestream air velocity without the downwash considered, α_o is the initial wing root incidence, $\alpha_{twist}(y)$ is the increased angle of attack due to the twist of the wing relative to the root incidence.

Combining Equations 3.A.1 and 3.A.3, and solving for the circulation, $\Gamma(y)$, at each spanwise location, y, shows that

$$\Gamma(y) = \frac{1}{2}\, c(y)\, C_l(y)\, V(y) \tag{3.A.7}$$

where,
$$V(y) = V_\infty(y) + v_{xind}(y) \tag{3.A.8}$$

hence,
$$\Gamma(y) = \frac{1}{2}\, c(y)\, C_l(y)\, (V_\infty(y) + v_{xind}(y)) \tag{3.A.9}$$

Including the term for $C_L(y)$ gives,
$$\Gamma(y) = \frac{1}{2}\, c(y)\, [C_{lo}(y) + C_{l\alpha}(y)\alpha(y)]\, [V_\infty(y) + v_{xind}(y)] \tag{3.A.10}$$

Also, including the term for $\alpha(y)$ gives,
$$\Gamma(y) = \frac{1}{2}\, c(y)\, [C_{lo}(y) + C_{l\alpha}(y)\, (\alpha_o + \alpha_{twist}(y) + \alpha_{ind}(y))]\, [V_\infty(y) + v_{xind}(y)] \tag{3.A.11}$$

Now inserting $v_{normal}(y)/V(y)$ for $\alpha_{ind}(y)$ gives,
$$\Gamma(y) = \frac{1}{2}\, c(y)\, [C_{lo}(y) + C_{l\alpha}(y)\, (\alpha_o + \alpha_{twist}(y) + \frac{v_{normal}(y)}{V(y)})]\, [V_\infty(y) + v_{xind}(y)] \tag{3.A.12}$$

Expanding $V(y)$ gives,
$$\Gamma(y) = \frac{1}{2} c(y)\, [C_{lo}(y) + C_{l\alpha}(y)\, (\alpha_o + \alpha_{twist}(y) + \frac{v_{normal}(y)}{V_\infty(y) + v_{xind}(y)})][V_\infty(y) + v_{xind}(y)] \tag{3.A.13}$$

Now rearranging terms,
$$\begin{aligned}\Gamma(y) &= \frac{1}{2}\, c(y)\, C_{lo}(y)\, [V_\infty(y) + v_{xind}(y)] \\ &+ \frac{1}{2}\, c(y)\, C_{l\alpha}(y)\, [\alpha_o + \alpha_{twist}(y)]\, [V_\infty(y) + v_{xind}(y)] \\ &+ \frac{1}{2}\, c(y)\, C_{l\alpha}(y)\, v_{normal}(y)\end{aligned} \tag{3.A.14}$$

or giving,
$$\begin{aligned}\Gamma(y) &= \frac{1}{2}\, c(y)\, C_{lo}(y)\, V_\infty(y) + \frac{1}{2}\, c(y)\, C_{lo}\, v_{xind}(y) \\ &+ \frac{1}{2}\, c(y)\, C_{l\alpha}(y)\, [\alpha_o + \alpha_{twist}(y)]\, V_\infty(y) \\ &+ \frac{1}{2}\, c(y)\, C_{l\alpha}(y)\, [\alpha_o + \alpha_{twist}(y)]\, v_{xind}(y) \\ &+ \frac{1}{2}\, c(y)\, C_{l\alpha}(y)\, v_{normal}(y)\end{aligned} \tag{3.A.15}$$

Note that y formally is the spanwise coordinate axis, but is also used as the arc-length variable here. Also, note that $v_{normal}(y)$ is the induced velocity normal or perpendicular to the section at y.

The circulation shed at any spanwise location can be determined by the spanwise rate of change of circulation of the wing, $d\Gamma(y)/dy$. This shed circulation determines the strength of the ng vortex sheet at that location.
The strength of the trailing vorticity then determines the induced air velocity at any spanwise location.

The end result of this is that the solution is found for $\Gamma(y)$ as given in Equation 3.A.9, from which the loading at any location along the span of the wing is determined, as per Equation 3.A.1.

For the vortex lattice method the bound vortex system is the discretized form of $\Gamma(y)$, and vortex sheet is discretized into n trailing vortex filaments. These are semi-infinite line vortices each of strength determined by $(d\Gamma(y)/dy)\Delta y$, where Δy is the spanwise distance between vortex filaments.

The method of solution is to find the simultaneous solution for n equations, where n is the number of trailing vortex filaments and also the number of the bound vortex elements.

When the discretization of the vortex system has taken place the equations may be rewritten in indicial form.

Starting with the bound vortex at the spanwise location y with the discretized bound vortex segment designated at that point labelled as j, then

$$\Gamma(y) = \Gamma_j \qquad \textbf{(3.A.16)}$$

and the trailing vortex filaments are represented by

$$\frac{d\Gamma(y)}{dy}\,\Delta y = \gamma_i \qquad \textbf{(3.A.17)}$$

The strength of the bound vortex element at point j is the sum of all of the trailing vortex filaments outboard of that point as given by

$$\Gamma_j = \sum_{i=j}^{n} \gamma_i \qquad \textbf{(3.A.18)}$$

Now, the normal velocity component at point j along the wing due to the trailing vortex system is

$$v_{normal_j} = \sum_{i=j}^{n} \gamma_i \, c_{ij} \qquad \textbf{(3.A.19)}$$

where, c_{ij} is the influence coefficient of the trailing vortex filament i at point j of the bound vortex. (i.e. c_{ij} is the coefficient which includes all of the information regarding the geometry from the vortex i to the point j which is used to define the induced normal velocity at the point j due to vortex i.)

Now notice that some portions of the terms will be constants. Therefore, the following substitutions may be made.

$$Const1_j = \frac{1}{2}\, c(y_j)\; C_{l_\alpha}(y_j) \tag{3.A.20}$$

$$Const4_j = \frac{1}{2}\, c(y)\; C_{l_o}(y) \tag{3.A.21}$$

$$Const3_j = Const4_j \cdot V_\infty(y) \tag{3.A.22}$$

$$Const5_j = \alpha_o + \alpha_{twist}(y) \tag{3.A.23}$$

$$Const2_j = Const3_j \cdot Const5_j \cdot V_\infty(y) \tag{3.A.24}$$

$$Const6_j = Const1_j \cdot Const5_j \tag{3.A.25}$$

Finally, we get the result that

$$\begin{aligned}\Gamma_j = {} & Const3_j + Const4_j \cdot v_{xind_j} + Const2_j \\ & + Const1_j \cdot Const5_j \cdot v_{xind_j} + Const1_j \cdot v_{normal_j}\end{aligned} \tag{3.A.26}$$

Or simplified more as,

$$\Gamma_j = Const3_j + Const2_j + (Const4_j + Const6_j)\, v_{xind_j} + Const1_j \cdot v_{normal_j} \tag{3.A.27}$$

Recall that

$$\Gamma_j = \sum_{i=j}^{n} \gamma_i$$

And recalling that the normal velocity component induced by the trailing vortex filaments is

$$v_{normal_j} = \sum_{i=j}^{n} \gamma_i\, c_{ij}$$

where, c_{ij} is the influence coefficient of the trailing vortex filament i at point j of the bound vortex for the normal velocity component.

And writing the normal velocity component induced by the bound vortex elements as

$$v_{normal_j} = \sum_{i=1}^{n} \Gamma_i\, g_{ij} \tag{3.A.28}$$

where, g_{ij} is the influence coefficient of the bound vortex element i at point j of the bound vortex for the normal velocity component.

And letting the streamwise (x-axis) velocity component induced by the bound vortex elements as

$$v_{xind_j} = \sum_{i=1}^{n} \Gamma_i\, d_{ij} \tag{3.A.29}$$

where, d_{ij} is the influence coefficient of the bound vortex element i at point j of the bound vortex for the streamwise velocity component.

Therefore,

$$\sum_{i=j}^{n} \gamma_i = Const3_j + Const2_j$$
$$+ (Const4_j + Const6_j) \sum_{i=1}^{n} \Gamma_i \, d_{ij} \qquad (3.A.30)$$
$$+ Const1_j \left[\sum_{i=1}^{n} \gamma_i \, c_{ij} + \sum_{i=1}^{n} \Gamma_i \, g_{ij}\right]$$

Finally, we get the result

$$\sum_{i=j}^{n} \gamma_i = Const3_j + Const2_j$$
$$+ (Const4_j + Const6_j) \left(\sum_{i=1}^{n} \left(\sum_{k=i}^{n} \gamma_k \, d_{ij}\right)\right) \qquad (3.A.31)$$
$$+ Const1_j \left[\left(\sum_{i=1}^{n} \gamma_i \, c_{ij}\right) + \left(\sum_{i=1}^{n} \left(\sum_{k=i}^{n} \gamma_k \, g_{ij}\right)\right)\right]$$

Now we can solve this set of n equations for the values for the strengths of the trailing vortex filaments γ_i and hence also for the strengths of the bound vortex elements Γ_j, which will in turn give us the values for spanwise load distribution $l(y)$.

The solution is not straight forward due to the double summations and γ_i appears on both sides.

The linearizing assumptions are that the wing is nearly planar and hence the self-induced velocity of the bound vortex system is negligible. (But, for a vertical winglet the wing is non-planar.)

However, notice that if the linearizing assumptions are made then the terms with the double summation drop out and the solution is simple, which uses the induced velocity due to the trailing vortices only. In that case we are left with,

$$\sum_{i=j}^{n} \gamma_i = Const3_j + Const2_j + Const1_j \left(\sum_{i=1}^{n} \gamma_i \, c_{ij}\right) \qquad (3.A.32)$$

or moving all of the terms with γ_i to the one side gives,

$$\sum_{i=1}^{n} \gamma_i \, (k + Const1_j \, c_{ij}) = Const3_j + Const2_j$$
$$where, \; k = 1 \, , \; i \geq j \qquad (3.A.33)$$
$$k = 0 \, , \; i < j$$

This is in the form of a system of linear equations

$$\sum_{i=1}^{n} A_{ji} \, \gamma_i = B_j \qquad where, \; j = 1, 2, \ldots, n \qquad (3.A.34)$$

This is easy to solve for γ_i using Gaussian Elimination, from which Γ_i can be determined.

Next, the non-planar effects can be considered by taking this initial solution as a starting point for the next step of the solution.
The solution for the spanwise loading is determined using the downwash from the trailing vortex system. Once this is done then the induced velocity field from the bound vortex elements can be fed back into the

equations above (Equation 3.A.31) and treated as constants, then the solution can be recalculated using Equation 3.A.35. This provides an iterative method to arrive at a more accurate value for the spanwise circulation distribution and loading.

For the final phase of the solution, once the linear solution is found, i.e. $d\Gamma(y)/dy$ and $\Gamma(y)$, the information for the bound vortex and the trailing vortex system is used to determine the aerodynamic forces that the wing produces. During this phase of the calculations all of the information is calculated and stored separatedly with regard to the profile drag, the induced drag, and the induced lift along the arc of the wing.

APPENDIX 3.B

Explanation of the Linear Taper Modification to the Elliptical Wing and the Winglet "Family" Modelled

One of the comparisons is to be between a simple elliptical wing and the same with a winglet attached. However, an elliptical wing has a zero tip chord which makes attachment of a finite chord winglet somewhat difficult. Therefore the elliptical wing has been modified to produce a finite tip chord. Figure 3.1 shows the method of extrapolating to a finite tip on an elliptical wing. In order to produce the modified elliptical wing, the elliptical wing used is one with a linear trailing edge and elliptically curved leading edge. The modification was such that there was a tangent taken to the elliptical curve at some designated spanwise location. Then that tangent line was used to extrapolate to the same span as the original elliptical wing. Of course, since the total wing area would have been increased due to the increase tip area, the wing chord was adjusted all along the span to produce the same wing area as the basic elliptical wing. This chord adjustment produced a final wing with winglet with the same area and aspect ratio as the basic elliptical wing, hence comparisons are made correctly between resulting wings.

For an elliptical wing, the chord at any spanwise location is given by c where,

$$c = c_o \left(1 - \left(\frac{y}{b/2}\right)^2\right)^{1/2} \tag{3.B.1}$$

Now at the tip of the elliptical modified wing, the new wing tip chord is given by,

$$c_{tip} = c_r + (1-r) \left(\frac{dc}{dy}\right)\Big|_t \tag{3.B.2}$$

and at any spanwise location within the linear taper region, the wing chord is given by,

$$c = c_r + \left(\frac{y}{b/2} - r\right) \left(\frac{dc}{dy}\right)\Big|_t \tag{3.B.3}$$

where, $(dc/dy)|_t$ is the derivative of the chord function at the tangent point, and where,

$$\frac{dc}{dy}\Big|_{\frac{y}{b/2}=r} = \left(\frac{-c_o r}{b/2}\right) (1-r^2)^{1/2} \tag{3.B.4}$$

which then gives for the chord at any spanwise location within the linear taper,

$$c\Big|_{\left(\frac{y}{b/2}\right)} = c_o(1-r^2)^{1/2} + \left(\frac{y}{b/2} - r\right) \left[\left(\frac{-c_o r}{b/2}\right) (1-r^2)^{-1/2}\right] \tag{3.B.5}$$

This method of modifying the elliptical wing was used to produce three different winglet sizes, based on the linear taper of the elliptical wing from $(y/(b/2)) = 0.7$, 0.8, and 0.9 of the wing span. For these, Winglet1 corresponds to the taper from $(y/(b/2)) = 0.7$, Winglet2 corresponds to the taper from $(y/(b/2)) = 0.8$, and Winglet3 corresponds to the taper from $(y/(b/2)) = 0.9$. This produces the three winglets in order of size such that: Winglet1 > Winglet2 > Winglet3. Specifically, Winglet 1 span $\approx$ 1.24340 $\times$ Winglet 2 span $\approx$ 1.78920 $\times$ Winglet 3 span. Also, note that with this "family" of winglets, the winglet area equals $(3/8)\times(\text{winglet span})^2$. This gives $\text{Area}_{\text{Winglet1}} \approx 1.54605 * \text{Area}_{\text{Winglet2}} \approx 3.20128 \times \text{Area}_{\text{Winglet3}}$.

For the winglet family used these were the other defining characteristics. The winglet span is equal to 1.0 times the modified elliptical wing tip chord, i.e. the tip chord which was produced by the linear extrapolation from the designated spanwise location on the elliptical wing. All of the winglets examined were vertical winglets (winglet cant angle = 90°). The winglets have no sweep of their quarter chord line. The winglet root chord equals (0.5 × winglet span). The winglet root is set at a zero toe-in angle with respect to the freestream direction. The winglet tip chord equals one quarter of that winglet span. Hence, the winglet has 0.5 taper ratio and the winglet A_R = 5.3. At the winglet tip, the toe-in is set at 6°. The quarter chord line of the winglet at the winglet root is aligned with the quarter chord line of the main wing at the main wing tip. Figure 3.2 shows a sketch of a typical winglet. For this comparision, the main wing airfoil is the NACA 64_3-618. The winglet airfoil is the UA(2)-180 (Marsden, 1988).

These three sizes of winglets were then attached to the four wings used in the study. These wings are: the ellipitcal and taper ratios 0.4, 0.6, and 1.0. Note that when the winglets were on the modified elliptical wings the winglet spans were always equal to the modified wing tip chord. However, when those same winglets were on the tapered wings they had three different ratios of winglet span to wing tip chord. Table 3.B.1 gives the winglet sizes for the particular aspect ratios are given to provide an idea of the actual size of the winglets used.

Also, note that the exact same *size* of winglet is used on each of the four wing types when they are compared at the same A_R. This means that for two different wing shapes, at the same aspect ratio and wing span, they will have the exact same winglet attached. Hence, comparisons between different planform wing shapes of the same aspect ratio and span can be made and still be meaningful. However, note that for wings of different aspect ratio, the winglet is actually a different physical size. This is since the winglet span is based on the wing tip chord of the modified elliptical wing. This produces larger winglets for low aspect ratios than for high aspect ratios. Note that since the winglets are scale versions of one another, the area of say winglet 1 on a wing of A_R1 is inversely proportional to the area of winglet 1 on a wing of A_R2, such that: $(\text{Area}_{\text{Winglet1}} / \text{Area}_{\text{Winglet1}}) = (A_R2 / A_R1)$.

Table 3.B.1. Wing and Winglet Information for the current study.

Wing Aspect Ratio	Wing Span (m)	Winglet 1 Span (m)	Winglet 2 Span (m)	Winglet 3 Span (m)	Winglet 1 Area (% main)	Winglet 2 Area (% main)	Winglet 3 Area (% main)
6.0	10.297	0.892	0.718	0.499	1.690	1.093	0.528
8.0	11.890	0.773	0.622	0.432	1.268	0.820	0.396
10.0	13.293	0.691	0.556	0.386	1.014	0.656	0.317
12.73	15.000	0 613	0.493	0.342	0.797	0.515	0.249
15.0	16.281	0.564	0.454	0.315	0.676	0.437	0.211
20.0	18.800	0.489	0.393	0.273	0.507	0.328	0.158

Also, note the area of the winglets with respect to the main wing planform areas. For all aspect ratios of the test cases used and shown main wing planform area is 17.67146 m^2.

CHAPTER 4

ROLL-UP OF THE TRAILING VORTEX SHEET BEHIND A LIFTING WING CONSIDERING THE EFFECTS OF BOUNDARY LAYER THICKNESS

4.1 INTRODUCTION

For the last 70 years, since Prandtl (1921) and even earlier back to Lanchester (1907), numerous researchers have studied the phenomenon of vortex sheet roll up. Even today the area attracts much interest, hence, adding to the body of accumulated knowledge has become very challenging.

Multitudes of vortex sheet roll-up simulation methods have been attempted, some more successfully than others. However, with all of the work that has been done, it is even more remarkable that there remains such uncertainty about the roll-up process and how it is influenced by the main wing characteristics.

Significant past effort has been focused on the development of efficient wing systems, their vorticity distributions, and the shed vorticity. Much of that work has concerned the subject of the tangential velocity distribution through a trailing vortex core, yet a great deal of that work has dealt only with the case of a fully rolled up vortex (See Staubenbiel, 1984; Arakeri *et al.*, 1988, etc.). Also, especially in the mid 1970's, there was an abundance of research concerning the relationship between tangential velocity and radius during the period of vortex decay. The interest in the trailing vortex structure and decay arose mainly due its importance regarding vortex persistance and the implications for air traffic control. At that time and still today, the vortex wake hazard dictates the requirements for spacing between aircraft during flight and even more importantly in take-off or landing phases. Much of the work done in the 1970's did not continue into the next decade even though there was still much to be learned (likely financial constraints limited the continuation of the research). The importance of the vortex wake hazard alleviation has become a dominant issue again in recent years. This has been due to the need for increased air traffic at many airports where there is no opportunity for growth in physical size. Also, in the last couple of years, several aircraft accidents have been thought to be caused by aircraft encounters with the wake from preceding aircraft. These accidents occurred even though the standard rules for separation were being adhered to at the time. There have been indications that some aircraft are producing trailing vortex wake structures which are more intense than would be normally predicted by the aircraft weight and airspeed. The end result is that there remains room for improvement in the prediciton of the trailing vortex wake structure.

The importance of the process of vortex sheet roll-up has been recognized by many researchers. However, a literature review revealed that amidst all of the numerical simulation and experimental work that has been done, there does not seem to be any clear indication of a time dependent relationship between the boundary layer thickness on the lifting wing, the rolling up vortex sheet, and the tangential velocity profile in the resulting vortex core, especially the maximum tangential velocity in the developing core.

Thus, this work will attempt to add to the understanding of the significance of the trailing vortex sheet structure on the evolving vortex core structure. In particular, this research has focused on examining the time dependent relationship between the boundary layer thickness, the rolling up vortex sheet, and the structure and velocity profile of the developing vortex core (especially the core size, the maximum tangential velocity, and the minimum pressure in the evolving trailing vortex core).

This work has been prompted by some preliminary wind tunnel experiments at the University of Alberta which have provided some indication that the boundary layer thickness of a wing would affect the rolling up vortex sheet and hence the radius of and the tangential velocity profile in the developing vortex core. Based on this preliminary experimental work, some numerical simulation has been done which does indicate that a wing with a thick boundary layer will produce a developing vortex core which has a lower maximum tangential velocity at a larger radius than another wing at the same C_L but with a thinner boundary layer.

As stated by Sarpkaya (1989), "The ultimate objective of the simulation via vortex dynamics is the acquisition of new insights rather than accurate predictions. The flow simulated by the numerical model may not be physically realizable even under controlled laboratory conditions." Although the model accuracy is not ignored, with this in mind, the goal of this study was to use a simple vortex model, but to concentrate on obtaining some new insight. Hence, the vortex sheet was modelled with multiple rows of Rankine vortices, as shown in Figure 4.1. The multiple row method may not be experimentally reproducible, however the method will be shown to shed new light on the vortex sheet roll-up problem.

To date, this numerical simulation has only considered the case of an elliptically loaded, planar wing with various boundary layer thicknesses. This wing produces a single trailing vortex core from each semi-span during the vortex sheet roll-up. In the future, the investigation will proceed to cover systems which model a varying boundary layer thickness over the wing and a multiple winglet system.

4.2 REVIEW OF RELATED MATERIAL

The reader is referred to Chapter 2 which gives a literature review summarizing the necessary basics of vorticity and provides references for more comprehensive reviews of vortex dynamics.

4.2.1 Some Theoretical Basics of Vorticity

The Betz laws of conservation of vorticity were described by Donaldson *et al.* (1974) (and Betz 1933). These conservation laws show that a fully rolled up vortex sheet must produce a core region whose moments of vorticity are the same as that of the original vorticity distribution. The equations given by Betz also related the initial spanwise vorticity distribution to the radial distribution of vorticity in the emerging core of a rolling up trailing vortex wake.

4.2.1.1 Boundary Layer Thickness and the 2nd Moment of Vorticity

From the conservation laws of vorticity, a fully rolled up vortex sheet must produce a core region whose 2nd moment of vorticity is the same as that of the original vorticity distribution. For a fully rolled up vortex core the initial spanwise distribution of vorticity generally dominates the 2nd moment. However, in the very early stages of vortex sheet roll-up, the developing vortex core size must be dependent on the 2nd moment of vorticity locally in the wing tip region. The standard approaches using single rows of vortices do *not* consider that the vorticity may be distributed perpendicular to the trailing edge of the wing section. This is an oversight. In actual fact, the distribution of the vorticity is (can be) through the thickness of the shed boundary layer, producing a vortex sheet with finite thickness. Therefore, from the conservation laws of vorticity, the evolving core region possesses a 2nd moment of vorticity which is dependent on the contribution of the vortex sheet thickness to the 2nd moment of the vortex sheet especially in the region of roll-up.

Consider now the 2nd moment of vorticity about the centroid of vorticity of the developing core, $I_{p'}$, and the corresponding 2nd moments of the region about the vertical z'-axis, $I_{z'}$, and about the horizontal y'-axis, $I_{y'}$, where these axis are centered on the core. Now,

$$I_{p'} = I_{y'} + I_{z'} \tag{4.1}$$

but if $I_{y'} \ll I_{z'}$ then.

$$I_{p'} \approx I_{z'} \tag{4.2}$$

For the case of the planar elliptical wing loading being studied here, in the very early stages of roll-up the vortex sheet starts to roll up at the very tip where the greatest gradient of shed circulation occurs and the strongest vortices are shed. In this case, the initially rolling up sheet will produce a core which is highly dependent on the thickness of the sheet since the increment in the 2nd moment of vorticity due to the boundary layer thickness (in the vertical z direction) will be significant. This corresponds to the case where $I_{y'}$ is of the same order of magnitude as $I_{z'}$, therefore both must be considered in Equation

4.1. Note that much later, in the fully developed core, the boundary layer thickness and will produce little effect. Note that even a thick boundary layer gives a vortex sheet thickness which is small compared to the wing span. Thus, since this is the case for the initial vortex sheet, then $I_y \ll I_z$, and equation 4.2 applies due to the invariance of I_p, $I_p \approx$ initial I_z for the semi-span. Here I_y, I_z, and I_p are values for the wing semi-span. This result is the same as that from the Betz equation. This is because Betz's equations (1933) do not include this thickness effect, and that the 2nd moment of vorticity of the evolving core is dependent only on the spanwise distribution of vorticity in the outer vortex sheet region which is considered rolled up.

Notice that for a planar wing, the 2nd moment of vorticity of the semi-span is increased only by a small amount by the use of the vorticity distribution through the region of the boundary layer, relative to that due to the spanwise distribution. However, special note should be made that a nonplanar winglet system will significantly increase the 2nd moment of vorticity of the wing in the tip region, due to the distribution normal to the span. Hence, during early stages of vortex sheet roll-up the number of vortex cores and their sizes is changed significantly for wings employing winglets. Obviously, this will significantly alter the resulting downwash field, especially in the region near the wing tip. Recalling that the kinetic energy of the vortex system is related to the induced drag, then perhaps the effectiveness of nonplanar wings such as those with winglets is manifest in the vortex wake as an increase of the 2nd moment of vorticity by a significant amount as compared to a planar wing.

4.2.2 Boundary Layer Thickness and Vortex Core Sizes

There has been some (limited) work (i.e. McCormick (1954), Grow (1969)) examining the relationship between the wing boundary layer thickness and evolving trailing vortex core sizes and development. Grow (1969) examined this phenomenon experimentally, but was unable to predict any correlation between the thickness of the boundary layer on the bottom of a wing and the size of the evolving trailing vortex core. He attempted to correlate the boundary layer thickness from the bottom of the wing, since he thought that the boundary layer from the upper surface would not be wrapped into the core. However, those experimental investigations provided no conclusive results. Also, Chorin and Bernard (1973) used distributed Rankine vortices to numerically model the vortex sheet roll-up, yet they made no observations regarding the vortex sheet thickness and the radius of the evolving vortices.

On a similar problem, especially, noting the experimental results of O'Callaghan (1988) there does not appear to be a predictable relationship between the size of an evolving vortex core and the maximum tangential velocity in that core. However, O'Callaghan's work gave no consideration to the boundary layer thickness on the wing.

Many researchers starting with Kaden (1931) describe the tip edge of the shed vortex sheet as it develops into a trailing vortex core as a spiral of *infinite* length which is wound up even at $t = 0.0^+$ (Sarpkaya, 1989). Clearly, this can only be true if the boundary layer has zero thickness, since the thickness of the stretching vortex sheet and the distance between wraps of the spiral would have to be equal to zero, to allow the infinite number of wraps. Much effort, using computational techniques and numerical models of vortex sheets, has been expended on attempts to achieve as many wraps of the vortex sheet as possible without regard to experimental evidence which suggests that this is *not* the case.

This study was prompted by some preliminary experimental results which have suggested a connection between the boundary layer thickness and the vortex core development. Further experimental work is warranted to further investigate the correlation between the size of the vortex core and the boundary layer thickness. Preliminary wind tunnel work by this author has indicated that an increased boundary layer thickness leads to greater core radius and therefore a lower maximum tangential velocity, v_{tan}. The University of Alberta Mechanical Engineering Department possesses a wing section which has the characteristic that the boundary layer thickness increases rapidly between angles of attack $\alpha \cong 6°$ and $\alpha \cong 8°$ (corresponding to $C_L = 0.8$ and $C_L = 1.0$). During wake traverses only several chord lengths downstream from the wing trailing edge, the vortex core radius, r, was measured by using a pitot tube and it was found that the ratio of core radii was (r at $C_L = 1.0$) / (r at $C_L = 0.8$) $= 1.4$. However, based on other past work by O'Callaghan (1988), the maximum v_{tan} should remain nearly constant. Therefore based on the change of root circulation for the change of C_L this ratio should be 1.25 for the two core radii. Thus, there does seem to be a link between the boundary layer thickness and the developing vortex core radius near to the wing trailing edge.

4.2.3 Time Dependence of the Tangential Velocity Profile

This work also considers time dependence of the maximun tangential velocity in a developing trailing vortex core. Concerning such a time dependence, Baker (1979) hints that his method of applying the "Cloud in Cell" (CIC) technique to the roll-up of vortex sheets shows that maximum tangential velocity decreases as time increases. However, he does not follow this up or even comment further on it. Thus, this investigation examines the time dependence of the maximum tangential velocity through the emerging trailing vortex core from the elliptically loaded wing.

4.3 NUMERICAL STUDY

Numerical modelling of airfoils, wings, and vortex sheets has been the subject of much work over the years. Methods vary from point vortex methods, to vortex lattice methods, to the Cloud in Cell (CIC) method, to vortex panel methods, and others. Yet with the availability of all of the methods and the vastly increasing computational power, there is yet to be shown a clear and accurate method for the vortex sheet roll-up into the developing core region behind a lifting wing. This work does not pretend to be that *final solution*, however it is hoped that some additional and useful insight may be gained by the use of the vortex lattice method (VLM).

Some researchers consider other methods such as the Cloud in Cell (CIC) technique (as developed by Christiansen (1973) and Baker (1979)) amongst the more efficient computationally. The CIC method was developed for in partical simulations for use in plasma physics. The CIC method represents continuous regions of voriticity by areas of discrete vortices, then local centroids of vorticity are used to approximate behaviour of large numbers of the vortices. However the difficulty of developing the code and the corresponding input data in order to implement the boundary conditions may not prove beneficial (Sarpkaya (1989)), as compared to direct application of the Biot-Savart law. Sarpkaya (1989) also notes that "the time saved may be disappointingly small." As well, the use of the CIC method leads to solving a Poisson's equation, therefore only simple boundary conditions can be handled (Sarpkaya (1989)). The final result, therefore, is that even a simple winglet configuration is not feasible with the CIC method.

For this investigation, a relatively simple vortex lattice method is used which employs semi-infinite Rankine vortices to represent the trailing vortex filaments from the discretized trailing vortex sheet. The semi-infinite trialing vortices are continuous with the bound vortices to ensure the conservation of vorticity. However, the influence of the starting vortex is neglected. The trailing vortices are considered to remain parallel to the freestream direction. This method allows great flexibility in initial vortex sheet shapes and circulation distributions. The idea of Rankine vortex filaments is similar to that of Chorin and Bernard (1973). An additional feature that the model incorporates is a measure of thickness of the vortex sheet and a multiple row vortex discretization as a means of examining the behaviour of the vortex sheet thickness.

This method of using the VLM with Rankine cores and multiple rows of vortices has *not* been used previously to examine variation of maximum tangential velocity in an evolving vortex core as a function of boundary layer thickness, or at least there appears to be nothing published specific to this application. This simple model does give an indication of some relationship. Also, the relationship may be more obvious and accurate using a more complex model and more rigorous experimental work, however it is not clear that the extra work and expense to do so would be warranted.

As the trailing vortex sheet rolls up the sheet thickness may vary during the process. This model allows such variation of the vortex sheet thickness, hence this model provides new information concerning the stretching and thinning of the vortex sheet which is observed near the emerging core of the vortex roll-up region.

The problem of solving the spanwise loading of wings is the starting point for this vortex sheet method. The vorticity distribution of a lifting wing is discretized then the VLM method solves for the strength of the discrete vortex distribution. This requires the simultaneous solution of a set of *n* equations. The computing memory requirements and time for the solution is of the order n^2. Therefore, the standard discrete vortex approximation to a vortex sheet roll-up is performed using only single rows of vortices to represent the sheet. Using this method one arrives at the standard multiple turn spiral of the sheet rolling up into the developing core region. As well, there is always a chaotic motion of the vortices within the center of the developing core which is considered to be a breakdown of the model. One solution is the amalgamation of the discrete vortices into a single vortex core (as per Moore 1974), but this problem of the core development using discretized vorticity has no certain solution. Various methods are used but no one has been proved to be *the* correct method, and all must be used with care so that the errors introduced by the amalgamation do not become unacceptably large.

Studying the problem, one finds that the discretized vortex sheet using the single row approximation does give an indication of vortex sheet stretching since the arc length of the sheet must increase during formation of the spiral core section. Nevertheless, thinning of the vortex sheet is *not* observable with the single row methods, even if the discretization is done using Rankine vortex filaments, to produce an approximation to finite thickness of the sheet.

Herein lies the advantage of the multiple row representation of the discretized vortex sheet. The use of the multiple rows representation allows the boundary layer thickness to be more realistically incorporated. The result is a single more realistic spiral with a developing core which tends to show a more uniform vorticity distribution and seems more reasonable than some previous models.

A major disadvantage is the increased computational time requirements for the extra rows of vortices. However, if additional information and insight is available through the use of this method then the extra cpu time is well spent.

The numerical simulation for this investigation involved only symmetrically loaded wings, hence the vortex sheet was assumed to be symmetrical. This allowed only the vortex system for one semi-span of the wing to be followed through time, although that of other semi-span was required and used for calculating induced velocities. Therefore, when referring to the number of vortices representing the vortex sheet it should be noted that the numbers given are those representing one semi-span only.

4.3.1 Initial Conditions and Conditions Modelled

Numerical simulation has been done with up to 2500 Rankine vortices (per semi-span) to represent the vortex sheet, and the induced velocity is calculated using the Biot-Savart law for all the Rankine vortices. The thickness of the sheet is represented by the Rankine core diameter of each vortex in the sheet, such that the number of rows of vortices multiplied by the vortex core diameter of each row equals the boundary layer thickness (and the vortex sheet thickness).

Once the spanwise loading is determined (the elliptical loading), the discretized trailing vortex sheet is then allowed to roll-up beyond the trailing edge of the wing. The movement of the trailing vortex filaments was modelled using an Explicit Eulerian approach. Fluid theory shows that the vortices in a fluid will be convected with the induced flow field (Truesdell 1954). The induced velocity calculations for a vortex are similar to those shown in Chapter 3 (sec 3.2.1.3). Therefore, for the trailing vortex wake movement, the air velocity at each vortex filament is calculated for the positions where the vortices are initially located, then the trailing vortex filaments are moved to their new position at the end of the time step, Δt, and so on.

Note that the calculations were based on given numbers of vortices per *semi-span*, although those of the other semi-span were included for calculating induced velocities. A cosine spatial vortex filament distribution from the centerline to the wing tip gave sufficient detail in the roll-up region at early time periods. The cosine function was chosen to give better spatial resolution in the tip region than would a uniform spacing, while at the same time reducing the circulation shed in each of the vortex filaments near the tip. The value of the circulation for each vortex filament was calculated from the incremental change of circulation along each section of the span. For this study an elliptical spanwise loading was used (however, any spanwise loading could have been chosen).

During the modelling of the roll-up of a discretized vortex sheet from a wing with a monotonically decreasing loading function, for example the elliptical function used here, the roll-up starts at the wing tips. Thus, the critical time steps are determined by the vortex spacing and circulation in the tip region.

The vortex sheet which is modelled here is that shed from an elliptical wing. The test cases considered here were based on the following conditions. The wing root circulation value is chosen to be fixed at $\Gamma_o = 10.0\ \mathrm{m^2/s}$ such that at V=60 m/s, the result is L = 5804 N and C_L = 0.1315, for the typical wing with 10.0m span and 2.0m root chord. The value of the root circulation could be varied, however the actual effect of a greater value of root circulation would be to increase the roll-up rate. Therefore, to observe the effect of different wing root circulations (and hence different C_L) values it is reasonable, at least for a first approximation, to just look at a later time period. This follows since induced velocities due to a vortex are proportional to the circulation of that vortex. Thus, for example, if results were desired for $\Gamma_o = 20.0\ \mathrm{m^2/s}$ (i.e. $C_L = 0.2630$) at $t = 0.1$s then it would be reasonable to examine results for $\Gamma_o = 10.0\ \mathrm{m^2/s}$ (i.e. $C_L = 0.1315$) at $t = 0.2$s, and so on.

To examine the effect of the boundary layer thickness (b.l.t.), the b.l.t. is varied from 0.010m (0.1% span) to 0.100m (1.0% span). The specific values used were b.l.t. = 0.01m, 0.05m, 0.10m. The lower values would correspond to laminar flow and the larger values would correspond to a wing with turbulence and even some degree of separation.

4.3.2 Boundary Layer Thickness and Vortex Sheet Thickness Related to the Vortex Core Size

For any wing section in a fluid flow there exists in the wake of the wing a velocity defect region which represents a momentum loss due to the wing drag. This momentum loss is used to calculate the value of the drag coefficient, C_D, for the section. The shape of this velocity defect region is dependent on distance from the trailing edge of the wing. Immediately at the trailing edge of the wing but still adjacent to the surface of the wing, the no-slip boundary condition of viscous flow forces the fluid velocity to be zero with respect to the wing surface. Immediately behind the wing the boundary layers from both the top and bottom surfaces must diffuse together. The vortex sheet which is shed from the trailing edge of the wing is confined to this region of the combined boundary layers. Henceforth, the thickness of this combined vortex sheet - boundary layer may be referred to as the *vortex sheet thickness* (v.s.t) or the boundary layer thickness (b.l.t.). Initially downstream, there still exists a wake region of zero fluid velocity with respect to the wing. Within a short distance downstream viscous diffusion would cause the boundary layer - vortex sheet to thicken, however, near the wing tip the trailing vortex sheet immediately starts to roll-up into a single core for a plain wing. (For wings in general, centers of trailing vortex sheet roll-up occur at local maximums of the abs($d\Gamma/dy$).)

The vortex sheet thickness will be shown to be important to the developing vortex core radius. Initially, only the thickness of the sheet at the wing tip is relevant since the vortex sheet at the tip immediately starts to roll-up into the vortex core. During the time taken for the vortex sheet to roll-up the vortex sheet may increase in thickness (by viscous diffusion of the velocity defect region) at the regions not yet rolled up. However, especially for the portion of the trailing vortex sheet near the developing vortex core there is a tendency for the vortex sheet to be stretched and thinned as it is rolled into the core. Thus, it is this combined effect which determines the actual vortex sheet thickness at any spanwise location during vortex core development. For this case study, the b.l.t. or the v.s.t. is assumed constant along the span except for the effects of stretching and thinning.

4.3.3 The Vortex Sheet Model with Rankine Cores

The boundary layer of a wing, was modelled by an approximately rectangular region of uniform vorticity at any spanwise location. For the simple simulation, the boundary layer thickness was done by the use of Rankine vortices to simulate the vortex sheet. This produces a uniform distribution of vorticity over the area of the vortex cores. Thus, the boundary layer thickness was given as the product of the number of rows of vortices and the diameter of the vortex filament cores.

The focus of this study was to examine the vortex sheet roll-up behind a lifting wing. The focus was on the influence of the wing boundary layer thickness on the vortex sheet roll-up process and the evolving trailing vortex core structure.

This relatively simple vortex lattice model employs Rankine vortices to represent the trailing vortex filaments from the discretized trailing vortex sheet. The use of this simple model allows great flexibility in initial vortex sheet shapes and circulation distributions. The idea of Rankine vortex filaments is similar to that of Chorin and Bernard (1973) with the additional feature that the model incorporates a measure of thickness of the vortex sheet.

Due to the spanwise distribution of the number of vortex filaments with this model there were circular areas of vorticity overlapping to give greater vorticity intensity (vorticity per unit area) at the tip region. This model provides increased vorticity intensity by allowing the overlap of vortex cores in the spanwise direction. Recall that the vortex sheet discretization was produced by a cosine distribution of the number of vortices along the span. This means there are regions at inner span locations where the vortices do not touch and regions at outer span locations where the vortices overlap. Others have allowed the same situation. For instance, Shelley, Meiron, and Orszag (1993) also allow vortex core overlap in their viscous fluid simulation.

At first glance th[illegible] roblem with this method. Strictly speaking, the vortex "lines" can not occupy the same sp[illegible] time (Truesdell, 1954). This result comes from the fact that point vortex lines cor[illegible] simal) material lines and that different material lines can not occupy the same spa[illegible] ne (Truesdell, 1954).

However, there is uncertainty if areas of vorticity can overlap in viscous flow. That is to say, the ensemble averaged areas of vorticity due to the entwined regions containing point vortices may not be constrained by the same requirements. The assumption made for this work is that the regions of the cores of t[illegible] railing Rankine vortex filaments *may* overlap.

[illegible] past, the idea of Rankine cores representing the vortex filaments has been used for the modelling of vortex sheet roll-up (Sarpkaya (1989), Chorin & Bernard (1973)). To date, however, this method has not bee[illegible] sed to examine the variation of maximum v_{tan} as a function of boundary layer thicknes[illegible] at least there appears to be nothing published specific to this application.

This simple model does give an indication of some relationship. Also, the relationship may be more obvious and accurate using a more complex model and more rigorous experimental work, however it is not clear that the extra work and expense to do so would be warranted.

4.3.4 Velocity Profile Through a Vortex Core

For the purposes of this numerical investigation, the velocity traverses through the core were done in a manner similar to the way they would be done in a wind tunnel. In a wind tunnel one would attempt to make a wake traverse through the center of the developing vortex core region. For this numerical work, the center of vorticity was determined for the vortex filaments which initially comprised the outboard 10%

of the number of vortex filaments. Then the developing core was scanned in a spanwise direction at a vertical position corresponding to the center of vorticity of those same vortex filaments that were initially the outboard 10% of the total. Note that at $t=0.0$ the "core" is not clearly defined, but the core begins to emerge at the very tip. The scan line then passes right through this "core." This method of using the center of vorticity of those vortex filaments that initially comprised the outer 10% of the total number of vortices proved quite satisfactory for locating the evolving vortex core. Figure 4.1 and Figure 4.2 shows a typical scan line and the vortex filaments during roll-up (the view zoomed in at the tip region). (Recall that the wing semi-span is 5.0 m, and notice that the plots are such that the spanwise location is given in meters.)

4.4 RESULTS

The results here first show results of numerical scans for the velocity profiles for various boundary layer thicknesses. Then the effect of varying the number of rows of vortices and the number of vortices is considered. The number of rows will be shown to affect the roll-up process, especially the vortex sheet stretching and thinning near the developing core. Lastly, the numerical instabilities are considered. The 2nd moment of vorticity is discussed along with the effect of the time step for the vortex movement. Also, the Kelvin-Helmholtz instability is described and discussed.

The results shown are based on the figures given later. The Figures 4.3 to 4.8 show velocity profiles and the effect of boundary layer thickness. Figures 4.9 to 4.14 show velocity profiles and the effect of various number of rows and vortices. The remaining figures are arranged in sets according to the number of rows of vortices and number of vortices per row. For each set the velocity profile is shown for times t = 0.0s to 1.0s, then the vortex positions are plotted for the same times. Figures 4.15 to 4.23 give 5 rows of 100 vortices for b.l.t. = 0.050m. Figures 4.24 to 4.31 give 3 rows of 100 vortices for b.l.t. = 0.050m. Figures 4.32 to 4.38 give 2 rows of 100 vortices for b.l.t. = 0.050m. Figures 4.39 to 4.48 give 1 row of 300 vortices for b.l.t. = 0.050m. Figures 4.49 to 4.56 give 3 rows of 100 vortices for b.l.t. = 0.100m.

4.4.1 Numerical Scans for Velocity Profiles

The work shows that a thicker boundary layer gives significantly decreased maximum tangential velocities in a larger core in the rolling up trailing vortex at the early times.

The series of figures beginning at Figure 4.3 and ending at Figure 4.8 shows the velocity profiles through the rolling up vortex core region for 1 row of 300 vortices per semi-span for the times t=0.0s to 1.00s for boundary layer thicknesses, b.l.t. = 0.010m, 0.050m, and 0.100m. Recall that a planar wing is being modelled, therefore there is no dihedral. As a result, note that at t=0.0s the "core" which will be at the very end of the vortex sheet is at the same height as the rest of the vortex sheet, hence the velocity traverse and profile passes *through* the vortex sheet along the span.

As can be seen from these numerical simulations, a thicker boundary layer produces a trailing vortex core with lower maximum v_{tan} and a larger radius, at the early stages when a small percentage of the vorticity is rolled up. As noted earlier (theoretical basics section), at later times of the roll-up sequence the vortex sheet thickness is less important since the 2nd moment of vorticity term then is dominated by the spanwise distribution of vorticity *not* the distribution perpendicular to the wing trailing edge.

4.4.2 Velocity Profile Comparisons for Various Numbers of Vortices and Number of Rows of Vortices

Comparisons of the resulting velocity profiles for a variety of numbers of vortices as well as numbers of rows of vortices show that the profiles are fairly constant for a wide range of combinations. See the sequence of figures starting at Figure 4.9 and ending at Figure 4.14. The comparisons are done for the specific case of b.l.t. =0.050, however, the generalization can safely be made to other vortex sheet thicknesses. As will be shown later, the differences due to different numbers of vortices and numbers of rows is insignificant compared to the differences due to changing the vortex sheet thickness.

4.4.3 The Vortex Core Size

There is a need to define the vortex core size for a partially rolled up vortex sheet. This need arises in trying to calculate the vorticity, circulation, and vorticity intensity in the vortex core. In a Rankine vortex the average vorticity is simply $(\Gamma/\pi a^2)$. In a symmetrical completely rolled up vortex core the *average* vorticity is still simply $(\Gamma/\pi r^{*2})$ where r^* is radius at which all of the vorticity is encompassed. However, in a partially rolled up vortex sheet there is no clear definition, especially since the core is significantly asymmetric.

One possible definition is the radius to the maximum v_{tan}, labelled as r'. Examination of literature will show that this is by far the most popular definition. However, with this definition there arises a problem because the core region is far from symmetric. Noting the figures (i.e. Figure 4.15, Figure 4.16, Figure 4.39, Figure 4.40) showing the tangential velocity for a rolling up sheet, the asymmetry is obvious. Note, that for the experimental work which was done it has been found efficient to use the radial location, r', to the maximum v_{tan}.

As per Roberts (1983) another possible definition is the radius to the location where the tangential velocity is the same as it would be for a potential vortex, r^* (that is to the radius r^* at which all of the vorticity is encompassed). For this definition one needs to determine or specify the strength and location of that corresponding potential vortex.

Observing the curve of v_{tan} vs r for a vortex, one can see that all of the vorticity for a Rankine vortex is contained within the radius to the location where v_{tan} is maximum. Note that only for a Rankine vortex do the three definitions become equal, i.e. $a = r' = r^*$. The definition of a for the vortex core radius will be employed for this numerical work when referring to the Rankine vortex filaments. However, when referring to the evolving vortex core one of the other definitions will be used, but will be specified each time used.

Comparisons of the core sizes from this model with other work is of interest. Figures 4.3 to 4.8 show velocity profiles through the delveloping vortex core from t=0.0s to 1.0s. Recall that for this study the wing span is 10.0m, and V=60 m/s, therefore t=0.5s corresponds to a downstream distance of 3.0b and t=1.0s corresponds to a downstream distance of 6.0b. Examining Figure 4.7 shows that for the wing with b.l.t.=0.100 gives $(r'/b) \approx ((4.68\text{-}4.57)/10.0) = 0.011$ at t=0.5s. Similarly, Figure 4.8 shows that for the wing with b.l.t.=0.100 gives $(r'/b) \approx ((4.565\text{-}4.41)/10.0) = 0.0155$ at t=1.0s. Recall from Chapter 2 (section 2.2.3) that the values found experimentally with a hot-wire anemometer by Corsiglia *et al.* (1973) for an elliptical wing loading were $(r'/b) \approx 0.010$ to 0.015. Also, Roberts (1983) had found $(r'/b) \approx 0.018$. Thus, the results of this VLM model are in very good agreement with those of other researchers.

4.4.4 Velocity Profile Through a Vortex Core

The tangential velocity profile in a developing vortex core is shown to be modified by varying the boundary layer thickness near the wing tip. Specifically, increased thickness of the boundary layer is shown to reduce the maximum tangential velocities during the initial stages of vortex roll-up, which is shown to be consistent with the laws of vorticity conservation.

The sequence of figures starting at Figure 4.3 and ending with Figure 4.8 shows the velocity profile through the evolving trailing vortex core for 1 row of 300 vortices and three different vortex sheet (boundary layer) thicknesses (namely: b.l.t.=0.010m, 0.050m, and 0.100m). As well, the figures of velocity profiles are given for 3 rows of 100 vortices at different vortex sheet thicknesses (namely: b.l.t.=0.050m and 0.100m) (Figure 4.24, Figure 4.25, Figure 4.49, Figure 4.50). These all clearly support the idea of decreases in maximum v_{tan} and increases in the radius of the core with increased vortex sheet thickness, and most noticeably the size of the core to the radial position encompassing all of the vorticity in the roll-up region.

Figures showing the velocity profile for various combinations of numbers of rows and numbers of vortices. These are given as follows: for 1 row of 300 vortices (Figure 4.3, Figure 4.39, Figure 4.40), for 2 rows of 100 vortices (Figure 4.32), for 3 rows of 100 vortices (Figure 4.24, Figure 4.25, Figure 4.49, Figure 4.50), and for 5 rows of 100 vortices (Figure 4.15, Figure 4.16).

Note that in the velocity profile figures, mainly at t=0.00s, there occur local perturbations or 'jiggles' in the plots. These perturbations are most pronounced for fewer vortices in the spanwise direction, especially for 100 vortices at t=0.00s, and the 'jiggles' are smaller for a thicker vortex sheet. For example, compare Figure 4.24, Figure 4.25, Figure 4.49, Figure 4.50 and Figure 4.39, Figure 4.40 noting especially the curves for t=0.00s. The plots are not smooth because the induced velocity is calculated using the Biot-Savart law for all the Rankine vortices. When doing the scan through the core region (based on the centroid of the outboard 10% of the vortex filaments according to initial locations) it is inevitable that the traverse passes very close to some of the Rankine vortex filaments (recall Figure 4.1 and Figure 4.2). Notably, for planar wings as examined here, at t=0.00s the scan is done along the line of the initial vortex filament distribution. There are no actual singularities, however, when traversing very close to any one vortex there is a significant contribution due to that vortex. The 'jiggles' are larger for fewer spanwise vortices because the effect of the adjacent vortex filament is much more significant (recall that these are Rankine core type vortex filaments). Also, recall that the size of the Rankine core with the linear velocity profile is dependent on the vortex sheet thickness. This correlation means that the thick vortex sheet produces the reduced size of 'jiggles'. Also, notice that for $t > 0.00$s, since the scan line does not go directly through or along the vortex sheet the curves are mostly smooth except in the core region itself where the scan may pass close to vortices.

A feature also noticeable is that for $t > 0.00$s there is invariably a discrete step in the velocity profile (not just a local perturbation). These step changes occur at the position where the traverse passes through another wrap of the vortex sheet or another clump of vortex filaments. Observing Figure 4.2 one readily observes the sheet crossing by the traverse and the corresponding jump in the tangential velocity. Basically, the jump occurs because the traverse point is then outside of the core and encompasses all of the vorticity (note the similarity to the velocity profile for a Rankine vortex).

Another feature is observable through all of the figures showing the time dependent relations for the velocity profiles for the evolving core. That feature is that the absolute maximum tangential velocities generally occur at the beginning of roll-up, and decrease later in the roll-up sequence. This arises from the fact that the vorticity density of the vortex sheet near the tip is greater than that portion of the sheet near the root of a lifting wing with an elliptical spanwise load distribution, and for virtually any practical, smooth, monotonically decreasing spanwise loading. Thus when the sheet starts to roll up, the highest vorticity density portion rolls up first creating a core region which is very small and has large vorticity. This leads to the occurrence of high tangential velocities in the very small core.

4.4.5 Vortex Sheet Stretching and Thinning

The main distinguishing property of this numerical model is that the vortex sheet roll-up incorporates a feature with multiple rows of vortex filaments for consideration of the wing boundary layer thickness. This vortex sheet thickness may vary during the roll-up process, hence this model provides insight concerning the stretching and thinning of the vortex sheet which is most clearly observed near the roll-up region. (Notice that most of the figures showing the vortex sheet rolling up show just the tip region of the wing, since the sheet is merely a straight line of rows of vortices at the inner spanwise locations. As well, recall that the wing semi-span is 5m, and note that the plots are such that the spanwise location is given in meters.)

The sequence of figures starting from Figure 4.17 at t=0.00s to t=1.00s presents 5 rows of 100 vortices and most dramatically show the phenomenon of vortex sheet stretching and thinning. The other multiple row tests also show this as observed with the 3 rows of 100 vortices as seen in the two sequences of figures starting from Figure 4.26 and Figure 4.51, and with the 2 rows of 100 vortices as seen in the sequence of figures starting from Figure 4.33. However, as these figures show, the greater the number of rows the better the sheet thinning is observed. Also, it is interesting to notice the reduced propensity for the Kelvin-Helmholtz instability to develop at early times with multiple rows, and especially for the thicker vortex sheet or boundary layer. However, the Kelvin-Helmholtz instability does still occur later in time as evidenced by the local clumps of vortex filaments at larger times for each of the numbers of rows and numbers of vortices.

Also, for a single row of vortices, it is useful to notice the sequence of figures from Figure 4.41 to Figure 4.48 at t=0.01s to t=10.00s. These present 1 row of 300 vortices and do not show the phenomena of vortex sheet thinning, although stretching is apparent by the increased separation between vortices of the sheet near the core. The continuity equation of 2-D flow would imply the thinning of the sheet during the stretching, but this is not immediately obvious with this single row representation.

4.4.6 Amalgamation of Discrete Vortices

Amalgamation of discrete vortices into a single vortex core is still a problem with no obvious solution. The problem seems to be caused by the very act of discretizing the continuous vorticity distribution. Various techniques have been used but no one method has been proven to be *the* correct method.

Moore (1974) and others have used arbitrary cut-off schemes to amalgamate 2-D line vortices into a core region during roll-up. For instance, Moore (1974) developed the scheme whereby once any vortices had wrapped more than 270° around the evolving core they would be dumped into that core region forming a new core at the center of vorticity of the combination. Moore's method has been widely adopted. Obviously, this and any other schemes are all approximate and only attempt to give a general idea of the flow, but more importantly they attempt to save computational time.

For this model (at this time) there was no attempt to amalgamate vortices in the core region. Sarpkaya (1989) notes that merging (amalgamating) like signed vortices decreases the 2nd moment of vorticity. This is another motive for not merging vortices. As well, not amalgamating and so creating a single core, ensures that there are no singularities in the core region, although there are some local spikes in the velocity profile as mentioned in the section concerning the velocity profile through a vortex core.

4.4.7 Numerical Instabilities

Two numerical instabilities are common for this type of model. The one deals with the growth of the 2nd moment of vorticity which should be invariant. The other deals with the Kelvin-Helmholtz instability and the erratic movement of vortices. These instabilities may occur even though the spanwise location of the center of vorticity is invariant.

4.4.7.1 **The 2nd Moment of Vorticity Invariant**

The 2nd moment of vorticity is one of the invariants of the vortex wake shed from a lifting wing. Numerical modelling of the movement of the discretized vorticity must consider the effect of the time step size on this invariant to avoid significant errors.

According to Chorin and Bernard (1973) who used finite Rankine type vortex cores to discretize and model vortex sheet roll-up, a necessary condition for the stability of the numerical method is that $(v_{tan}\Delta t = u_{tan}\Delta t =)\ u_{\theta}\Delta t \ll a$. This means that for strong vortices (i.e. with large circulation) the time increment for calculation must be smaller than for weak vortices. For example, comparing one vortex with circulation $\Delta\Gamma$ and time increment Δt at some radius, and another vortex with circulation $2\Delta\Gamma$ then one would need to use $\Delta t/2$ at that same radius.

The time step requirement given here dictates the maximum distance that a particular vortex is moved due to the induced velocity from another vortex. For a moment, consider the case of only two vortices, specifically the vortex movement due to the induced velocity from the other vortex. Note that the induced velocity at the center of vortex #2 is tangential about the center of the vortex #1, and vice versus. During a discrete finite time step the vortex is moved in that tangential direction. However, the vortex is displaced radially at the same time since the motion is truly tangential only in the limit as $\Delta t \rightarrow 0.0$. This radial movement of vortices during the tangential movement during each time step causes the growth of the 2nd moment of vorticity. Since the 2nd moment of vorticity is not invariant in this case, the magnitude of this 2nd moment growth is a source of some concern. If the changes can be kept small, then the error accumulation should be of small concern.

Table 4.1 shows the values of the time step, Δt, used in this model. For each cases studied, the value of $(v_{tan\text{-}max}\Delta t)$ is included here where, $v_{tan\text{-}max} = \gamma_{max}/(2\pi a)$. The value of γ_{max} is that of the last shed trailing vortex filament, and a is the radius of the Rankine core of that vortex filament. Table 4.1 also shows the value of the 2nd moment of vorticity, where the 2nd moment of vorticity about the center of vorticity is given by I_p, for times t=0.0s, 0.5s, and 1.0s. Note that for the conditions modelled t=1.0s corresponds to a downstream distance of 60m or 6 span lengths. The results show that for all combinations of numbers or rows and numbers of vortices that after t=0.5s the 2nd moment has increased 0.8%, and that after t=1.0s the 2nd moment has increased 2.8%. Also, shown for 1 row of 300 vortices that after t=5.0s the 2nd moment has increased 23%, and that after t=10.0s the 2nd moment has increased 29%. This is considered to be an acceptable increase in the error for this study.

4.4.7.2 **Kelvin-Helmholtz Instability**

During the study, a Kelvin-Helmholtz type instability occurred during the rolling up sheet. This instability is similar to that found in real flow shear layers. The Kelvin-Helmholtz instability is seen by the localized clumping of vortices.

Note also that the use of different numbers of vortices per semi-span (i.e. 100 or 300) leads to instabilities in different locations, hence the instabilities are certainly due to numerical initial conditions and not error accumulations. During the study the first occurrence of the Kelvin-Helmholtz instability for 1 row of 500 vortices per semi-span was found to occur at the same location for both time steps Δt = 0.00001s and Δt = 0.0001s, which indicated that the initial instability was due to the discretized vortex spacing and not the choice of the time step. This would imply that any irregularity on a wing may cause this Kelvin-Helmholtz instability in a real flow.

It is interesting to note that with the use of two or more rows of vortices the apparent Kelvin-Helmholtz instabilities are delayed and almost disappear in the immediate roll-up region where the sheet is being stretched, at least for early times. The figures with 5 rows of 100 vortices and 3 rows of 100 vortices show this (see sequences of figures starting at each of Figure 4.17, Figure 4.26, and Figure 4.51). Also, noticeable was that this Kelvin-Helmholtz instability was reduced for the thicker vortex sheet or boundary layer (compare the sequences of figures starting at Figure 4.26 and at Figure 4.51). For long time periods, the Kelvin-Helmholtz instabilities still occurred for all systems modelled. The Kelvin-Helmholtz instability is seen by "clumps" of vortices in Figures 4.21 to 4.23, 4.30 to 4.31, and 4.45 to 4.48.

4.4.8 Sequence of Vortex Sheet Amalgamation into the Emerging Vortex Core

The effect of the boundary layer thickness has been shown to be important. Another interesting property to note is the specific portion of the vortex sheet which is being amalgated into the emerging vortex core. Clearly from the single row models the vortex sheet is pulled into the emerging core. The multiple row examples show the same result plus other information not shown with the single row concerning the sequence of roll-up of the rows of vorticity.

Specifically, the sequence of vortex sheet amalgamation in the core is shown in the examples where the thickness of the vortex sheet is represented by multiple rows of vortices. Notice that vortices from the bottom row(s) of the vortex sheet are wrapped into the core slightly before the vortices from the top row(s) of the vortex sheet. However, note that all of the figures showing the multiple row representation of the vortex sheet show that even at the earliest times $t \geq 0.0^+$ vortices from the top row of the vortex sheet do move into the emerging vortex core. Noting that the rows all started with the same number of vortices in the spanwise direction, the top row can be seen to have moved into the emerging core at the beginning of roll-up. This contradicts the assumption made by Grow (1969) that only the boundary layer on the bottom of a wing would move into the emerging core, and hence that the thickness of the boundary layer on the bottom of a wing would influence the trailing vortex core size.

4.5 CONCLUSIONS

The study of the phenomenon of vortex sheet roll-up has produced a plethora of results via methods in vortex dynamics, however much remains to be learned. This work has focused on applying a simple vortex lattice computer model to add to the understanding of the phenomenon of trailing vortex sheet roll-up behind a lifting wing.

From this work there are clear indications that a wing's boundary layer thickness may influence the initial roll-up of the vortex sheet trailing off the lifting wing. However, after roll-up has been completed the effect of the boundary layer can be seen only in the slightly increased 2nd moment of vorticity due to the vortex sheet thickness, which is small compared to that due to spanwise variation of loading. This is of importance since the vortex distribution and *near* wing vortex sheet roll-up phenomenon have the most influence on change of induced drag.

The VLM model was shown to give excellent agreement with other research and experimental studies of vortex core sizes. This model showed that at a downstream distance of $3.0b$ to $6.0b$ the vortex core size was given as $(r'/b) \approx 0.011$ to 0.0155, respectively, which is in excellent agreement with others who give values of $(r'/b) \approx 0.010$ to 0.018 in the fully rolled trailing vortex core.

The work showed that a thicker vortex sheet - boundary layer gives significantly decreased maximum tangential velocities in a larger core in the rolling up trailing vortex, especially during the early stages of roll-up. Recalling from the literature review of Chapter 2 that the kinetic energy of the wake is related to the induced drag, this may have significance in explaining the induced drag differences possible with different wing tip shapes.

Also observed in this chapter was that the maximum tangential velocities generally occur at the location of the developing vortex core and at the beginning of roll-up, and decrease later in the roll-up sequence, regardless of the boundary layer thickness. Specifically, the current work showed that the maximum tangential velocity does decrease as time increases with the greatest values of the tangential velocity occurring immediately as a sheet begins roll-up. Since the vortex core size and the maximum tangential velocity influences the pressure drop through a vortex core, perhaps the inception of cavitation by a marine propeller may be reduced or controlled by boundary layer control near the propeller tip.

The VLM model using single rows of vortices gave velocity profiles in the developing vortex core region which were similar to those found using multiple rows of vorticies, when modelling the same boundary layer thickness. Therefore, a single row model seems adequate for use when the induced velocity field of the emerging vortex core is being determined.

The use of multiple rows of vortices for the discretization of the trailing vortex sheet provides more insight into the vortex sheet behaviour and the emerging vortex core. Specifically, the multiple row feature of this model provides some insight concerning the stretching and thinning of the vortex sheet which is observed near the roll-up region, since the sheet thickness may vary during the roll-up process. The stretching and thinning shown by this model helps to demonstrate a realistic number of wraps of the vortex sheet around the emerging trailing vortex core. The continuity equation of 2-D flow implies the thinning during the stretching of a vortex sheet, however this is not immediately obvious with a single row of vortices representing the vortex sheet. Therefore, notice should be made that the phenomenon of stretching and thinning of the vortex sheet is observed most easily when a greater number of rows of vortices are used to represent the vortex sheet.

Another feature that the multiple row representation of the vortex sheet showed was that even at the earliest times $t \geq 0.0^{*}$ during vortex sheet roll-up the vortices from the top row of the vortex sheet do move into the emerging vortex core. This result is different from assumptions used by other researcher who have investigated the connection between boundary layer thickness and trailing vortex core development.

This work has been done using trailing vortex filaments with Rankine vortex cores which remain a constant size during the vortex sheet roll-up. Turbulent diffusion has not been considered, but would likely smooth the discontinuities between the wraps of the vortex sheet in the developing core region and produce a smoother velocity profile through the emerging core.

Recommendations for Future Research

Further experimental work planned by this author will include measurements of the trailing vortex sheet thickness and velocity profiles which can be varied by changing the boundary layer thickness on the wing and winglet using a boundary layer transition device at the desired chordwise location. At the same time, wake traverses will make measurements of vortex core size, tangential velocity profiles, and kinetic energy for various wing arrangements. In that work, consideration should be given to possibly increasing the roughness of the wing in the tip region so to increase the boundary layer thickness in that region and perhaps increase the initial core size. Time will allow the rest of the sheet to thicken by diffusing outwards before it is rolled up into the core. Hence, for a small increase in profile drag at the tip, a larger trailing vortex core may be produced, with the resulting decrease in induced drag, and significant drop in maximum tangential velocity.

The numerical modelling of a 2-D wing section uses opposite signs of vorticity distributed along the upper and lower surfaces. Therefore, at the trailing edge the trailing vortices should have both signs of vorticity. However, since the number of vortices to be modelled would be doubled if that were done, the usual procedure is to simply add together the two signs of vorticity, leaving only the one single signed vortex trailing off in the wake. This may be inaccurate since as noted by Lang (1985) regarding experimental investigation, the modelling of shear layers has shown the need for both signs to correctly model development of the large scale structure in the resulting flow. Future work by this author will include modelling the trailing vortex sheet roll-up using both signs of vorticity.

Non-planar wing systems should be investigated, i.e. wings with winglets, to determine the effect of a multiple row model on the trailing vortex core development from a wing with winglets, with the goal to reduce the maximum tangential velocities in the fully developed trailing vortex core.

The computational time requirements for the vortex roll-up studies with the VLM limit the scope of the studies. This has motivated the author to continue to develop a method for correcting the radial movement of vortices during the tangential movement of each time step. This will allow the time steps to be increased and the wake roll-up simulations made more quickly, without sacrificing the numerical control of the invariants of vorticity.

4.6 REFERENCES

Arakeri, V.H., H. Higuchi and R.E.A. Arndt. 1988. A Model for Predicting Tip Vortex Cavitation Characteristics. Transactions of the ASME. *Journal of Fluids Engineering* 111:495-501.

Baker, Gregory R. 1979. The "Cloud in Cell" Technique Applied to the Roll Up of Vortex Sheets. *Journal of Computational Physics* 31:76-95.

Betz, A. 1933. *Behaviour of Vortex Systems*. National Advisory Committee for Aeronautics, Technical Memorandum, NACA-TM-713.

Chorin, A.J. and P.S. Bernard. 1973. Discretization of a Vortex Sheet, with an Example of Roll-up. *Journal of Computational Physics* 13:423-429.

Christiansen, J.P. 1973. Numerical Simulation of Hydrodynamics by the Method of Point Vortices. *Journal of Computational Physics* 13:363-379.

Corsiglia, V.R., N.A. Chigier, and R.G. Schwind. 1973. Rapid Scanning, Three Dimensional Hot-Wire Anemometer Surveys of Wing-Tip Vortices. *Journal of Aircraft* 10(12):752-757.

Donaldson, C. duP., R.S. Snedeker, and R.D. Sullivan. 1974. Calculation of Aircraft Wake Velocity Profiles and Comparison with Experimental Measurements. *Journal of Aircraft* 11(9):547-555.

Grow, T.L. 1969. Effect of a Wing on Its Tip Vortex. *Journal of Aircraft* 6(1):37-41.

Kaden, H. 1931. *"Aufwicklung einer Unstabilen Unstetigkeits Flache," Ingen. Arch.*, Vol. 2: 140-168. (Also R.A.E. Library Trans. No. 43).

Lanchester, F.W. 1907. *Aerodynamics*. Constable & Co., Ltd. London.

Lang, D. 1985. *Laser Doppler velocity and vorticity measurements in turbulent shear layers*. Ph.D. thesis. Graduate Aeronautical Laboratories. California Institute of Technology.

McCormick, B.W. 1954. *A Study of the Minimum Pressure in a Trailing Vortex System*. Ph.D. Thesis. Dept. of Aeronautical Engineering, Pennsylvania State University, Pennsylvania.

Merkl, C.S. 1988. *Winglet Research a Literature Review*. For D.S.S. Contract No. W7707 -0046/01-OSC.

Moore, D.W. 1974. A Numerical Study of the Roll-up of a Finite Vortex Sheet. *Journal of Fluid Mechanics* 63(2):225-235.

O'Callaghan, William J. 1988. *The Induced Drag Reduction Mechanism of Wingtip Surfaces from Studies of the Lift Curve and Vortex Wake*. M.Sc. Thesis, University of Alberta.

Prandtl, L. 1921. *Applications of Modern Hydrodynamics to Aeronautics*. NACA Report No. 116.

Roberts, L. 1983. *On the Structure of the Turbulent Vortex*. AGARD CP 342. Aerodynamics of Vortical Type Flows in Three Dimensions. Advisory Group for Aeronautical Research and Development, NATO, France.

Sarpkaya, Turgut. 1989. Computational Methods with Vortices -- The 1988 Freeman Scholar Lecture. Transactions of the ASME. *Journal of Fluids Engineering* 111:5-52.

Shelley, M.J., D.I. Meiron, and S.A. Orszag. 1993. Dynamical Aspects of Vortex Reconnection of Perturbed Anti-Parallel Vortex Tubes. *Journal of Fluid Mechanics* 246:613-652.

Staufenbiel, R.W. 1984. Structure of Lift-Generated Rolled-Up Vortices. *Journal of Aircraft* 21(10).

Truesdell, C. 1954. *THE KINEMATICS OF VORTICITY*. Indiana University Press.

Table 4.1 Vortex Lattice Model Time Step Values.

# of vortices x # of rows	b.l.t. (m)	a (m)	γ_{max}	$(v_{tan\text{-}max}\Delta t)$ $(=(\gamma_{max}/2\pi a)\Delta t)$ (m)	Δt (s)	I_p at t=0.0s I_p at t=0.5s I_p at t=1.0s	%ΔI_p at t=0.5s %ΔI_p at t=1.0s
100 vortices/row x 5 rows	0.050	0.005	0.0314	1.0×10^{-5}	10^{-5}	0.0488998 0.0493088 0.0502512	+0.8% +2.8%
100 vortices/row x 3 rows	0.050	0.0083	0.0524	1.0×10^{-5}	10^{-5}	0.0488992 0.0493084 0.0502510	+0.8% +2.8%
100 vortices/row x 2 rows	0.050	0.0125	0.0785	1.0×10^{-5}	10^{-5}	0.0488980 0.0493071 0.0502516	+0.8% +2.8%
200 vortices/row x 1 rows	0.050	0.025	0.0785	0.5×10^{-5}	10^{-5}	0.0493521 0.0497689 0.0507288	+0.8% +2.8%
200 vortices/row x 2 rows	0.050	0.0125	0.0393	0.5×10^{-5}	10^{-5}	0.0493584 0.0497729 0.0507317	+0.8% +2.8%
300 vortices/row x 1 row	0.050	0.025	0.0524	0.33×10^{-5}	10^{-4}	0.0495064 0.0499253 0.0509210 0.060905 I_p @ t=5s 0.06395 I_p @ t=10s	+0.8% +2.8% +23% +29%
300 vortices/row x 1 row	0.100	0.050	0.0524	0.167×10^{-5}	10^{-4}	0.0495064 0.0499209 0.0509126	+0.8% +2.8%

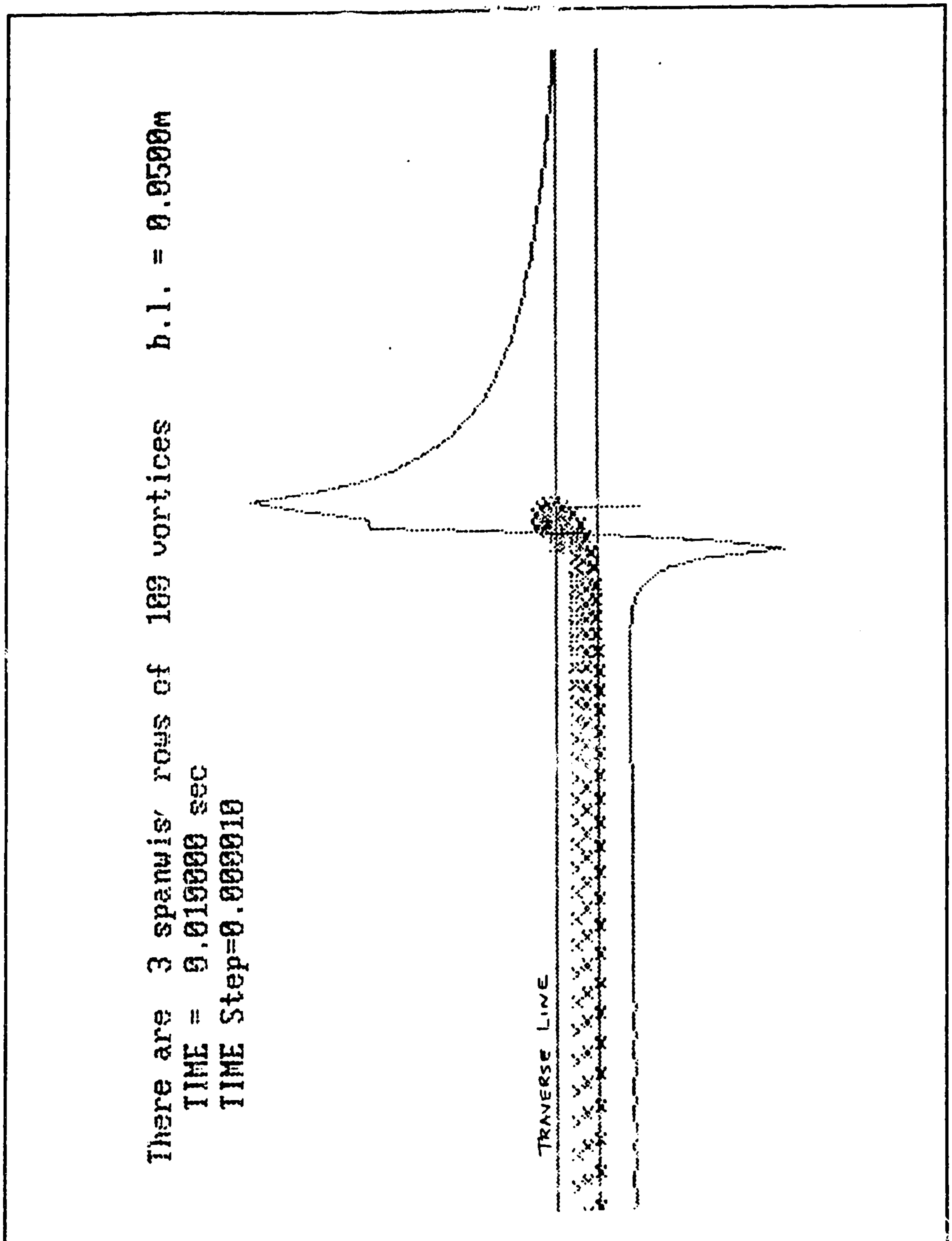

Figure 4.1 Velocity profile from wake traverse via numerical scan through vortex core region using 3 rows of 100 vortices, b.l.t.=0.050, t=0.01s

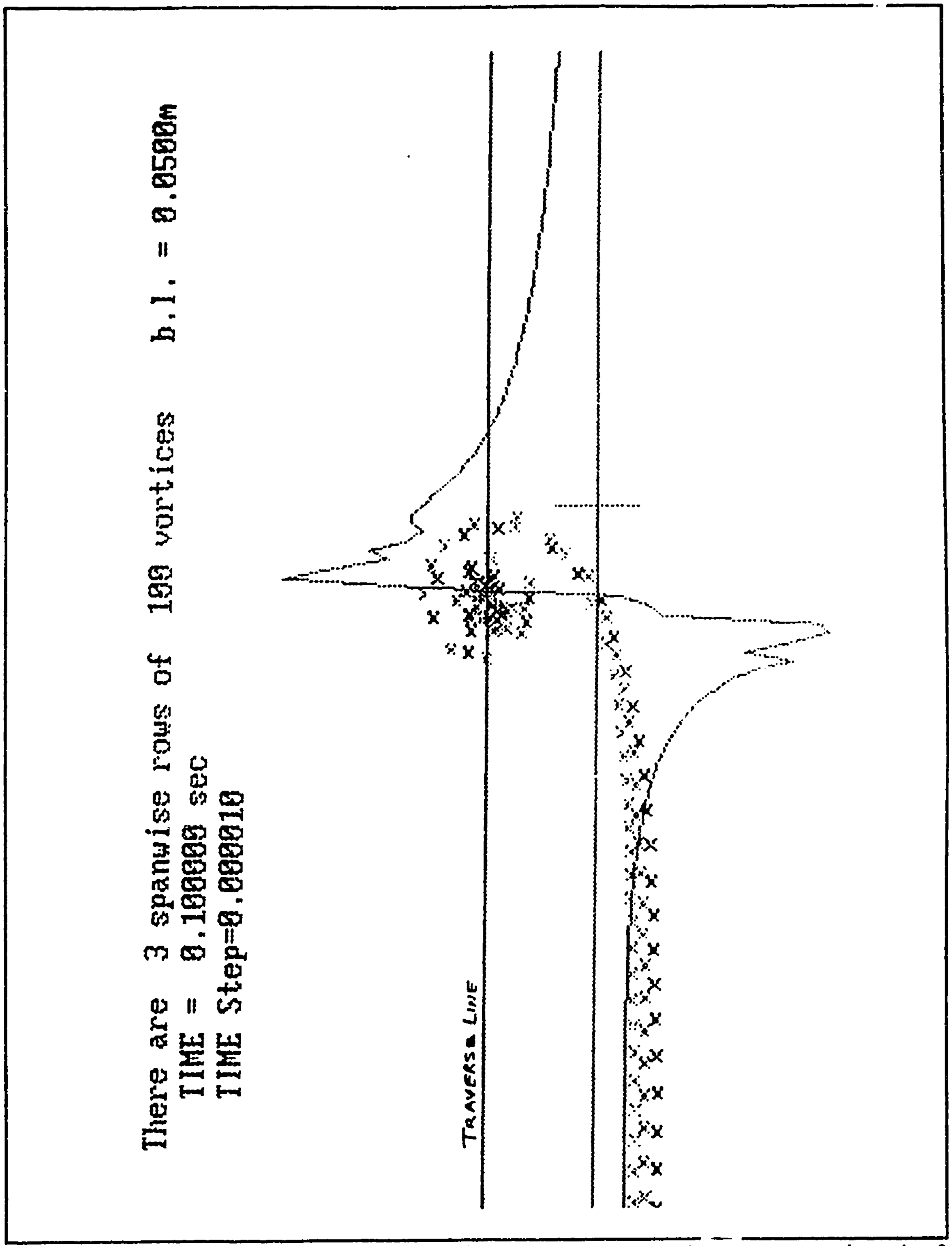

Figure 4.2 Velocity profile from wake traverse via numerical scan through vortex core region using 3 rows of 100 vortices, b.l.t.=0.050, t=0.10s

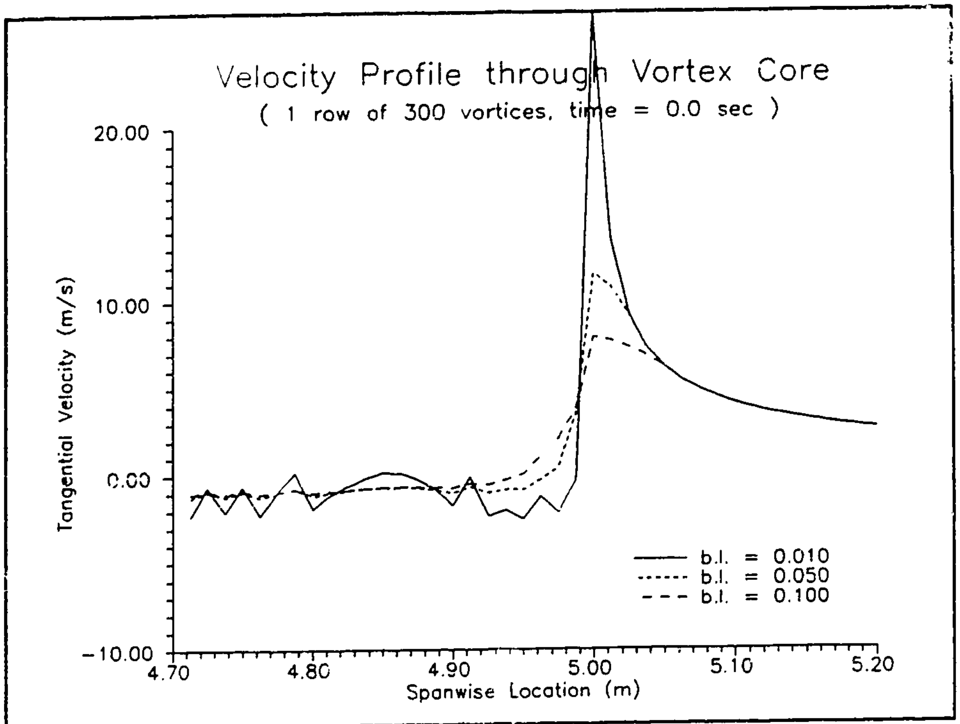

Figure 4.3 Velocity profiles with 1 row of 300 vortices at t=0.00 and b.l.t. = 0.010, 0.050, 0.100

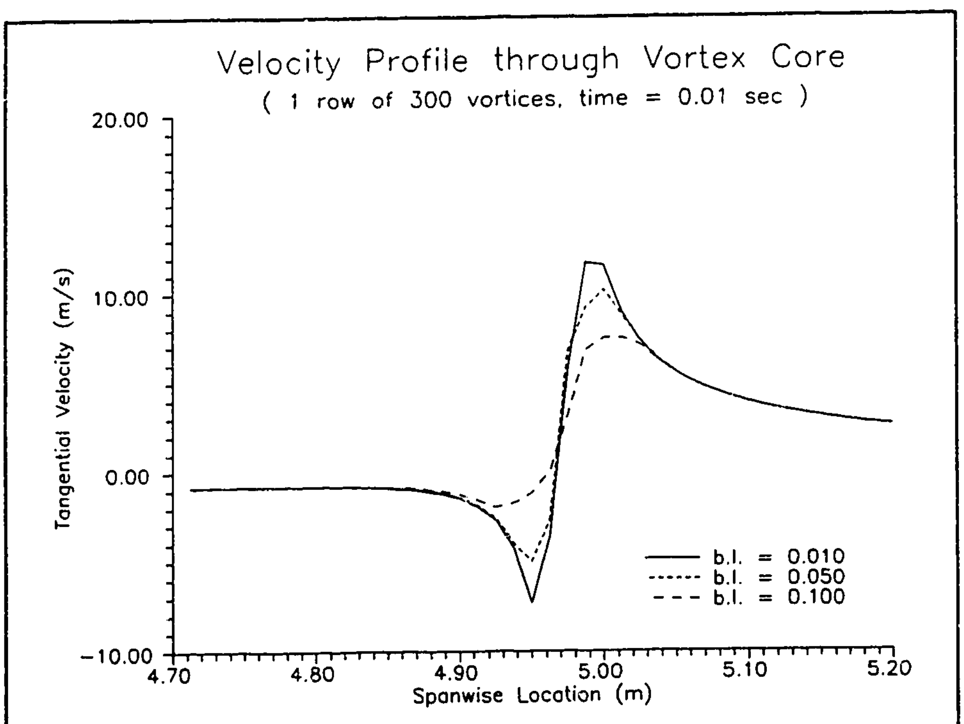

Figure 4.4 Velocity profiles with 1 row of 300 vortices at t=0.01s and b.l.t. = 0.010, 0.050, 0.100

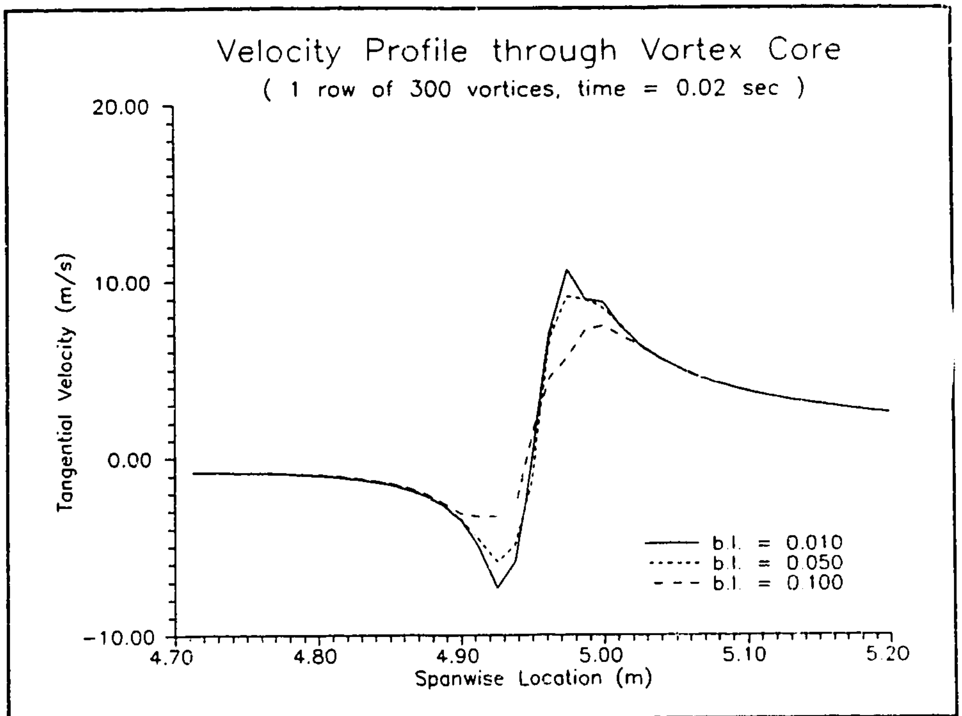

Figure 4.5 Velocity profiles with 1 row of 300 vortices at t=0.02s and b.l.t. = 0.010, 0.050, 0.100

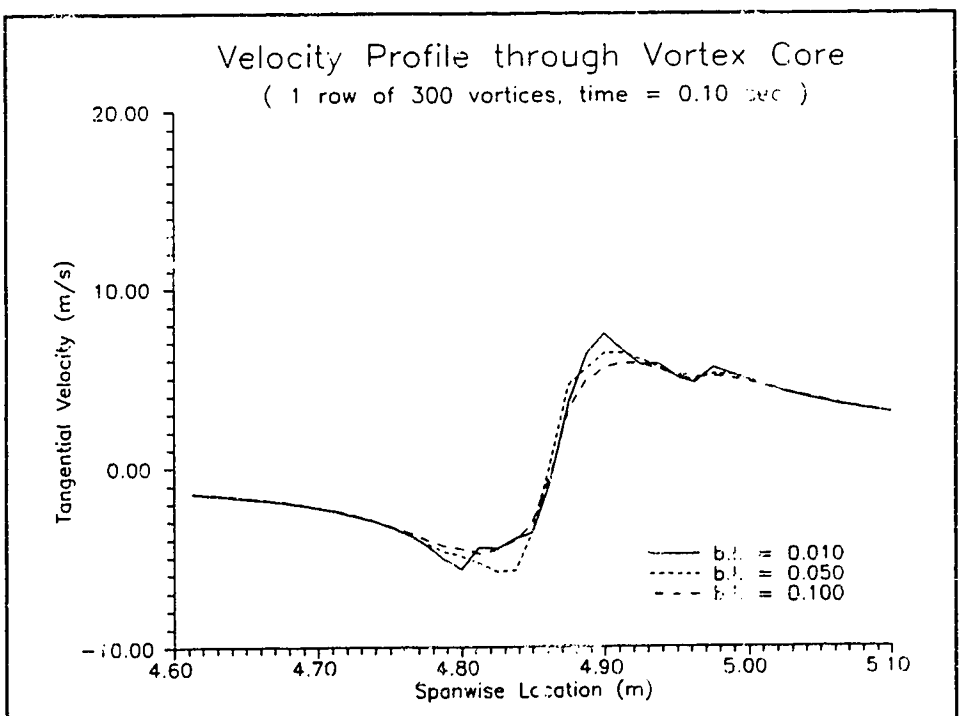

Figure 4.6 Velocity profiles with 1 row of 300 vortices at t=0.10s and b.l.t. =0.010, 0.050, 0.100

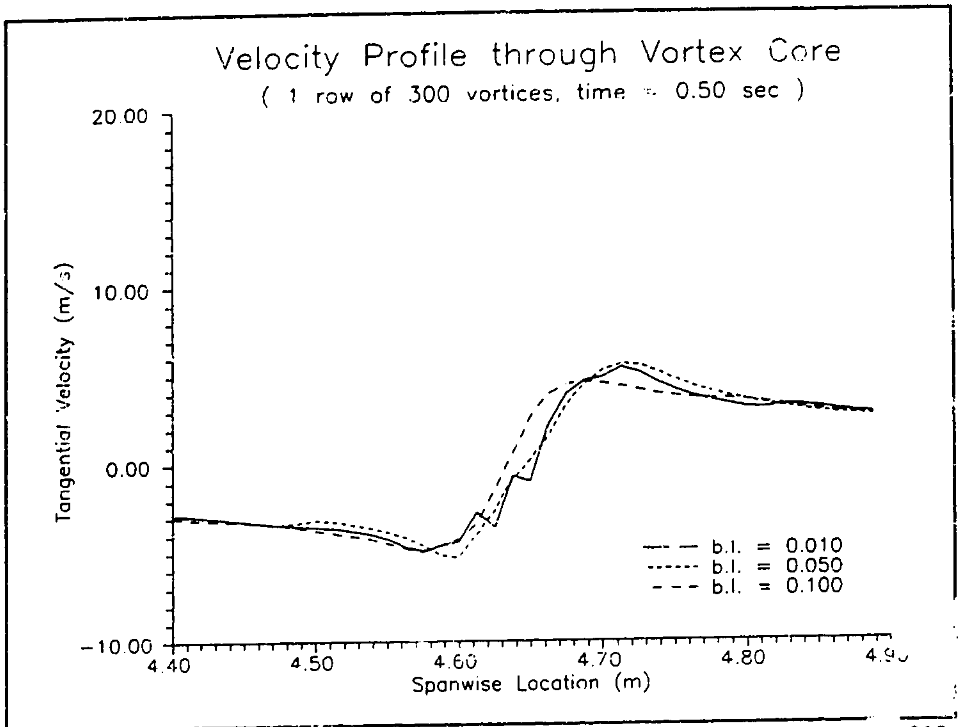

Figure 4.7 Velocity profiles with 1 row of 300 vortices at t=0.50s and b.l.t. = 0.010. 0.050, 0.100

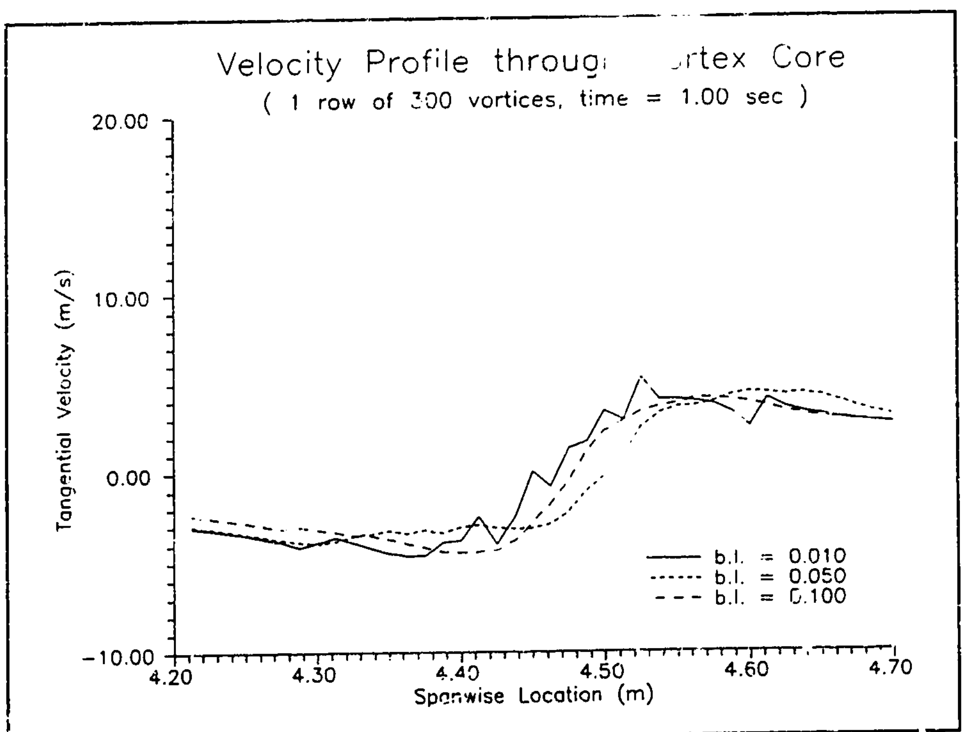

Figure 4.8 Velocity profiles with 1 row of 300 vortices at t=1.00s and b.l.t. = 0.010. 0.050, 0.100

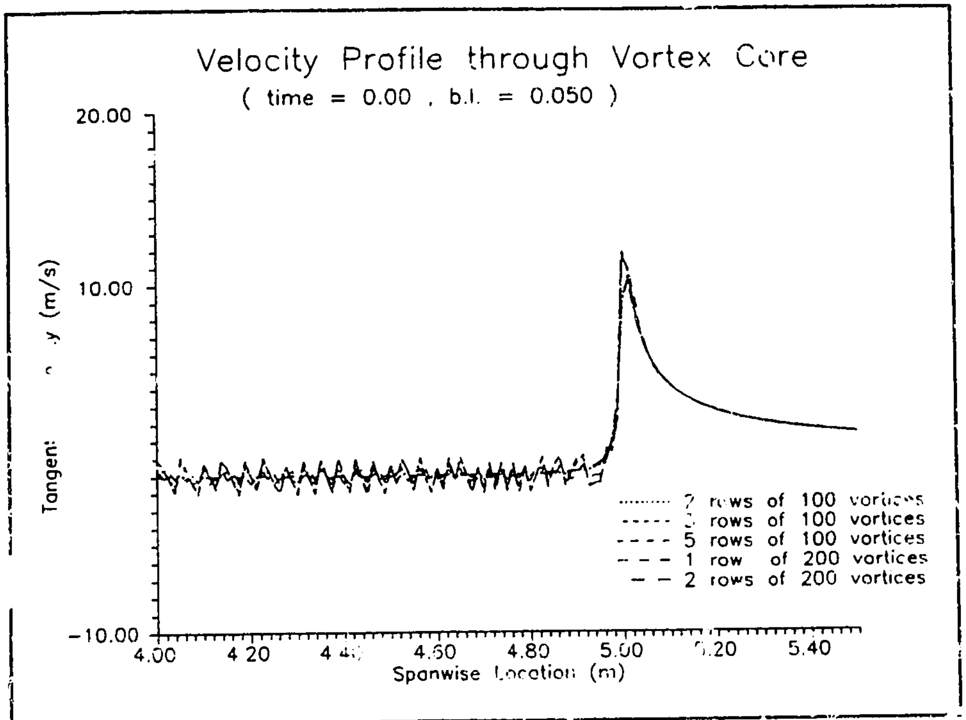

Figure 4.9 Comparisons with b.l.t. = 0.050 and various numbers of rows of vortices at t=0.00s

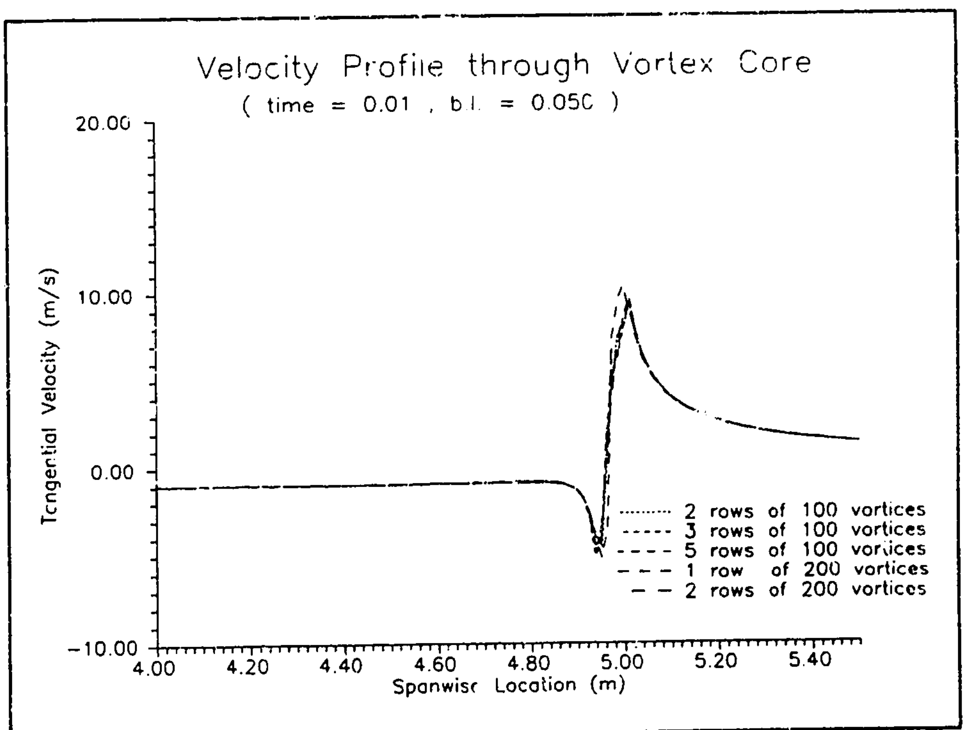

Figure 4.10 Comparisons with b.l.t. = 0.050 and various numbers of rows of vortices at t=0.01s.

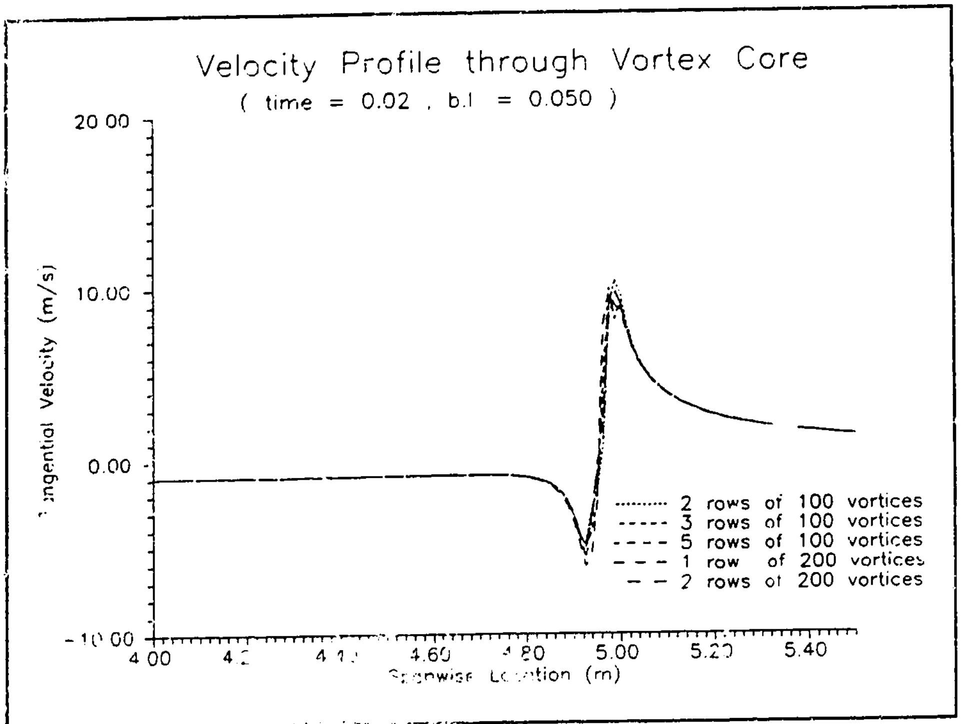

Figure 4.11 Comparisons with b.l.t. = 0.050 and various numbers of rows of vortices at t=0.02s

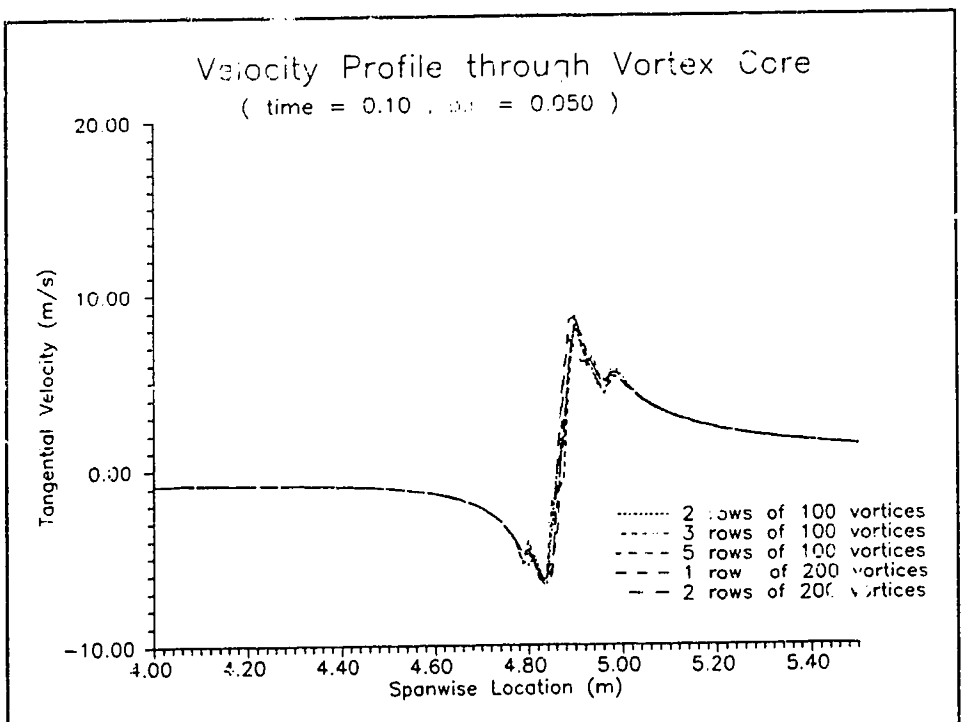

Figure 4.12 Comparisons with b.l.t. = 0.050 and various numbers of rows of vortices at t=0.10s

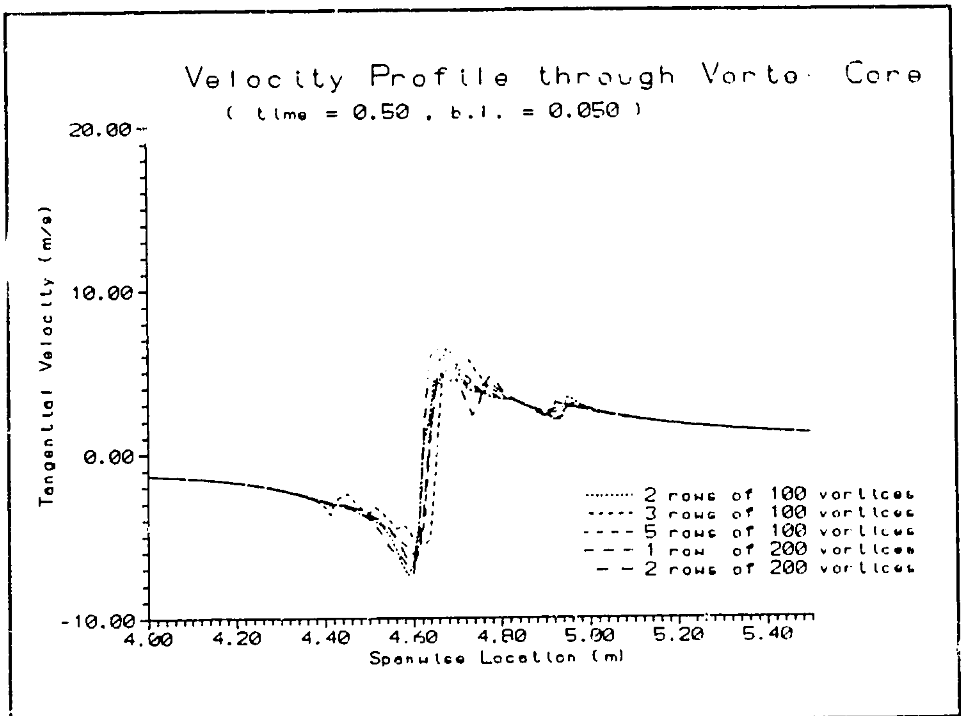

Figure 4.13 Comparisons with b.l.t. = 0.050 and various numbers of rows of vortices at t=0.50s

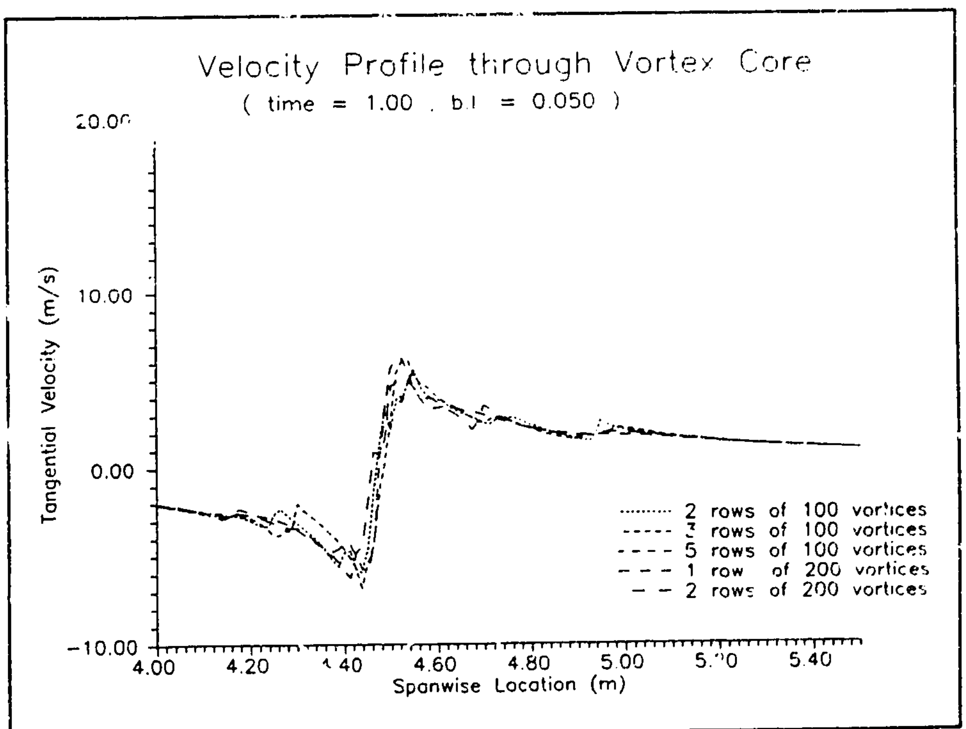

Figure 4.14 Comparisons with b.l.t. = 0.050 and various numbers of rows of vortices at t=1.00s

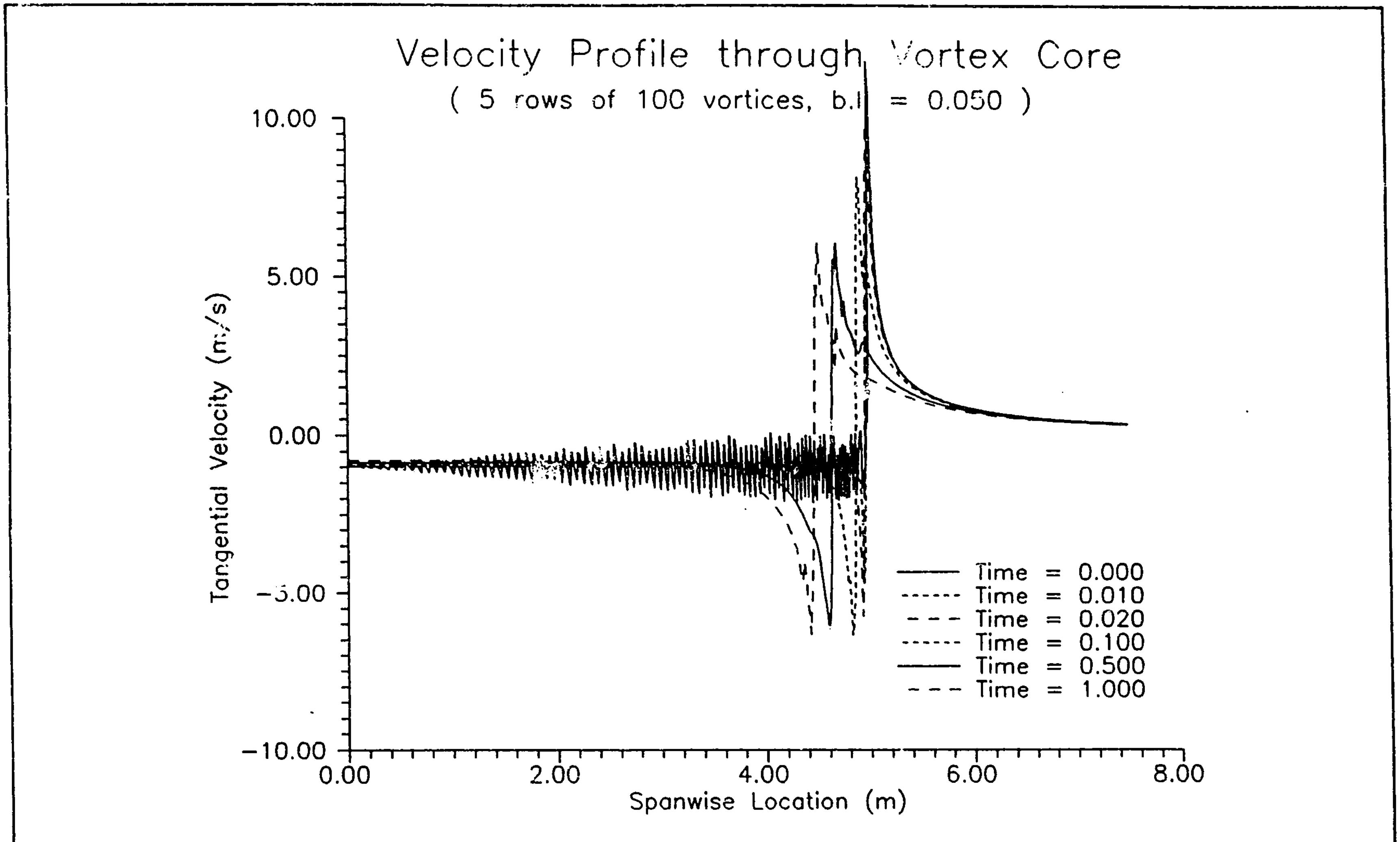

Figure 4.15 Velocity profile through vortex core using 5 rows of 100 vortices, and b.l.t. =0.050

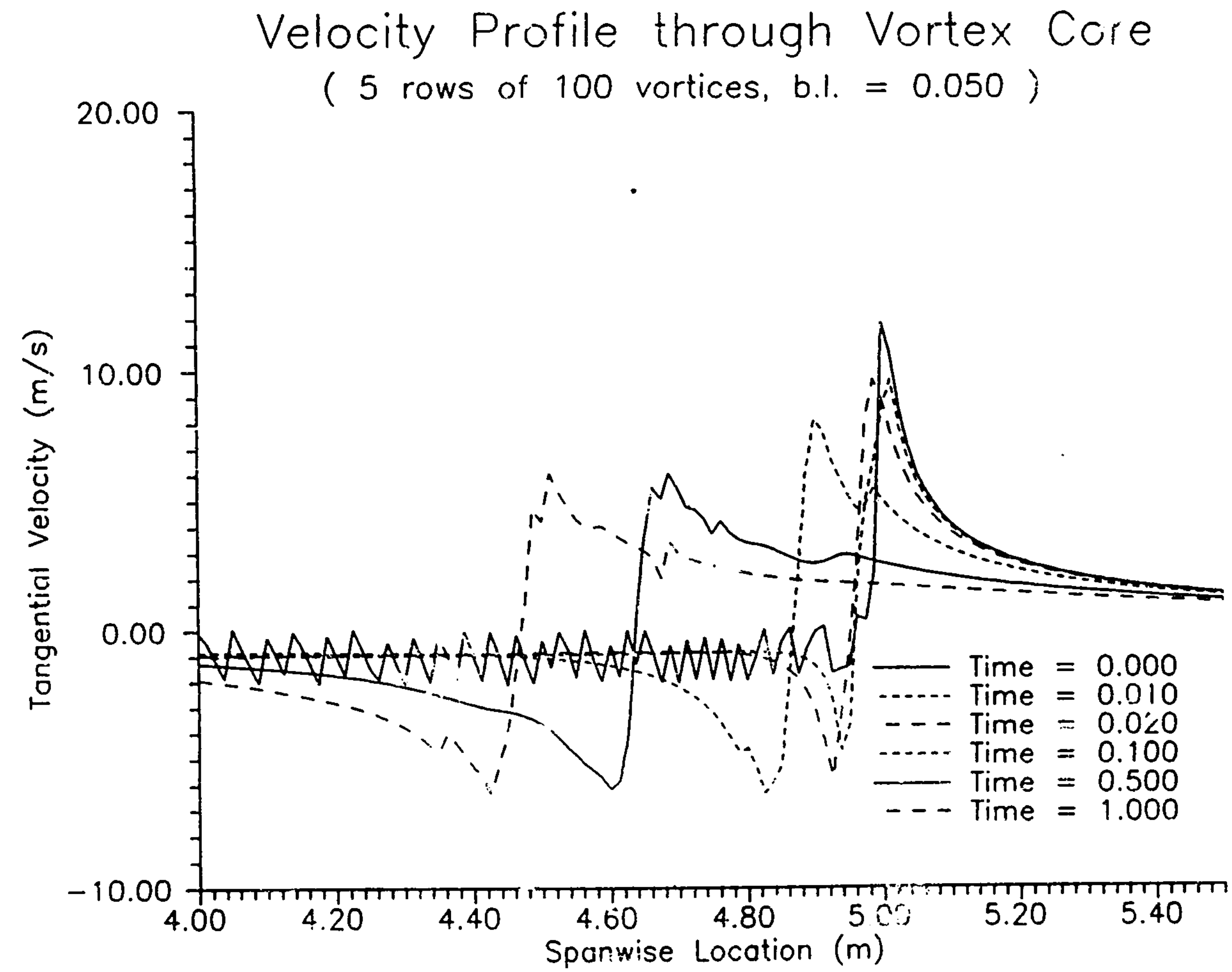

Figure 4.16 Velocity profile through vortex core using 5 rows of 100 vortices, and b.l.t.=0.050. View Zoomed in at tip.

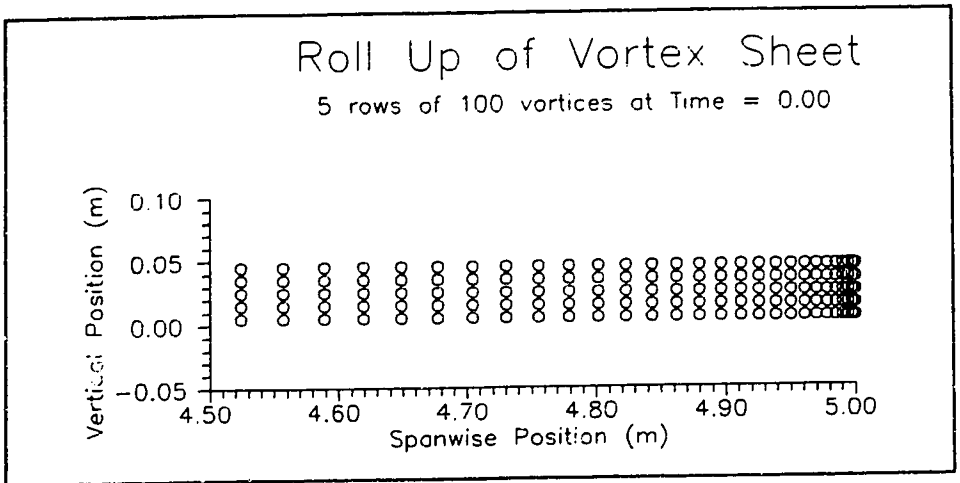

Figure 4.17 5 rows of 100 vortices, b.l.t. = 0.050, at t=0.00s.

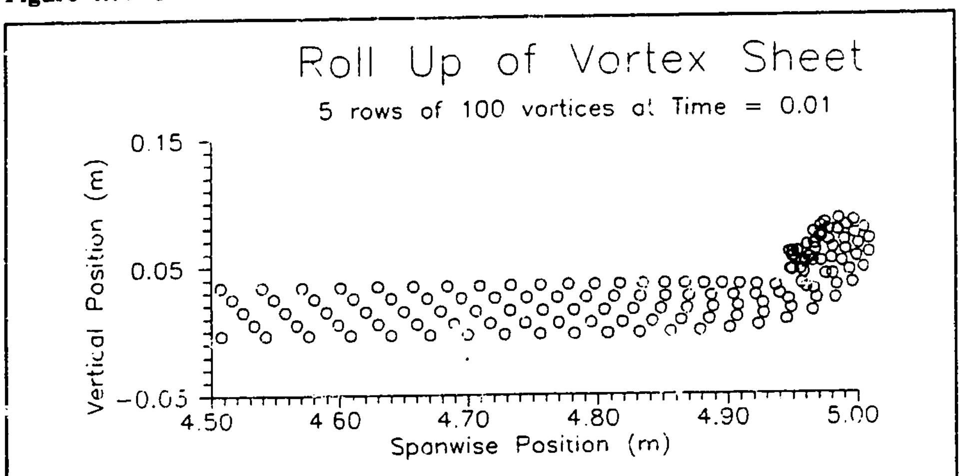

Figure 4.18 5 rows of 100 vortices, b.l.t. = 0.050, at t=0.01s

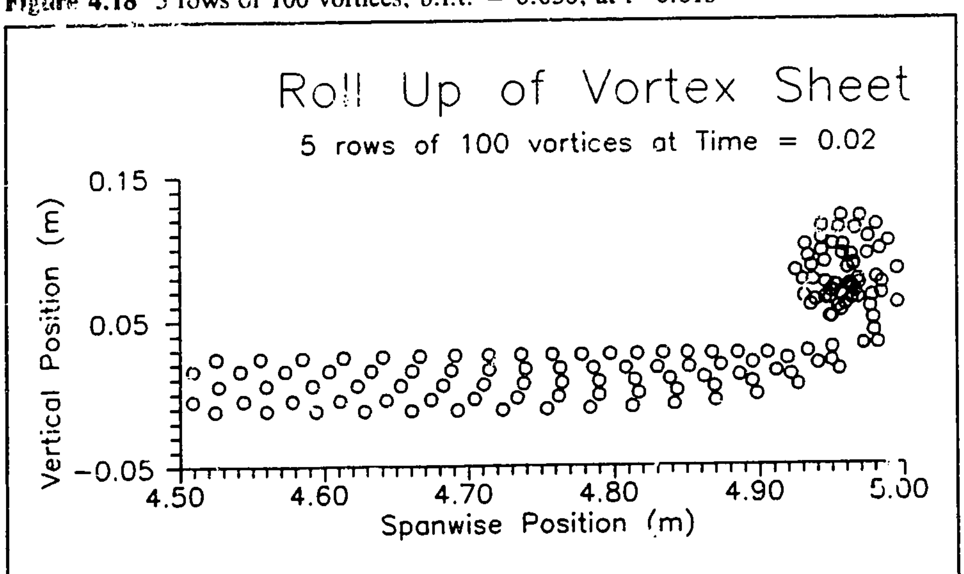

Figure 4.19 5 rows of 100 vortices, b.l.t. = 0.050, at t=0.02s

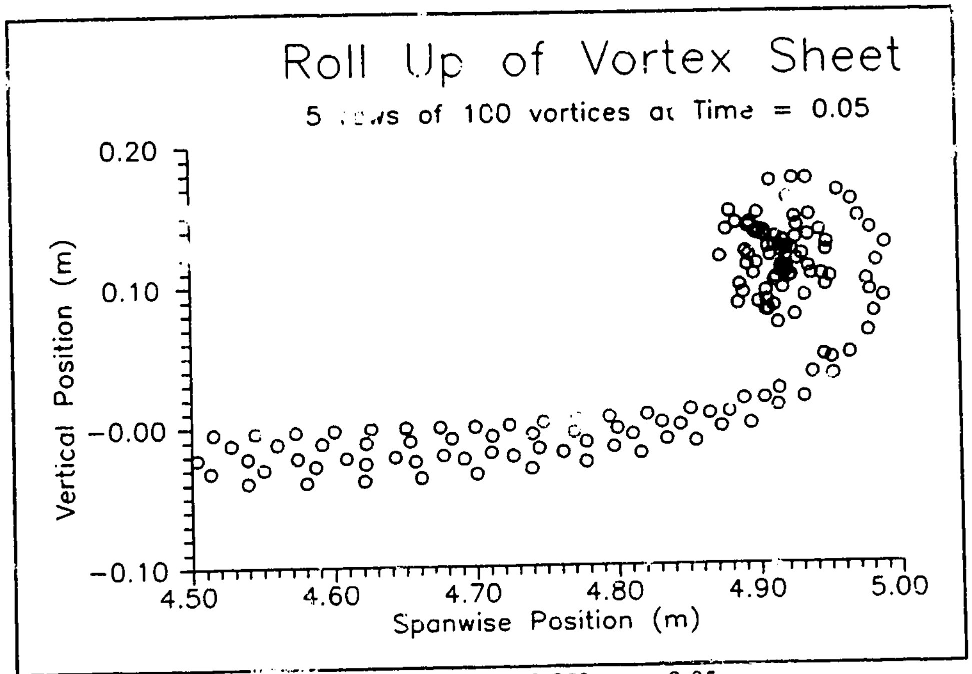

Figure 4.20 5 rows of 100 vortices, b.l.t. = 0.050, at t=0.05s

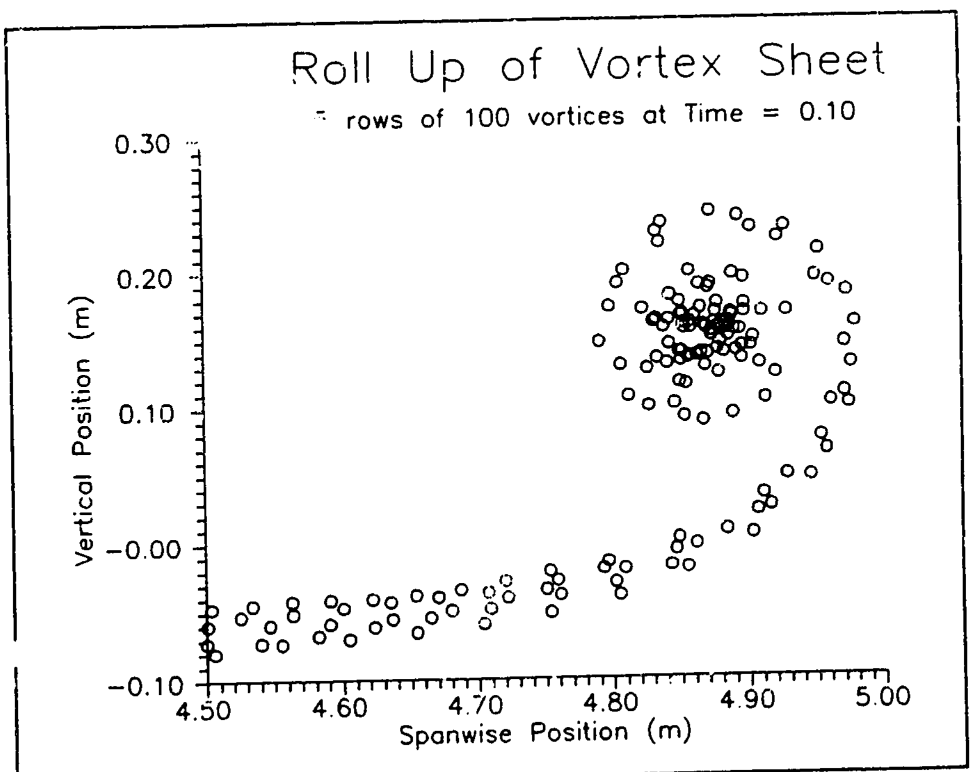

Figure 4.21 5 rows of 100 vortices, b.l.t. = 0.050, at t=0.10s

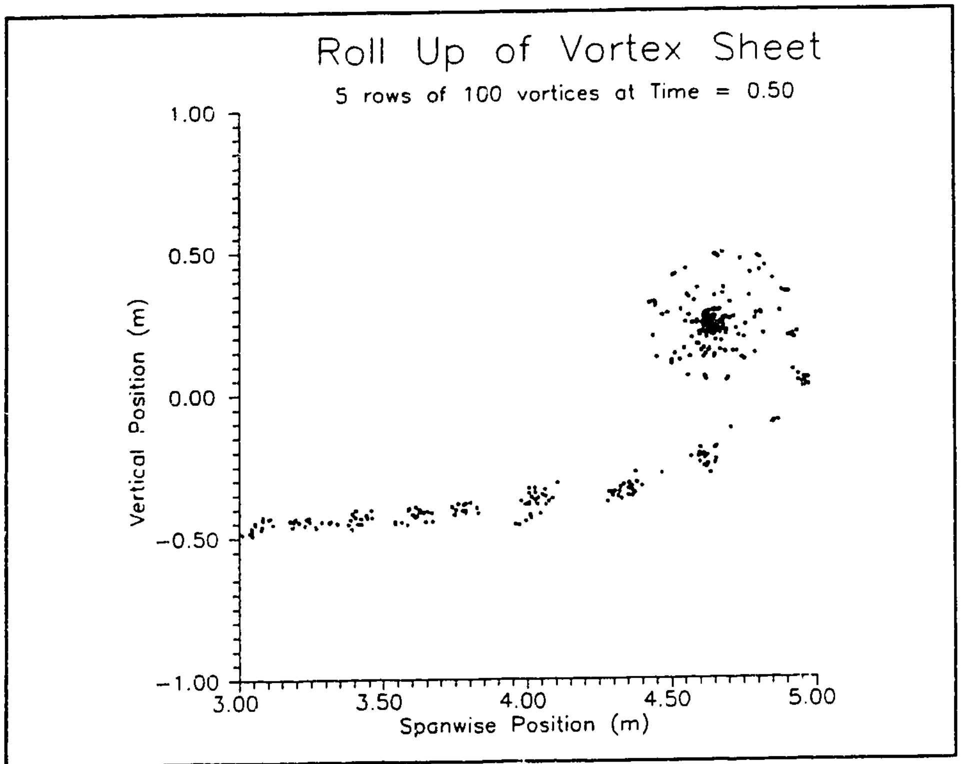

Figure 4.22 5 rows of 100 vortices, b.l.t. = 0.050, at t=0.50s

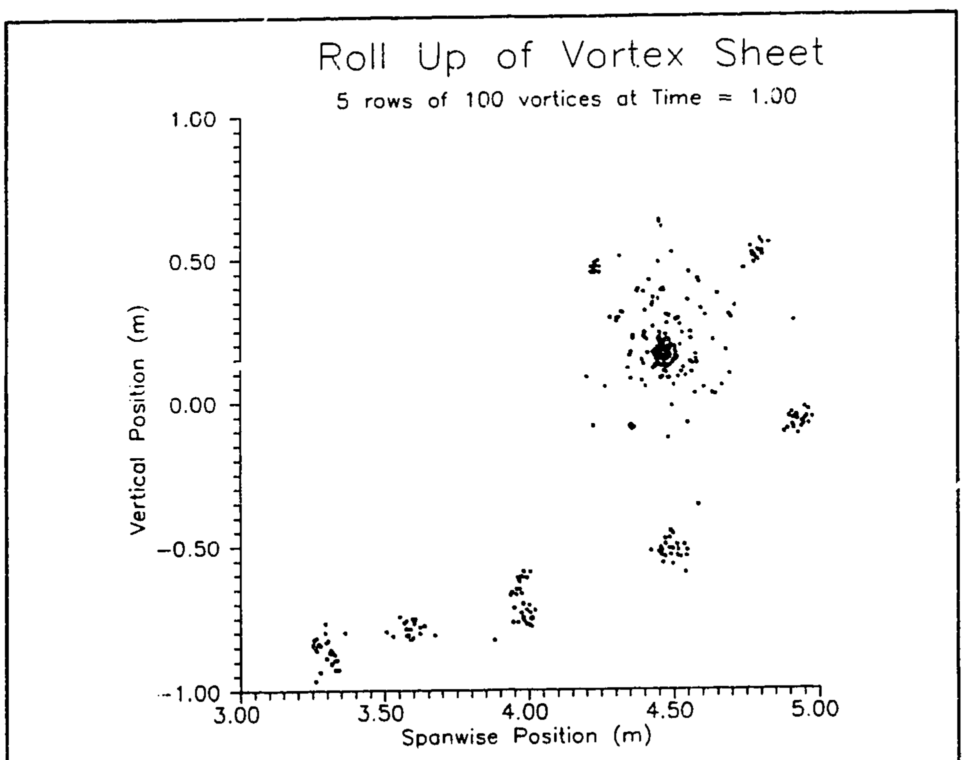

Figure 4.23 5 rows of 100 vortices, b.l.t. = 0.050, at t=1.00s

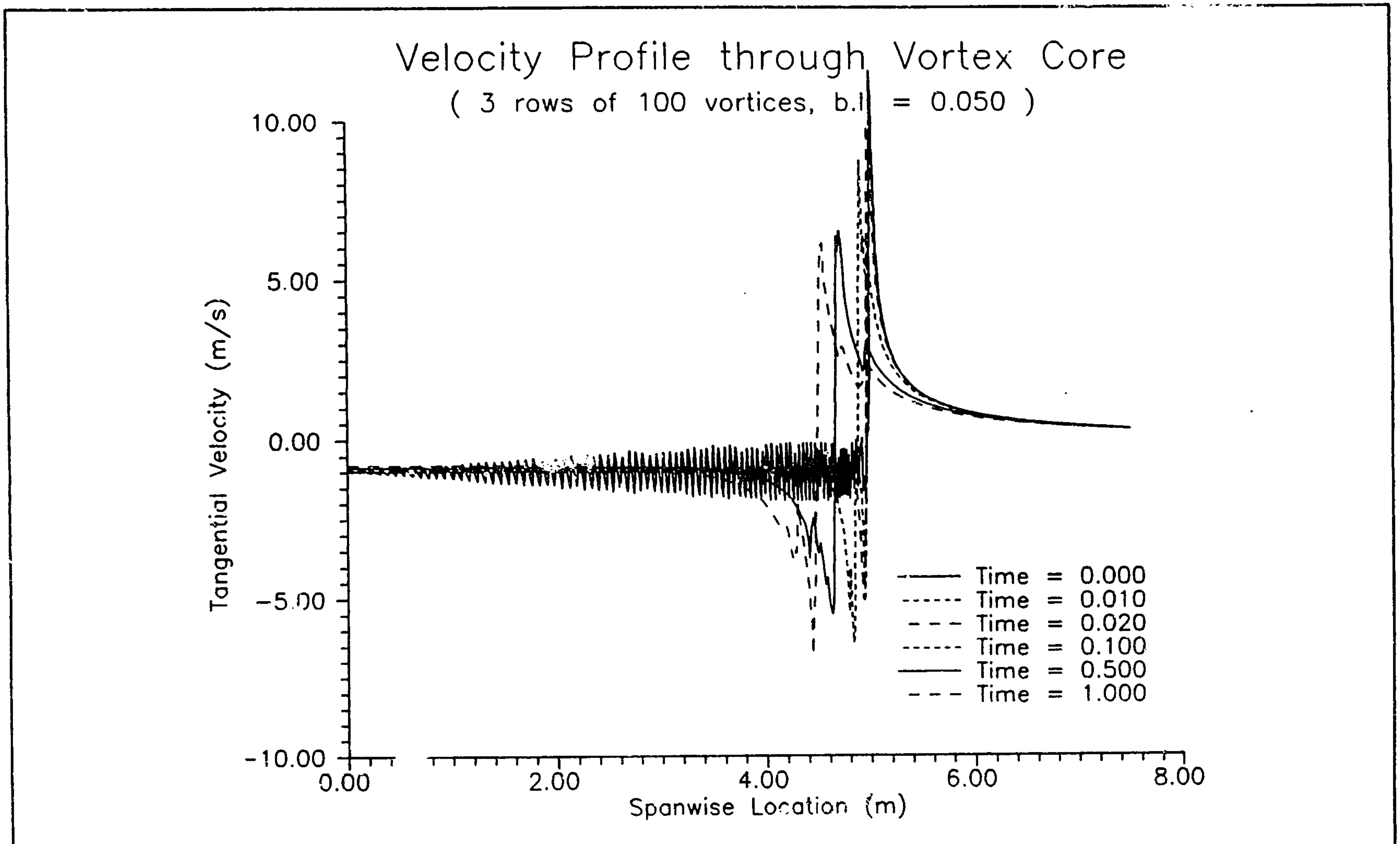

Figure 4.24 Velocity profile through vortex core using 3 rows of 100 vortices, and b.l.t. =0.050

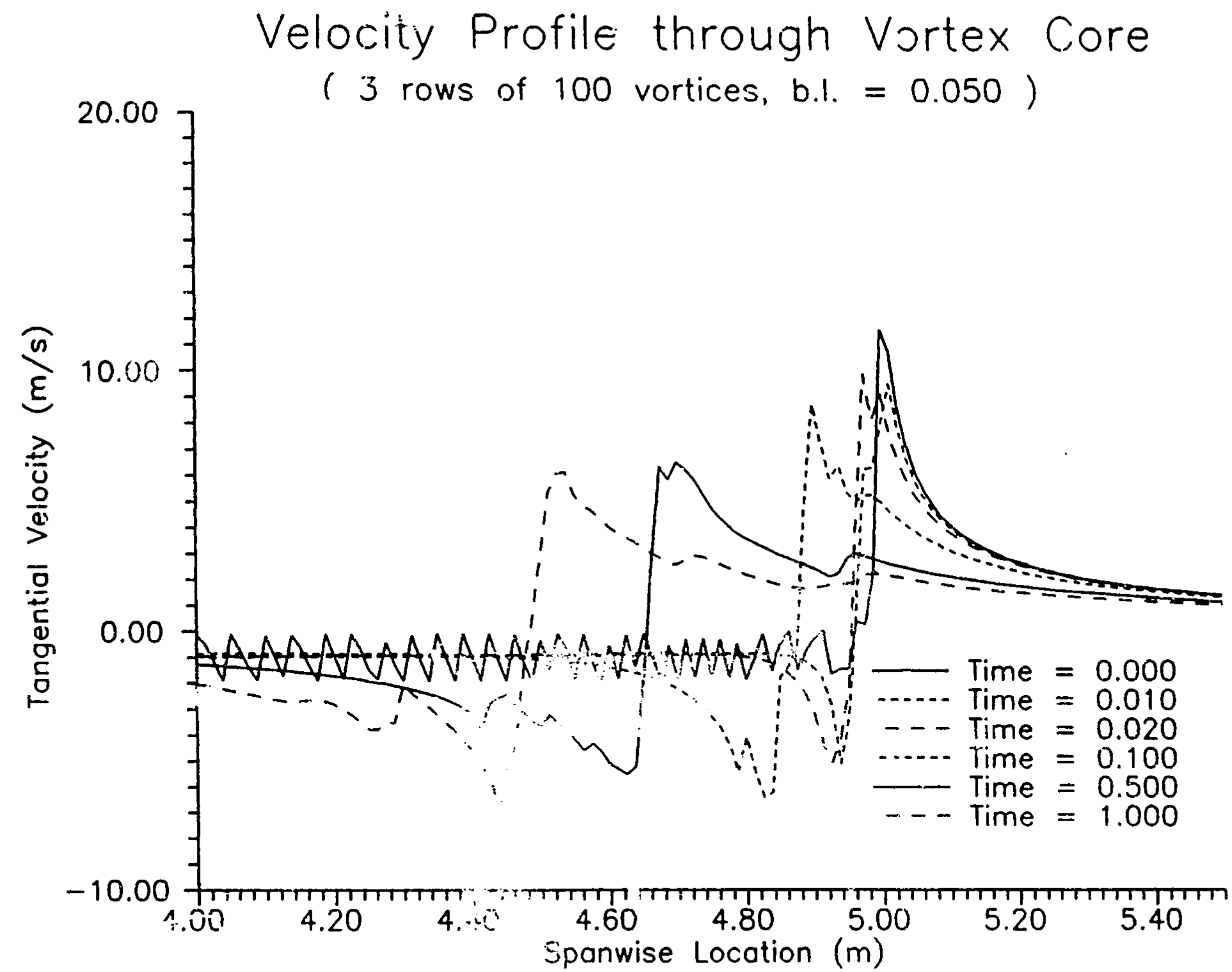

Figure 4.25 Velocity profile through vortex core using 3 rows of 100 vortices, and b.l.t. =0.050. View Zoomed in at tip.

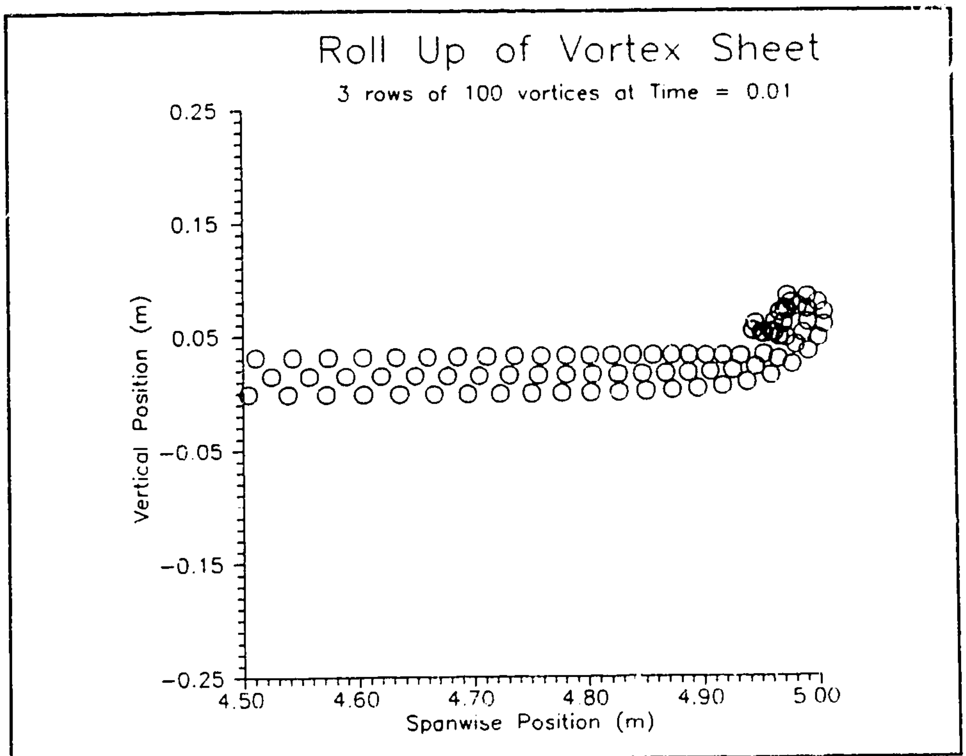

Figure 4.26 3 rows of 100 vortices, b.l.t. = 0.050, at t=0.01s

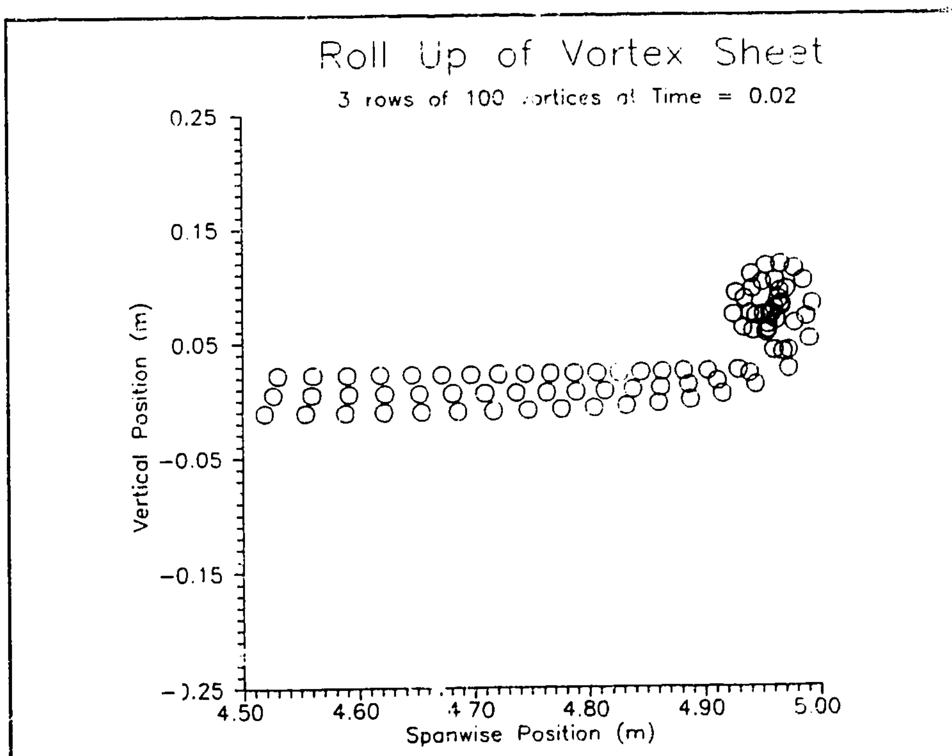

Figure 4.27 3 rows of 100 vortices, b.l.t. = 0.050, at t=0.02s

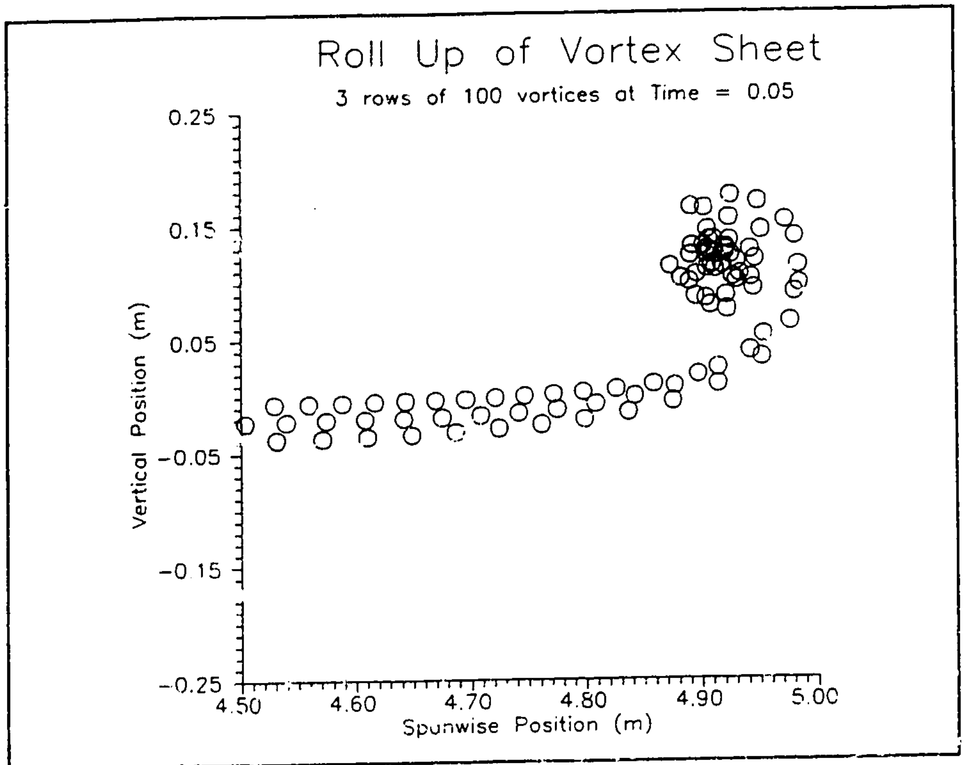

Figure 4.28 3 rows of 100 vortices, b.l.t. = 0.050, at t=0.05s

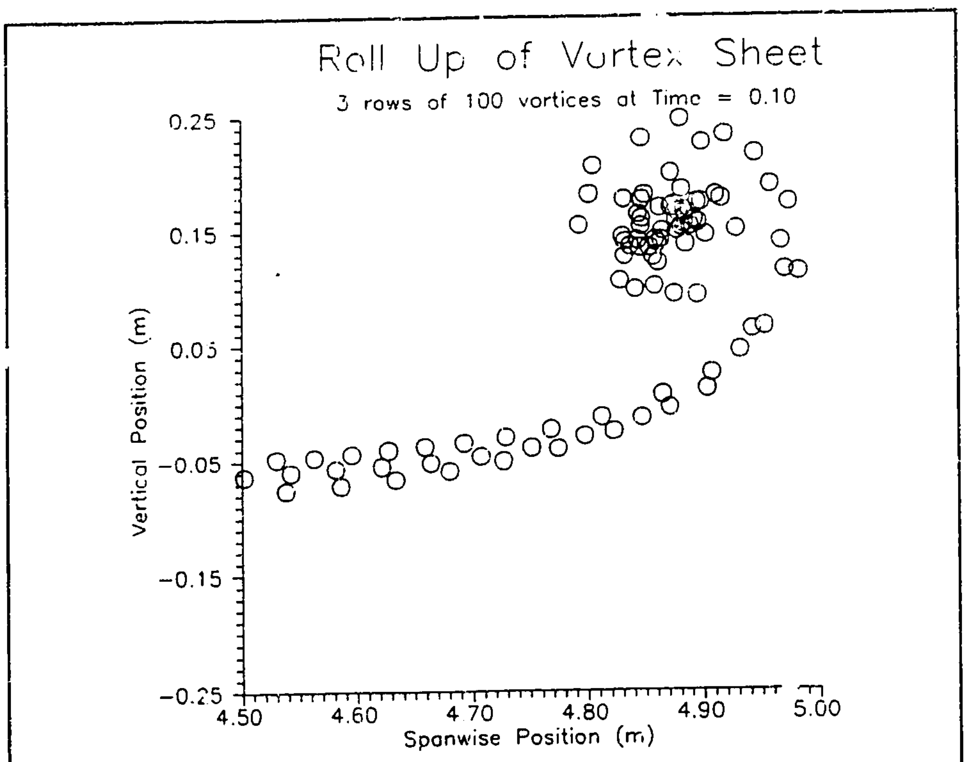

Figure 4.29 3 rows of 100 vortices, b.l.t. = 0.050, at t=0.10s

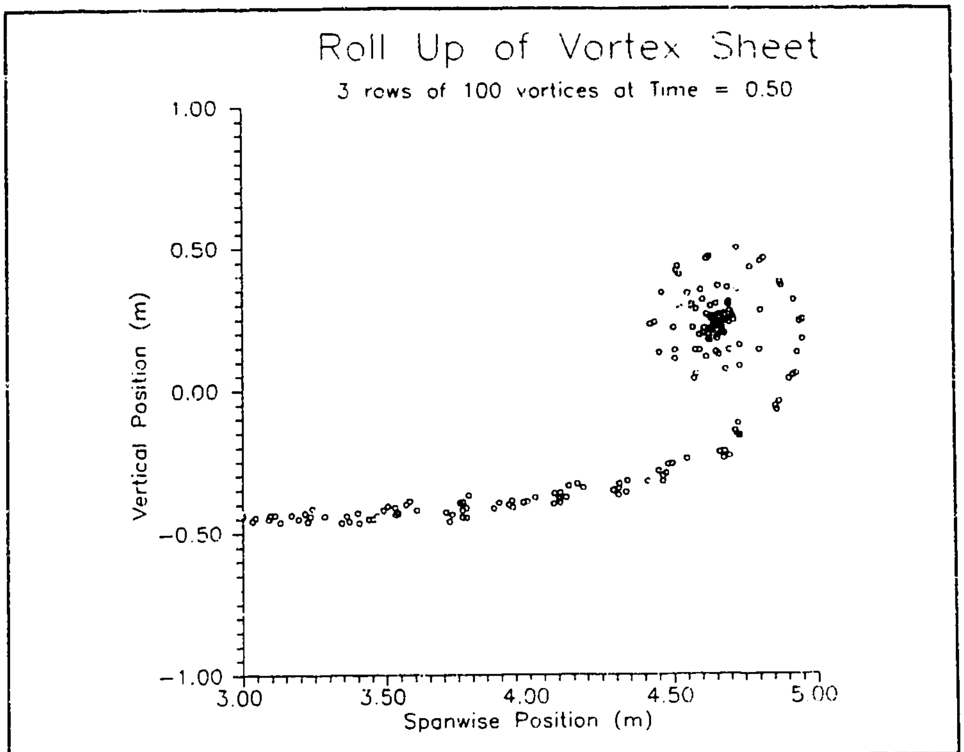

Figure 4.30 3 rows of 100 vortices, b.l.t. = 0.050, at t=0.50s

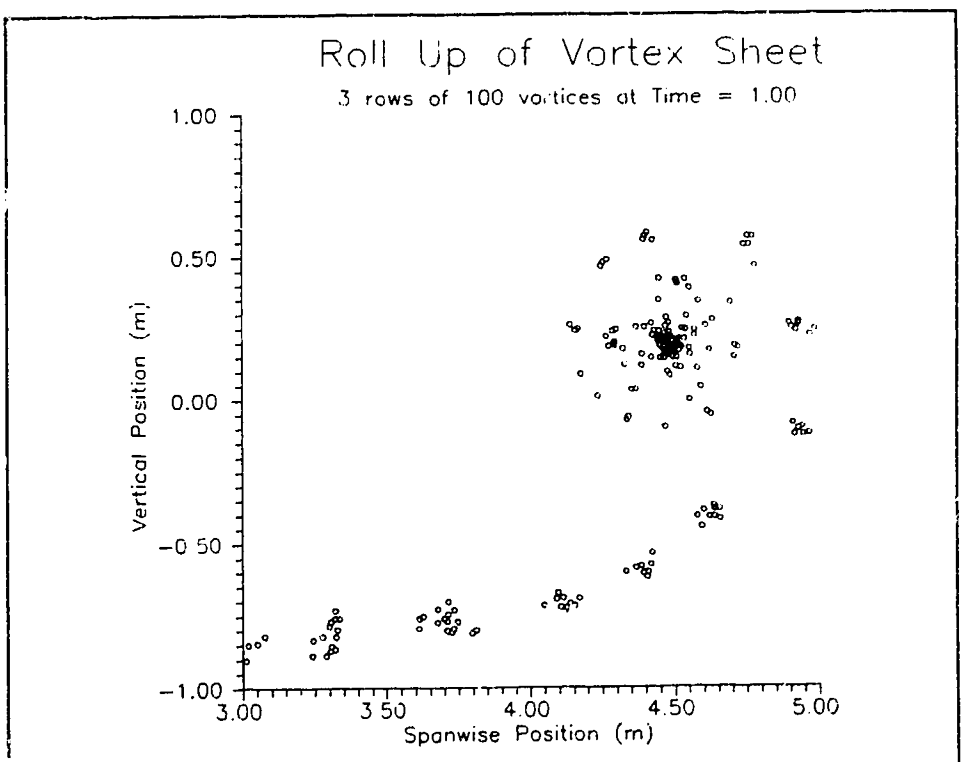

Figure 4.31 3 rows of 100 vortices, b.l.t. = 0.050, at t=1.00s

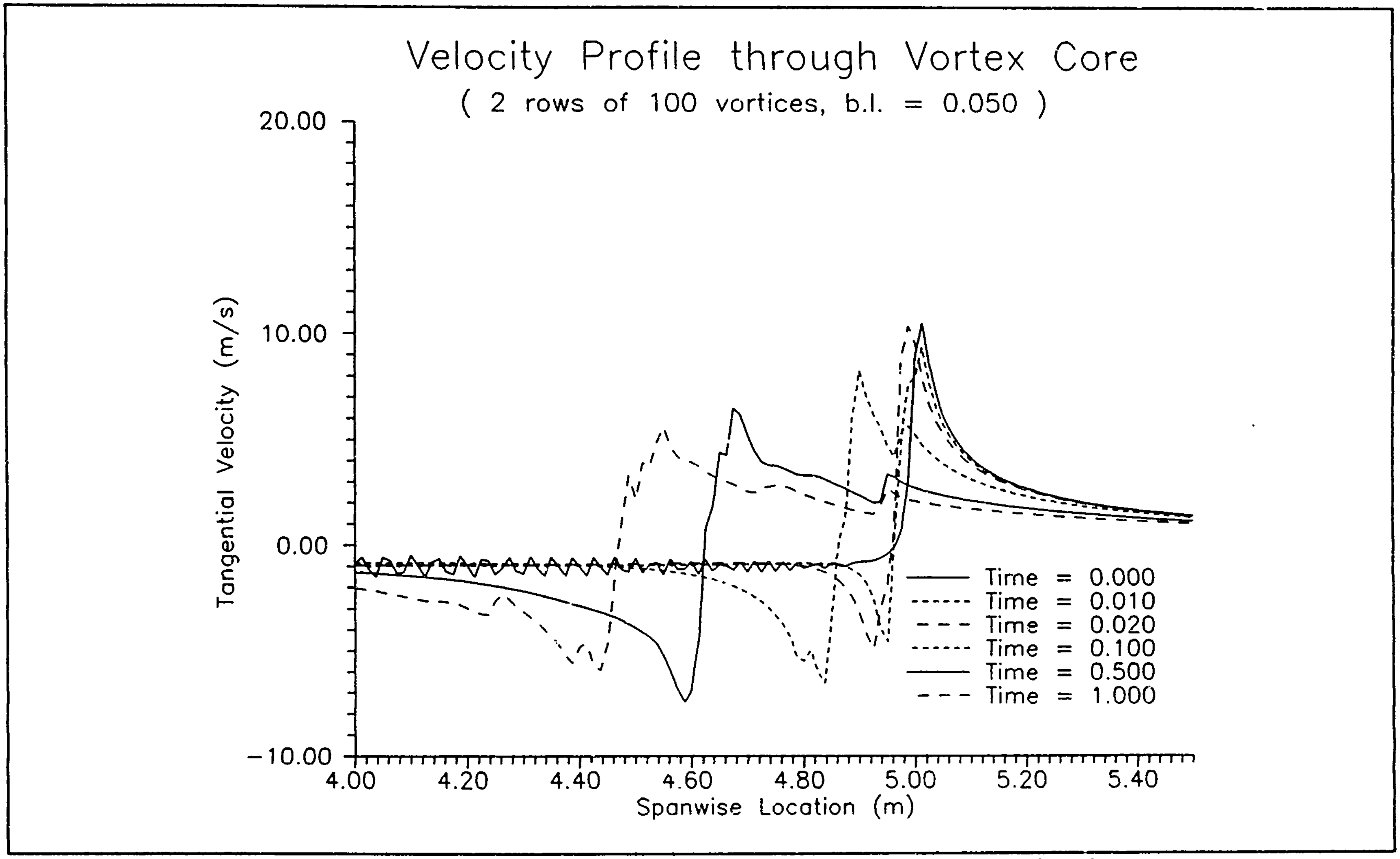

Figure 4.32 Velocity profile through vortex core using 2 rows of 100 vortices, and b.l.t.=0.050. View Zoomed in at tip.

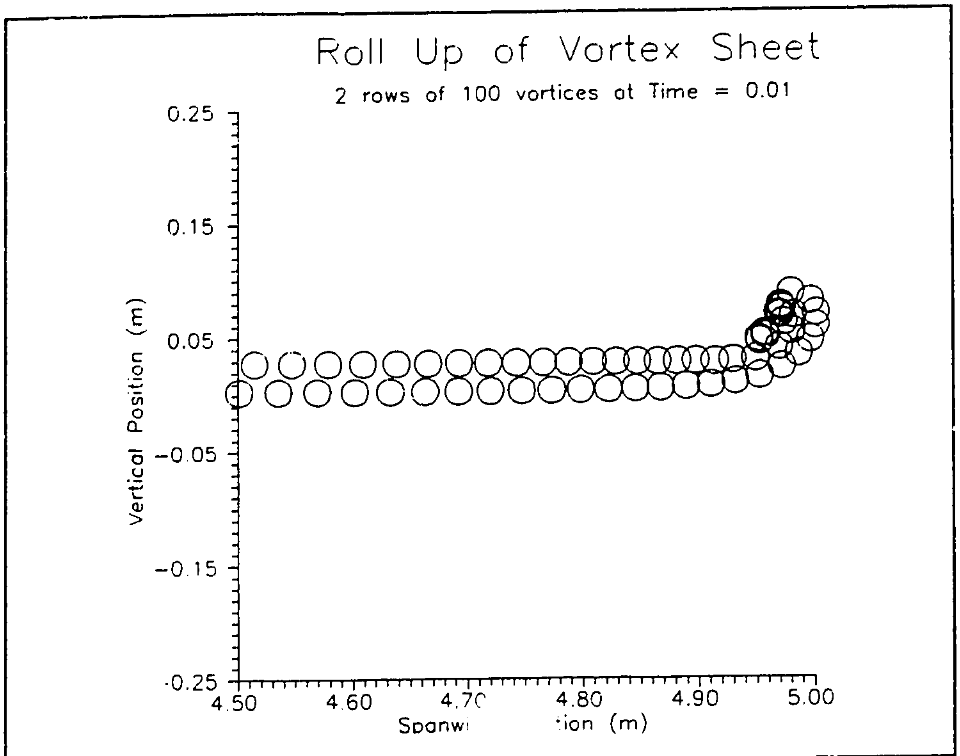

Figure 4.33 2 rows of 100 vortices, b.l.t. = 0.050, at t=0.01s

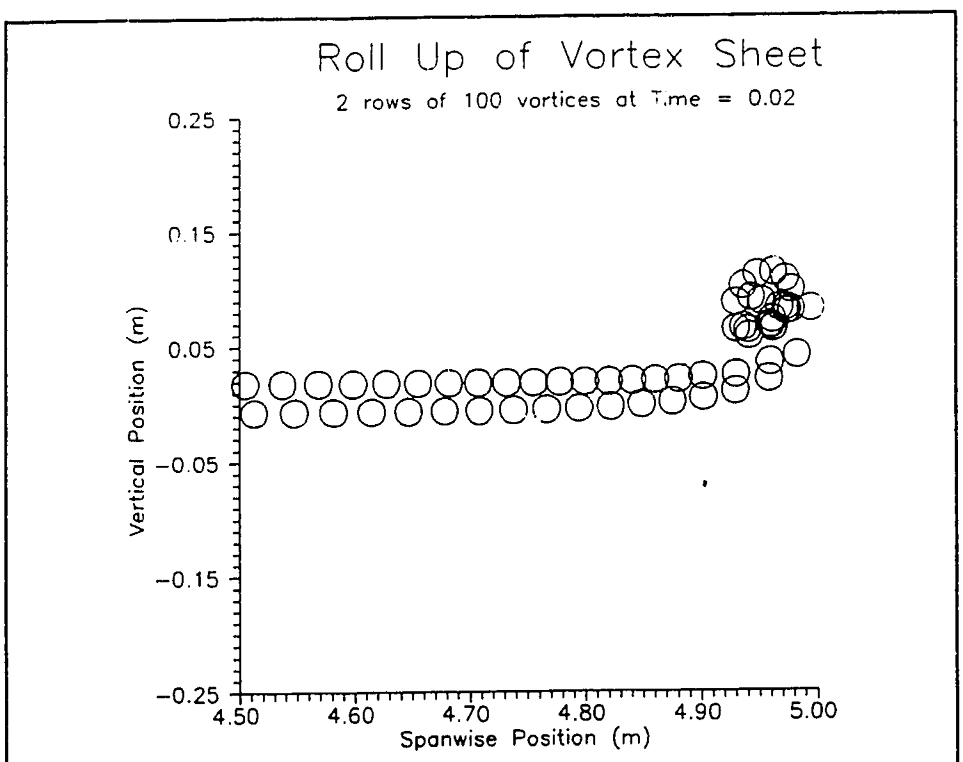

Figure 4.34 2 rows of 100 vortices, b.l.t. = 0.050, at t=0.02s

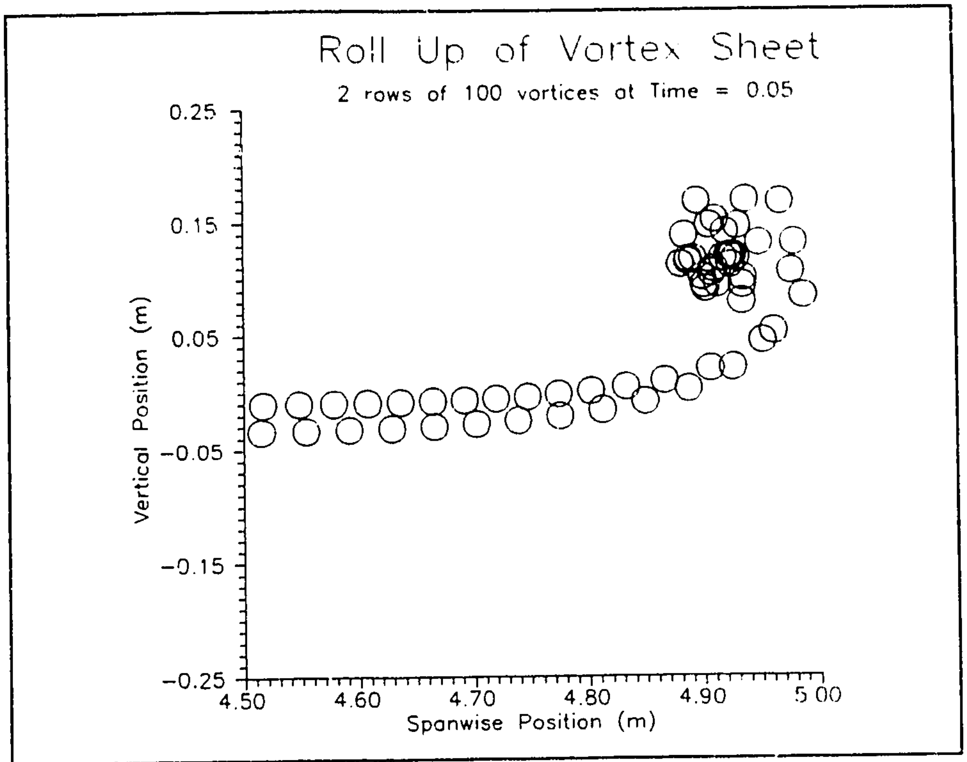

Figure 4.35 2 rows of 100 vortices, b.l.t. = 0.050, at t=0.05s

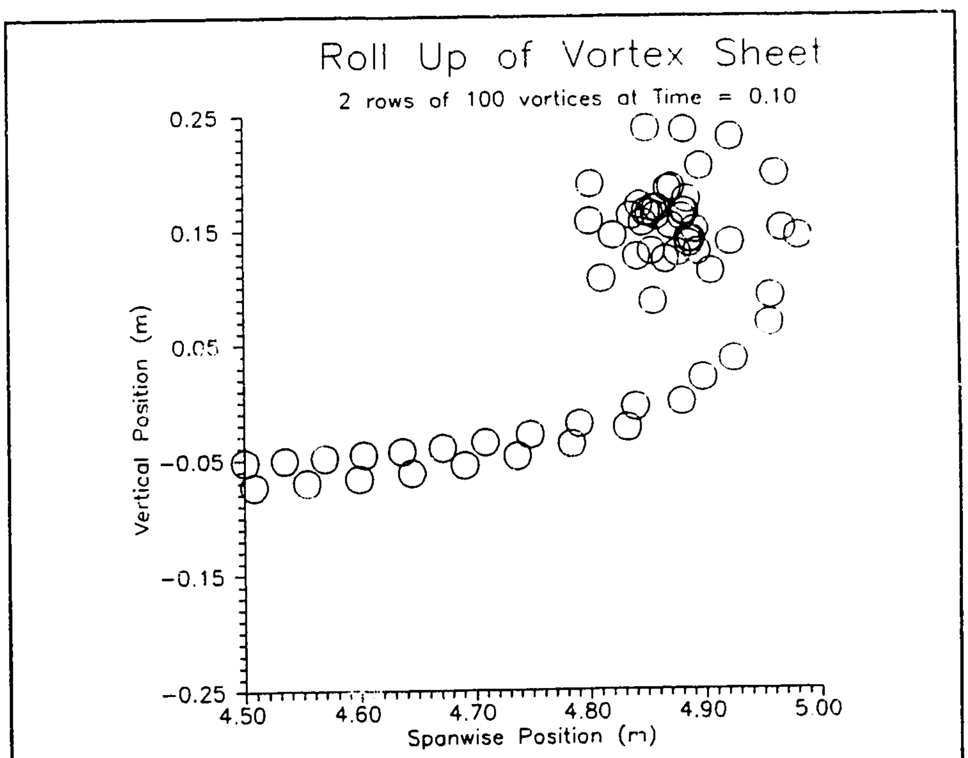

Figure 4.36 2 rows of 100 vortices, b.l.t. = 0.050, at t=0.10s

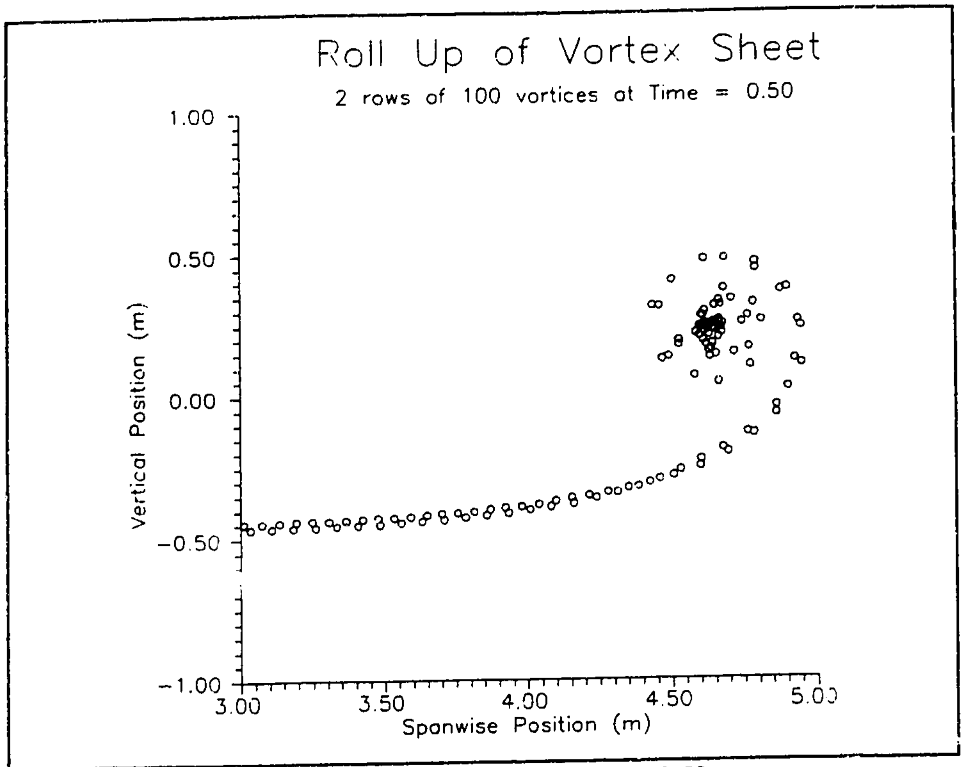

Figure 4.37 2 rows of 100 vortices, b.l.t. = 0.050, at t=0.50s

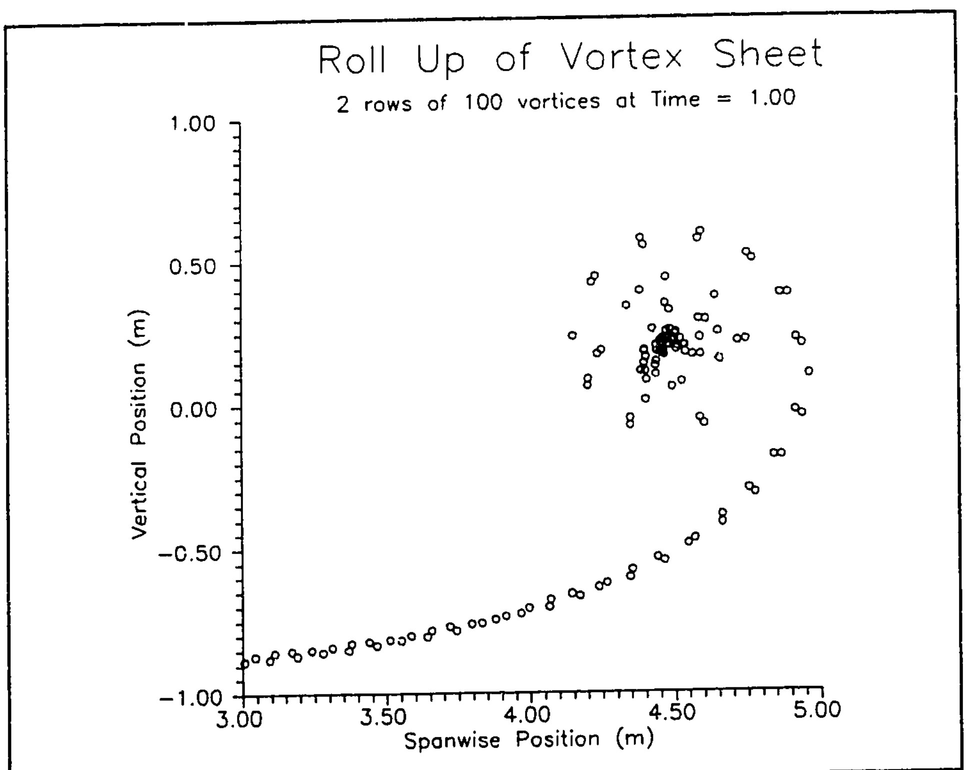

Figure 4.38 2 rows of 100 vortices, b.l.t. = 0.050, at t=1.00s

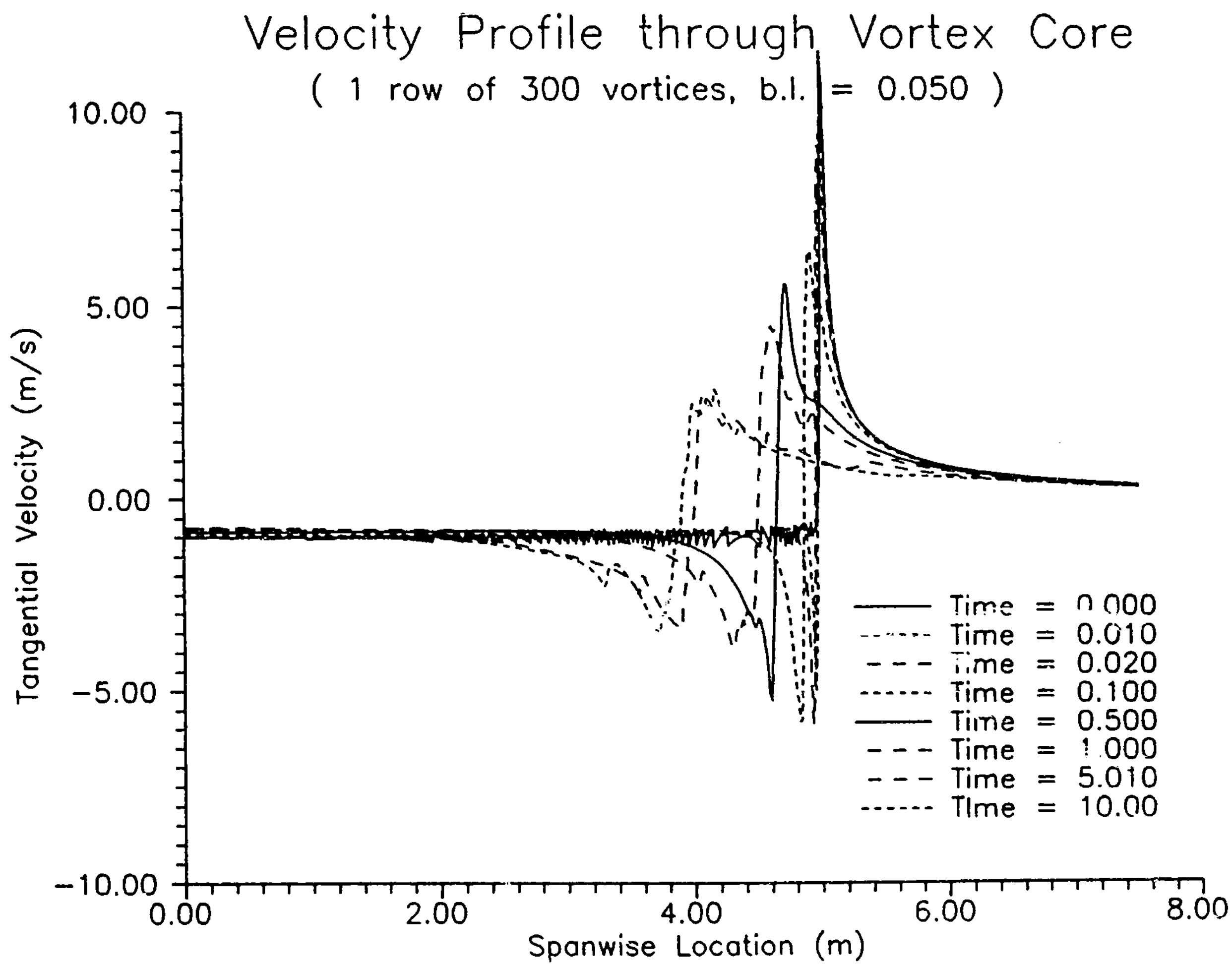

Figure 4.39 Velocity profile through vortex core using 1 row of 300 vortices, and b.l.t. =0.050

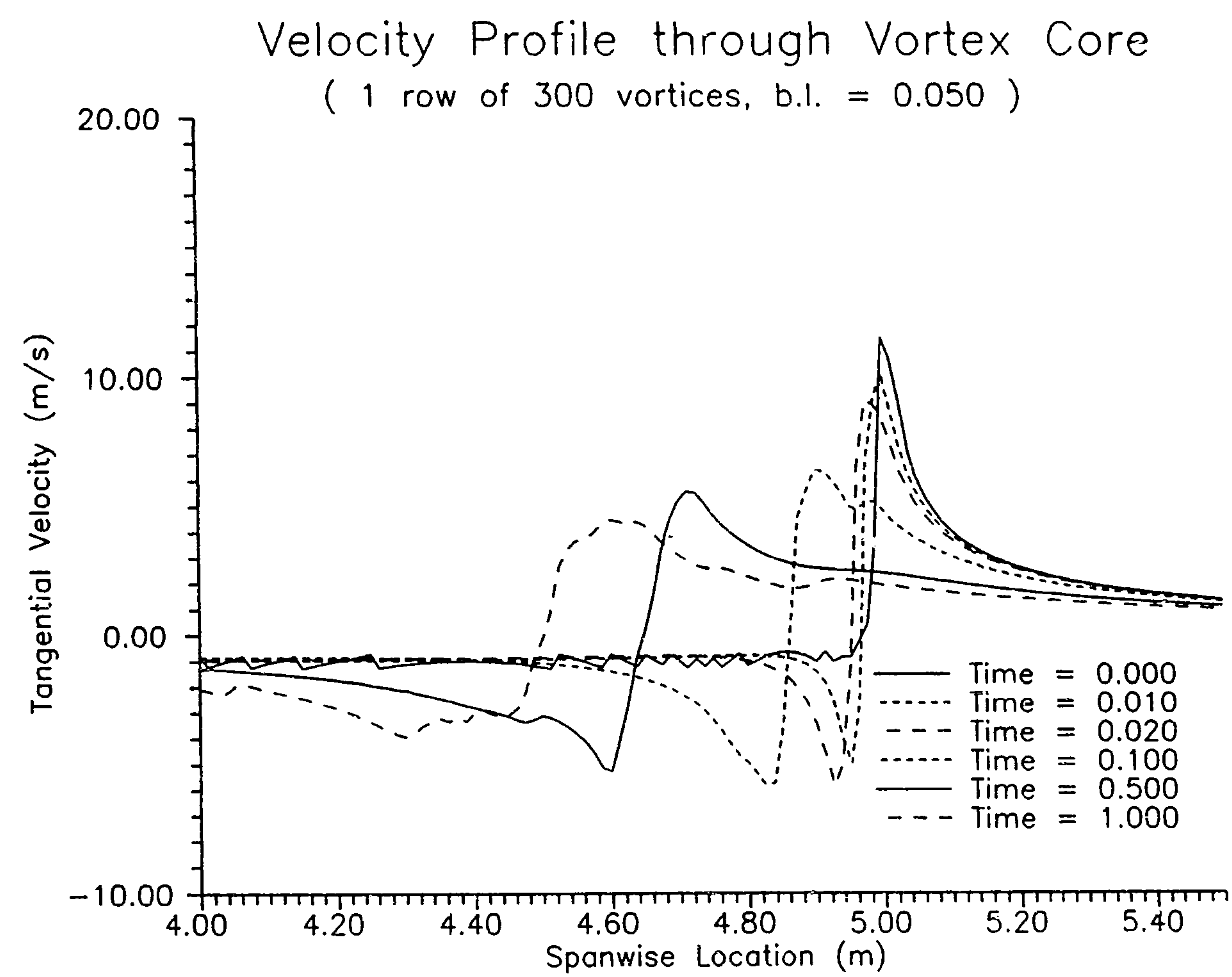

Figure 4.40 Velocity profile through vortex core using 1 row of 300 vortices, and b.l.t.=0.050. View Zoomed in at tip.

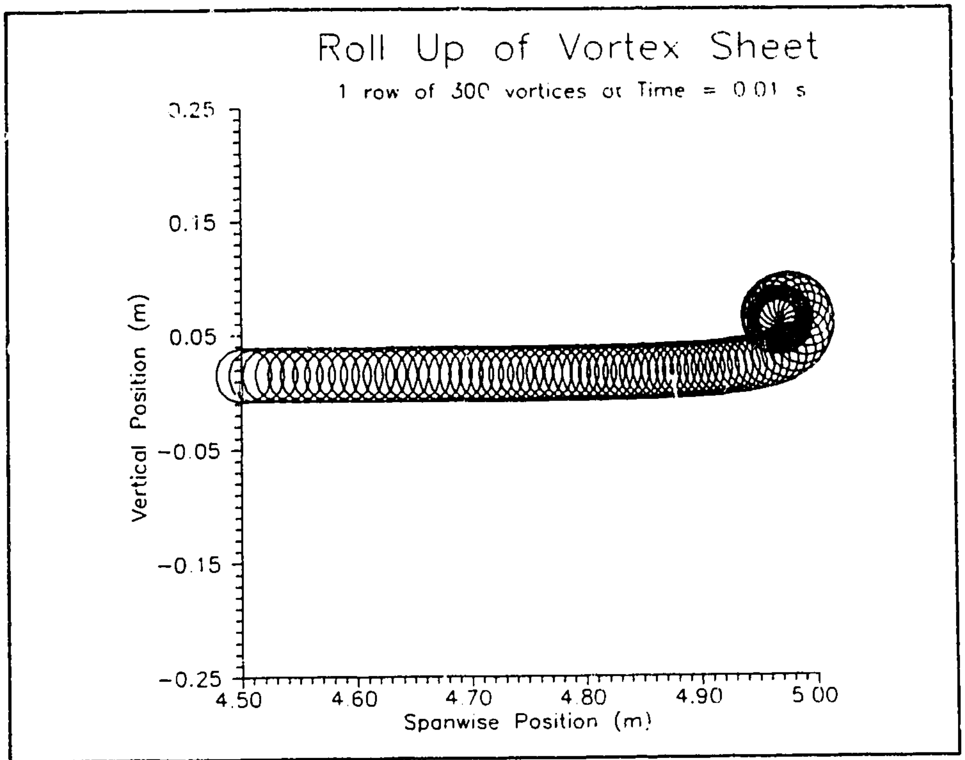

Figure 4.41 1 row of 300 vortices, b.l.t. = 0.050, at t=0.01s

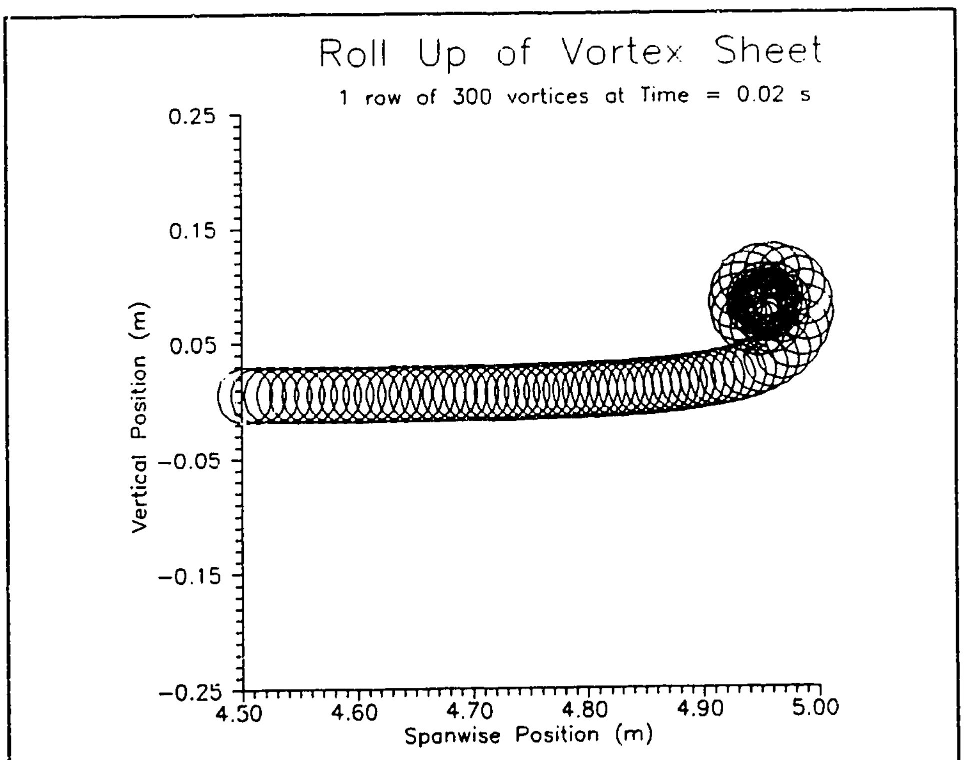

Figure 4.42 1 row of 300 vortices, b.l.t. = 0.050, at t=0.02s

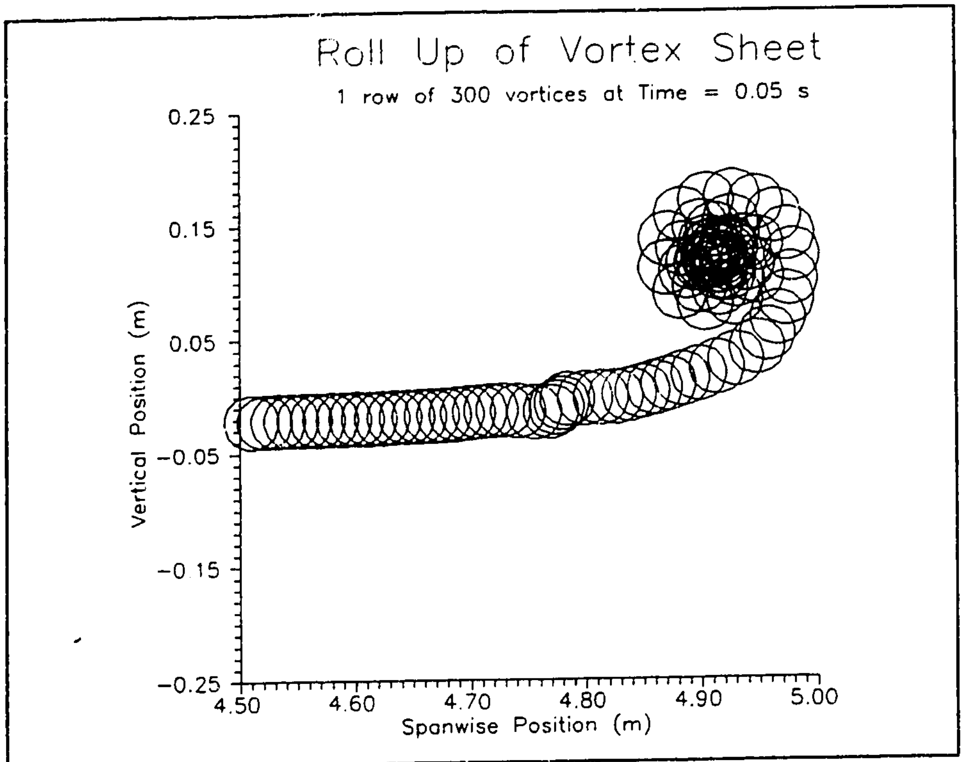

Figure 4.43 1 row of 300 vortices, b.l.t. = 0.050, at t=0.05s

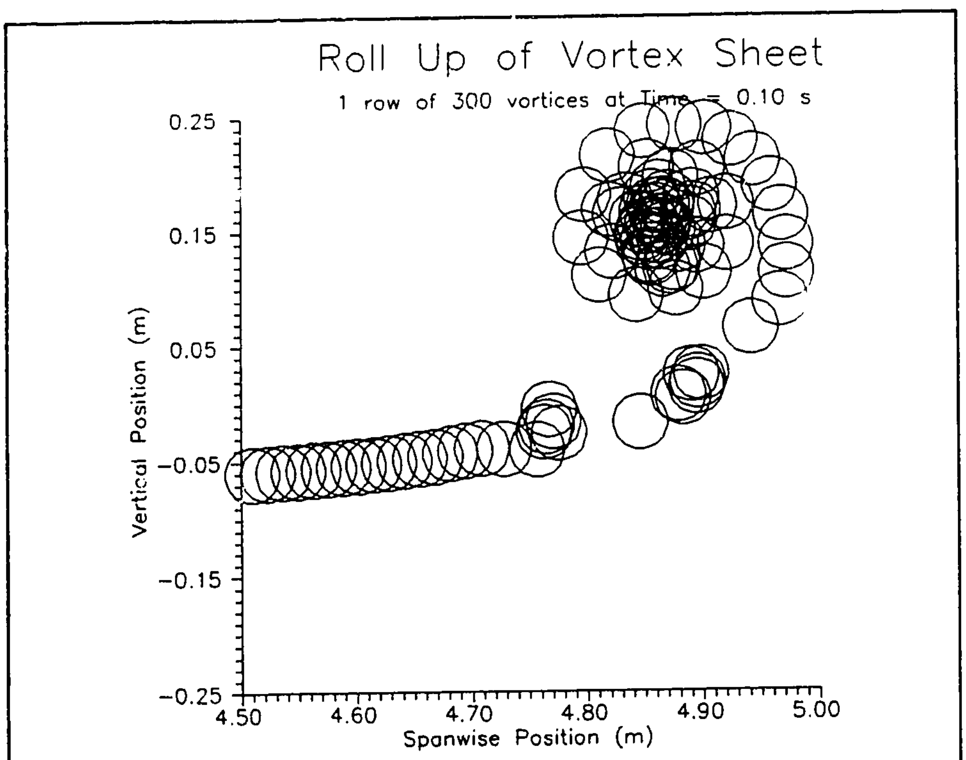

Figure 4.44 1 row of 300 vortices, b.l.t. = 0.050, at t=0.10s

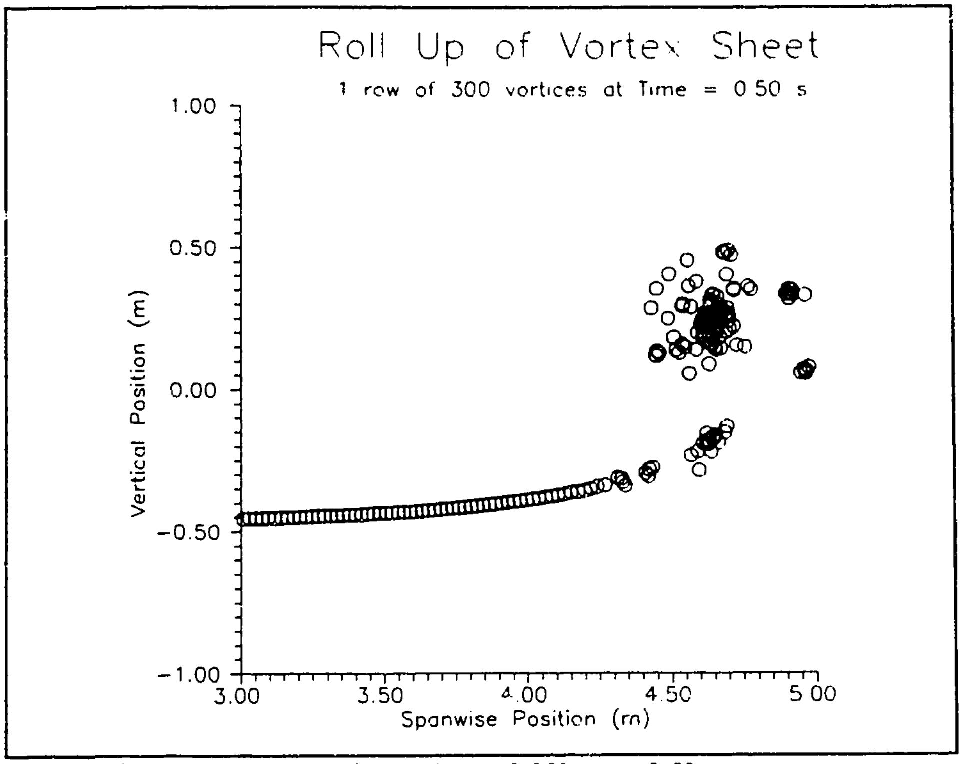

Figure 4.45 1 row of 300 vortices, b.l.t. = 0.050, at t=0.50s

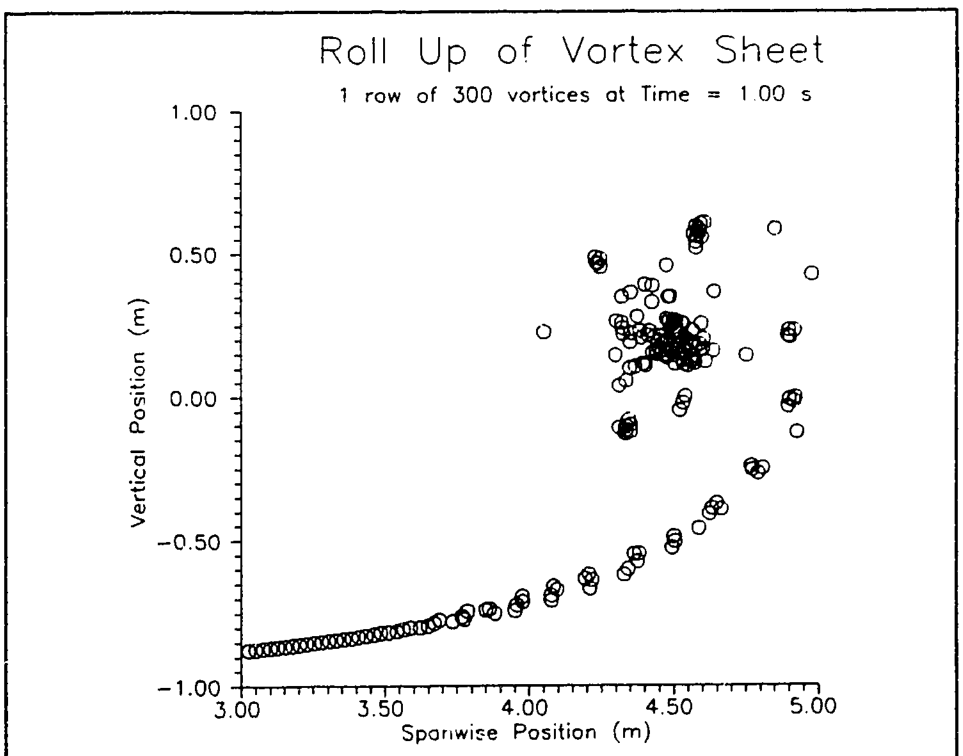

Figure 4.46 1 row of 300 vortices, b.l.t. = 0.050, at t=1.00s

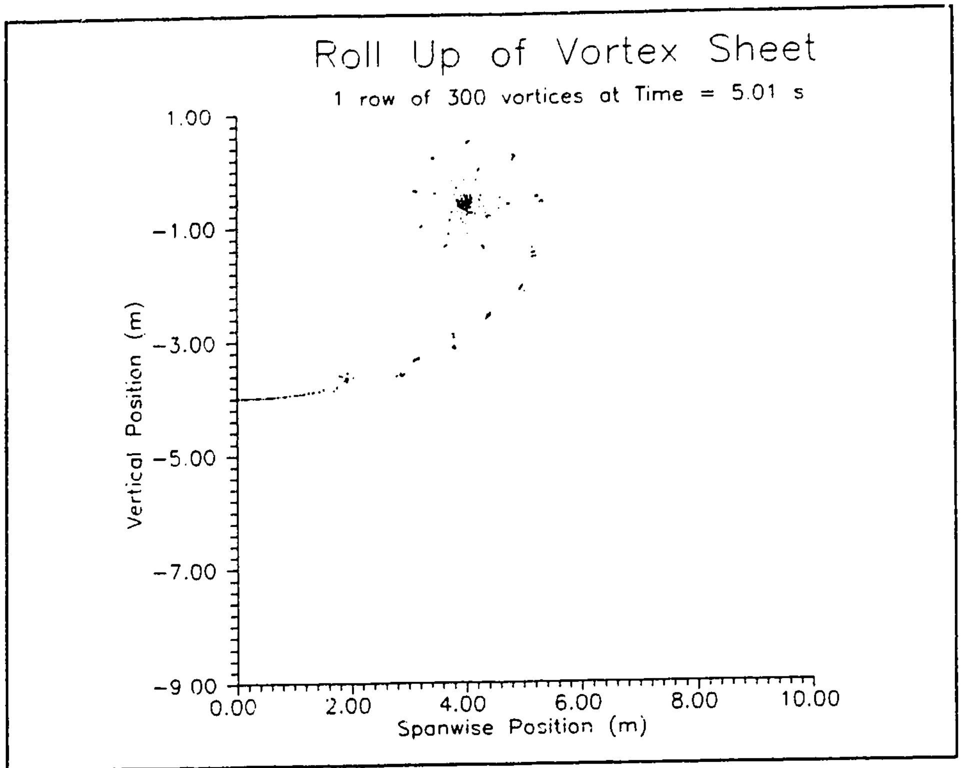

Figure 4.47 1 row of 300 vortices, b.l.t. = 0.050, at t=5.00s

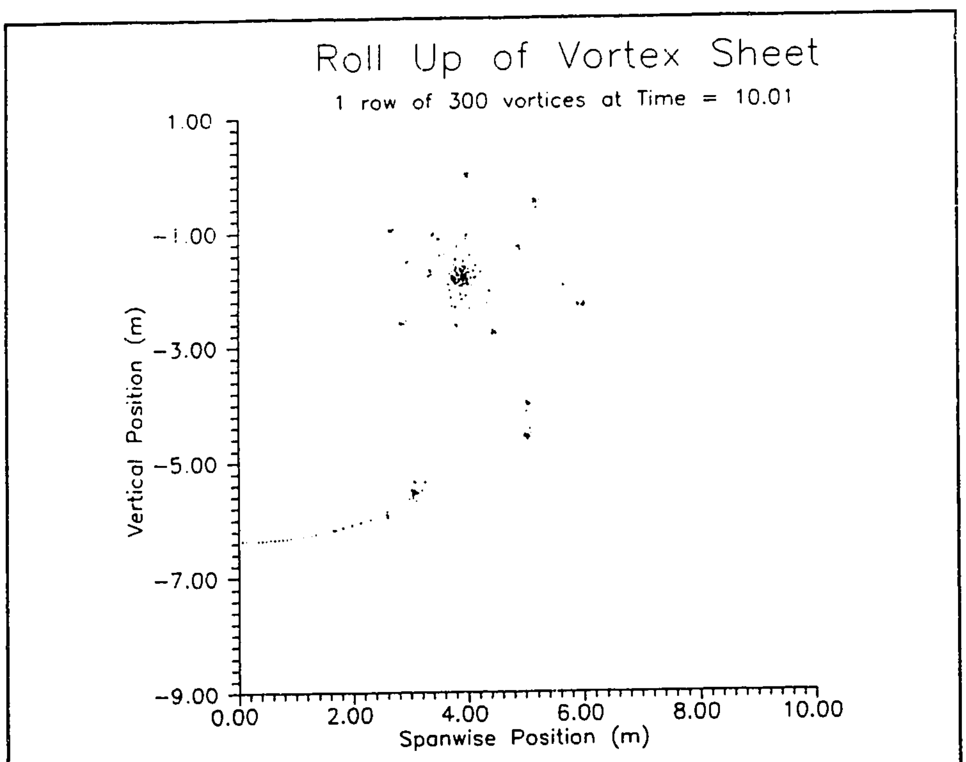

Figure 4.48 1 row of 300 vortices, b.l.t. = 0.050, at t=10.00s

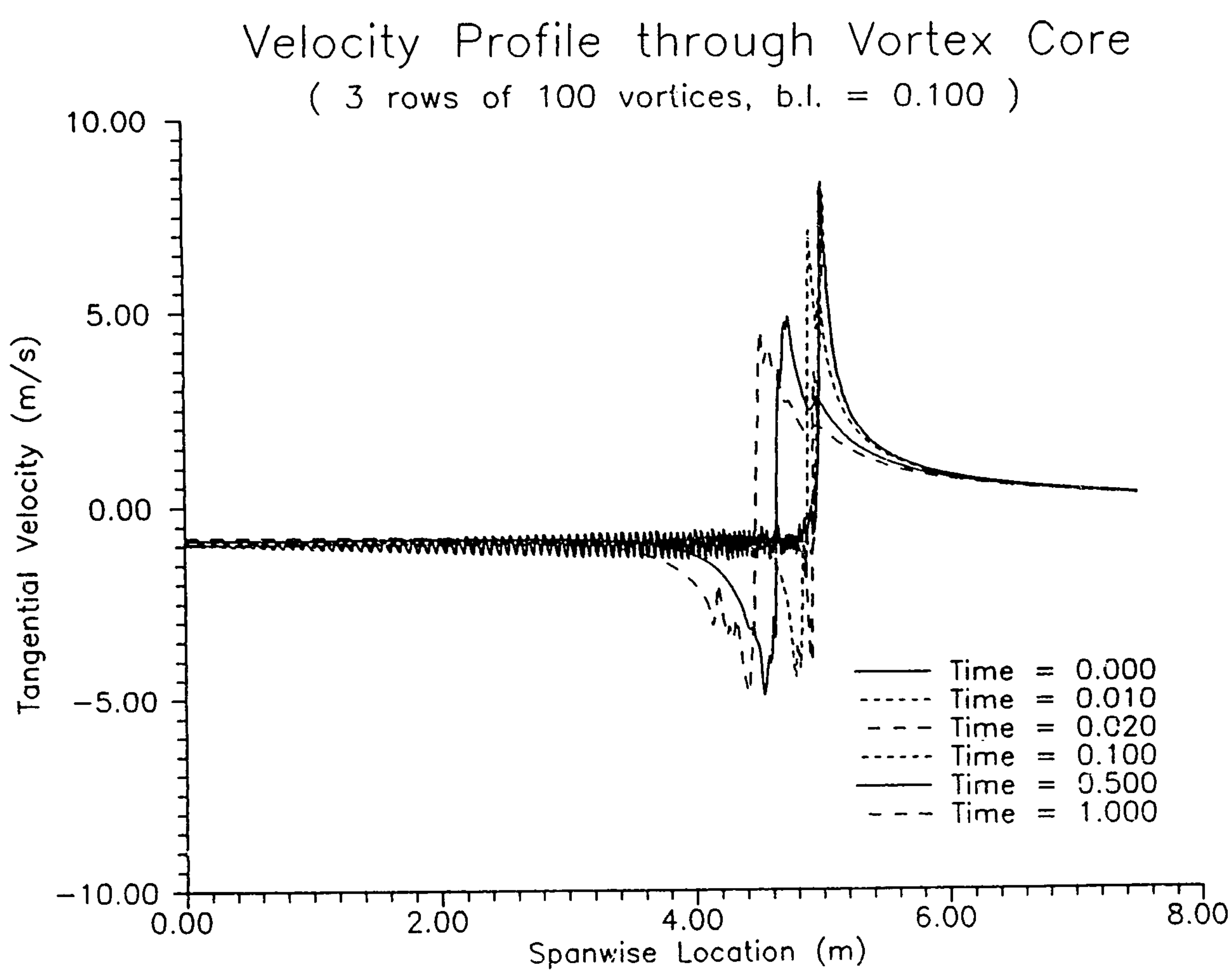

Figure 4.49 Velocity profile through vortex core using 3 rows of 100 vortices, and b.l.t. =0.100

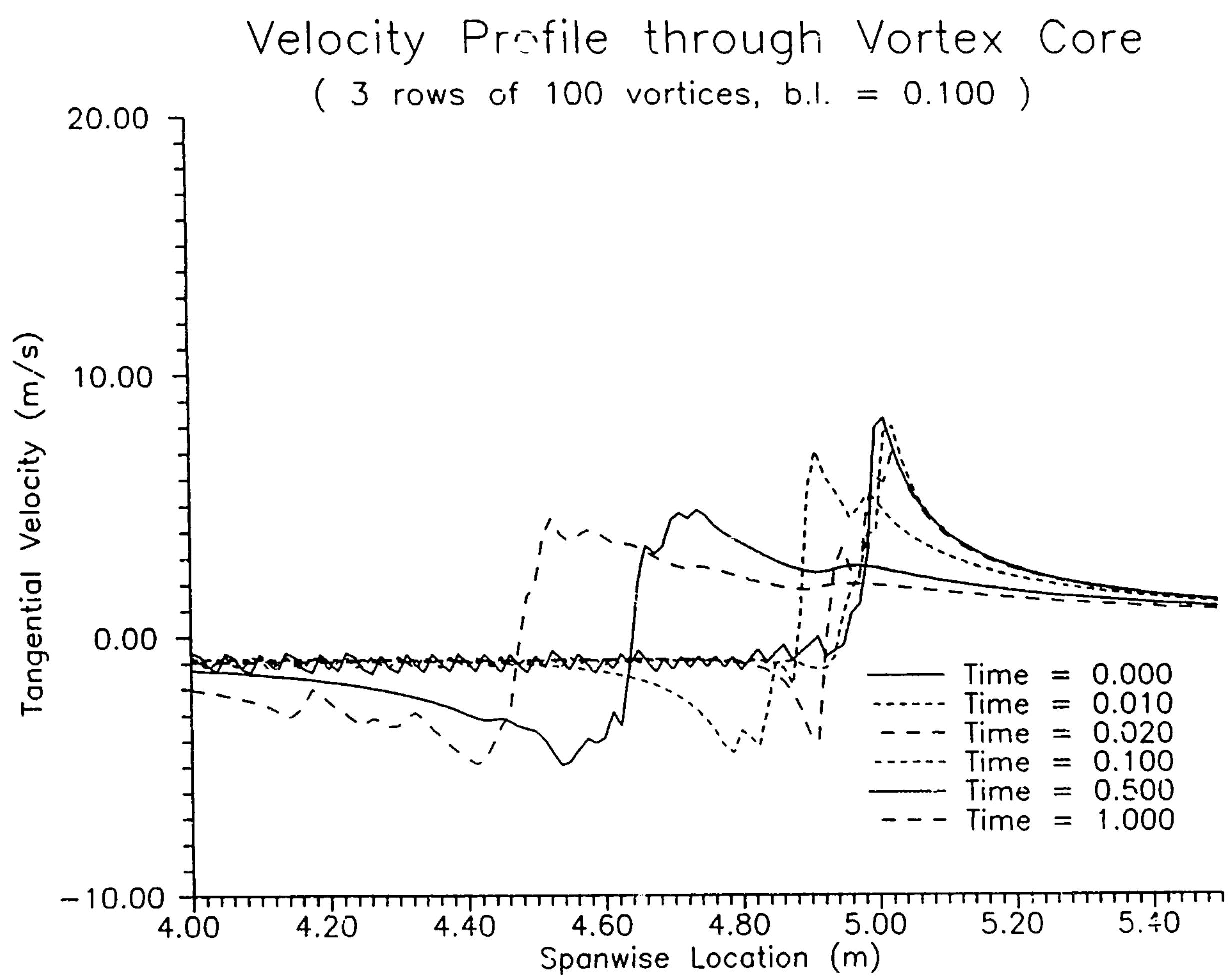

Figure 4.50 Velocity profile through vortex core using 3 rows of 100 vortices, and b.l.t.=0.100. View Zoomed in at tip.

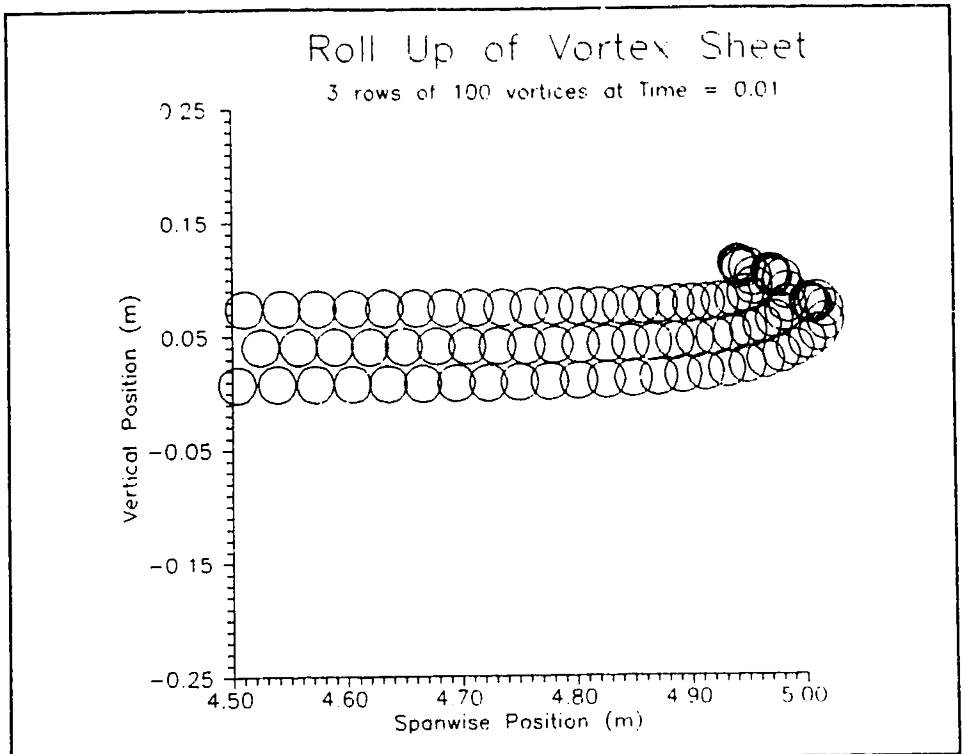

Figure 4.51 3 rows of 100 vortices, b.l.t. = 0.100m, at t=0.01s

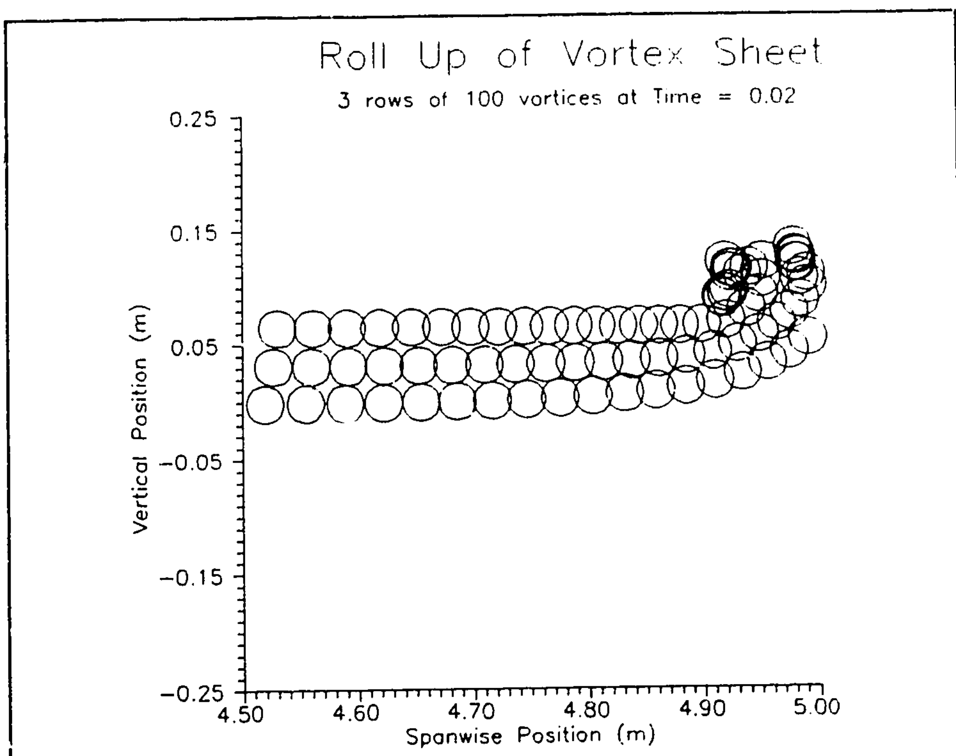

Figure 4.52 3 rows of 100 vortices, b.l.t. = 0.100m, at t=0.02s

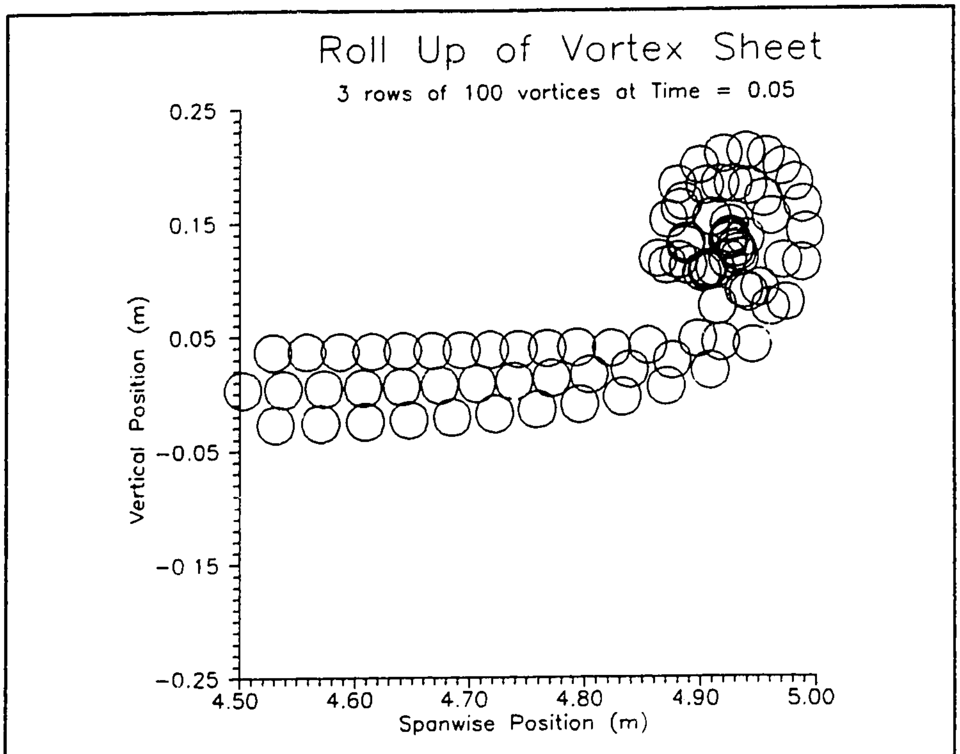

Figure 4.53 3 rows of 100 vortices, b.l.t. = 0.100m, at t=0.05s

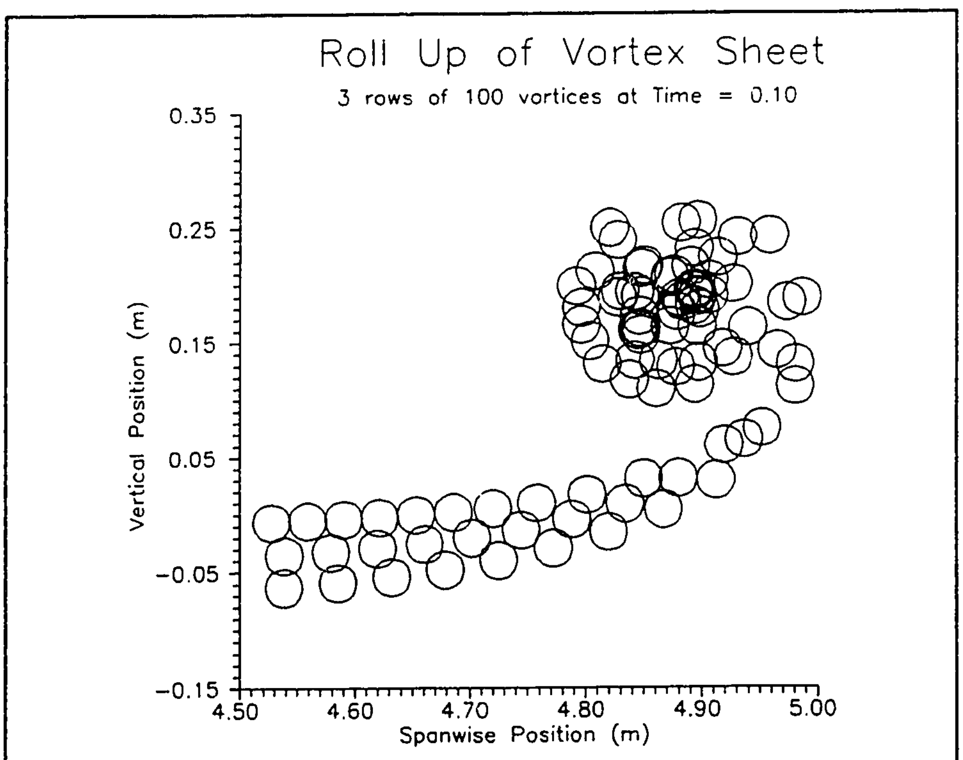

Figure 4.54 3 rows of 100 vortices, b.l.t. = 0.100m, at t=0.10s

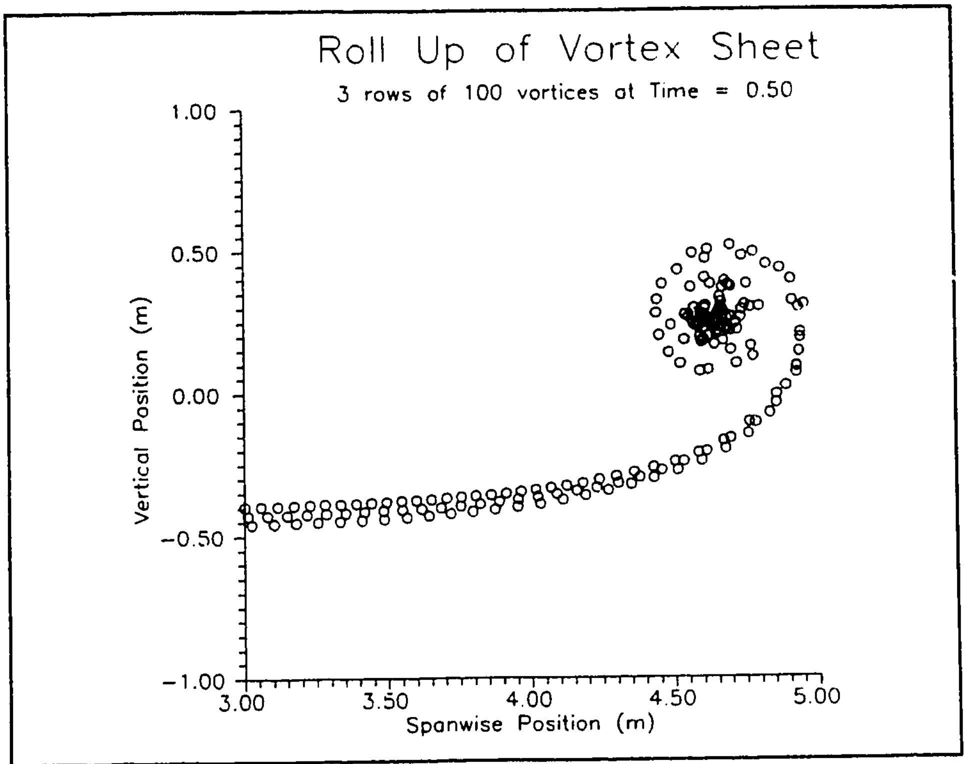

Figure 4.55 3 rows of 100 vortices, b.l.t. = 0.100m, at t=0.50s

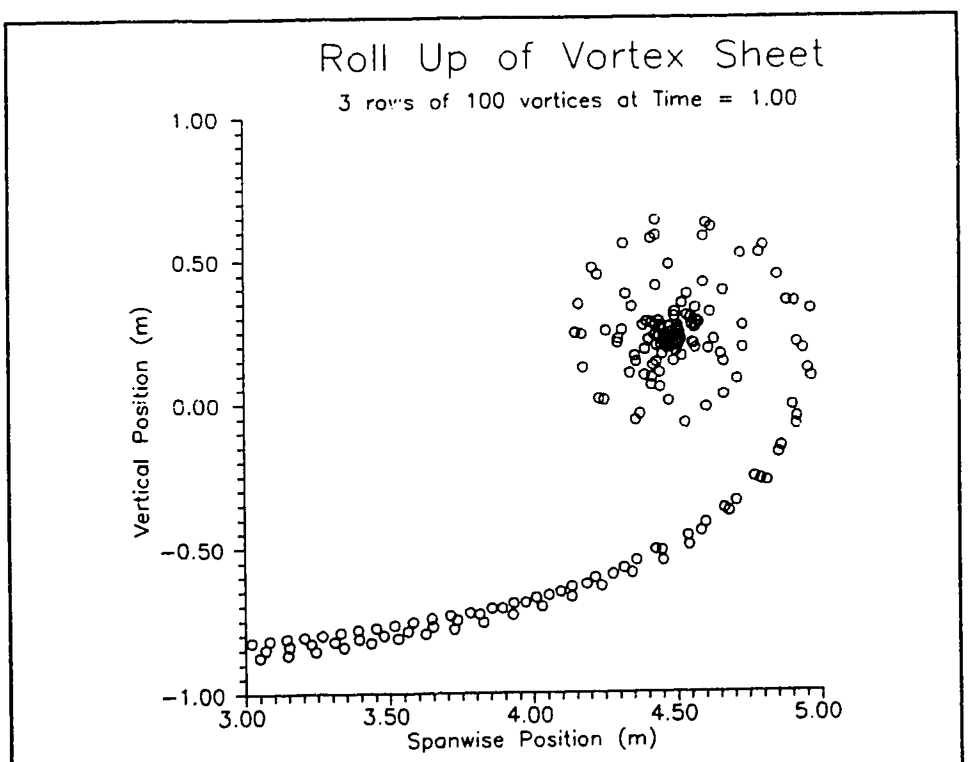

Figure 4.56 3 rows of 100 vortices, b.l.t. = 0.100m, at t=1.00s

CHAPTER 5

ANTI-ICING FLUID DEPOSITION on RUNWAYS[1]

5.1 INTRODUCTION

This research project involved the computer simulation of the movement of anti-icing fluid droplets in the wake of three aircraft which were considered typical for the Canadian operation during the use of anti-icing fluids. The focus was to determine the fluid movement and the resulting lateral distribution of the deposition of anti-icing fluid on the ground. The anti-icing fluid movement in the wake of these aircraft is modelled during the aircraft's take-off ground run. Finally the resulting fluid deposition on the ground surface is determined, giving the depth of the fluid and the distribution of the fluid on the runway and the adjacent ground surface. The researcher has developed programs for aircraft spanwise load distributions and for the spray movement and final deposition.

The three aircraft studied include the BOEING 737-300, BOEING 747, and the Airbus A320. Information regarding the spanwise wing loading for these aircraft within ground effect for representative phases of the take-off roll was unavailable. Hence, determining the wing loading for each aircraft composed the first phase of the research. For that phase, the aircraft wing geometry and performance was determined or specified for various conditions of the ground take-off run. This included the spanwise variation of the slat and flap deflections, giving the lift curve information for all spanwise locations. The wing geometry combined with the aircraft velocity data, the induced velocity field due to the wake (which was assumed rigid for the spanwise loading calculations), and the atmospheric conditions was sufficient to then determine the spanwise wing loading using a vortex lattice method.

Once the spanwise wing loading for each aircraft was calculated (based on a rigid wake, i.e. a trailing vortex system which was *not* rolling up), the wake roll-up and development was determined. The

---

1 A version of this chapter was presented at the 5th CASI Aerodynamics Symposium, Canadian Aeronautics and Space Institute 42nd Annual Conference, Montreal, Quebec. May 08-10, 1995.

method used represented the trailing vortex system (the aircraft wake) as a system of semi-infinite vortex filaments trailing from the wing. Then for the wake roll-up the vortex filament movement within the induced velocity field was modelled using an Explicit Eulerian approach.

Finally, the anti-icing fluid movement in the developing wake was calculated, using a Lagrangian method to track particle movement and deposition. For part of this study, the information concerning the drop size spectrum for the anti-icing fluid was unavailable. As a result, the assumption was made that the anti-icing fluid leaves the wing in droplet form in pre-determined sizes. Hence the simulations were done for fluid droplet sizes deemed to be representative of those typical for the temperature conditions during the fluid usage (drop diameters of 100μm and 200μm). Later in the study information concerning the dropsizes for both Type I and II anti-icing fluids became available for the BOEING 737 aircraft take-off run. Type I fluids gave drop diameters ranging from $\sim 150\mu$m to $\sim 213\mu$m and Type II fluids gave drop diameters ranging from $\sim 940\mu$m to $\sim 1110\mu$m at the two aircraft speeds modelled during the take-off run. This data was interpolated and extrapolated as needed to supply information for the Airbus A320 and the BOEING 747 take-off runs.

The final results of the research are in the form of anti-icing fluid particle movement (or droplet trajectory) plots, as well as plots of the ground deposition of anti-icing fluid laterally (i.e. in a spanwise direction) across the runway and adjacent areas. The plots showing the anti-icing fluid droplet movement trajectories, as well as the plots of spanwise distribution of anti-icing fluid were used as a means of evaluation. Final tabulated results show the amount of anti-icing fluid which lands on the 200 foot wide runway. The results are given as percentages of the initial fluid which leaves the aircraft at any location along the runway. As well, the calculations provided a measure of the amount of anti-icing fluid which can be considered to be lost as an aerosol to the atmosphere, again given as percentages of the initial fluid which leaves the aircraft at any location along the runway.

5.2 THE RELEVANT THEORY

5.2.1 Theory for the Wing Loading and the Trailing Vortex Wake

The vortex lattice method (VLM) was used to determine the wing loading and the development of the vortex wake. The reader is referred to Chapter 3 for a description of the VLM.

5.2.1.1 Vortex Sheet Roll-Up

This study considers the drop movement in the wake of the aircraft, therefore the roll-up and development of that trailing vortex sheet must be considered. Vorticity is first shed from the trailing edge region of the wing as a vortex sheet. The circulation distribution, $\Gamma(y)$, on a three dimensional wing is determined largely by the planform, airfoil shape, wing twist, and flap deflection along the span. Hence, those parameters of the wing determine $d\Gamma(y)/dy$, also. The vortex sheet starts to roll up at local maximums of $d\Gamma(y)/dy$ (Donaldson *et al.*, 1974). For conditions of a smooth planform and no flap deflection, the vortex sheet rolls up, starting at the wing tips, into two discrete vortices trailing the wing. With the flap deflection for take-off conditions, there is more than one center of vorticity roll-up in the near wake. The shed vortex sheet rolls up starting at the positions of the local maximum $d\Gamma(y)/dy$, specifically at the tips of the flaps and at the wingtips, into discrete vortices. These later amalgamate into a trailing vortex from each semi-span, giving the more familiar pair of counter rotating tip vortices one from each semi-span. Figure 5.1 shows a general idea of the vortex sheet roll-up for the conditions of a smooth planform and no flap deflection.

A wing with flap deflection will produce a multiple core vortex system, in the early stages. In these early stages of the wake development, the local centers of vorticity determine the local vortex core development. These vortex cores will wrap or rotate around each other in the wake. A feature to note with this multiple vortex is that when the vortices rotate around each other, alternately one vortex core then the other descends downward more than a single shed vortex would have. This is significant in the movement of fluid droplets near the ground plane. Later in the wake development downstream, the center of vorticity of the wing semi-span as a whole is dominant, and the multiple vortex cores merge to become a single vortex core per semi-span.

5.2.1.2 The Induced Velocity of a Vortex

The development and movement of the aircraft wake is determined largely by the induced velocity field of that wake (i.e. the shed vortex sheet). Also note that the movement of any anti-icing fluid drop is determined by this same induced velocity field. As will be discussed later, the trailing vortex filaments are modelled as semi-infinite line vortices, parallel to the longitudinal axis of the plane, with a Rankine core. The bound vortices are modelled as finite vortex elements.

5.2.1.3 Ground Plane Effects

For an aircraft free of nearby boundaries, the center of vorticity of each wing which is similar in nature to the center of gravity, would remain at a constant spanwise location during the roll up process. However, for the conditions concerning the anti-icing fluid movement, i.e. during the take-off ground run, the actual pattern of vortex sheet roll up is influenced greatly by the nearby ground plane. When an aircraft is near the ground, the presence of the ground restricts the downward airflow from under the wing. For theoretical equivalence the method of image vortices can be used. It should be noted that the image vortex method neglects the viscous effects concerning the lateral airflow outboard from under the wing, which may result in the production of secondary vortices. Under the image vortex method, the ground plane is modelled with a set of mirror image vortices (where the ground plane itself acts as a reflecting mirror). Thus, the method of image vortices is used to ensure zero normal flow through the ground plane, but also shows the increased spanwise outboard flow from under the wing. Image vortices mirror both the bound and trailing vortex system.

5.2.2 Theory for the Droplet Movement

5.2.2.1 Drag Theory As Applied To Droplets

The theory for drag on droplets has been quite well developed in the past few decades. This has been the result of research for the application of sprays using nozzles, and as a result of the desire to improve understanding of the formation and development of clouds in the atmosphere. For the purposes of this study certain assumptions are made about the anti-icing fluid droplets themselves. The majority stem from the fact that most droplets of concern with anti-icing fluid are less than 1200 microns in diameter, D_{drop}, as discussed later under drop size assumptins. Others are more related to the movement of the mass of the anti-icing fluid droplets after departure from the wing. Appendix 5.A gives a more complete coverage of the assumptions for the computer model for droplet movement.

There are two forces on the droplet which dominate its motion, that due to gravity and that due to drag. Hence the droplet movement is determined by these two forces and the inertia of the droplet. Gravity has the obvious effect of pulling the drop toward the ground. The drag force on the drops tend to move the drops along with the local airflow. The resultant drag force, D, on the droplet is due to the relative velocity of the droplet with respect to the air, V_{rel}. Since the droplets which are being considered are generally less than 1000 microns, they are assumed to remain perfectly spherical in shape. Note that the Type II anti-icing fluids produce drop diameters in the 1000 μm range, however only slight changes in the drag coefficient would occur. The non-spherical condition is neglected since the error introduced for that assumption is small in light of other approximations made in determining the size of the fluid drops. Consequently, the fluid drops can be treated as rigid spheres which simplifies the calculation of the drag coefficient of each drop, C_D. Under that assumption,

$$C_D = f(R_e) = f(\frac{\rho_{air} V_{rel} D_{drop}}{\mu_{air}}) \tag{5.1}$$

$$D = \frac{1}{2} \rho_{air} V_{rel}^2 C_D (\frac{\pi}{4} D_{drop}^2) \tag{5.2}$$

Note that the function for $C_D = f(R_e)$ is based on a steady state drop model. That means that the C_D used is for a drop at a constant R_e. The deceleration of the drop will have a small effect on the C_D, such that the C_D in the steady state case will tend to under predict the C_D of a decelerating drop. However, this is a very small amount and not entirely known, therefore the influence of the deceleration of the drop is neglected for calculations of the C_D. See Appendix 5.A for the equations used to determine the relation for $C_D = f(R_e)$.

Additionally, the assumption is made that each droplet of fluid leaving the wing is acted on independently of all other droplets. This means that the wake of one droplet does not affect the movement of the next droplet. This simplifies the individual droplet drag calculations so that each droplet is treated as being the only droplet in the wake.

5.3 THE COMPUTER MODELS

The research involved the computer simulation of anti-icing fluid movement in the wake of three aircraft. The modelling was done in two stages. The first stage involved determining the wing spanwise loading for each of the aircraft. Based on that spanwise load distribution, the trailing vortex wake was modelled for each of the aircraft at two speeds representative of their take-off ground roll. (These two speeds were chosen based on an approximate speed at which the anti-icing fluid first started flow-off and another speed just prior to rotation.) The second stage involved the anti-icing fluid movement simulation. The fluid droplet movement in the aircraft wake was calculated by using data generated concerning the vortex wake development from the first program. The following pages briefly describe the two programs. Appendix 5.B provides information regarding the program which is used and the input and output files.

5.3.1 The Computer Model for the Aircraft Wing Loading and the Wake

5.3.1.1 The Aircraft Wing Loading and the Vortex Lattice Model

The model used for determining the aircraft wing loading is a simplified vortex lattice model with a rigid wake. By the term "rigid wake" it is meant that the trailing vortex filaments remain in their initial positions attached to the wing and trail off to infinity. Hence, the induced velocity field used in determining the wing loading is that due to those trailing vortices while attached to the wing. Figure 5.2 shows the main set up of the vortex lattice system on the wing. The wing spanwise circulation distribution and loading is determined by simultaneous solution of the equations for $l(y) = \rho V\Gamma(y)$; where $\Gamma(y)$ is dependent on $C_\ell(y)$ which is dependent on the induced velocity at y, which is itself dependent on $\Gamma(y)$. The total circulation contained in the system of trailing vortex filaments from each wing is equal to the total circulation generated by the wing. The local circulation at any spanwise location of the wing is considered to be produced by the bound vortex element, which is a vortex element located at 25 percent chord of that spanwise element. The spanwise extent of each bound vortex element is determined by the initial spanwise separation of the two trailing vortex filaments, where the initial separation is determined by the spanwise discretization method. The one vortex filament trails off the inboard side of the spanwise element, while the other vortex filament trails off the outboard side of the spanwise element. These trailing vortex filaments are attached to the wing at 25 percent local chord so as be continuous with the bound vortex elements.

The aircraft wake model is based on a standard take-off operation such that each aircraft is travelling along the runway *prior* to rotation. As a result, the aircraft is *not* producing lift equal to its weight and the aircraft is basically level with the ground while it is travelling during the ground roll. This means that the angle of attack of the wing is determined by the wing incidence, along with the aircraft velocity and the induced velocity field generated by both the bound and the shed vorticity, and the image vortex system. Note that any headwind component is neglected and only the crosswind component is taken to be a concern. The instantaneous aircraft speed is used to determine the conditions at a given position along the take-off run. The spanwise loading is determined by the spanwise circulation distribution and a rigid wake. Then once the loading is determined, the wing sheds vorticity which rolls up starting at the positions of maximum rate of change of circulation with spanwise location, specifically at the tip of the flaps and at the wingtips into discrete vortices which then amalgamate into two counter rotating tip vortices, one from each wing semi-span.

5.3.1.2 **The Trailing Vortex Wake Model**

Once the spanwise loading is determined the discretized trailing vortex sheet is then allowed to roll-up beyond the trailing edge of the wing. The movement of the trailing vortex filaments was modelled using an Explicit Eulerian approach. Fluid theory shows that the vortices in a fluid will be convected with the induced flow field. The induced velocities are calculated in the same manner as given in Appendix 3.A and Chapter 3 (section 3.2.1.3) for the induced velocity of a vortex. Therefore, for the trailing vortex wake movement, the air velocity at each vortex filament is calculated for the positions where the vortices are initially located, then the trailing vortex filaments are moved to their new position at the end of the time step, Δt, and so on.

5.3.1.3 **The Ground Plane Model**

As indicated earlier, the ground plane is modelled using the image vortex method. Although the actual runway will have a slight crown, the assumption is made that the ground plane is a flat horizontal plane. For this method, image vortices are used which are of the same magnitude but opposite sign to that of the real vortices. These image vortices are located on a line which runs perpendicular to the ground surface through the real vortices, and at a distance below the ground surface equal to the perpendicular distance of the real vortex above the ground plane. Thus, the method of image vortices is used to ensure zero normal flow through the ground plane. At the same time there is an increased spanwise outboard flow from under the wing. Image vortices mirror both the bound vortex elements and each of the vortex filaments in the trailing vortex system. Hence, the resultant induced velocity field which affects the wake development and the anti-icing fluid movement is due to the total number of real plus image vortices modelled.

As discussed in the literature review of Chapter 2, trailing vortices in the vicinity of the ground plane cause the formation of secondary vortices. However, since these seem to be most relevant for longer time frames than for the movement of most anti-icing fluid drops, the influence of the secondary vortices and the vortex bounce phenomenon is not included in this study.

5.3.1.4 **Tail Plane Effects**

For this model, the effects of the tail are neglected. Hence, in both the computations for the wing loading and the trailing vortex wake, as well as those for the anti-icing fluid movement in the wake, the vortex system from the tail is not considered. The tail rudder is assumed to be in a neutral position, even for crosswind take-off conditions. In that case the rudder will produce no side loads and hence shed no wake. As well, during the ground roll for each aircraft considered for this report, the assumption is made that the horizontal tail plane is not producing any lift, positive or negative. In flight, the tail produces a negative lift force as a consequence of longitudinal stability requirements. As a result of the negative lift, a vortex system will develop, similar in nature to that of the main plane, but of opposite sign. The wing must produce an additional amount of lift to counter the negative lift of the tail. Hence, the lift of the wing can be considered to be equal to the all up weight of the aircraft, and the increased circulation of the wing will be cancelled by the circulation of the tail. The effects of the tail plane of a conventional aircraft, on the wake of the aircraft, can usually be neglected since the contribution is small compared to that of the main wing (in the order of 10 percent).

5.3.1.5 The Fuselage Effects

In the computations for the wing loading and the vorticity distribution, the fuselage for the each of the aircraft is modelled in that the wing is considered to extend through the fuselage. However, the fuselage is not considered to produce significant lift. Hence, the wing lift is decreased linearly from the wing root to the aircraft centerline.

Another significant effect of the aircraft fuselage would be to shelter or block crosswind effects on droplets before they have passed the tail of the aircraft. The blocking effect of the fuselage on the crosswind is unknown and entirely neglected in this model. As a result, the fluid droplets will be affected by any crosswind immediately after leaving the wing.

5.3.1.6 The Aircraft Engines

The aircraft engines produce the thrust to propel the aircraft. Hence, obviously, the engines produce localized but strong longitudinal air velocities. However, for the purposes of this study the longitudinal displacement of the anti-icing fluid along the runway is not of any significant concern. Also concerning the engines, although not strictly true, the lateral air flow is treated as independent of the longitudinal air flow due to the engines. Some lateral or crossflow velocities may be associated with the large rate of air entrainment due to the jet engines on these aircraft. However, this information was unavailable for the current study. Also, in light of other approximation made for this study, the effect of the jet engines on the lateral dispersion of anti-icing fluid is not likely significant, hence neglected for this study.

The aircraft engines may have an influence on the drop sizes in the regions near the jet efflux. The high velocity fields generated may contribute to break up any large droplets that may leave the wing. Since no information was available concerning this phenomenon, this factor is neglected in the model. Therefore, the fluid droplets are assumed to remain constant in diameter after the anti-icing fluid flow-off.

5.3.2 The Computer Model for the Droplet Movement

5.3.2.1 Fluid Droplet Movement

The computer model for the fluid drop movement is based on a Lagrangian method. The essence of the Lagrangian method is that each of the fluid drops or particles is stepped through space in discrete increments of time. For each drop simulated, at each time step the drop's position and velocity are used to determine its acceleration. Then the drop is stepped to its next time step location using the acceleration and velocity at the previous location. Note that this is done for each and every drop until the end of the simulation. Hence, approximately 1000 drops are used to represent the fluid shed from the wing, then the results can be scaled linearly to fit any actual flow-off rate and aircraft velocity.

The initial conditions (location and velocity) for each drop simulated are determined by the point of release of the drop from the wing. Then drop location is used to determine the induced velocities at that drop. The relative velocity of the drop to the air at the drop location is determined by the drop velocity combined with the induced velocities and crosswind. The relative velocity is then used to calculate the drop's Reynolds number and then the drag *coefficient* for each drop. From that the drag *force* on the drop is calculated. Then the drop *acceleration* and a new drop velocity and location calculated for the end of that time increment.

A Runge-Kutta fourth order method is used for the integration. The efficiency is not the best for a fixed time step. However, for use in this model a variable time step is employed. The time step is modified based on the change in the droplet Reynolds number each time interval. Continually making the time step size modification allows the method to be reasonably fast while still maintaining accuracy of drop movement.

5.3.2.2 Induced Air Velocity at the Droplet Position

The induced air velocity at each drop location is calculated in the same manner as that for the induced velocity for the wake development. Thus, the number of calculations per drop is proportional to the number of trailing vortex filaments (and bound vortex elements). This reason required using a minimum number of trailing vortex filaments which would give a satisfactory measure of span loading, while yet being manageable for the drop movement calculations. The calculations for the wing loading and the wake development was done using 45 vortices per semi-span.

In the near wing condition, all components of vorticity are used to determined the induced flow field at a drop. However, in order to improve computational speed the model was simplified once the drops were a significant distance behind the aircraft. After a short time of modelled drop movement (two seconds, somewhat arbitrarily chosen) the influence of the bound vortex elements is neglected. The contribution from those elements is very small at that time and the calculation of that insignificant contribution is expensive computationally (that being even more than for the trailing vortices). For instance, after two seconds the BOEING 737-300 will have moved forward 79 m at the lower speed and 113 m at the higher speed. Recall that the induced velocity for a vortex decreases as 1/r. Therefore, the induced velocity due to the bound vorticity (which are finite length vortex elements) will be much less than that due to the trailing vortices which are acting almost like infinite line vortices at that time *and* typically have their axis closer to the drops in the more distant wake.

5.3.2.3 **Deposition Calculations**

The anti-icing fluid drops are tracked until they hit the ground or for the first 20 seconds of their modelled movement, which ever comes first. The time of 20 seconds is used since it was found that at that time most significant drop movement was complete. The drops which do not impact the ground plane in the first 20 seconds are considered to remain airborne and are lost to the atmosphere. During the simulation, the location of each droplet is recorded every 0.25 seconds of modelled time, and used later to plot the drop trajectories for each aircraft and configuration. Finally, the lateral deposition of the anti-icing fluid is calculated for the drops which landed and were deposited on the ground. This information is then used to plot the spanwise deposition patterns, and then tabulate the percentage of the initial fluid which lands on the runway and the percentage of the initial fluid which is considered lost.

5.3.3 Computer Model Verification

The simulation of the anti-icing fluid movement involves two distinct problems, the wing loading and vortex wake roll-up, and the fluid drop movement within that wake. Therefore the verification of the computer model is done in two steps. The first will examine the validity of the calculated wing loading, the shed vortex wake and the ensuing vortex wake development. The second examines the movement of the anti-icing fluid drops within the velocity field of the vortex wake and the atmospheric influence.

5.3.3.1 **Aircraft Wing Loading and Vortex Wake Model**

Determining the wing spanwise loading for each of the aircraft was the first step towards calculating the drop movement. However, each aircraft uses airfoils developed by the respective companies and thus due to the proprietary nature of the information, the exact data concerning the lift curves for various take-off flap settings was not available. Hence, as will be discussed further in the section concerning conditions modelled, the performance of the aircraft wings was approximated by specifying the lift curves at the different spanwise locations.

The flap settings for each of the aircraft was determined by consulting the Aircraft Flight Manual or Operations Manual for the respective aircraft. Appendix 5.C gives all of the information needed and used for the simulation of each of the aircraft.

The calculated wing loading is as expected for these aircraft under these take-off conditions with the flap settings chosen. As well, as shown in Appendix 5.C the calculated C_{Lmax} at the stall speeds corresponds well with information gleaned from other references concerning each of these aircraft. This reasonable correlation lends credibility to the results of this portion of the computer model dealing with calculating the wing loading. Further discussion is given in the results section, later.

The initial vortex wake structure is dependent on the wing loading. The ensuing wake development is then dependent on the initial vortex wake structure and its self-induction within ground effect. The results section shows samples for these aircraft, which are consistent with other works in the related area of aerial spraying. The results here are consistent with those found by Donaldson *et al.* (1974) for a wing with flaps, although those results do not include any ground effect.

Note that the phenomenon of the wake movement while the aircraft is still on its ground roll is not typically modelled. The usual case is to model the wake development in free flight conditions far from the influence of the ground plane. Occasionally, modelling of the wake is done for spraying conditions where the aircraft is flying near but still above the ground.

5.3.3.2 **Drop Movement Model**

Precise verification of the model is difficult since this appears to be the first computer simulation research to be done examining the ground deposition of anti-icing fluid. Some very crude observation of ground deposition has been made, however actual measurement of depth of deposition has not yet taken place. These two reasons were the main motivation for this phase of the research program. (Note that funding for this research and much information was made available by the Dryden Commission of Transport Canada.)

Comparisons with existing data from aerial spraying operations research is of limited usefulness. However, some will be done to give a qualitative confirmation of the reasonableness of the results.

The work by Morris, *et al.* (1984) shows some experimental deposition information for an AgTruck aircraft. The reasonableness of modelling aerial spray deposition even using a very simple horseshoe vortex system has been shown by Merkl (1989). That study examined a spray aircraft which was considered to have simple wing geometry with no flap deflection. Merkl (1989) showed that spray deposition could be reliably modelled with a much simpler model. This was because the spray movement happened after much of the vortex system had rolled up in to the two trailing vortices.

For a previous model used by the author (Merkl 1989), the trailing vortex system was modelled using discrete trailing vortices located at an initial separation given by the center of vorticity for the wing. That research involved aircraft with simple wing geometry and no flap deflections, such that single vortices were produced from each wing. The time for vortex sheet roll up is significant, but with regards to the average time for droplet movement it could be neglected. The separation of the trailing vortices could be calculated exactly, for aircraft of various loadings. For example, in *unconfined* flow conditions, ie. far from the ground, for an elliptically loaded wing the initial lateral vortex spacing is $(\pi/4) \times$Span or about 78% Span. Using that method provided very good correlation with actual spray deposition results from NASA research using a Cessna AGtruck spray plane (Merkl, 1989). Using the improved distribution of discretized trailing vortex filaments has enhanced the accuracy of deposition calculations.

Some of the reasons will be presented for the differences between the current problem of anti-icing fluid deposition and that of aerial spraying.

Some of the differences involved are concerning the aircraft used. For aerial spraying operations the aircraft are generally (if not always) flown in a clean configuration. That means that the spray aircraft have flaps retracted, producing a relatively simple geometry and wing load function. The aircraft which are studied here are typical of those used when anti-icing fluid is applied. These are the BOEING 737-300, BOEING 747, and Airbus A320. For the condition of take-off ground run the aircraft will invariably have their flaps deployed for take-off position. The two BOEING aircraft use a triple slotted trailing edge main flap and a leading edge slat. The A320 uses a single slotted trailing edge main flap and a leading edge slat. These complex geometries produce a much more complex trailing vortex wake. Of particular note is that the wing loading over the region of the main flaps will be substantially increased with the flaps deployed. This will produce a strong gradient in the circulation distribution on the wing and hence lead to a strong trailing vortex at that location. In contrast, the simple wings of the typical spray plane will typically have the strongest vortex develop in the wing tip region. This will have significant ramifications for the movement of drops in the wake.

Another factor is that in the anti-icing fluid deposition study all of the aircraft are jet aircraft. Aerial spray aircraft are predominantly propeller driven. The jet engines of the jet aircraft are designed to produce thrust with minimum swirl velocity since that would be a waste of energy. However, the propeller produces a significant swirl velocity in its wake. This propwash has a significant effect on the spray movement. The effect is generally countered by asymmetric nozzle placement on spray planes. Comparison with aerial spray results would necessarily have to consider this very significant phenomenon.

The matter of the fluid distribution is also a problem for consideration. For an aircraft with the anti-icing fluid applied the fluid distribution is intended to be of uniform thickness over the entire wing. Assuming that the fluid flows in the chordwise direction and off the trailing edge of the wing, this means that the volume of fluid flow-off at any spanwise location is dependent on the wing chord at that location. For spray operations, the spray is typically released much more uniformly across the span of the wing. The result is that the case of the anti-icing fluid will produce a much greater deposition near the centerline or wing root.

The location for initial anti-icing fluid flow-off is not clearly known. Most of the fluid flows off at the trailing edge of the main section of the wing chord, and some leaves from the flap region and trailing edges. For aerial spraying, nozzles are typically attached below and perhaps behind the trailing edge of the wing. The distance may be as much as 0.5m below the wing trailing edge. This difference has a lot of impact on the initial air velocity to which the drops are subjected.

The anti-icing fluid flow-off velocity is basically in the local freestream direction and the magnitude is much less than that of the free stream velocity. The spray plane nozzles impart a predetermined initial velocity to the spray. The significance is that the initial velocity is usually not in the free stream direction.

The drop sizes of anti-icing fluids in flow off are also a matter of some uncertainty. However, the study examined cases using the recommended sizes and also used some hypothetical sizes ranges in order to broaden the research results.

5.4 CONDITIONS MODELLED

Now that some of the background theory and computer models have been considered, the specific conditions and variables which were modelled will be examined in greater detail. These conditions include those involving each of the aircraft, the anti-icing fluid and its movement and deposition, and the atmospheric conditions. For each of the aircraft the general performance conditions are given, as well as the airfoil data for the wing sections, and the take-off flap and slat settings. For the anti-icing fluid, consideration was given to the initial fluid distribution on the aircraft, the initial conditions for the fluid drop movement, and various other conditions pertinent to the drop movement. Next, the specifics involved in determining the anti-icing fluid spanwise deposition patterns are considered. Finally, the atmospheric conditions are dealt with which are of concern to the fluid movement.

5.4.1 Aircraft Variables and Conditions

5.4.1.1 Aircraft General Conditions

Three aircraft are modelled which are considered to be typical of those used in the Canadian operation during the use of anti-icing fluids. These are the BOEING 737-300, BOEING 747, and the Airbus A320. The aircraft were modelled in typical take-off configurations during their respective ground rolls. Table 5.1 summarizes the conditions modelled. (The complete sets of information and statistics which were used to model the each of these aircraft is given in Appendix 5.C)

The aircraft were modelled at a *typical* take-off weight as determined from the Operations or Flight Manuals for each of the aircraft. Note that the weight is not necessarily the maximum take-off weight for the conditions, but merely an upper range value for the weight which was thought to be representative for the conditions typical for the periods of operation during the use of anti-icing fluid.

Considered next were the two ground roll speeds used for each aircraft. For each aircraft a low speed of 75 knots was used since the early stages of anti-icing fluid flow-off typically occur at least by that speed. The other speed is different for each aircraft. The higher speed for each aircraft is one which is *lower* than the rotation speed, V_R, but higher than the aircraft stall speed gear up, V_S. For the BOEING 737-300, that speed is 56.625 m/s (110 kt). For the BOEING 747, that speed is 77.216 m/s (150 kt). For the Airbus A320, that speed is 66.921 m/s (130 kt). The higher speed is used since the anti-icing fluid is required to be essentially off the wing prior to lift off. Hence, these two speeds bracket the range of concern for the anti-icing fluid movement. (Note that the odd values for the speeds given in SI units are used to equate to the speeds given in Imperial units.)

Table 5.1: Aircraft and Basic Conditions Modelled.

Aircraft	Velocity	Take-Off Mass (Weight)	Flaps δ_f
BOEING 737-300	V = 56.625 m/s (110 kt) V = 38.608 m/s (75 kt)	47 000 kg (460 913 N) (103 617 lb)	15°
BOEING 747	V = 77.216 m/s (150 kt) V = 38.608 m/s (75 kt)	335 658 kg (3 291 681 N) (740 000 lb)	10°
Airbus A320	V = 66.921 m/s (130 kt) V = 38.608 m/s (75 kt)	70 000 kg (686 466 N) (154 324 lb)	15°

5.4.1.2 Airfoil Data for the Wing Sections

Each of the aircraft studied use airfoils developed by the respective companies. Due to the proprietary nature of the information, the exact data concerning the lift curves for various take-off flap settings was not available. Hence, performance of the aircraft wings was approximated by specifying the lift curves at the different spanwise locations. Some information was gleaned from papers presented at the AGARD Symposium on High-Lift Systems Aerodynamics (AGARD CP-415), October 1992. Those papers included the ones by Flaig and Hilbig (1992), and others. Also, data regarding the performance of a single slotted flapped airfoil has been acquired in past studies in the University of Alberta wind tunnel. Data from the University of Alberta wind tunnel shows that a value for $C_{Lo} \simeq 1.7$ is not unreasonable even for a single slotted flap at a flap angle, $\delta_f = 15°$. The leading edge slats affect the maximum lift coefficient, C_{Lmax}, of the wing section but are considered to not affect the zero angle of attack lift coefficient, C_{Lo}. For a particular airfoil section, neither the slat nor flap settings significantly influence the lift curve slope, $dC_L/d\alpha$, however the flaps do affect the zero incidence lift coefficient, C_{Lo}, and they both affect the maximum lift coefficient, C_{Lmax}. The data sets for each of the aircraft reflect this.

5.4.1.3 The Take-Off Flap and Slat Settings for the Aircraft and the Corresponding Airfoil Data

The flap settings for each of the aircraft was determined by consulting the Aircraft Flight Manual or Operations Manual for the respective aircraft. A typical take-off loading was considered. The trailing edge flap settings were determined for the modelled take-off load. For each of the aircraft, the leading edge flap or slat settings are controlled by the flap settings and are not independently controlled. Once the spanwise slat and flap settings were determined, that 2-Dimensional information was used to designate the lift curve slope, $dC_L/d\alpha$, the zero incidence lift coefficient, C_{Lo}, and the maximum lift coefficient, C_{Lmax} for each of the spanwise wing sections. Table 5.2 gives the airfoil data used for determining the wing spanwise loading.

Table 5.2: Aircraft Spanwise Airfoil Settings and Data.

Aircraft	Wing Spanwise Section and Flap Settings	$dC_L/d\alpha$	C_{Lo}	C_{Lmax}
BOEING 737-300	on the main flaps (a triple slotted flap) at δ_f = 15°	6.1	2.00	4.0
	Outboard of the flaps, but still where leading edge slats are used	6.1	0.50	3.0
	Outboard of ailerons and leading edge slats	6.1	0.25	2.5
BOEING 747	on the main flaps (a triple slotted flap) at δ_f = 10°	6.1	1.80	4.0
	Outboard of the flaps, but still where leading edge slats are used	6.1	0.50	3.0
	Outboard of ailerons and leading edge slats	6.1	0.25	2.5
Airbus A320	on the main flaps (a single slotted flap) at δ_f = 15°	6.1	1.70	4.0
	Outboard of the flaps, but still where leading edge slats are used	6.1	0.50	3.0
	Outboard of ailerons and leading edge slats	6.1	0.25	2.5
	On vertical winglet	6.1	0.25	2.0

As noted in the previous section, the airfoil data was proprietary to the companies, therefore the C_{Lmax} values given here were chosen due to uncertainty of the actual values. However, as will be shown in the results, for the ground roll conditions that were modelled, the local wing section C_ℓ values did not reach or approach these specified C_{Lmax} values.

Appendix 5.C gives the overall lift coefficients for each of the aircraft as a whole. These are calculated based on the exposed wing area with flaps retracted, *not* the gross wing area.

5.4.2 Anti-Icing Fluid Considerations

The following sections discuss considerations and assumptions concerning the anti-icing fluid and its movement which were not covered in the discussion of the particle-wake interaction computer model.

5.4.2.1 Initial Fluid Distribution on the Aircraft Wing Surfaces

During aircraft operations in the conditions requiring anti-icing fluid usage, the anti-icing fluid is sprayed onto the upper surface of an aircraft wing with an attempt to maintain a uniform thickness of the layer (approximately 0.030 in (0.76 mm)). As a result, the volume or mass of fluid which leaves the wing at any spanwise location along the trailing edge is directly proportional to the area from which that fluid originates. For this research the assumption is made that the fluid at any spanwise location simply moves longitudinally along the chord of the wing and there is no spanwise fluid flow on the wing. The fluid then flows off at the trailing edge of the main wing and the trailing edges of the flaps. For the simulation, this means that the mass of fluid leaving the wing is dependent on the local chord. Also, the variation of the mass flow-off rates as a function of location along the span and time were not available for this study. Thus the assumption was made that fluid would flow off all locations along the entire wing span regardless of the aircraft location along the runway.

5.4.2.2 Initial Droplet Locations and Velocities

The initial conditions which govern the movement of the anti-icing fluid drops include the initial locations of the drops in 3-dimensional space and the initial velocities of the drops as they leave the wing of the aircraft.

As indicated above, the initial spanwise locations for the anti-icing fluid drops are governed by the distribution of the mass of the fluid on the wing. (See additional comments under section: Anti-Icing Fluid Drop Sizes.) Then the anti-icing fluid droplets leave the wing from the trailing edge region. Actually most of the fluid may leave the wing at the junction of the main wing and flaps (as observed in video footage from tests at Chicago O'Hare Airport, 1992). For the computer simulations, the assumption is made that the initial location of the droplets is determined by a hypothetical wing trailing edge location, see Figure 5.3. That position of the wing trailing edge is given by rotating the local chord through the angle of attack of the wing (during ground roll this equals the wing incidence). The hypothetical trailing edge point is then given by the location where the trailing edge of the wing would be with zero flap deflection.

Another unknown parameter is the initial drop velocity, which is determined by the flow-off velocity (magnitude and direction) of the anti-icing fluid. For these simulations, the *magnitude* of the initial velocity of the fluid droplets has been approximated by Boluk (1994a) for a BOEING 737 take-off run. For Type I fluid, Boluk calculated the flow-off velocity magnitude relative to the wing to be ~0.80 m/s at all aircraft speeds. For Type II fluid, Boluk calculated the flow-off velocity magnitude relative to the wing to be ~0.25 m/s at an aircraft speed of 38.308 m/s (75 kt), and ~0.38 m/s at an aircraft speed of 56.625 m/s (110 kt). For the Airbus A320 and the BOEING 747, the flow-off speeds were assumed to be the same as that of the B737 at the two speeds (even though the A320 and 747 have a higher upper speed modelled). These flow-off speeds were used for emitting fluid droplets from the wing trailing edge. The initial velocity *direction* is parallel to the angle of attack of the wing. It turns out that the initial velocity is not all that critical since the small droplets (i.e. ~200 μm) reach their terminal velocities in approximately the first 0.1 seconds. The larger droplets take slightly longer to reach their terminal velocity, but that still is not important since longitudinal displacement is not of any real concern for the purposes of this study. Only the vertical component of the initial velocity will significantly influence the lateral displacement of fluid droplets. Noting that the initial velocity direction is determined by the wing angle of attack, which equals the angle of incidence during the ground roll, it is clear that the vertical component of the initial droplet velocity is small.

5.4.2.3 **Anti-Icing Fluid Mass and Volume Flow-Off Rates**

Boluk (1994a) approximated the anti-icing fluid mass flow-off rates for the BOEING 737 aircraft during its take-off run. These mass flow-off rates, dm/dt, are for the whole aircraft. For Type I fluid, over the speed range concerned, $dm/dt \cong 2.5$ kg/s, for the BOEING 737. Using a fluid density of 1000 kg/m^3, this results in a volume flow-off rate, $dVol/dt \cong 2.5\times10^{-3}$ m^3/s. Since actual information was not available for the BOEING 747 and Airbus A320, the flow-off rates for these aircraft were assumed to be proportional to the BOEING 737 based on the exposed wing area flaps retracted. This gives for the B747, $dVol/dt \cong 13.25\times10^{-3}$ m^3/s; and for the A320, $dVol/dt \cong 2.99\times10^{-3}$ m^3/s. Note that for Type I fluid these volume flow-off rates were applied to both the upper and lower speeds considered.

For Type II fluid, on the BOEING 737 at 38.608 m/s (75 kt) $dVol/dt \cong 1.80\times10^{-3}$ m^3/s, while at 56.625 m/s (110 kt) $dVol/dt \cong 2.20\times10^{-3}$ m^3/s. (Again using a fluid density of 1000 kg/m^3.) Again, since actual information was not available for the BOEING 747 and Airbus A320, the flow-off rates for these aircraft were assumed to be proportional to the BOEING 737 based on the exposed wing area flaps retracted. This gives for the B747 at 38.608 m/s (75 kt) $dVol/dt \cong 9.54\times10^{-3}$ m^3/s, while at 77.216 m/s (150 kt) $dVol/dt \cong 11.66\times10^{-3}$ m^3/s; and for the A320 at 38.608 m/s (75 kt) $dVol/dt \cong 2.15\times10^{-3}$ m^3/s, while at 66.921 m/s (130 kt), $dVol/dt \cong 2.63\times10^{-3}$ m^3/s.

5.4.2.4 **Droplet to Droplet Interference**

The mass of anti-icing fluid leaving the wing is about 63 kg total for the BOEING 737-300, about 335 kg total for the BOEING 747, and about 76 kg total for the Airbus A320. This is based on a fluid depth of 0.762 mm (0.030 in.) over the exposed wing area for each aircraft. All of the fluid flows off the wing during the take-off run, prior to rotation. Since, the fluid mass flow-off rate at any location is not large, the assumption is made that each droplet of fluid leaving the wing is acted on independently of all other droplets. This means that the wake of one droplet does not affect the movement of the next droplet.

This simplifies the individual droplet drag calculations so that each droplet is treated as being the only droplet in the wake.

5.4.2.5 Evaporation From Droplets and Change of Drop Size

For this study, the atmospheric conditions which lead to the use of anti-icing fluid (mainly, high humidity and temperatures near 0°C) are such that the evaporation from the fluid drops is negligible, and thus is neglected in the model. Hence, the droplets are assumed to be constant in size during their movement after flow-off.

5.4.2.6 Anti-Icing Fluid Density

The anti-icing fluid which is used is assumed to be a constant density over the range of temperatures concerned, -20°C to 5°C. That density is 1000 kg/m^3. Any errors introduced through this assumption will be small since the variation of droplet density with temperature should be rather small, only a fraction of a percent. (Unlike the variation of air density over the same temperature range.)

5.4.2.7 Anti-Icing Fluid Drop Sizes

The most significant parameter for drop movement is the drop size. Therefore, the drop size was varied for the study. For the first part of this study, the information concerning the drop size range for the anti-icing fluid was unavailable. As a result, the assumption was made that the anti-icing fluid leaves the wing in droplet form in pre-determined sizes deemed to be representative of those typical for the temperature conditions during the fluid usage. The two droplet diameters modelled were 100 μm and 200 μm. The 100 μm diameter drops correspond to the smallest sizes considered typical of those flowing off of the trailing edge of the wings of these aircraft. Note that the first part of the study assumed that for each test case the drop sizes were *constant* for all drops flowing off the wing at all spanwise locations.

For the second part of the study, information concerning the dropsizes for both Type I and Type II anti-icing fluids was available for the BOEING 737 aircraft take-off run from Boluk (1994a). Type I fluids gave drop diameters ranging from $\sim 150\mu$m to $\sim 213\mu$m and Type II fluids gave drop diameters ranging from $\sim 940\mu$m to $\sim 1110\mu$m at the two aircraft speeds modelled during the take-off run. This data was interpolated and extrapolated as needed (Boluk, 1994b) to supply information for the Airbus A320 and the BOEING 747 take-off runs. (Hence, overall, Type I fluids gave drop diameters ranging from $\sim 130\mu$m to $\sim 230\mu$m and Type II fluids gave drop diameters ranging from $\sim 870\mu$m to $\sim 1130\mu$m at the two aircraft speeds modelled during the take-off run.) Figures 5.4 and 5.5 show the drop sizes for the two anti-icing fluid types as a function of chord, for the aircraft involved at the two speeds considered. Note that the lower speed considered (38.608 m/s or 75 kt) was the same for each aircraft, hence the drop sizes were the same for the same chord of each aircraft. However, the second speed for each aircraft was just prior to rotation and thus was different for each aircraft. Therefore the drop sizes for each aircraft were different for the second speed modelled.

Note this author believes that the drop sizes for Type II fluid are suspect. The information provided for these drop sizes were determined by fluid flow-off from a flat plate into a free stream which was parallel to the flat plate, Boluk (1994b). For the fluid which flows-off from an actual main wing section, that fluid crosses the flap gap region and may intercept the faster air velocity flowing through the flap gap region. This fluid flow across the gap would likely lead to the formation of smaller drops, due to the increased shear on the drop as it intercepts that faster air flow.

This uncertainty of dropsizes for Type II fluid prompted a desire to know the effects of dropsize variation. Hence, a sensitivity analysis was done for Type II drop sizes flowing off the BOEING 737-300 wing. These were done for the three crosswind conditions. The study examined the effect of taking the dropsizes given by Boluk (1994a) and multiplying those by the factors 0.25, 0.50, 0.75, and 1.00.

Recall that the amount of fluid flow-off at any spanwise location depends on the chord of the wing at that spanwise location. Now since the drops released were all approximately the same size, this meant that the model released a *greater number* of drops from the inboard locations compared to the outboard locations.

5.4.2.8 **Spanwise Deposition Considerations**

Deposition of anti-icing fluid is of a concern both on the runway surface and on the areas adjacent to the runway. For this study the runway is considered to be 62 m ($\sim$200 ft) wide. The plots which show depth of deposition versus spanwise location do not specifically show the runway surface. However for the final tabulated data (given in Tables 5.3 to 5.7, later), the runway width is used to calculate the anti-icing fluid deposition on the runway surface as a percentage of the original mass (or volume) of anti-icing fluid flowing off the respective aircraft at the given speeds.

For the deposition simulations there were 1000 fluid droplets released from each aircraft. These were released such that the initial droplet spacing in a spanwise direction represented the fluid volume distribution across the span on the wing. However, for the plots of droplet paths only 100 droplets were shown as released from each aircraft, so as not to clutter the plots.

5.4.2.9 **Depth of Deposition of Fluid on the Runway**

Some actual flight tests have been performed at Chicago's O'Hare Airport (1992) by another research group. The study noted that there was NO deposition of anti-icing fluid on the runway surface. It should be noted that for a BOEING 737-300 aircraft the total fluid volume on the wing is 6.325×10^{-2} m^3, based on 0.030 in. initial fluid thickness. Then assume that *all* of the fluid is distributed uniformly over the runway width 61 m (200 ft) and for a length of 610 m (2000 ft). The result is a fluid depth of 1.7 μm (1.7×10^{-6}m). That depth is basically impractical to measure on the actual runway surface. Hence, it is no surprise that the investigators thought there was NO anti-icing fluid deposited on the runway while doing visual inspections for the fluid.

For the part of the study of Type I and Type II fluids, the actual depth of anti-icing fluid deposition on the runway was calculated since the mass flow-off rates were available. For the part of study examining the movement and deposition of dropsizes equal to 100μm and 200μm, the actual depth of anti-icing fluid deposition on the runway was not calculated since the mass flow-off rates were unknown. Spanwise deposition calculations give the volume and number of drops deposited in each one meter increment laterally across the runway. Recall that this is from approximately 1000 drops initially released for this portion on the study. One can then scale the plots to get the depth of fluid for a given flow-off rate and aircraft velocity.

The *depth* of fluid can be found as follows:

$$depth = \frac{Vol_{strip}\ \ dVol/dt}{Vel_{plane}\ \ Vol_{TotalDrops}} \tag{5.3}$$

where, Vol_{strip} is the volume of modelled fluid drops deposited in each 1.0 m increment of the lateral strip, $dVol/dt$ is the volume flow-off rate from the whole aircraft, Vel_{plane} is the aircraft speed, and $Vol_{\mathrm{Total\ Drops}}$ is the total volume of the $\sim$1000 drops which are modelled.

5.4.3 Atmospheric Conditions

Atmospheric conditions included the ambient temperature and the crosswind component. The ambient air temperature is significant in that lower temperatures produce higher air density and lower air viscosity. The drag force on the fluid droplets is dependent on the dynamic pressure, q, of the relative air velocity, V_{rel}. That is given by: $q = \frac{1}{2}\rho V_{rel}^2$. As well, the drag *force* is dependent on the drag *coefficient* which is a function of Reynolds number, which is a function of density and viscosity. (Note that for this portion of the model the airport elevation is considered to be sea level. The changes of atmospheric properties (specifically, air density) are basically a function of temperature.) Comparisons for most of the study were done at an ambient temperature of 0°C. In the part of the study examining Type I fluid drops, an addition set for comparison was done at an ambient temperature of -20°C, but only for a zero crosswind condition.

Wind is the main atmospheric phenomenon of significance. Note that any headwind component would lead to a simple longitudinal displacement of the anti-icing fluid along the runway length. Hence, the crosswind component is the only real concern. The crosswind will tend to carry the anti-icing fluid further downwind. The crosswind components which are modelled are always from the left wing toward the right wing. Three values were modelled: 0 m/s, 5.1477 m/s, and 10.2955 m/s (0 kt, 10 kt, and 20 kt, respectively).

5.5 RESULTS

5.5.1 Aircraft Loading and Wake Model

The following section discusses the results from the model for the aircraft wing loading, as well as the trailing vortex wake and the vortex wake development.

5.5.1.1 Aircraft Spanwise Loading and Lift Coefficient

For the three aircraft Figures 5.6 and 5.7 show plots of local spanwise lift coefficient versus spanwise location, $y/(b/2)$, for the two speeds concerned. There are several things to note about the figures. The A320 shows a higher lift coefficient along the span. This is mainly due to the wing root incidence (root-wing setting) of 3.66°, even though the aircraft only uses a single slotted flap at a setting of 15° and hence has a slightly lower $C_{L_0}(y)$ than the other two aircraft examined. The BOEING 737-300 has a triple slotted flap setting of 15° and wing root incidence of 1°. The BOEING 747 has a triple slotted flap setting of 10° and wing root incidence of 2°. The BOEING 737 flap angle of 15° gives it a greater $C_{L_0}(y)$ than the BOEING 747, even though the BOEING 747 has a greater wing incidence.

The plots for the spanwise loading for each of the aircraft are shown in Figures 5.8, 5.11, and 5.14. Figure 5.14 shows that a significant feature is the greater outboard loading of the Airbus A320 compared to the BOEING 737. Hence, even though they have similar wing spans, the A320 has further outboard center of vorticity. The A320 wing designed for a winglet application has greater outboard loading due to the planform (i.e. greater span flaps), so even without the winglet added it would have a greater outboard center of vorticity.

5.5.1.2 Aircraft Wing Bound and Shed Circulation

Plots of bound circulation and shed circulation for each of the aircraft are shown in Figures 5.9, 5.10, 5.12, 5.13, 5.15, and 5.16. Note that the bound circulation distribution, $\Gamma(y)$, shows a direct correlation with the spanwise lift distribution, $l(y)$. Similarly, note that the local maximums of the shed circulation, $d\Gamma(y)/dy$, shows a direct correlation with the centers of roll-up of the vortex sheet for each wing, see Figures 5.17 to 5.19.

5.5.1.3 Aircraft Trailing Vortex Wake Development

The initial trailing vortex wake development is shown for each of the aircraft in Figures 5.17 to 5.19. These figures show the positions of the 45 vortex filaments from $t = 0.0$ to $t = 1.0$ seconds for each of the aircraft. The vortex roll-up is seen to occur most rapidly at the wing tip. However, for each of the aircraft there also is another vortex core developing at the location of the end of the flaps. By comparison with the shed circulation plots, the roll-up can be seen to originate at the regions of local maximum shed circulation, $d\Gamma(y)/dy$. Recall that the trailing vortices are modelled as semi-infinite vortex lines parallel to the aircraft longitudinal axis (and aircraft velocity). Hence Figures 5.17 to 5.19 show the location of the axis of each of the vortices in the plane which is perpendicular to the longitudinal axis.

5.5.2 Anti-Icing Fluid Droplet Movement and Deposition

Results concerning the anti-icing fluid droplet movement in the wake and the lateral ground deposition comprise the most significant of the figures. These are presented from Figure 5.20 to Figure 5.68. Basically, two types of figures are shown for each of the aircraft. The figures are presented in sets of four per page. The first three figures in each set show the anti-icing fluid droplet trajectories or paths for the three crosswind components, and the fourth figure shows the depth of deposition of the fluid laterally across the runway. These sets of figures are given for each aircraft at the two ground speeds examined. Figures 5.20 to 5.44 give the plots for Type I anti-icing fluid and Figures 5.45 to 5.68 give the plots for Type II anti-icing fluid.

5.5.2.1 Anti-Icing Fluid Droplet Movement Trajectories

Some typical droplet paths or trajectories are shown for each of the aircraft at each of the conditions modelled. At the outset, note that the points shown are *not* all individual fluid drops. The plots present the movement of only 50 droplets leaving each wing (100 drops per aircraft). Showing more droplets would excessively clutter the figures. Note that for all plots of droplet paths or trajectories, the droplets are shown plotted as points along their path in 0.25 sec intervals during their modelled movement. This gives the *appearance* of many drops, but actually there are only 100 drops shown with each one being shown many times along its trajectory. These plots also show the effect of the initial droplet velocity by the distance the drop moves in that first interval. Noticeable is the fact that in general the drops decelerate to terminal velocity in the first 0.25 sec (at least in the vertical and lateral movement).

The droplet movement plots show a set of droplets which are all released at the same instant from the aircraft. The droplet positions are then plotted every 0.25 seconds (showing droplet path lines). The wing is shown by the straight line of the original positions of the droplets. Notice that both the trailing vortex system *and* the droplets are moving. Therefore especially the smaller anti-icing fluid droplets tend to be caught in and travel with the moving vortex system. Since the droplets are all released at one instant, there appear to be "humps" in the movement. If one watched behind the plane this would not appear since droplets would be released continuously, smoothing out the appearance. Also, note that when watching fluid come off a wing on video, one tends to observe one location and watches a progression of droplets move through that same region. This is noted since some readers may have observed videos of the anti-icing fluid movement in the aircraft wake.

5.5.2.2 **Depth of Deposition of Anti-Icing Fluid**

The depth of deposition of anti-icing fluid is based on the actual calculated deposition in discrete spanwise intervals of 1.0 m each. For the figures showing the depth of deposition, the curves shown are the "best-fit" curved lines using a 10^{th} order polynomial. Although the exact deposition data is not shown, the fitted curves help to show the trends. Also, overlaying two or more plots of the actual calculated values obscured the plots so that they were not easily interpreted. Figures 5.68 to 5.70 show samples of the curve fitting for the BOEING 737-300 at $V = 56.625$ m/s, for the three crosswinds and using Type I fluid. Note that since a finite number of fluid droplets were released (i.e. 1000 per aircraft), there are discrete values of droplets "collected" in each interval. As noted, the actual depth of anti-icing fluid on the runway was calculated in this study since the mass flow-off rates were known or estimated. Thus, the fluid depth at any spanwise location could be determined by appropriately scaling the spanwise deposition for any speed and flow-off rate.

Finally, the deposition plots give the amount of fluid that lands on the runway surface as well as the fluid that lands somewhere in the first 20 seconds. That is because the fluid drop movement is simulated for 20 seconds or until they hit the ground, which ever comes first. If a drop has hit the ground (considered as up to one inch above the ground) within the first 20 seconds, that droplet is considered as *landed*, otherwise it is considered as *lost*.

The figures show that for the lower speeds considered the depth is always greater than for the higher speed. This occurs since the Type I fluid flow-off rates used at both speeds are the same, and for Type II fluid the flow-off rate is ~ 1.8 kg/s at 75 kt and only ~ 2.2 kg/ at the higher speeds. Note that the BOEING 737-300 produced a maximum depth of about 2.0 μm for Type I fluid and 38.608 m/s (75 kt), and a maximum depth of about 2.2 μm for Type II fluid and 38.608 m/s (75 kt). The BOEING 747 produced a maximum depth of about 6.0 μm for Type I fluid and 38.608 m/s (75 kt), and a maximum depth of about 5.1 μm for Type II fluid and 38.608 m/s (75 kt). The Airbus A320 produced a maximum depth of about 1.8 μm for Type I fluid and 38.608 m/s (75 kt), and a maximum depth of about 3.4 μm for Type II fluid and 38.608 m/s (75 kt). The greatest depths occur near the position along the length of the runway where the aircraft have accelerated to the speed of about 38.608 m/s (75 kt), which is where the anti-icing fluids typically begin to flow-off. The actual distance along the runway would be different for each aircraft and would be dependent on the aircraft weight and the atmospheric conditions.

Another significant feature is seen in the plots of depth of deposition. That feature is that the maximum depth of fluid deposition generally occurs near or just slightly towards the upwind side of the centerline of the runway.

Presented at the SWIFT '94 conference, a study at NASA Wallops Island Flight Facility showed that Type II anti-icing fluid deposition as little as 0.4 gal U.S./1000ft^2 ($\sim 15.7\mu$m depth) produced measurable friction coefficient reduction using a K.J. Law Friction tester minivan (Cowper, Comfort, and Horne, 1994). Note should be given since this is the cumulative amount deposited by approximately seven take-offs by BOEING 737-300s, or about two or three take-offs by BOEING 747s. (Also note that at the conference, Comfort commented that amounts of Type II fluid greater than 0.4 gal U.S./1000ft^2 did not increase the friction coefficient *reduction*.)

5.5.3 Anti-Icing Fluid Deposition on Runway and Fluid Not Lost

The following tables show anti-icing fluid deposition on the runway surface and the fluid not lost. The runway is considered to be 62 m (~200 ft) wide. Recall that the anti-icing fluid is considered to be lost if it does not land on the ground anywhere in the first 20 seconds of the simulation. Tables 5.3 and 5.4, comparing Type I and Type II fluid, and Table 5.5 and 5.6 comparing dropsizes of 100 μm and 200 μm are based on an air temperature of 0°C. Note that the tables give values as percentages of the original mass (or volume) of anti-icing fluid flowing off the respective aircraft at the given speeds.

Tables 5.3 to 5.7 clearly show that a greater percentage of the initial fluid from the BOEING 737-300 lands on the runway than for the other two aircraft. As well, the trend appears that a greater wing span leads to *decreased* deposition on the runway and *decreased* fluid deposited within 20 seconds (i.e. NOT Lost) and hence *increased* fluid considered lost to the atmosphere. Note that comparison of the Airbus A320 with the BOEING 737-300 shows that the greater span of the A320 (33.91m) compared to the B737-300 (29.03m) dominates the fluid movement. This is the case even though the A320 has a further outboard wing loading than the B737-300. Also, note that the wing span of the BOEING 747 is 59.64m and that the runway is only 62m wide. Thus the wingtip of the BOEING 747 is right at the edge of this runway. This leads to *reduced* fluid deposition on the runway surface compared to the other two smaller span aircraft. This is the case even though the amount of anti-icing fluid which is deposited within the first 20 seconds is still high.

Another result clear from these tables is that larger drop sizes from the Type II fluid (870 to 1130 μm) produce greater depostion on the runway and less fluid lost than the smaller drops of the Type I fluid (130 to 230 μm).

The effect of a crosswind produces a result that was not necessarily expected. Tables 5.5 and 5.6 (using 100 and 200 μm drop sizes) show that under the influence of a light crosswind (5.148 m/s or 10 kt) the deposition on the runway *increases* compared to the zero crosswind condition. However, when the crosswind increases more (to 10.295 m/s or 20 kt) the deposition on the runway again *decreases*. The study also shows a similar trend with Type I fluid (Table 5.3), but the trend is not as clear with the larger drops of the Type II fluid (Table 5.4). This increased deposition on the runway is due to the fluid from the upwind wing being blown back onto the runway surface under the light crosswind condition. However, when the wind is stronger (10.295 m/s or 20 kt) much more of the fluid from the upwind and downwind side is blown completely off of the runway area. These observations for the variation of deposition with crosswind are made clear by examining the figures which plot the drop trajectories and those which plot the depth of deposition of fluid.

In the study examining drop sizes for Type I fluid, an addition set of data for comparison was done at an ambient temperature of -20°C, but only for a zero crosswind condition. The results are shown in Table 5.7. Comparisons with drop deposition at 0°C showed that there was not any dramatically significant difference of fluid deposition on the runway at the lower ambient temperature.

5.5.3.1 **Type II Anti-Icing Fluid Drop Size Sensitivity Analysis**

As mentioned earlier in the section regarding the conditions modelled for the anti-icing fluid drop sizes, the drop sizes predicted for the Type II anti icing fluid were suspect. Thus, a rough sensitivity analysis was done by varying the Type II fluid drop diameters. Other evidence showed that the Type II drop sizes were probably much smaller than those given by Boluk (1994a) and shown in Figure 5.5. Therefore, factors of 0.25, 0.50, 0.75, and 1.00 were applied to the drop diameters of the Type II fluid as shown in Figure 5.5. (i.e., for the BOEING 737-300 at V = 56.625 m/s, the drop diameters with the factor 1.00 were 940μm to 1050μm, and for the factor 0.25 the drop diameters were 235μm to 262μm.) Note that this analysis was done only for the BOEING 737-300. Table 5.8 shows the results of the fluid deposition on the runway and fluid not lost.

The data shows that for the BOEING 737, the results are relatively unchanged for factor 0.75, as compared to 1.00. Only slight change is noted for the factor 0.50, and it is no surprise that the most significant change is noted for the factor 0.25.

5.6 CONCLUSIONS

This study has examined anti-icing fluid movement and deposition by three typical Canadian transport aircraft under take-off conditions. The study was aimed at determining the spanwise movement and deposition of anti-icing fluid droplets. Some information regarding Type I and Type II anti-icing fluid drop sizes was available, thus the approximated drop diameters were used for each fluid type. As expected, the smaller Type I anti-icing fluid droplets (in the size range 130 μm to 230 μm) appear to drift much more than the larger Type II anti-icing fluid drops (in the size range 870 μm to 1130 μm).

As can be seen, for the cases of no crosswind, a substantial amount of anti-icing fluid is deposited on the 62 m ($\sim$200 ft) wide runway surface. For crosswind components of 5.148 m/s (10 kt) there is an increased fluid deposition near the centerline since the fluid from the upwind wing moves back onto the runway. For crosswinds of 10.295 m/s (20 kt) the off runway deposition is significant, especially for the smaller drops of the Type I anti-icing fluid. The 'obvious' conclusion that a crosswind causes greater off runway deposition is not necessarily correct, since moderate crosswinds appear to increase fluid deposition on the runway surface.

The results showed that the smaller span aircraft tend to produce an increased rate of anti-icing fluid deposition on the runway surface, when considering the percentage of the initial fluid. The larger BOEING 747 moves a greater percentage of the spray off of the runway surface, even though much of the spray will still be deposited on the adjacent areas.

The amount of anti-icing fluid deposited on the airport runway near the centerline was seen to be sufficient to produce potential reductions of the runway braking coefficient after the take-off of only a small number of aircraft.

Acknowledgements

This work was done by Merkl (1995) under contract for the **R & D Task Group** of the **Dryden Commission Implementation Project** of **Transport Canada**.

REFERENCES

Airbus A320 Flight Manual (Aircraft Operations Manual). Jun 30, 1993. Airbus. France.

Airbus A320 Maintenance Manual. Feb 01 ,1992. Airbus. France.

Anti-Icing Fluid Deposition Video. 1992. Chicago O'Hare Airport. D.C.I.P. R.& D. Task Group has copy of VHS video tape.

Beard, K.V. and H.R. Pruppacher. 1969. The determination of the terminal velocity and drag of small water drops by means of a wind tunnel. *Journal of the Atmospheric Sciences* 26:1066-1072.

BOEING 737-300 Airplane Flight Manual. Apr 11, 1985. BOEING Aircraft Co.

BOEING 737-300 Maintenance Manual. Oct 25, 1984. BOEING Aircraft Co.

BOEING 747 Aircraft Operations Manual. Oct 1, 1984. BOEING Aircraft Co.

BOEING 747 Maintenance Manual. Jan 15, 1974. BOEING Aircraft Co.

Boluk, Yaman. 1994a. Anti-Icing Fluid Drop Sizes, Contractor Report for D.C.I.P, to be received by ~ August, 1994.

Boluk, Yaman. 1994b. Private communication. July, 1994.

Cowper, B., G. Comfort, and W. Horne. 1994. Friction Tests Conducted With an Aircraft Tire And A Ground Vehicle on Various Surfaces Wetted with Water and Type II De-Icing Fluid. *SWIFT '94 Conference* (Surface Winter Ice and Snow Removal and Friction Testing), August 22-26, 1994. at Edmonton, Alberta, Canada.

Donaldson, C. duP., R.S. Snedeker, and R.D. Sullivan. 1974. Calculation of Aircraft Wake Velocity Profiles and Comparison with Experimental Measurements. *Journal of Aircraft* 11(9):547-555.

Eisner, von F. 1930. Das Widerstands Problem. *Proceedings of the 3rd International Congress for Applied Mechanics* 1:23-42. Stockholm, Sweden.

Flaig, A. and R. Hilbig. 1992. High-Lift Design for Large Civil Aircraft. *AGARD Conference Proceedings* CP-415 (Symposium on High-Lift Systems Aerodynamics). p. 31-3.

Goering, C.E., L.E. Bode, and M.R. Gebhardt. 1972. Mathematial modeling of spray droplet deceleration and evaporation. *Trans ASAE* 15(2):220-225.

Houghton, E.L. and N.B. Carruthers. 1982. *AERODYNAMICS FOR ENGINEERING STUDENTS., 3rd Ed.* Arnold. pp. 198-199, 254-255.

Hughes, R.R. and E.R. Gilliland. 1952. The mechanics of drops. *Chemical Engineering Progress* 48(10):497-504.

Jane's All the World's Aircraft 1974-75, pp. 283-285.

Jane's All the World's Aircraft 1993-94, pp. 118-120, 441-443, 443-446.

Langmuir, I. and K. Blodgett. 1946. *A Mathematical Investigation of Water Droplet Trajectories.* AAF TR No. 5418 (Contract No. W-33-038-ac-9151). Air Technical Service Command, U.S. Army Air Forces.

Lapple, C.E. and C.B. Shepherd. 1940. Calculation of particle trajectories. *Industrial and Engineering Chemistry* 32(5):606-617.

Manning, W.P. and W H. Gauvin. 1960. Heat and mass transfer to decelerating finely atomized sprays. *A.I.Ch.E. Journal* 6(2):184-190.

Marshall, W.R. 1954. Atomization and Spray Drying. *Chemical Engineering Progress Monograph Series* 50(2).

Mason, B.J. 1971. *The Physics of Clouds, 2nd Edition.* Claredon Press, Oxford.

Merkl, Craig S. 1989. *AERIAL SPRAYING: A Computer Simulation of the Spray Movement in the Aircraft Wake.* M.Sc. Thesis. University of Alberta.

Merkl, Craig S. 1995. *Anti-Icing Fluid Distribution on Runways.* Contractor Report for Transport Canada (Dryden Commission Implementation Project) TP 12426E. February, 1995.

Morris, D.J., C.C. Croom, C.P. vanDam, and B.J. Holmes. 1984. *An Experimental and Theoretical Investigation of Deposition Patterns from an Agricultural Airplane.* NASA Technical Paper 2348.

Ormsbee, A.I. and M.B. Bragg. 1978. *Trajectory Scaling Laws for a Particle Injected into the Wake of an Aircraft.* ARL 78-1 . Aviation Research Laboratory, University of Illinois at Urbana-Champaign.

Ranz, W.E. and W.R. Marshall. 1952a. Evaporation from droplets, Part I. *Chemical Engineering Progress* 48(3):141-146.

Ranz, W.E. and W.R. Marshall. 1952b. Evaporation from droplets, Part II. *Chemical Engineering Progress* 48(4):173-180.

Trayford, R.S. and L.W. Welch. 1977. Aerial spraying: A simulation and recovery of liquid droplets. *Journal of Agricultural Engineering Resources* 22:183-196.

Walton, L.R. and J.N. Walker. 1970. The trajectory of an evaporating water droplet falling in an airstream. *Trans ASAE* 13:158-161,167.

Table 5.3: Fluid Deposition on Runway and Fluid Not Lost, Type I Anti-Icing Fluid.

	Crosswind					
	0 m/s (0 kt)		5.148 m/s (10 kt)		10.295 m/s (20 kt)	
Aircraft and Velocity	% Fluid NOT Lost	% Fluid ON Runway	% Fluid NOT Lost	% Fluid ON Runway	% Fluid NOT Lost	% Fluid ON Runway
BOEING 737-300 with $\delta_f = 15°$ V = 56.625 m/s (110 kt)	99.8	70.1	99.9	75.2	99.9	65.7
V = 38.608 m/s (75 kt)	100.0	87.4	100.0	75.5	100.0	67.5
BOEING 747 with $\delta_f = 10°$ V = 77.216 m/s (150 kt)	99.5	30.9	99.8	48.2	98.5	44.2
V = 38.608 m/s (75 kt)	98.0	37.0	97.5	59.1	97.3	40.7
Airbus A320 with $\delta_f = 15°$ V = 66.921 m/s (130 kt)	99.1	50.7	99.4	67.8	99.5	46.5
V = 38.608 m/s (75 kt)	99.0	48.3	99.3	65.2	99.1	34.1

Table 5.4: Fluid Deposition on Runway and Fluid Not Lost, Type II Anti-Icing Fluid.

	Crosswind					
	0 m/s (0 kt)		5.148 m/s (10 kt)		10.295 m/s (20 kt)	
Aircraft and Velocity	% Fluid NOT Lost	% Fluid ON Runway	% Fluid NOT Lost	% Fluid ON Runway	% Fluid NOT Lost	% Fluid ON Runway
BOEING 737-300 with $\delta_f = 15°$ V = 56.625 m/s (110 kt)	100.0	97.7	100.0	97.8	100.0	93.1
V = 38.608 m/s (75 kt)	100.0	99.4	100.0	97.4	100.0	92.7
BOEING 747 with $\delta_f = 10°$ V = 77.216 m/s (150 kt)	100.0	69.8	100.0	78.4	100.0	76.6
V = 38.608 m/s (75 kt)	100.0	75.3	100.0	81.1	100.0	75.7
Airbus A320 with $\delta_f = 15°$ V = 66.921 m/s (130 kt)	100.0	96.5	100.0	90.2	100.0	86.8
V = 38.608 m/s (75 kt)	100.0	98.1	100.0	94.4	100.0	90.2

Note: Values are given as percentages of the original mass (or volume) of anti-icing fluid flowing off the respective aircraft at the given speeds.

Table 5.5: Fluid Deposition on Runway and Fluid Not Lost, Dropsize = 100 μm.

	Crosswind					
	0 m/s (0 kt)		5.148 m/s (10 kt)		10.295 m/s (20 kt)	
Aircraft and Velocity	% Fluid NOT Lost	% Fluid ON Runway	% Fluid NOT Lost	% Fluid ON Runway	% Fluid NOT Lost	% Fluid ON Runway
BOEING 737-300 with $\delta_f = 15°$ V = 56.625 m/s (110 kt)	~98.0	~64.6	~97.5	~68.0	~96.5	~46.2
V = 38.608 m/s (75 kt)	~96.0	~59.8	~89.1	~68.9	~90.1	~36.8
BOEING 747 with $\delta_f = 10°$ V = 77.216 m/s (150 kt)	~71.0	~33.8	~79.5	~36.5	~76.5	~32.7
V = 38.608 m/s (75 kt)	~63.0	~33.3	~65.5	~48.9	~70.5	~21.3
Airbus A320 with $\delta_f = 15°$ V = 66.921 m/s (130 kt)	~94.0	~46.8	~93.0	~58.1	~93.5	~33.7
V = 38.608 m/s (75 kt)	~65.0	~47.7	~84.0	~58.9	~80.0	~11.2

Table 5.6: Fluid Deposition on Runway and Fluid Not Lost, Dropsize = 200 μm.

	Crosswind					
	0 m/s (0 kt)		5.148 m/s (10 kt)		10.295 m/s (20 kt)	
Aircraft and Velocity	% Fluid NOT Lost	% Fluid ON Runway	% Fluid NOT Lost	% Fluid ON Runway	% Fluid NOT Lost	% Fluid ON Runway
BOEING 737-300 with $\delta_f = 15°$ V = 56.625 m/s (110 kt)	~100.0	~74.7	~100.0	~77.3	~100.0	~72.7
V = 38.608 m/s (75 kt)	~100.0	~84.8	~100.0	~73.7	~100.0	~67.7
BOEING 747 with $\delta_f = 10°$ V = 77.216 m/s (150 kt)	~100.0	~34.7	~99.5	~48.3	~99.0	~44.5
V = 38.608 m/s (75 kt)	~96.0	~34.0	~98.0	~55.6	~97.0	~35.7
Airbus A320 with $\delta_f = 15°$ V = 66.921 m/s (130 kt)	~100.0	~64.0	~100.0	~69.0	~100.0	~57.0
V = 38.608 m/s (75 kt)	~97.0	~48.5	~99.5	~64.8	~98.5	~37.6

Note: Values are given as percentages of the original mass (or volume) of anti-icing fluid flowing off the respective aircraft at the given speeds. (Note: values with " ~ " are done using 100 drops per semi-span.)

Table 5.7: Fluid Deposition on Runway and Fluid Not Lost, Type 1 Fluid, Ambient Temperature = -20°C.

	Crosswind	
	0 m/s (0 kt)	
Aircraft and Velocity	% Fluid NOT Lost	% Fluid ON Runway
BOEING 737-300 with $\delta_f = 15°$		
V = 56.625 m/s (110 kt)	~98.4	~74.5
V = 38.608 m/s (75 kt)	~100.0	~90.2
BOEING 747 with $\delta_f = 10°$		
V = 77.216 m/s (150 kt)	~100.0	~29.9
V = 38.608 m/s (75 kt)	~97.2	~38.1
Airbus A320 with $\delta_f = 15°$		
V = 66.921 m/s (130 kt)	~99.3	~42.6
V = 38.608 m/s (75 kt)	~97.8	~56.6

Note: Values are given as percentages of the original mass (or volume) of anti-icing fluid flowing off the respective aircraft at the given speeds. (Note: values with " ~ " are done using 100 drops per semi-span.)

Table 5.8: Fluid Deposition on Runway and Fluid Not Lost, Variation of Drop Sizes for Type II Anti-Icing Fluid.

	Crosswind					
	0 m/s (0 kt)		5.148 m/s (10 kt)		10.295 m/s (20 kt)	
Aircraft and Velocity	% Fluid NOT Lost	% Fluid ON Runway	% Fluid NOT Lost	% Fluid ON Runway	% Fluid NOT Lost	% Fluid ON Runway
Drop Diameters = 0.25 x Type II Drop Diameters from Figure 5.5						
BOEING 737-300 with δ_f = 15° V = 56.625 m/s (110 kt)	100.0	81.6	100.0	78.5	100.0	75.8
V = 38.608 m/s (75 kt)	100.0	97.2	100.0	81.1	100.0	76.2
Drop Diameters = 0.50 x Type II Drop Diameters from Figure 5.5						
BOEING 737-300 with δ_f = 15° V = 56.625 m/s (110 kt)	100.0	97.6	100.0	90.0	100.0	85.9
V = 38.608 m/s (75 kt)	100.0	99.4	100.0	92.9	100.0	88.4
Drop Diameters = 0.75 x Type II Drop Diameters from Figure 5.5						
BOEING 737-300 with δ_f = 15° V = 56.625 m/s (110 kt)	100.0	97.4	100.0	93.6	100.0	89.0
V = 38.608 m/s (75 kt)	100.0	100.0	100.0	97.1	100.0	90.4
Drop Diameters = 1.00 x Type II Drop Diameters from Figure 5.5						
BOEING 737-300 with δ_f = 15° V = 56.625 m/s (110 kt)	100.0	97.7	100.0	97.8	100.0	93.1
V = 38.608 m/s (75 kt)	100.0	99.4	100.0	97.4	100.0	92.7

Note: Values are given as percentages of the original mass (or volume) of anti-icing fluid flowing off the respective aircraft at the given speeds.

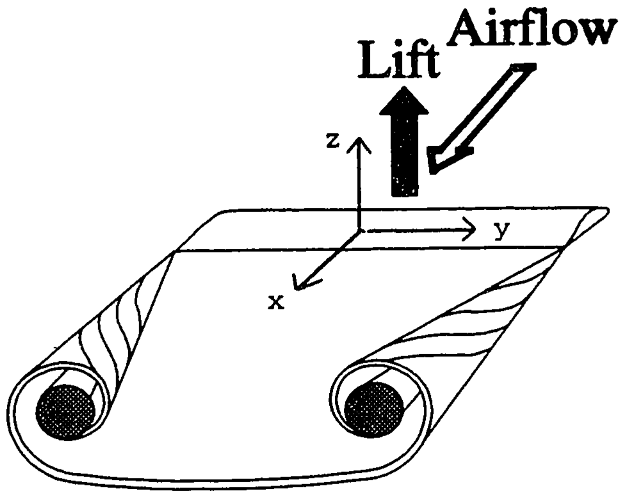

Figure 5.1 Vortex Sheet Roll-Up.

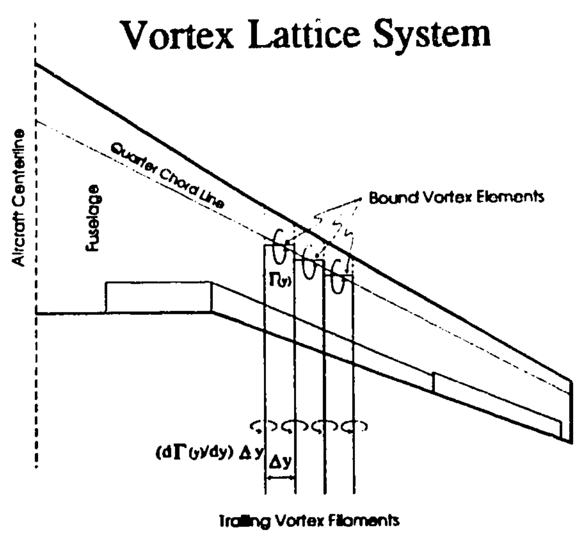

Figure 5.2 Simplified Vortex Lattice System.

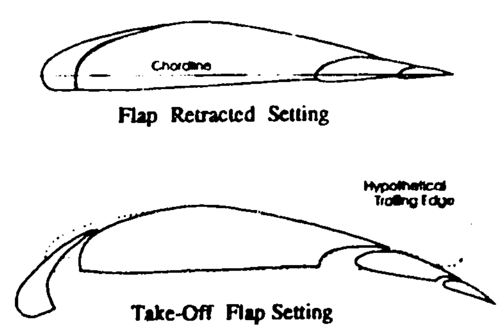

Figure 5.3 Anti-Icing Fluid Flow-Off Location.

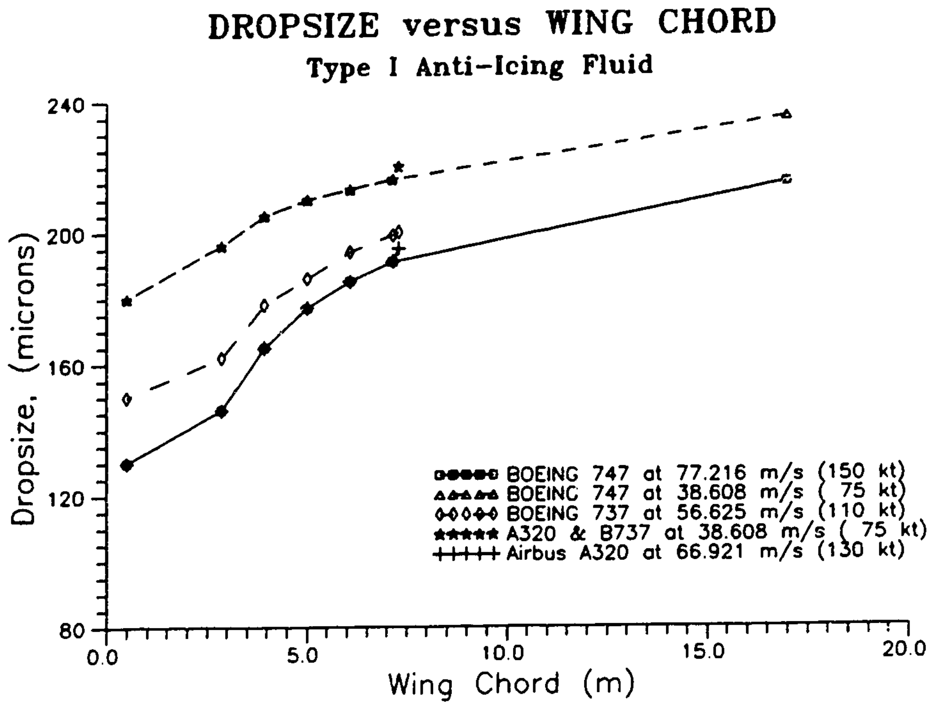

Figure 5.4 Drop Size versus Wing Chord. Type I Anti-Icing Fluid.

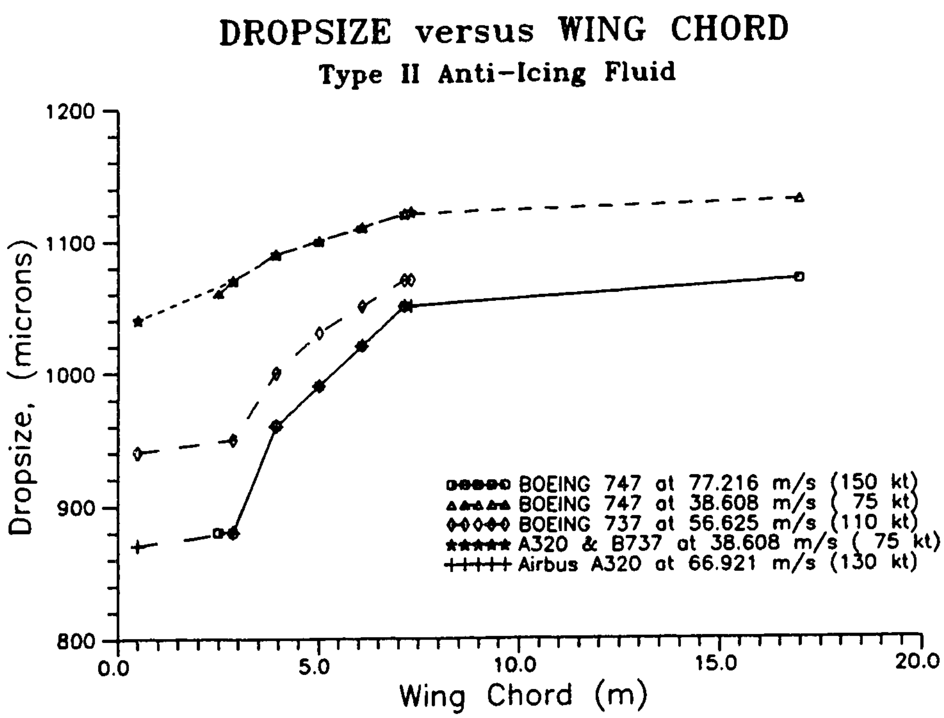

Figure 5.5 Drop Size versus Wing Chord, Type II Anti-Icing Fluid.

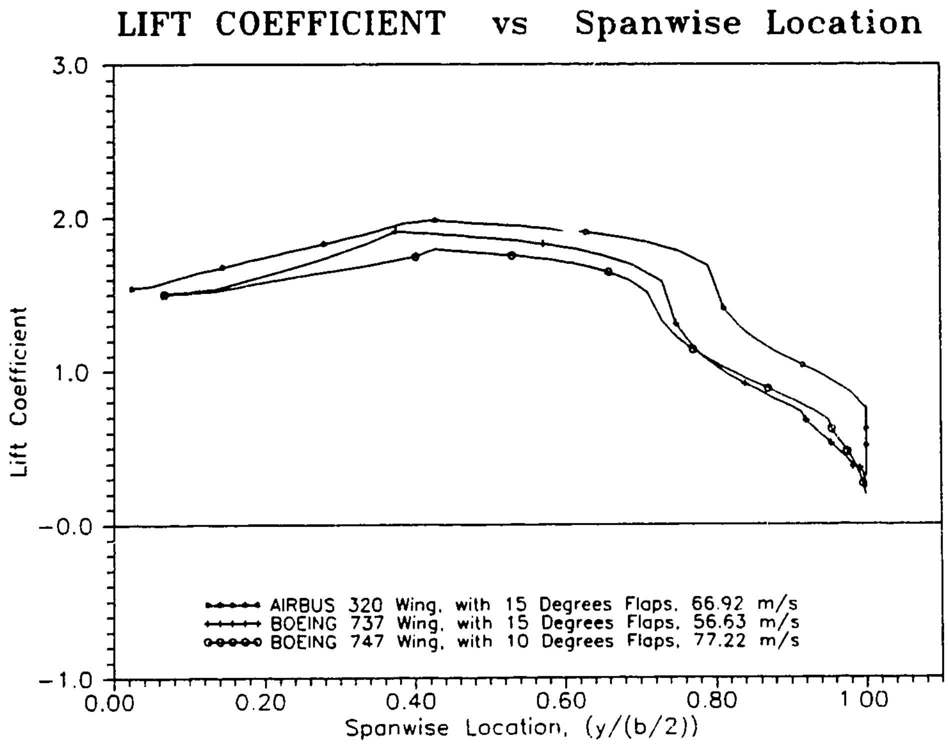

Figure 5.6 Lift Coefficient versus Spanwise Location for the three aircraft, just prior to rotation.

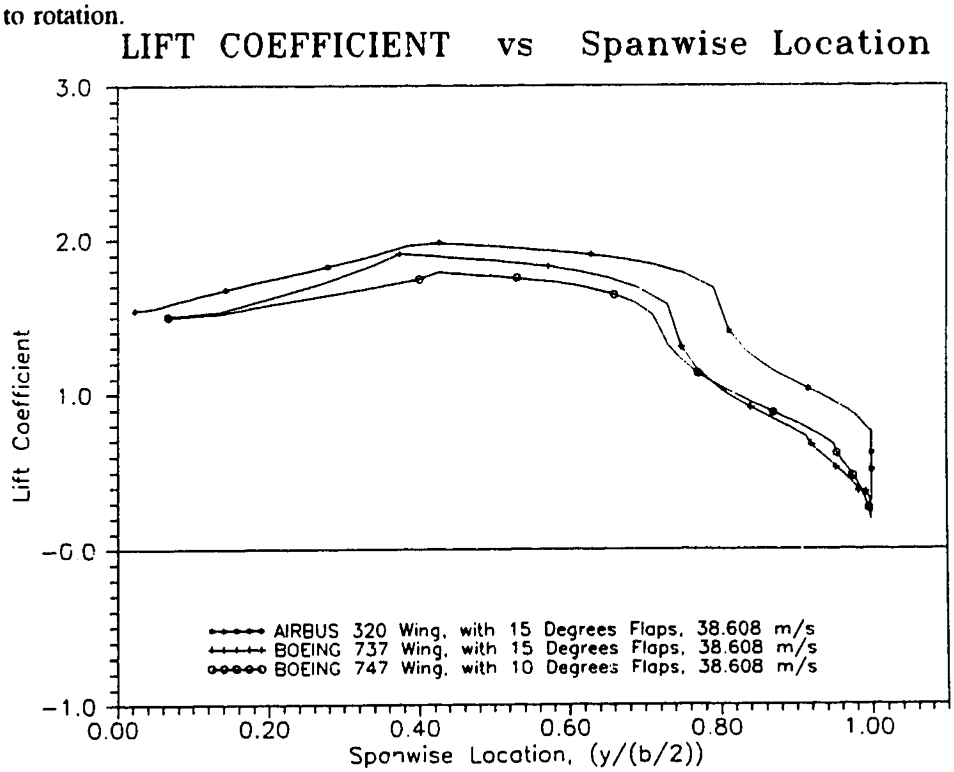

Figure 5.7 Lift Coefficient versus Spanwise Location for the three aircraft, V = 38.608 m/s (75 kt).

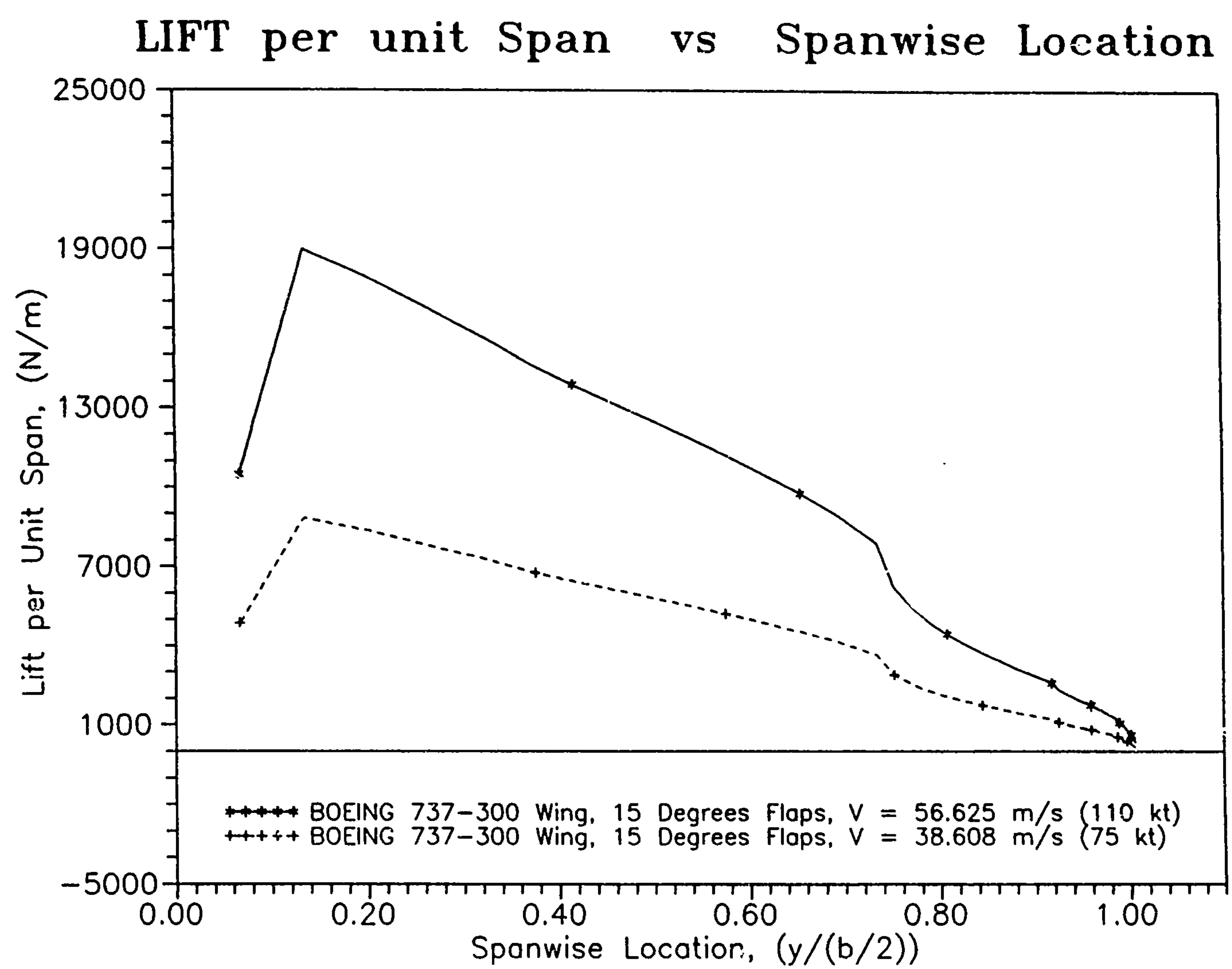

Figure 5.8 BOEING 737-300 Spanwise Lift Distribution, $\delta_f = 15°$.

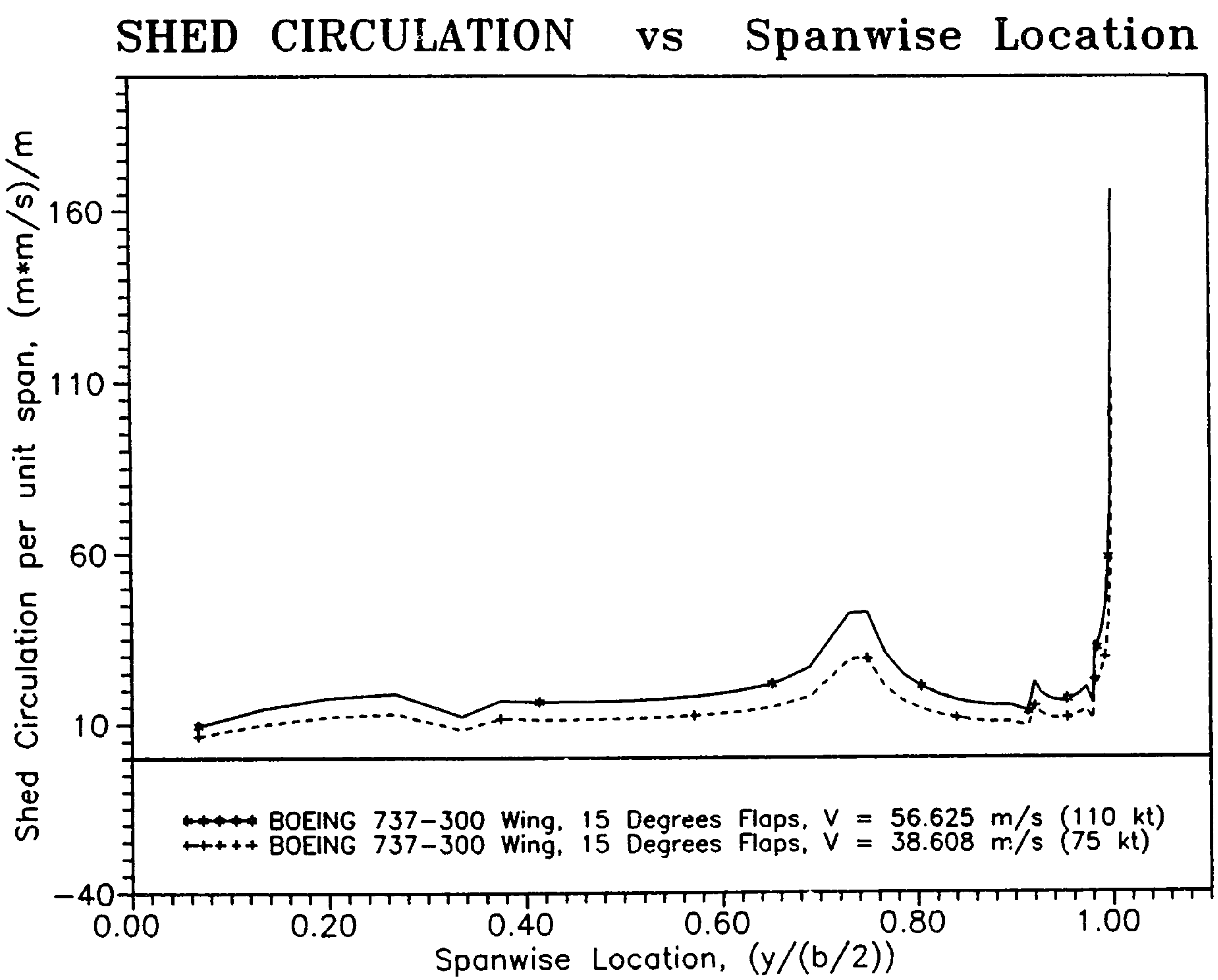

Figure 5.9 BOEING 737-300 Shed Circulation Distribution, $\delta_f = 15°$.

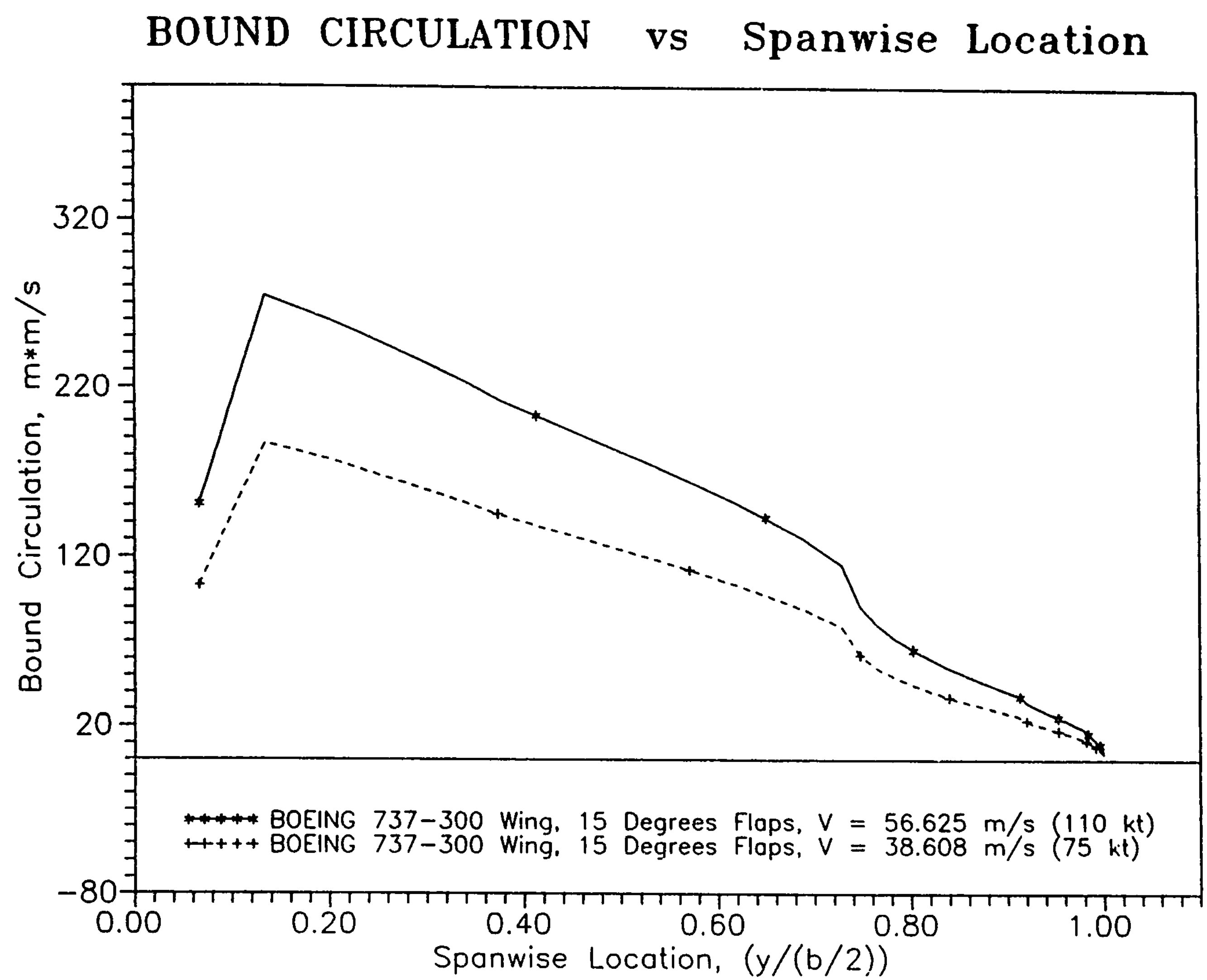

Figure 5.10 BOEING 737-300 Bound Circulation Distribution, $\delta_f = 15°$.

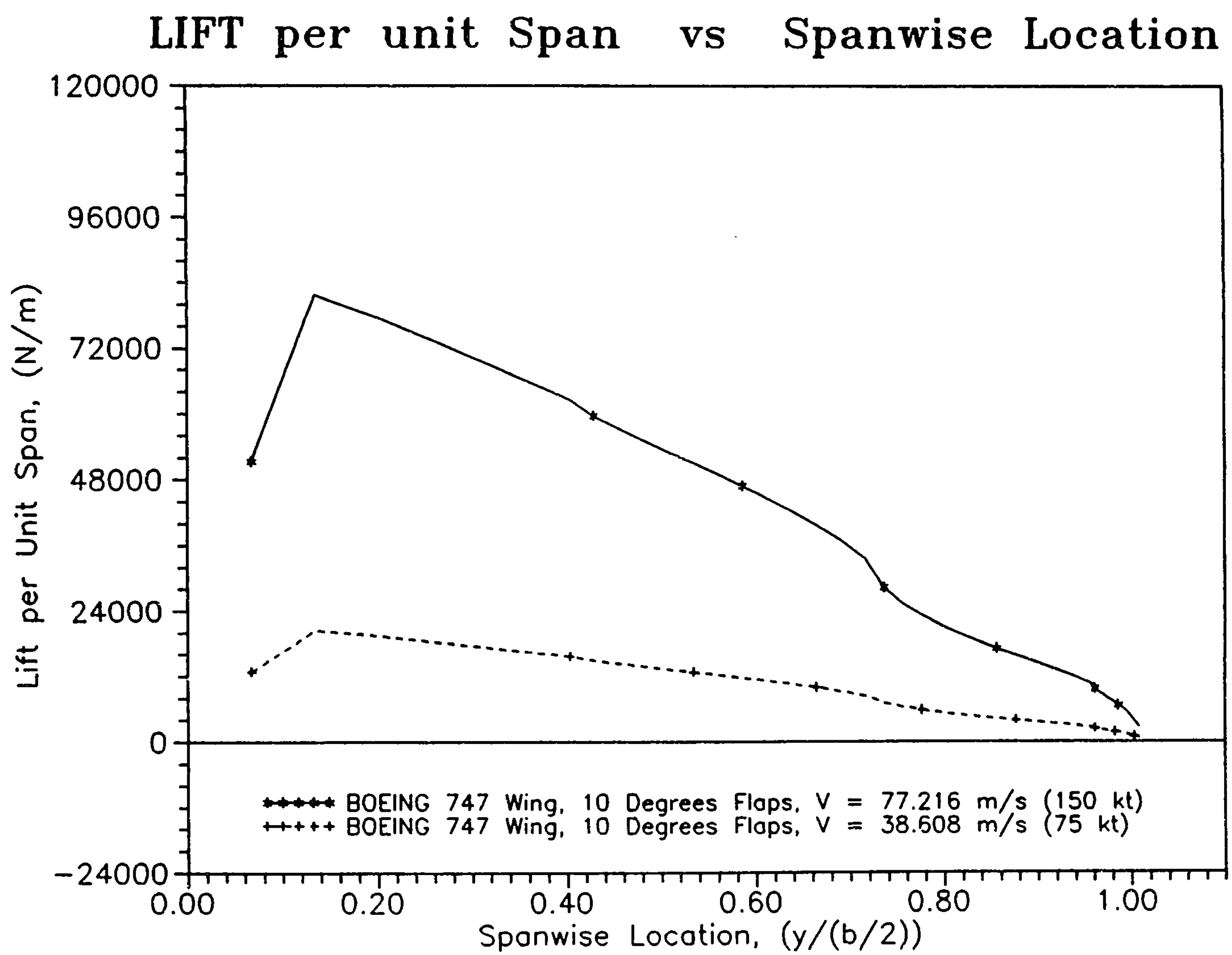

Figure 5.11 BOEING 747 Spanwise Lift Distribution, $\delta_f = 10°$.

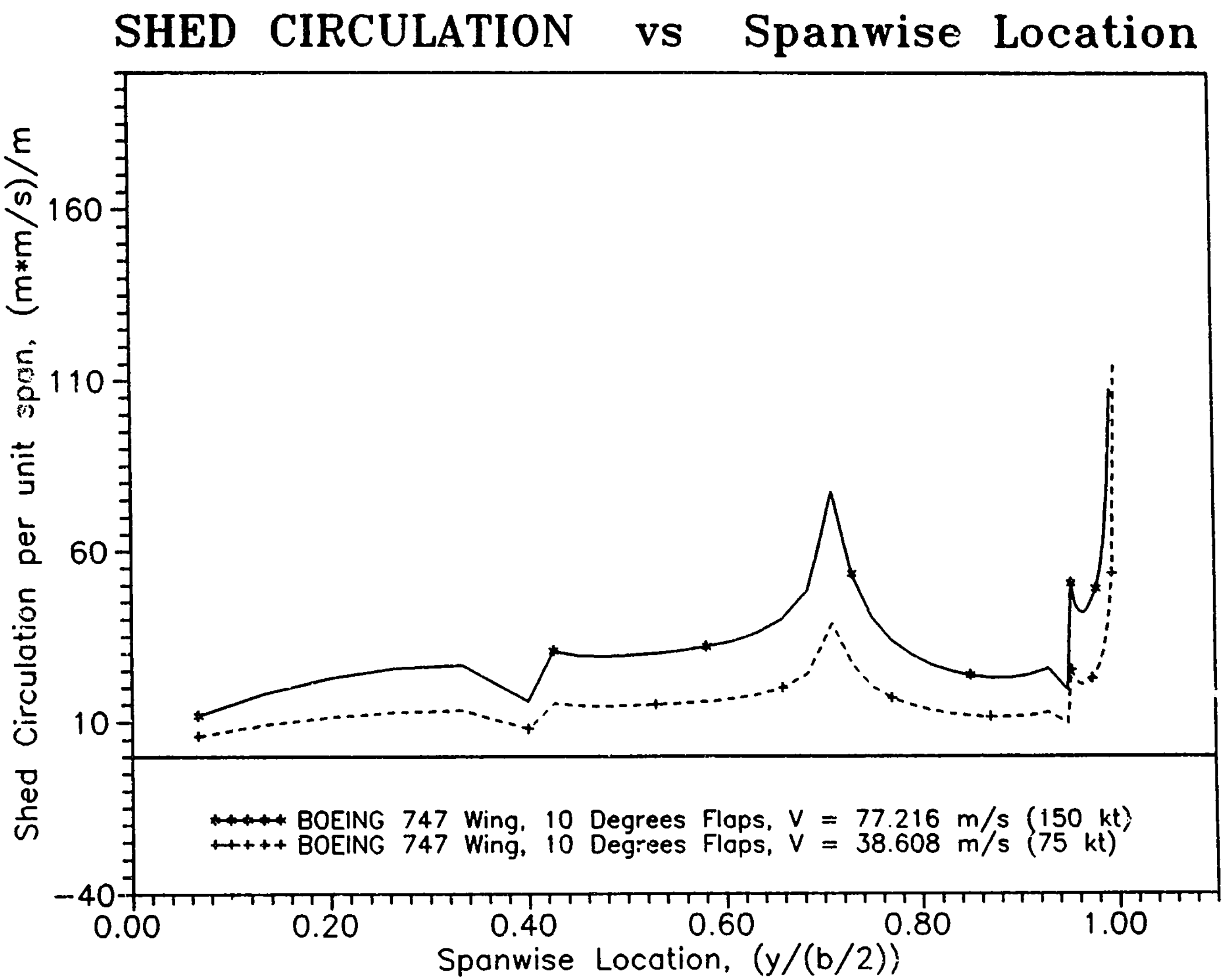

Figure 5.12 BOEING 747 Shed Circulation Distribution, $\delta_f = 10°$.

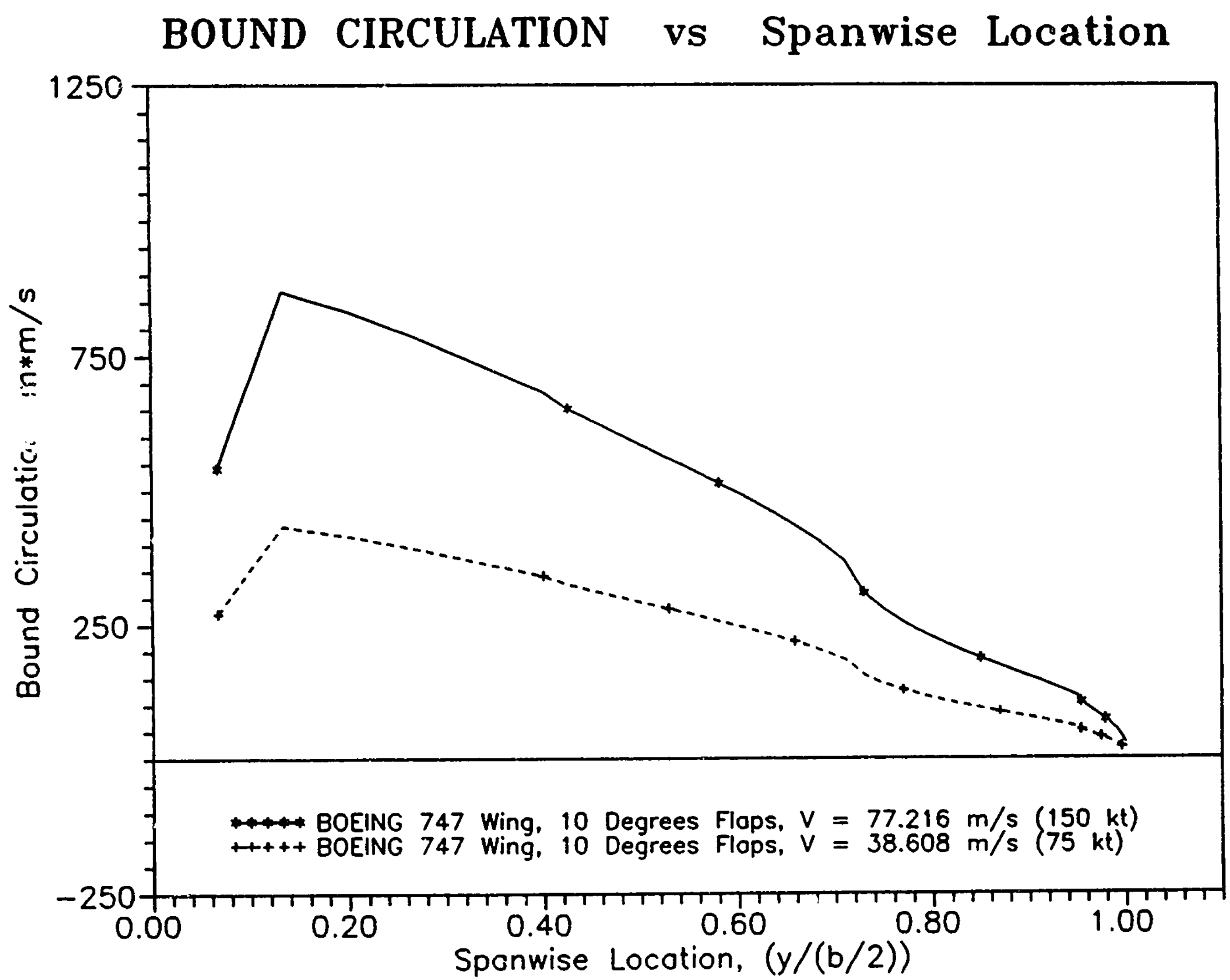

Figure 5.13 BOEING 747 Bound Circulation Distribution, $\delta_f = 10°$.

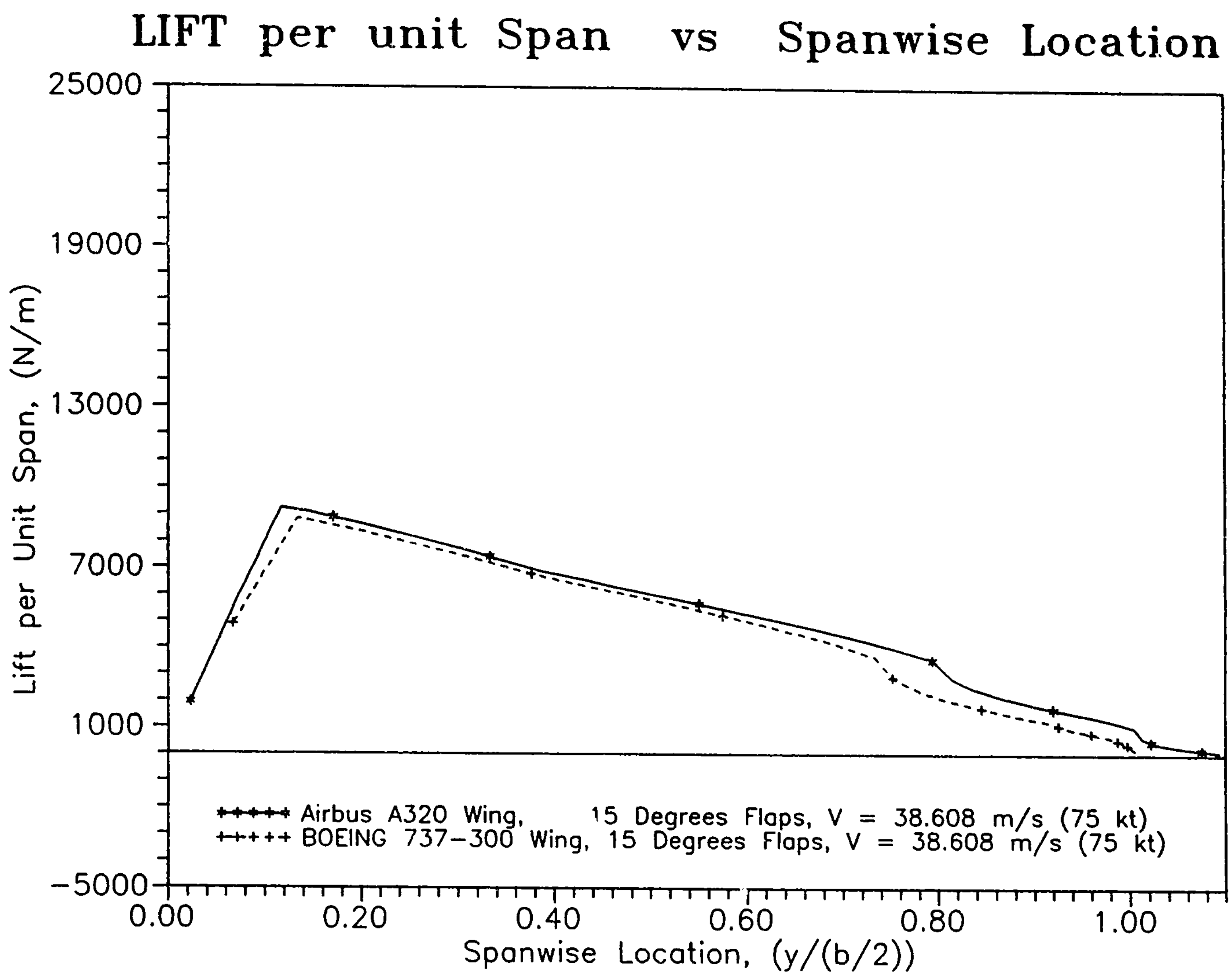

Figure 5.14 Lift versus Spanwise Location for two aircraft, V = 38.608 m/s (75 kt).

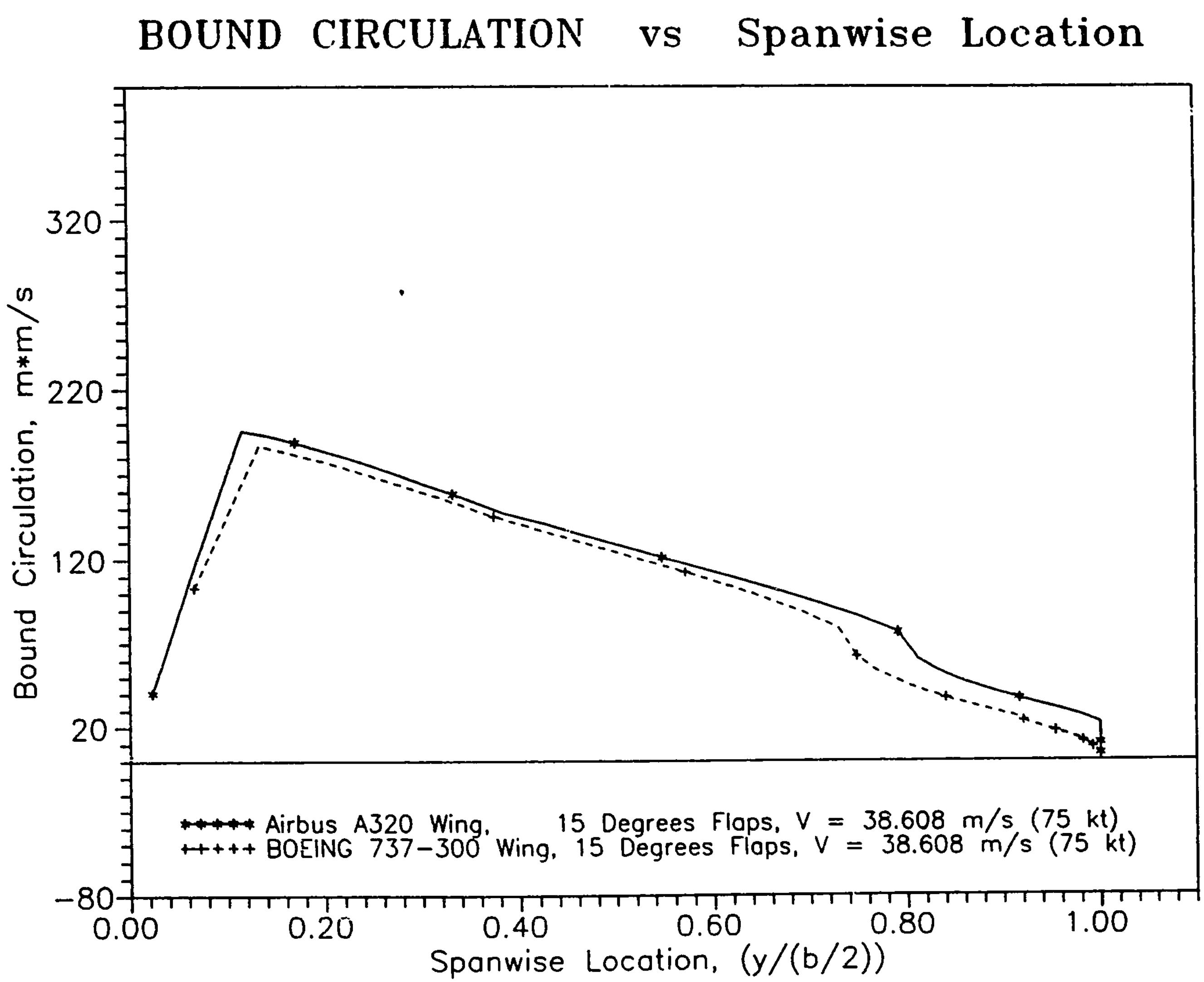

Figure 5.15 Bound Circulation versus Spanwise Location for two aircraft, V = 38.608 m/s (75 kt).

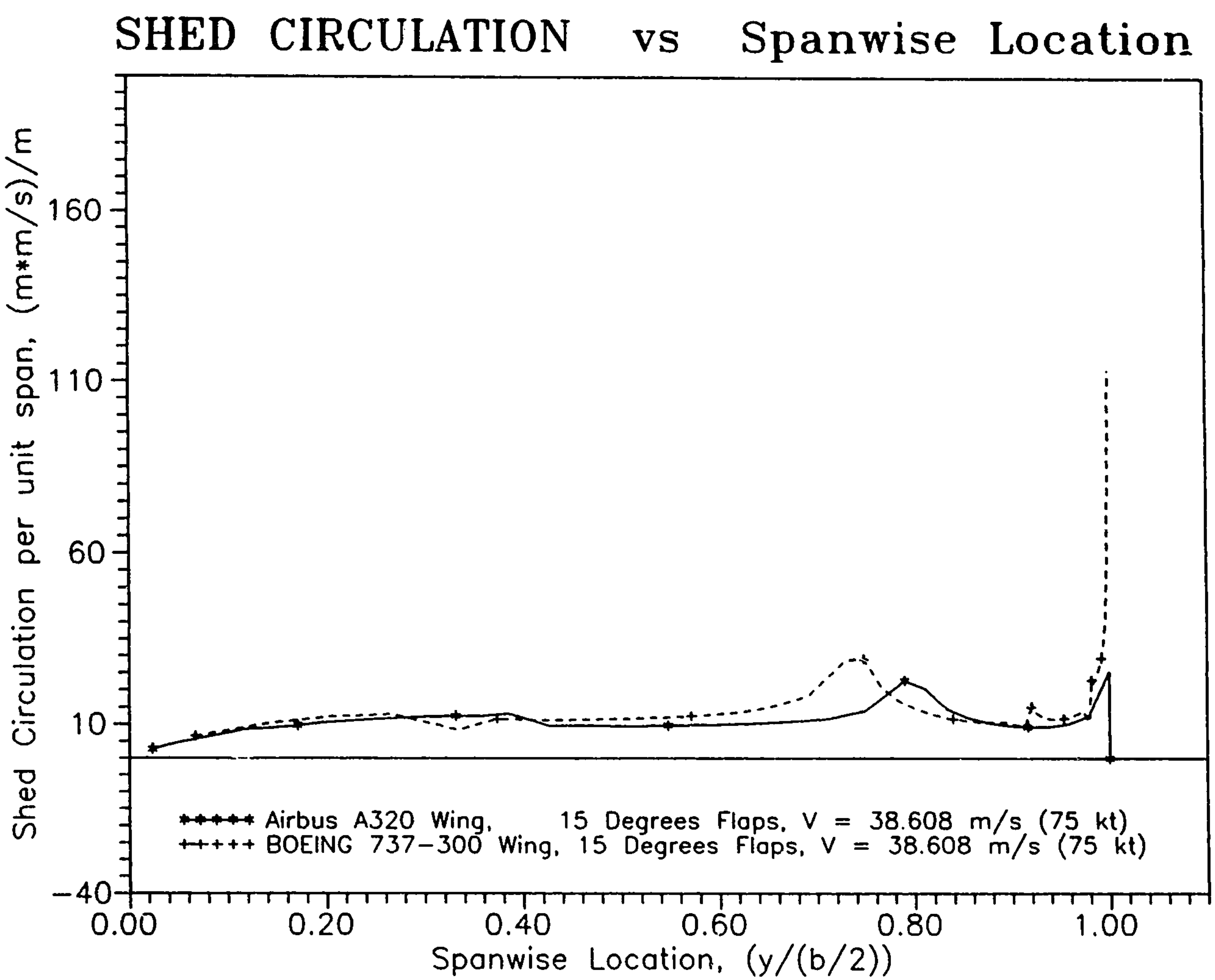

Figure 5.16 Shed Circulation per Unit Span versus Spanwise Location for two aircraft, V = 38.608 m/s (75 kt).

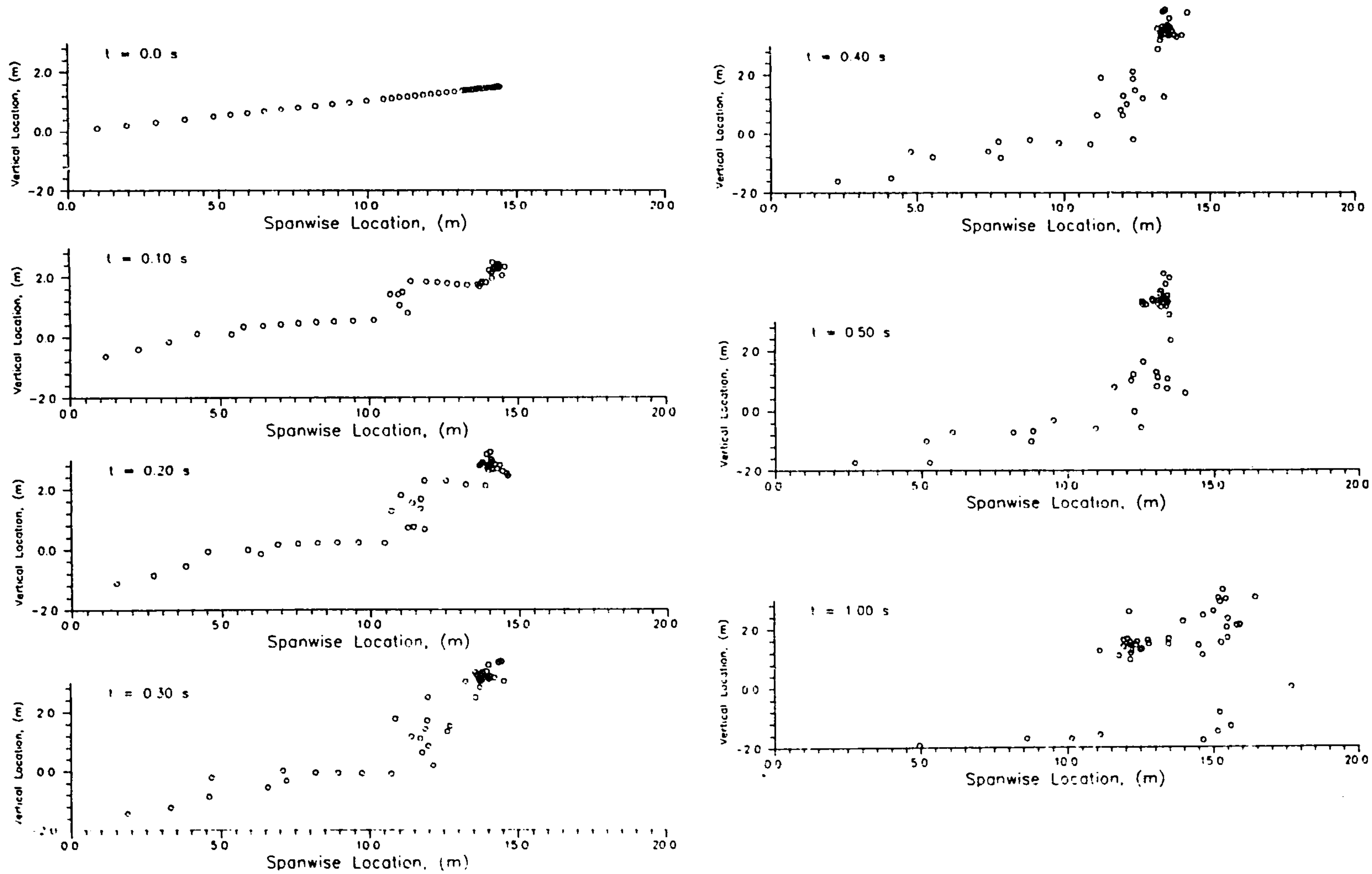

Figure 5.17 BOEING 737-300, $\delta_f = 15°$, Trailing Vortex Roll-Up.

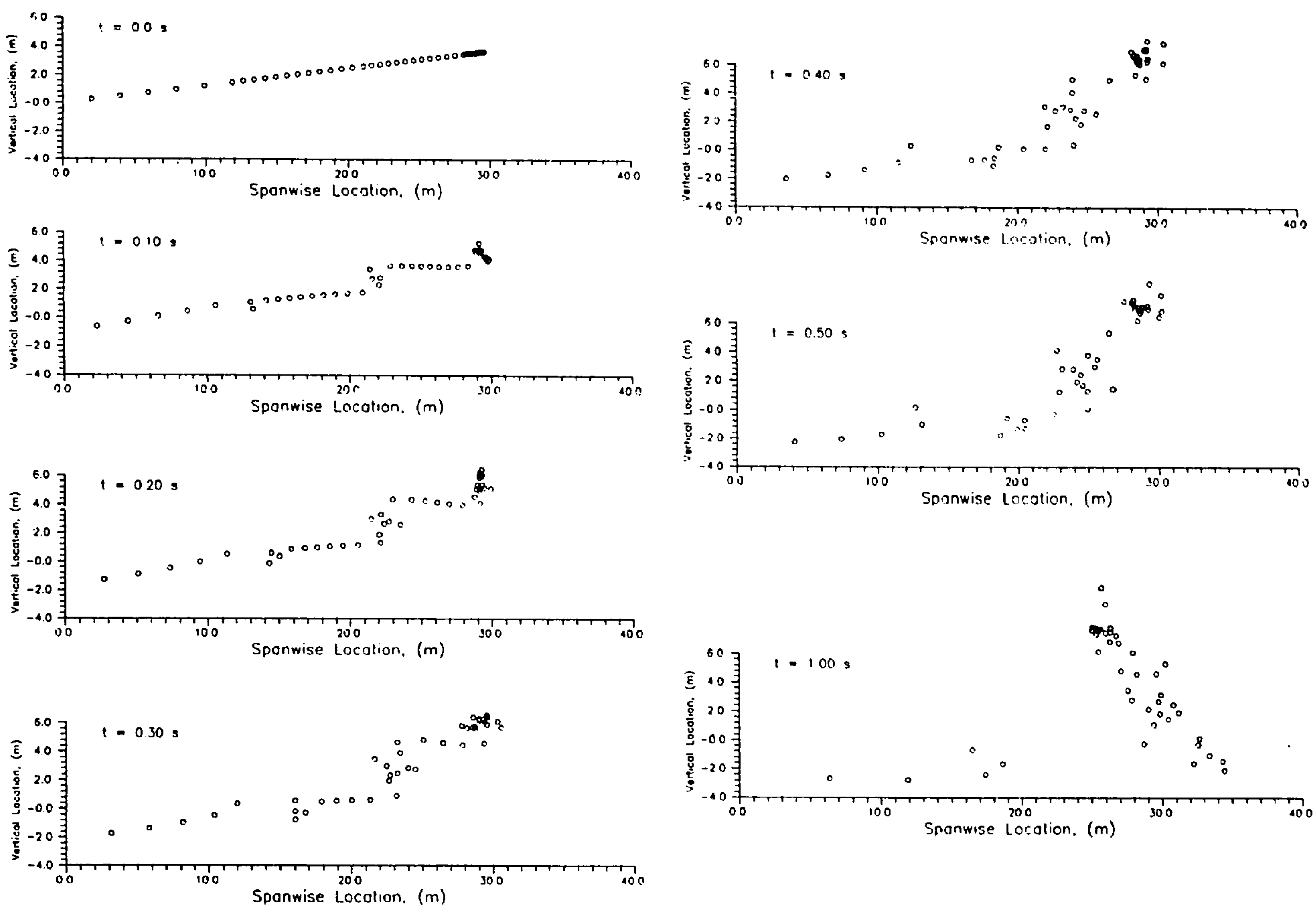

Figure 5.18 BOEING 747, $\delta_f = 10°$, Trailing Vortex Roll-Up.

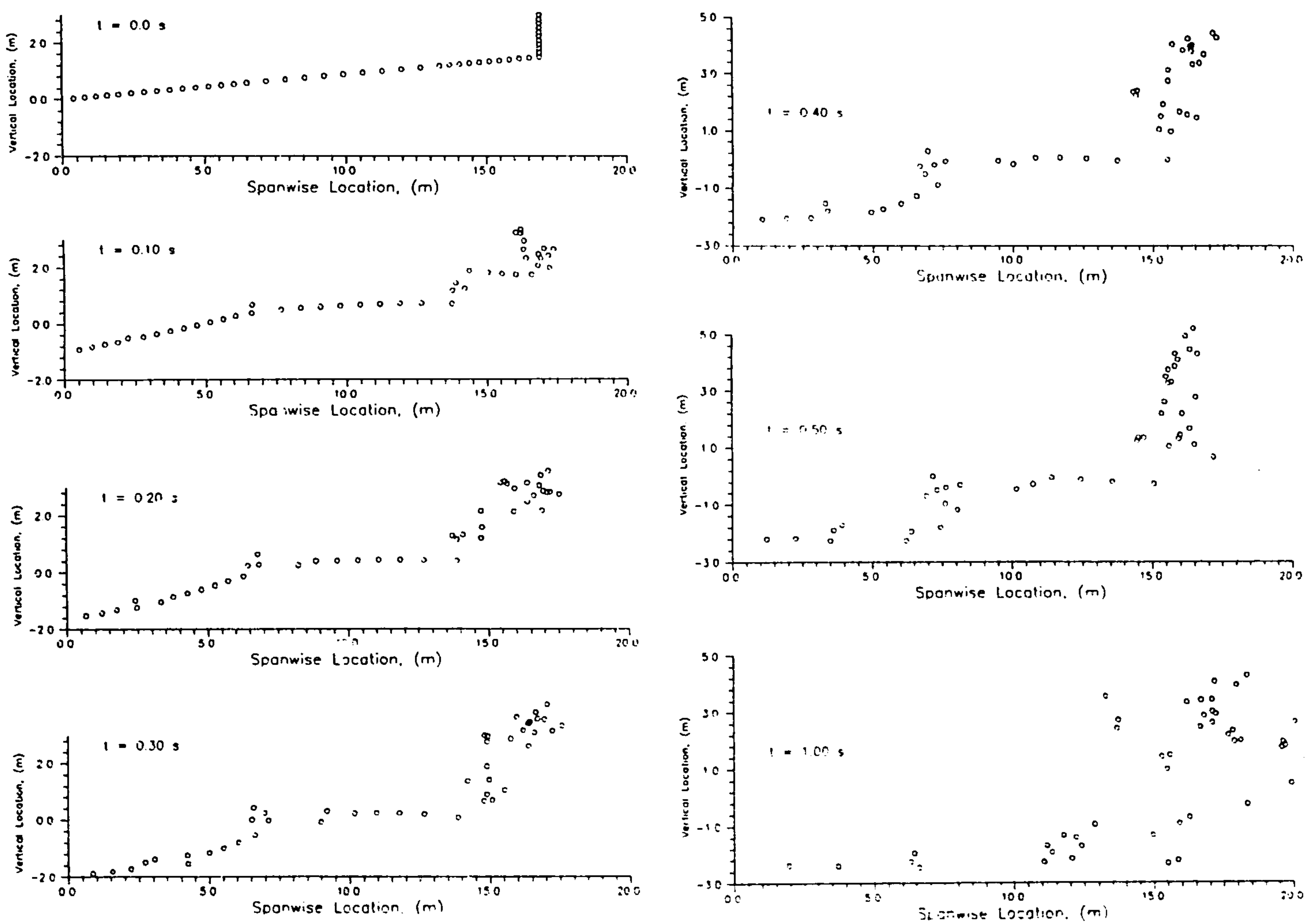

Figure 5.19 Airbus A320, δ_f = 15°, Trailing Vortex Roll-Up.

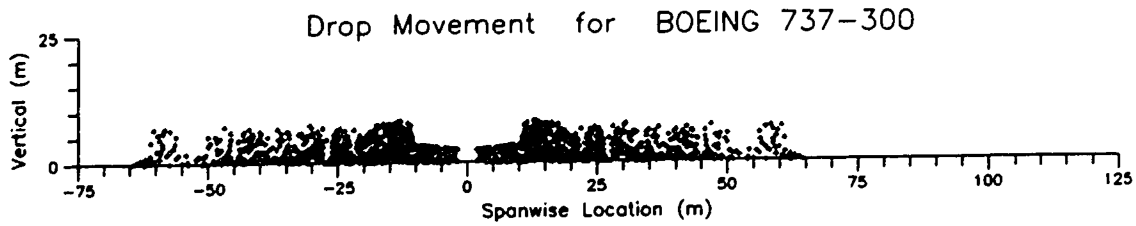

Figure 5.20 Drop Movement, BOEING 737-300, Speed = 56.625 m/s, Crosswind = 0 m/s, Type I Anti-Icing Fluid.

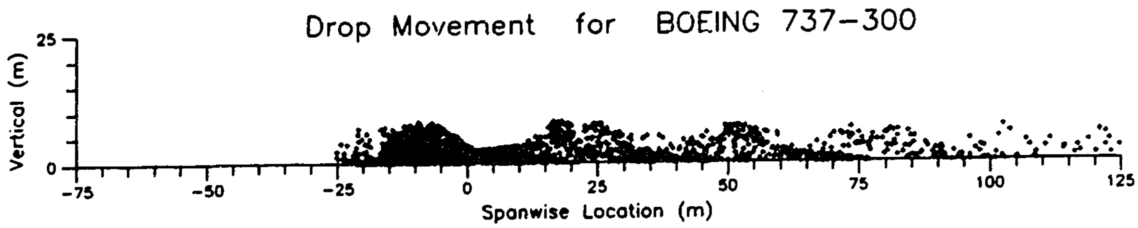

Figure 5.21 Drop Movement, BOEING 737-300, Speed = 56.625 m/s, Crosswind = 5.148 m/s, Type I Anti-Icing Fluid.

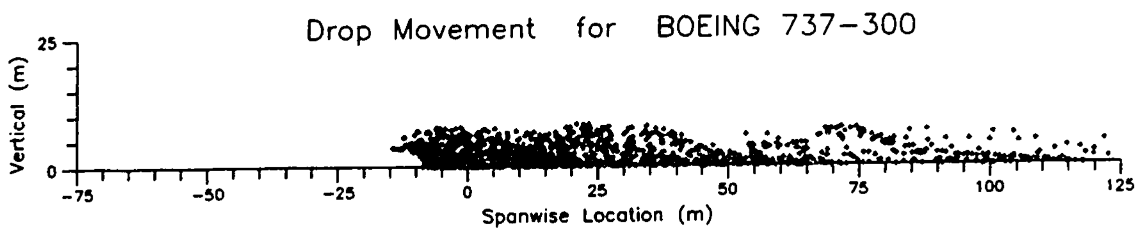

Figure 5.22 Drop Movement, BOEING 737-300, Speed = 56.625 m/s, Crosswind = 10.295 m/s, Type I Anti-Icing Fluid.

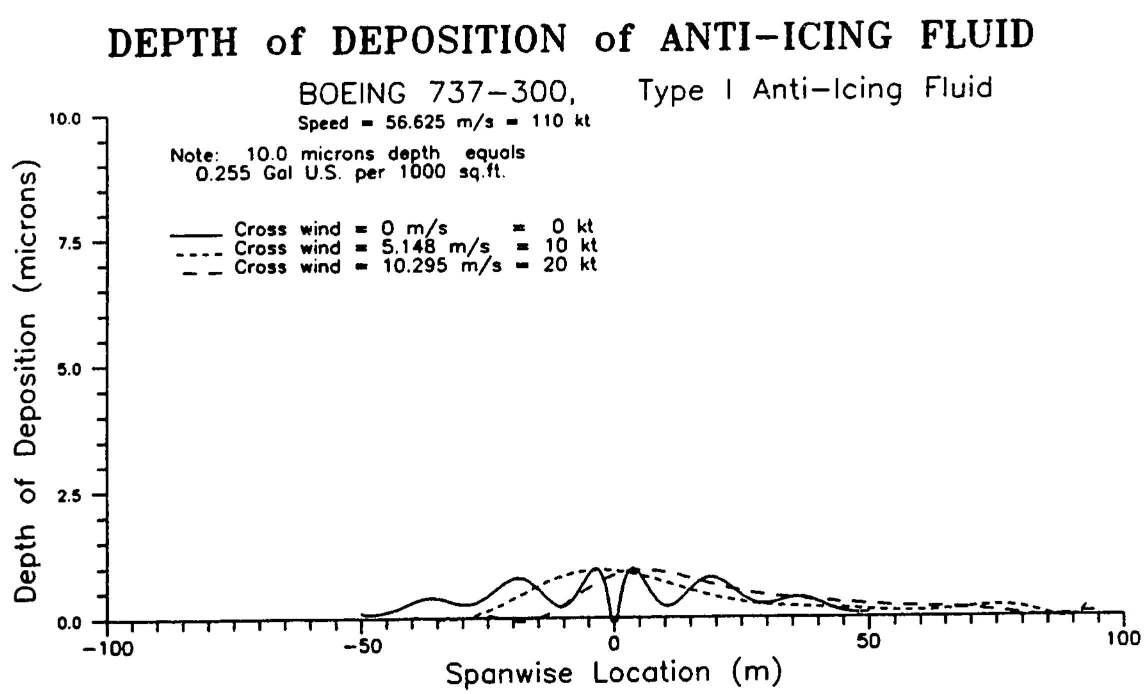

Figure 5.23 Depth of Deposition, BOEING 737-300, Speed = 56.625 m/s, Type I Anti-Icing Fluid.

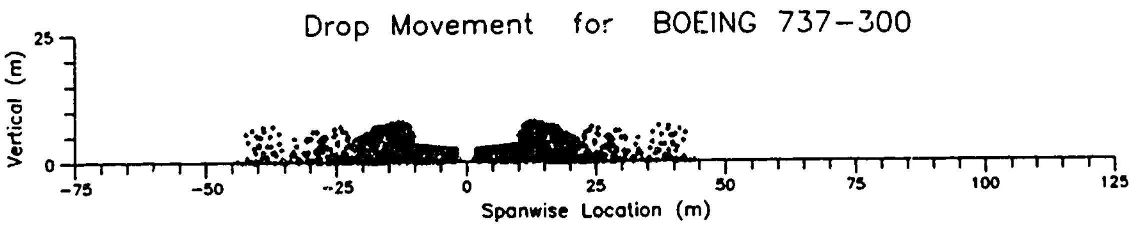

Figure 5.24 Drop Movement, BOEING 737-300, Speed = 38.608 m/s, Crosswind = 0 m/s, Type I Anti-Icing Fluid.

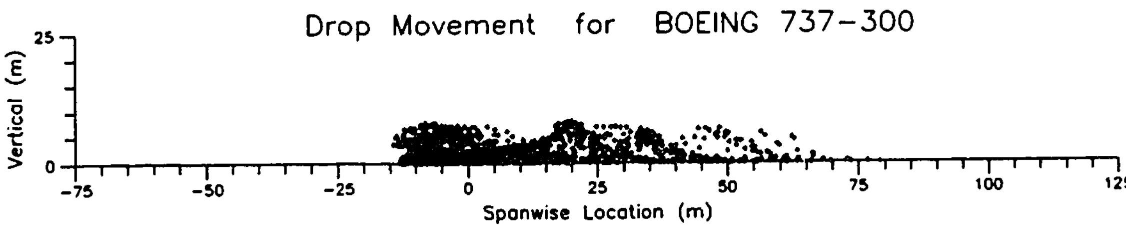

Figure 5.25 Drop Movement, BOEING 737-300, Speed = 38.608 m/s, Crosswind = 5.148 m/s, Type I Anti-Icing Fluid

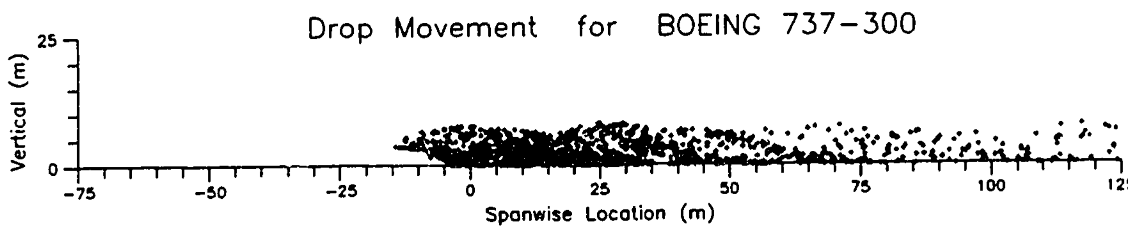

Figure 5.26 Drop Movement, BOEING 737-300, Speed = 38.608 m/s, Crosswind = 10.295 m/s, Type I Anti-Icing Fluid.

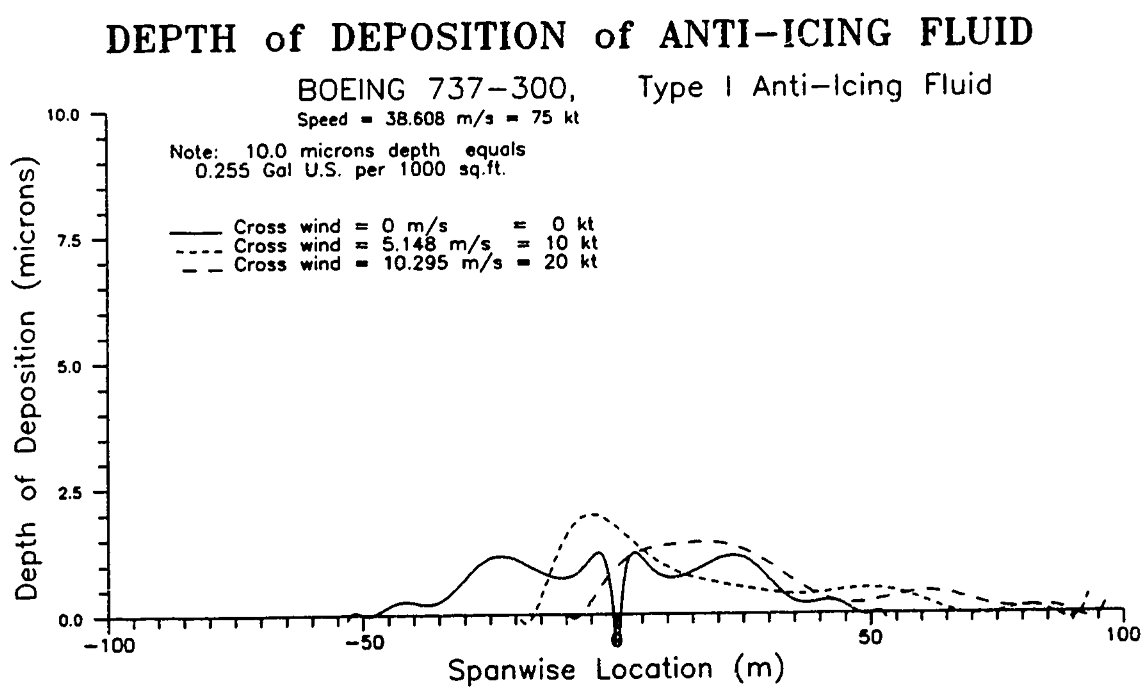

Figure 5.27 Depth of Deposition, BOEING 737-300, Speed = 38.608 m/s, Type I Anti-Icing Fluid.

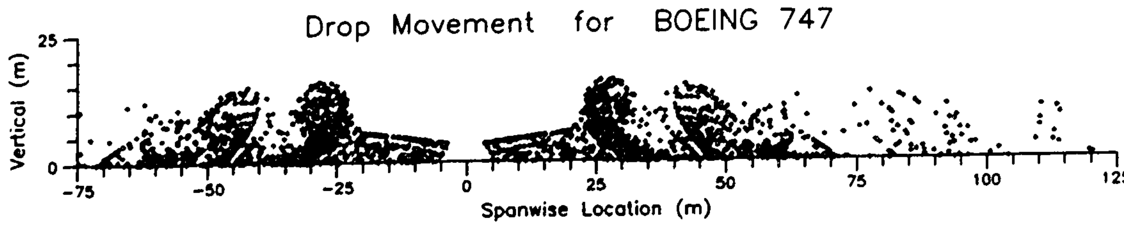

Figure 5.28 Drop Movement, BOEING 747, Speed = 77.216 m/s, Crosswind = 0 m/s, Type I Anti-Icing Fluid.

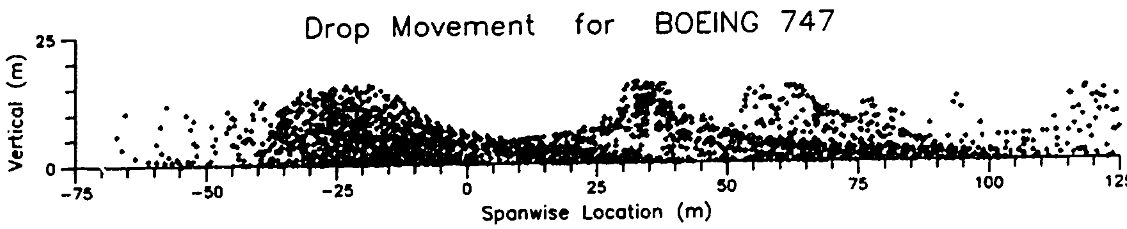

Figure 5.29 Drop Movement, BOEING 747, Speed = 77.216 m/s, Crosswind = 5.148 m/s, Type I Anti-Icing Fluid.

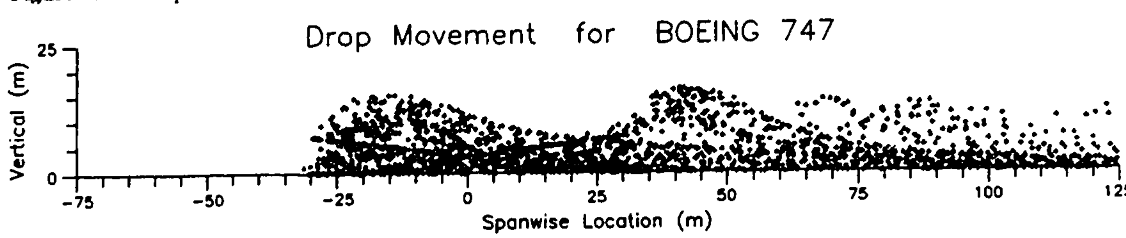

Figure 5.30 Drop Movement, BOEING 747, Speed = 77.216 m/s, Crosswind = 10.295 m/s, Type I Anti-Icing Fluid.

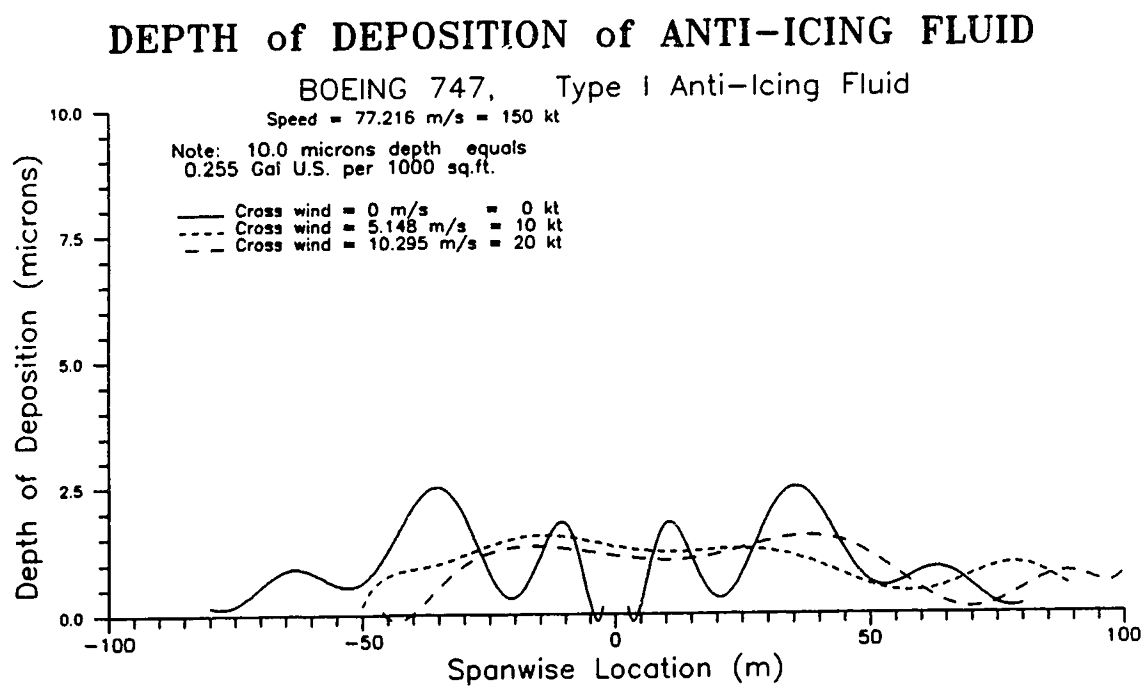

Figure 5.31 Depth of Deposition, BOEING 747, Speed = 77.216 m/s, Type I Anti-Icing Fluid.

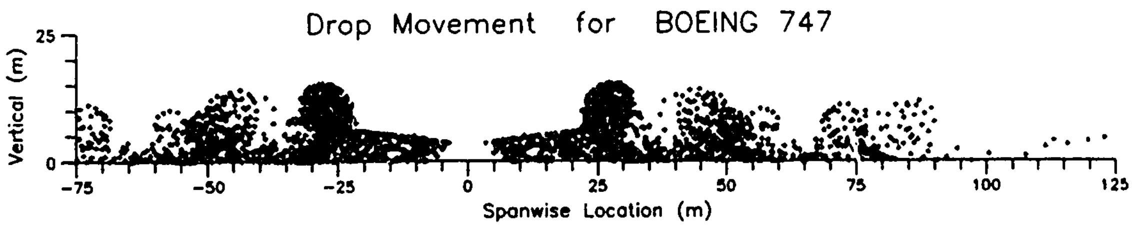

Figure 5.32 Drop Movement, BOEING 747, Speed = 38.608 m/s, Crosswind = 0 m/s, Type I Anti-Icing Fluid.

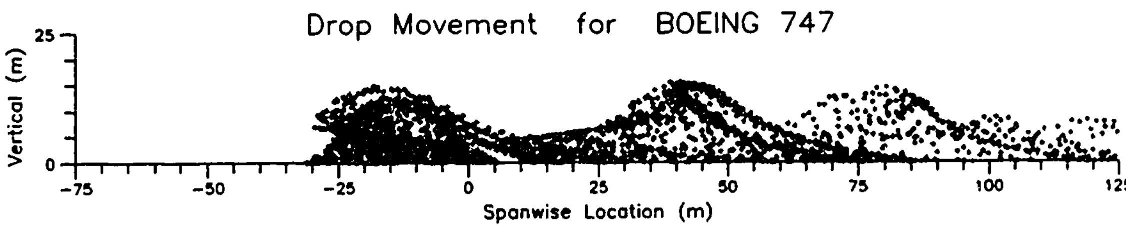

Figure 5.33 Drop Movement, BOEING 747, Speed = 38.608 m/s, Crosswind = 5.148 m/s, Type I Anti-Icing Fluid.

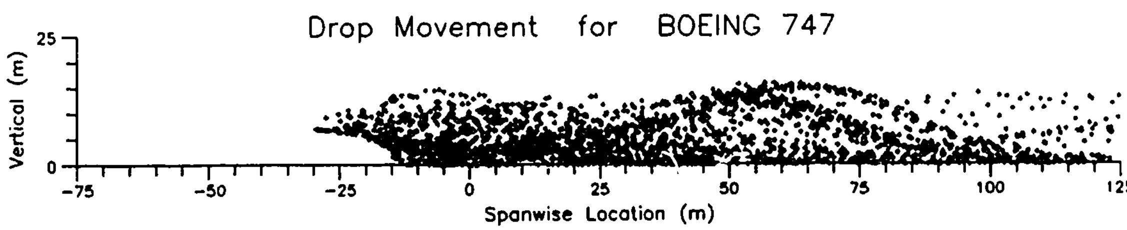

Figure 5.34 Drop Movement, BOEING 747, Speed = 38.608 m/s, Crosswind = 10.295 m/s, Type I Anti-Icing Fluid.

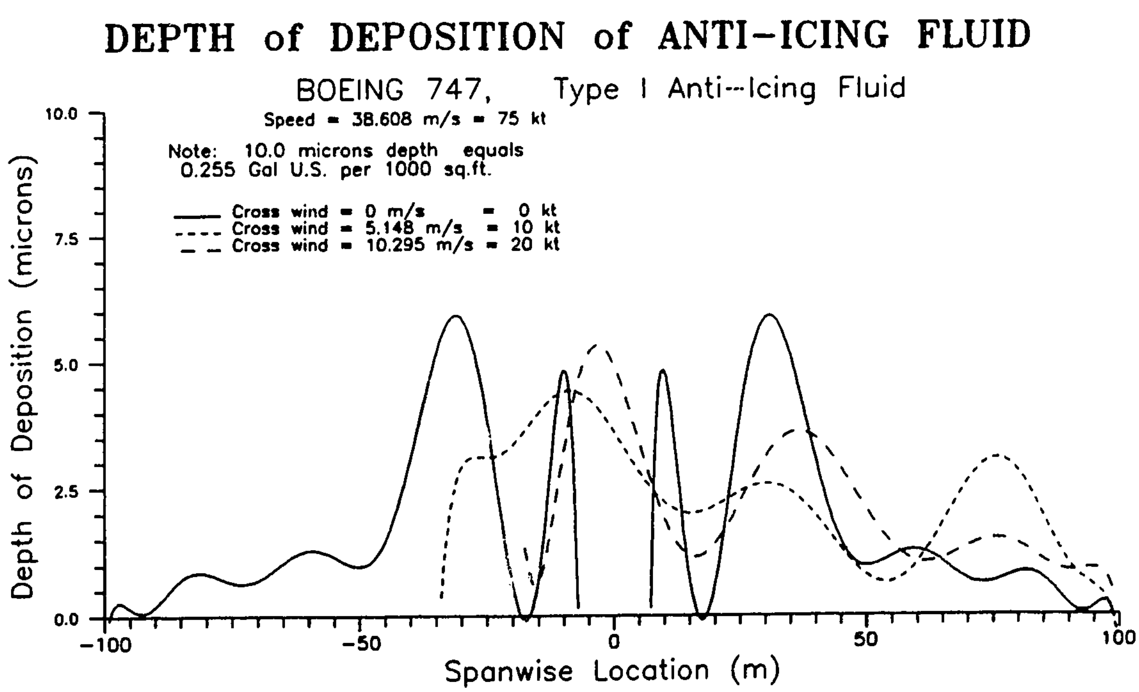

Figure 5.35 Depth of Deposition, BOEING 747, Speed = 38.608 m/s, Type I Anti-Icing Fluid.

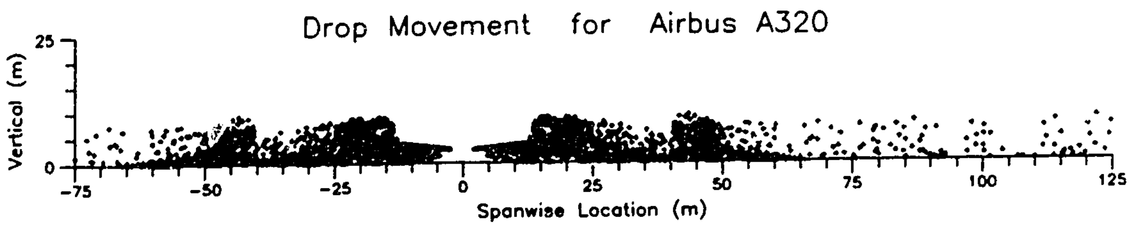

Figure 5.36 Drop Movement, Airbus A320, Speed = 66.921 m/s, Crosswind = 0 m/s, Type I Anti-Icing Fluid.

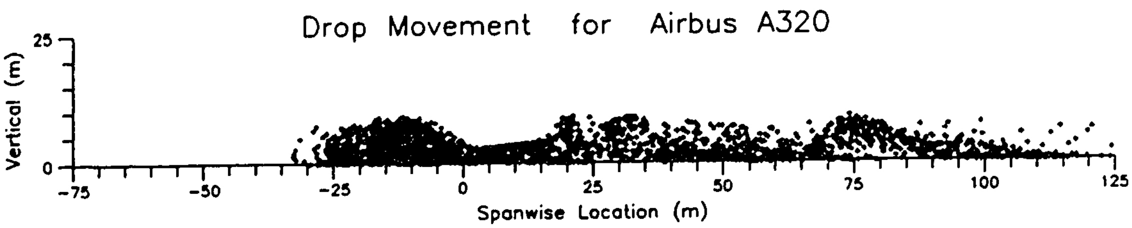

Figure 5.37 Drop Movement, Airbus A320, Speed = 66.921 m/s, Crosswind = 5.148 m/s, Type I Anti-Icing Fluid.

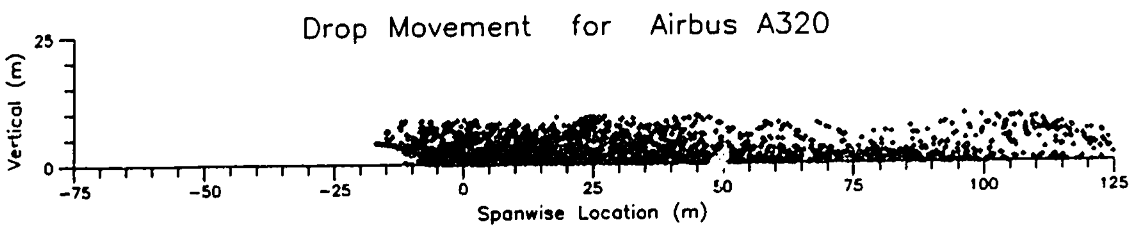

Figure 5.38 Drop Movement, Airbus A320, Speed = 66.921 m/s, Crosswind = 10.295 m/s, Type I Anti-Icing Fluid.

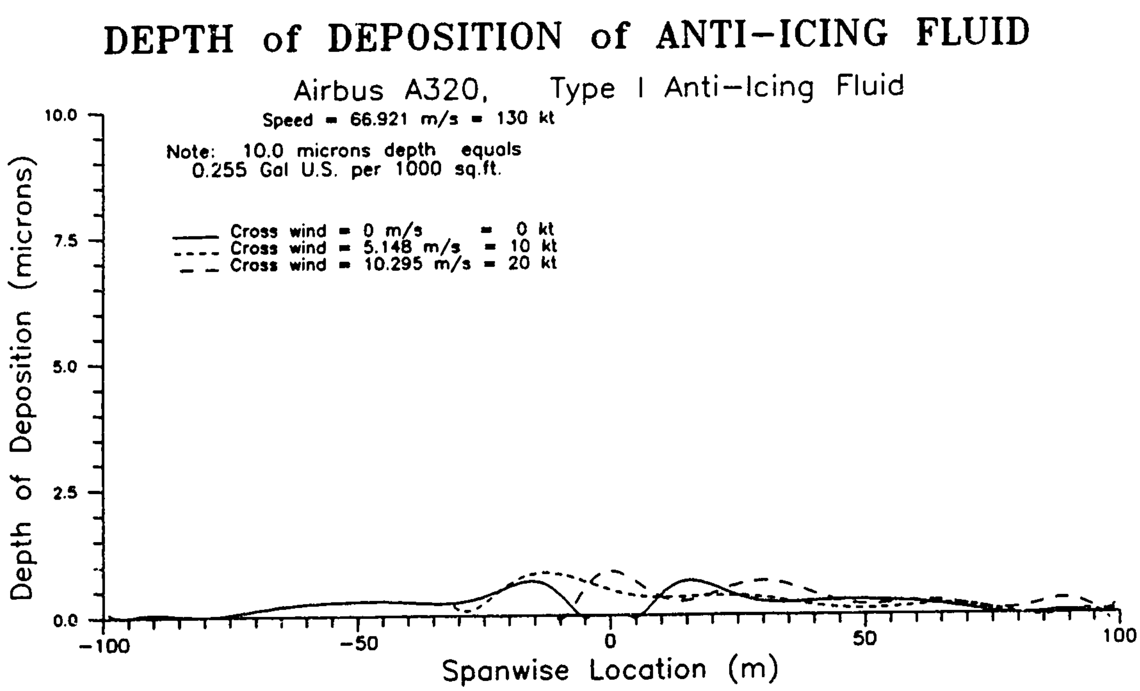

Figure 5.39 Depth of Deposition, Airbus A320, Speed = 66.921 m/s, Type I Anti-Icing Fluid.

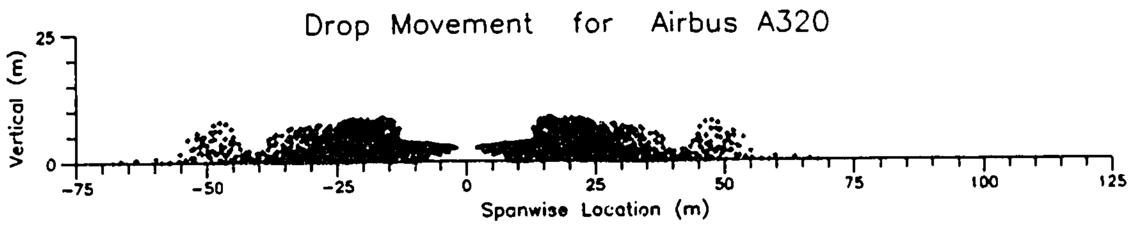

Figure 5.40 Drop Movement, Airbus A320, Speed = 38.608 m/s, Crosswind = 0 m/s, Type I Anti-Icing Fluid.

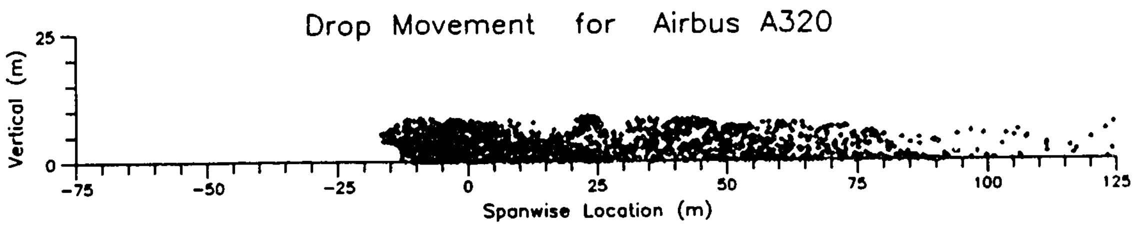

Figure 5.41 Drop Movement, Airbus A320, Speed = 38.608 m/s, Crosswind = 5.148 m/s, Type I Anti-Icing Fluid.

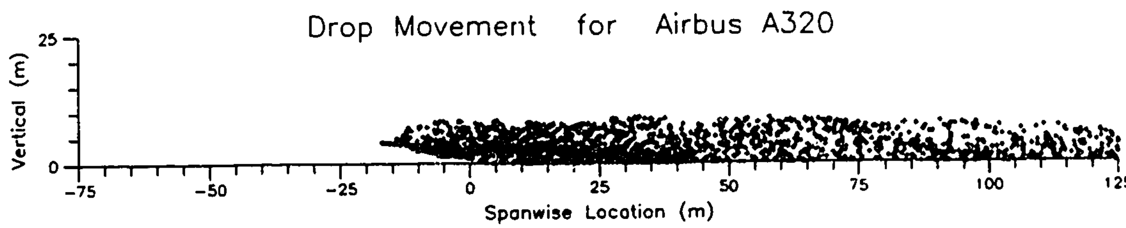

Figure 5.42 Drop Movement, Airbus A320, Speed = 38.608 m/s, Crosswind = 10.295 m/s, Type I Anti-Icing Fluid.

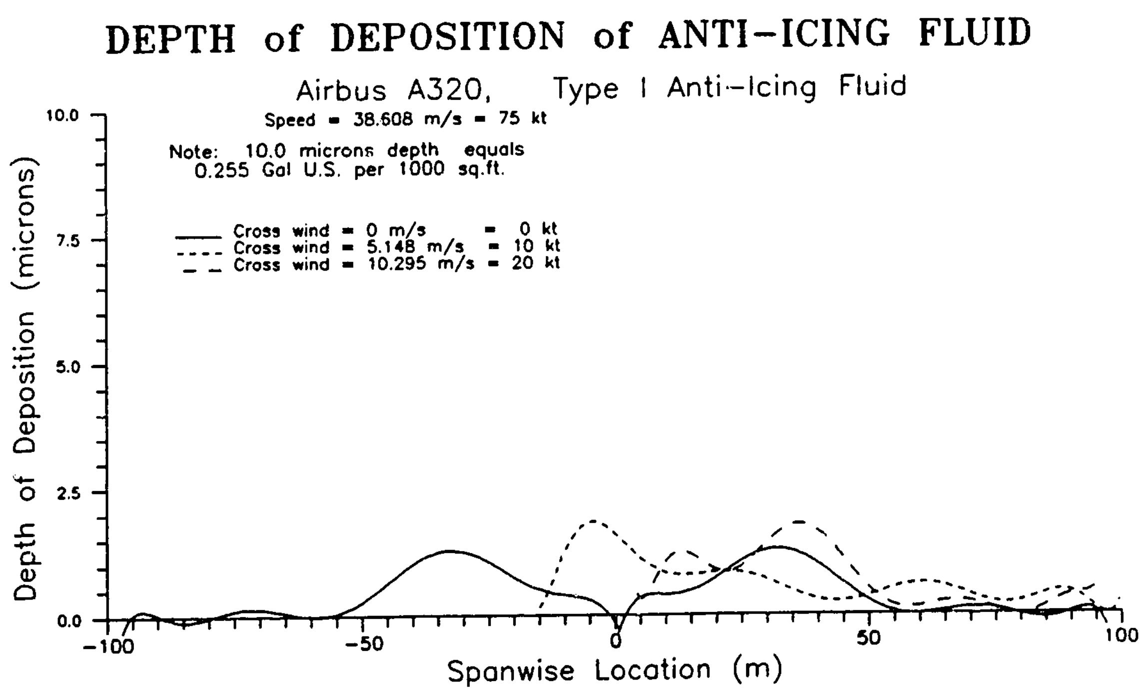

Figure 5.43 Depth of Deposition, Airbus A320, Speed = 38.608 m/s, Type I Anti-Icing Fluid.

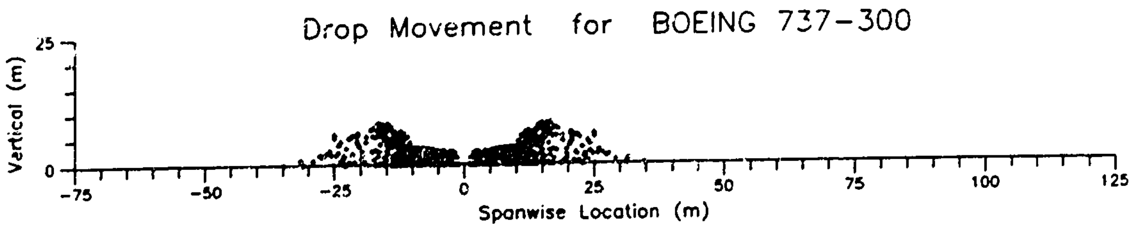

Figure 5.44 Drop Movement, BOEING 737-300, Speed = 56.625 m/s, Crosswind = 0 m/s, Type II Anti-Icing Fluid.

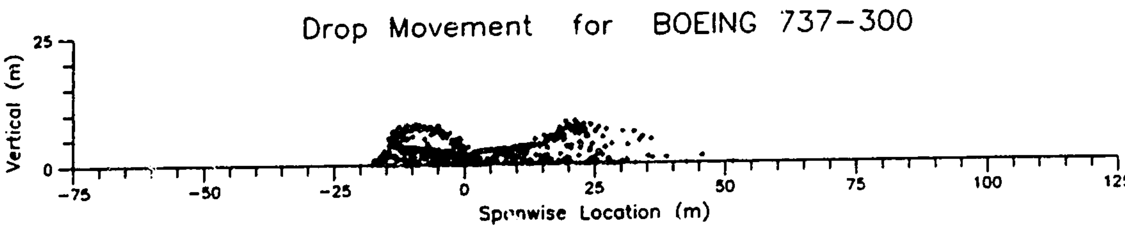

Figure 5.45 Drop Movement, BOEING 737-300, Speed = 56.625 m/s, Crosswind = 5.148 m/s, Type II Anti-Icing Fluid.

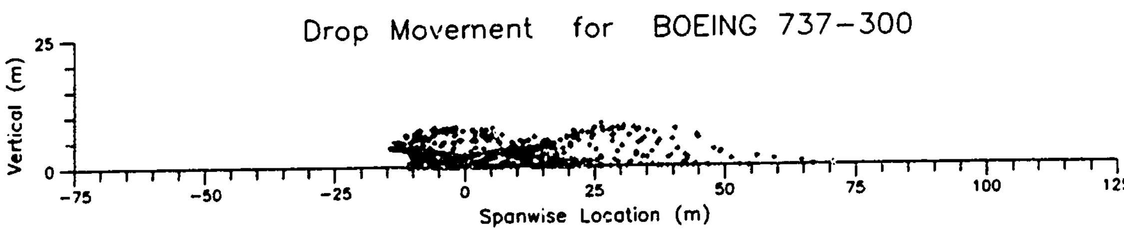

Figure 5.46 Drop Movement, BOEING 737-300, Speed = 56.625 m/s, Crosswind = 10.295 m/s, Type II Anti-Icing Fluid.

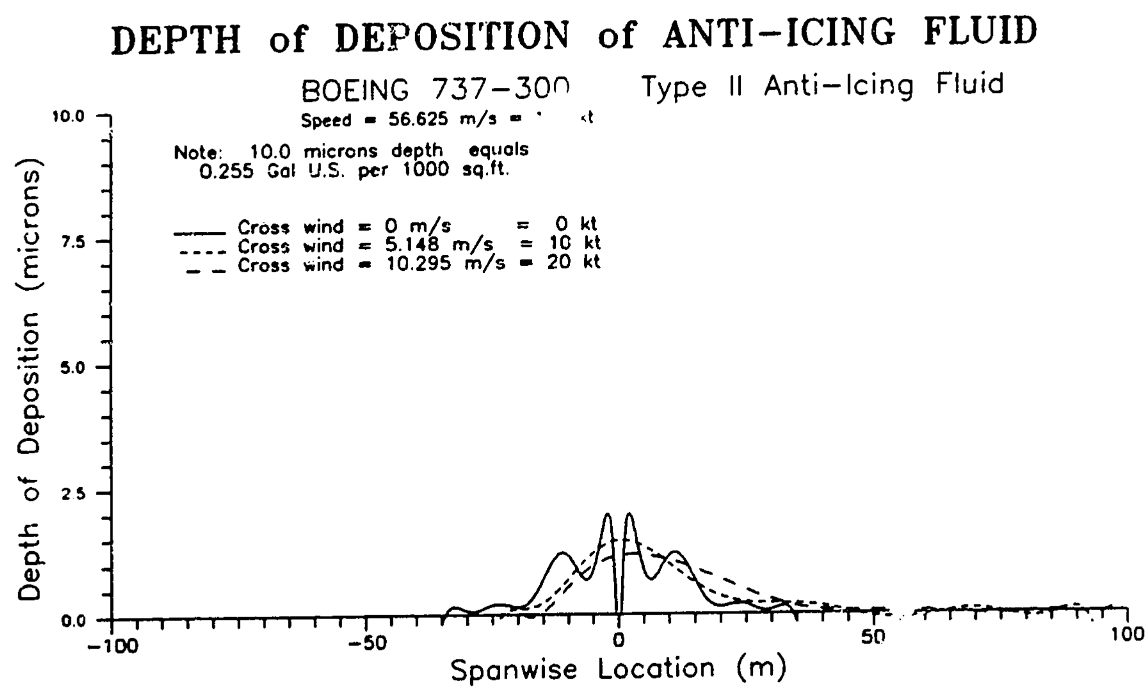

Figure 5.47 Depth of Deposition, BOEING 737-300, Speed = 56.625 m/s, Type II Anti-Icing Fluid.

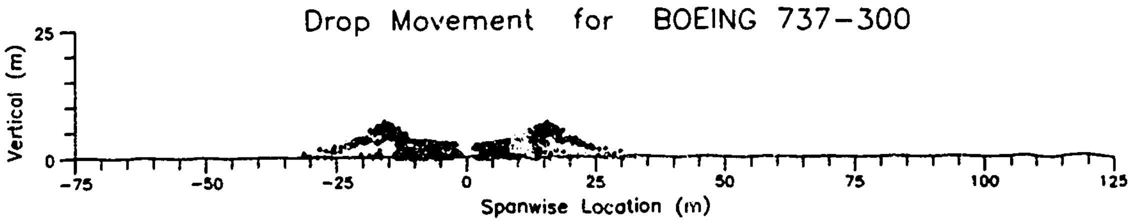

Figure 5.48 Drop Movement, BOEING 737-300, Speed = 38.608 m/s, Crosswind = 0 m/s, Type II Anti-Icing Fluid.

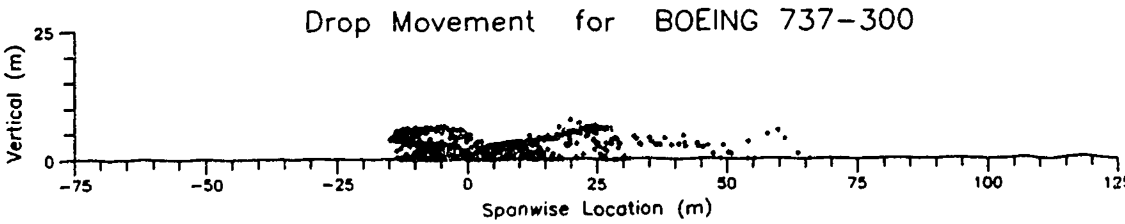

Figure 5.49 Drop Movement, BOEING 737-300, Speed = 38.608 m/s, Crosswind = 5.148 m/s, Type II Anti-Icing Fluid.

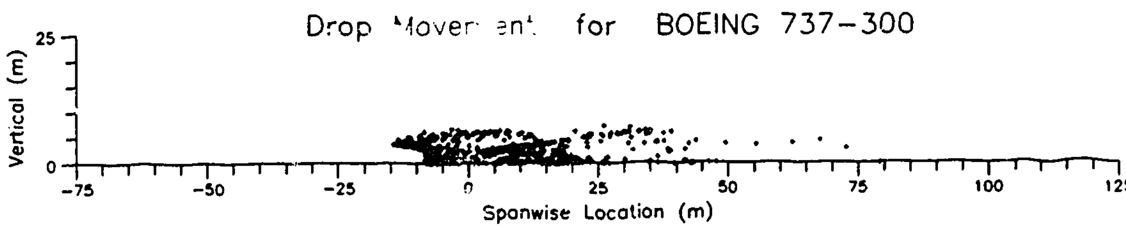

Figure 5.50 Drop Movement, BOEING 737-300, Speed = 38.608 m/s, Crosswind = 10.295 m/s, Type II Anti-Icing Fluid.

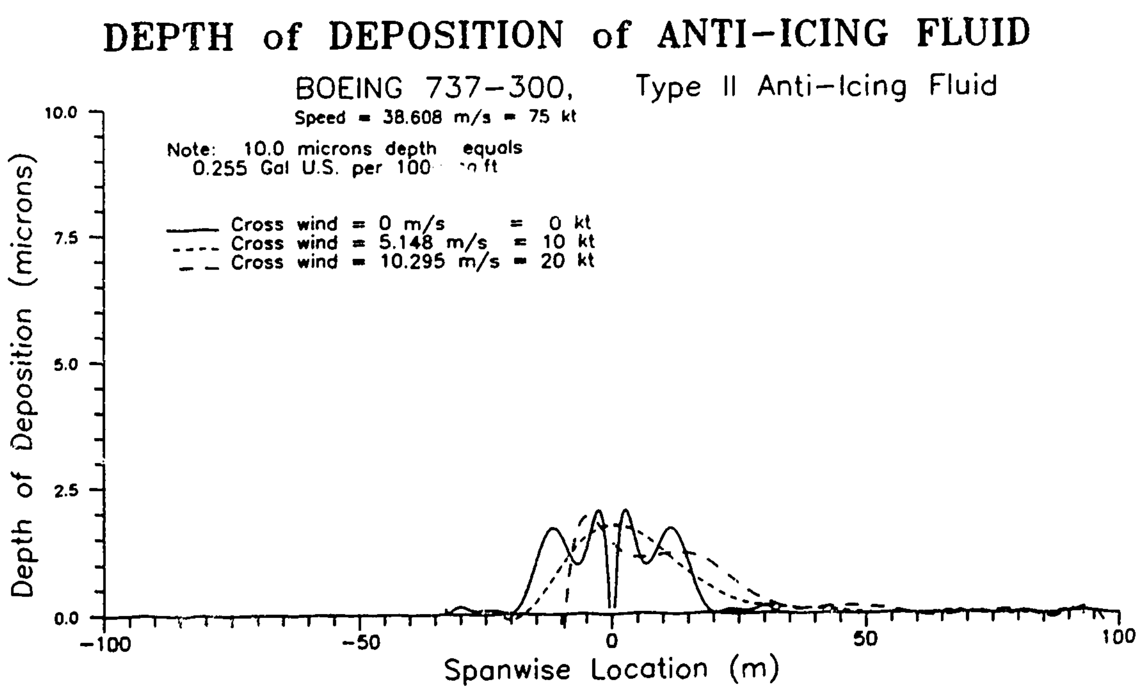

Figure 5.51 Depth of Deposition, BOEING 737-300, Speed = 38.608 m/s, Type II Anti-Icing Fluid.

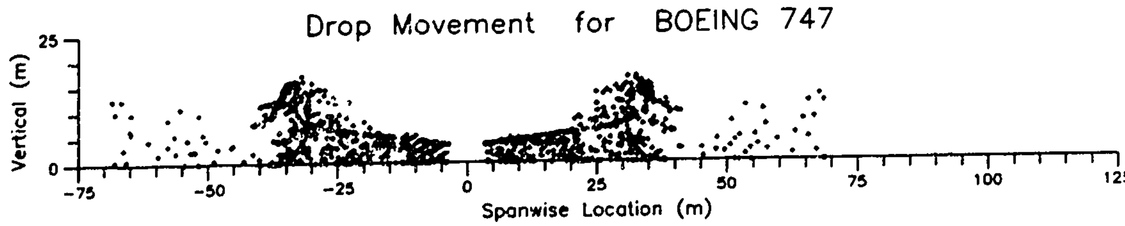

Figure 5.52 Drop Movement, BOEING 747, Speed = 77.216 m/s, Crosswind = 0 m/s, Type II Anti-Icing Fluid.

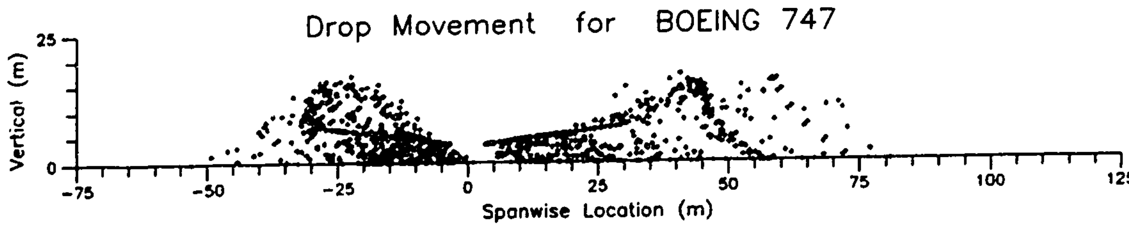

Figure 5.53 Drop Movement, BOEING 747, Speed = 77.216 m/s, Crosswind = 5.148 m/s, Type II Anti-Icing Fluid.

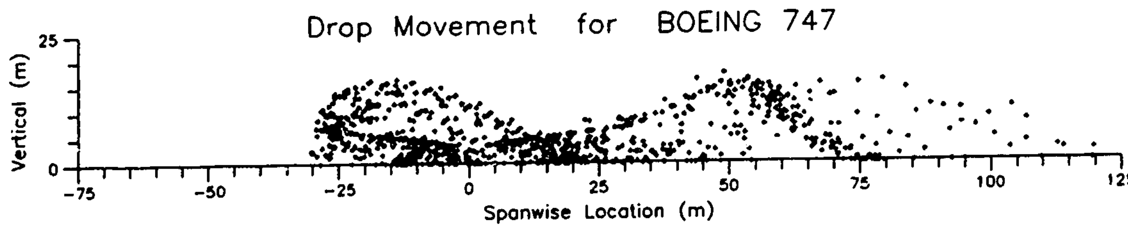

Figure 5.54 Drop Movement, BOEING 747, Speed = 77.216 m/s, Crosswind = 10.295 m/s, Type II Anti-Icing Fluid.

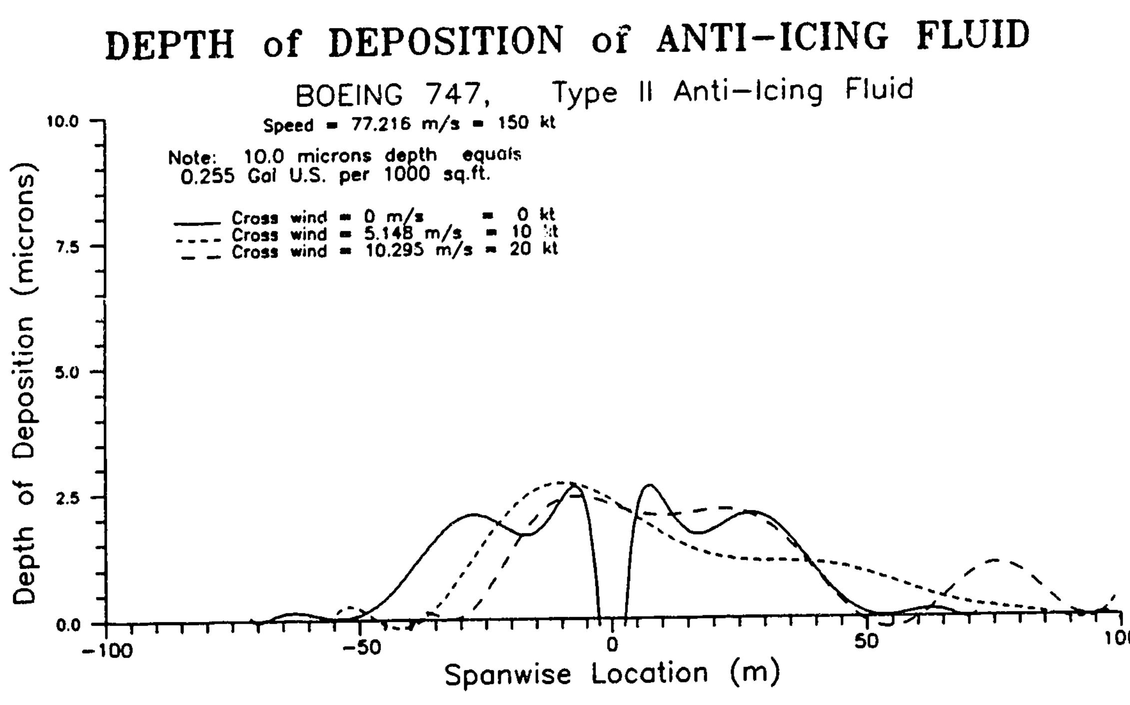

Figure 5.55 Depth of Deposition, BOEING 747, Speed = 77.216 m/s, Type II Anti-Icing Fluid.

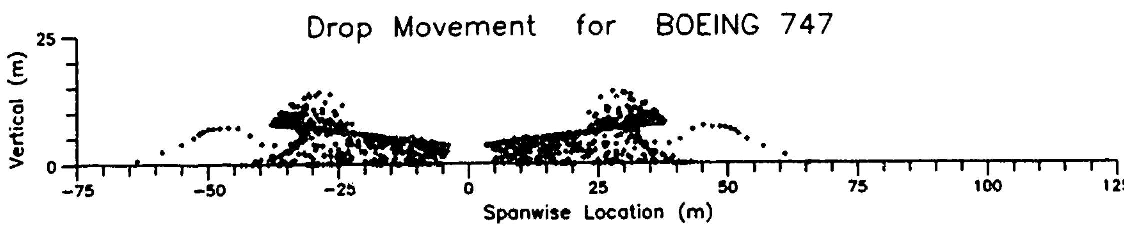

Figure 5.56 Drop Movement, BOEING 747, Speed = 38.608 m/s, Crosswind = 0 m/s, Type II Anti-Icing Fluid.

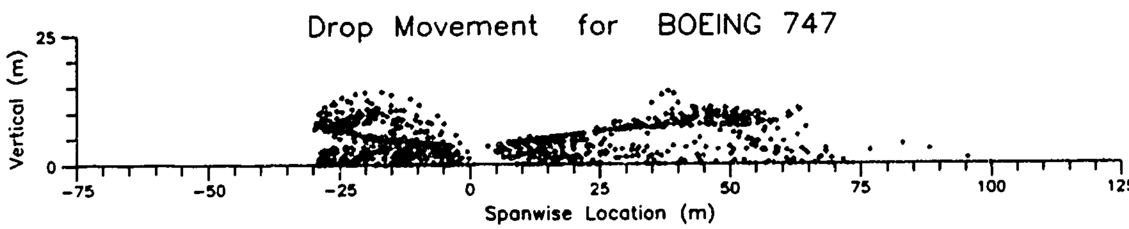

Figure 5.57 Drop Movement, BOEING 747, Speed = 38.608 m/s, Crosswind = 5.148 m/s, Type II Anti-Icing Fluid.

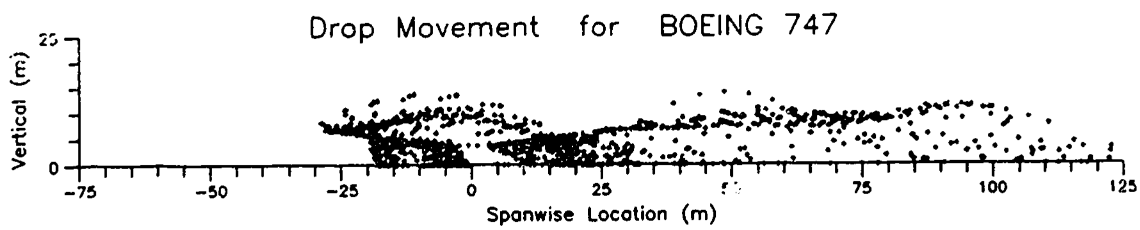

Figure 5.58 Drop Movement, BOEING 747, Speed = 38.608 m/s, Crosswind = 10.295 m/s, Type II Anti-Icing Fluid.

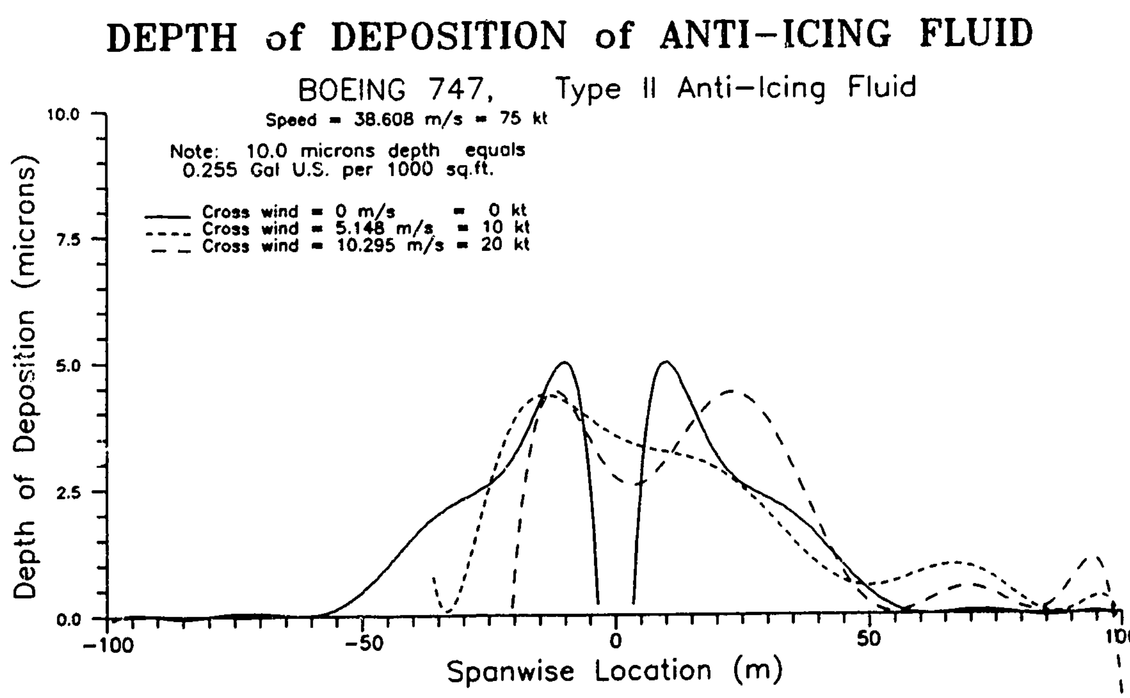

Figure 5.59 Depth of Deposition, BOEING 747, Speed = 38.608 m/s, Type II Anti-Icing Fluid.

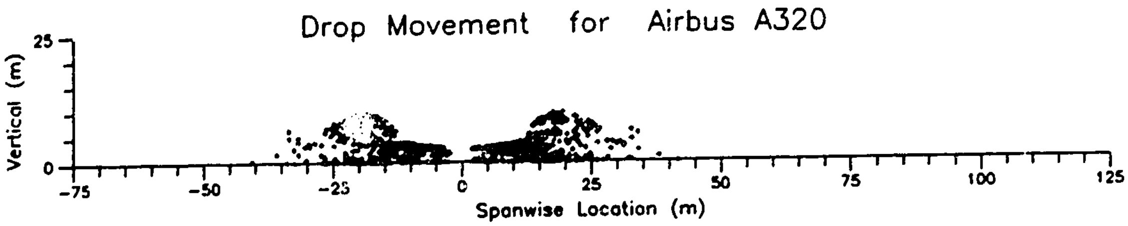

Figure 5.60 Drop Movement, Airbus A320, Speed = 66.921 m/s, Crosswind = 0 m/s, Type II Anti-Icing Fluid.

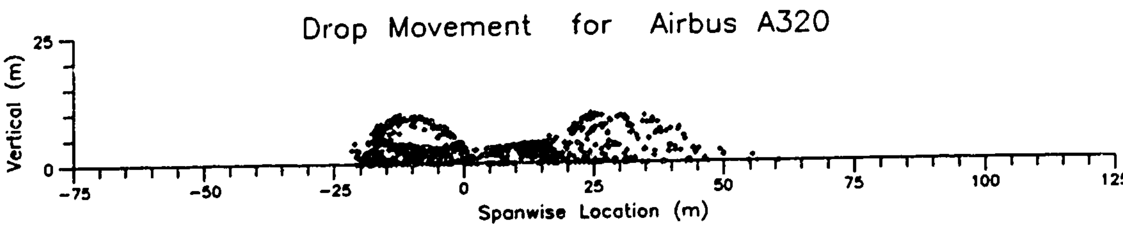

Figure 5.61 Drop Movement, Airbus A320, Speed = 66.921 m/s, Crosswind = 5.148 m/s, Type II Anti-Icing Fluid.

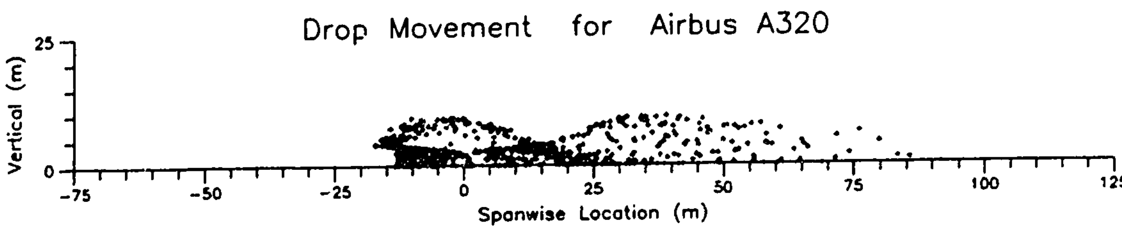

Figure 5.62 Drop Movement, Airbus A320, Speed = 66.921 m/s, Crosswind = 10.295 m/s, Type II Anti-Icing Fluid.

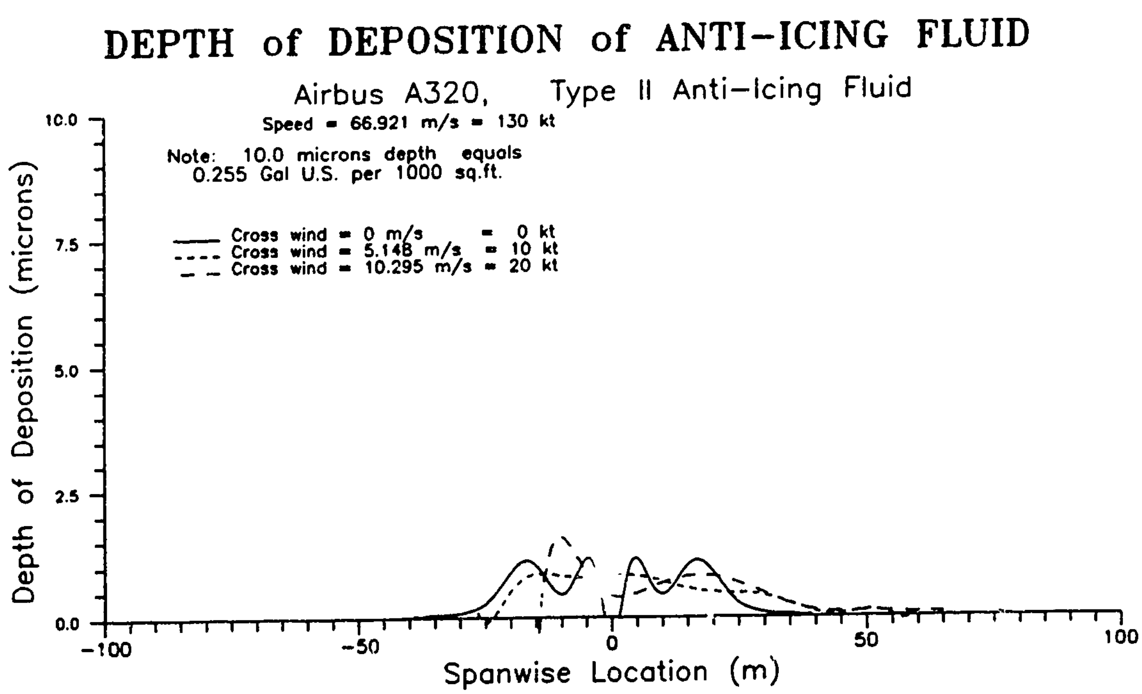

Figure 5.63 Depth of Deposition, Airbus A320, Speed = 66.921 m/s, Type II Anti-Icing Fluid.

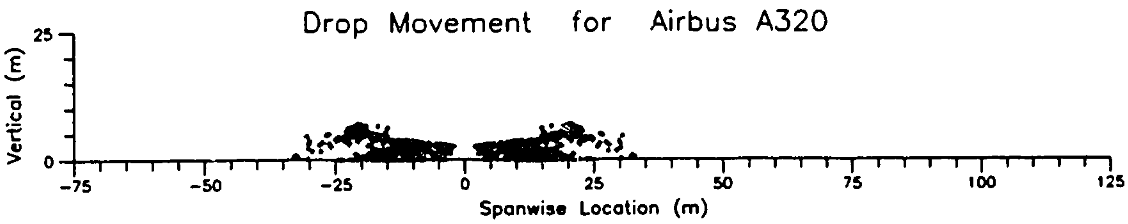

Figure 5.64 Drop Movement, Airbus A320, Speed = 38.608 m/s, Crosswind = 0 m/s, Type II Anti-Icing Fluid.

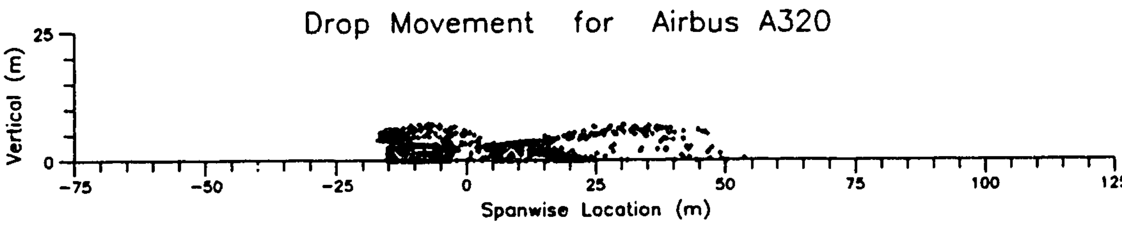

Figure 5.65 Drop Movement, Airbus A320, Speed = 38.608 m/s, Crosswind = 5.148 m/s, Type II Anti-Icing Fluid.

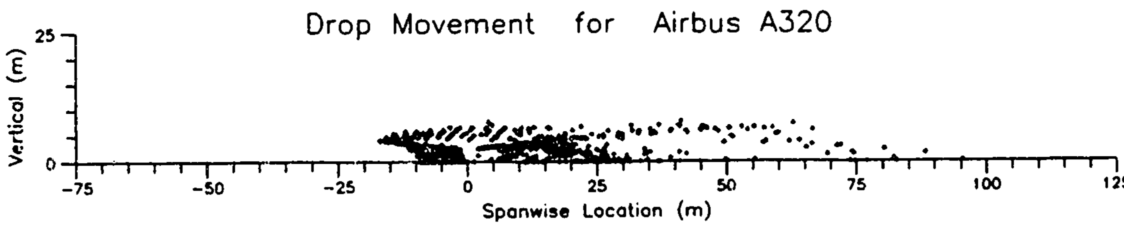

Figure 5.66 Drop Movement, Airbus A320, Speed = 38.608 m/s, Crosswind = 10.295 m/s, Type II Anti-Icing Fluid.

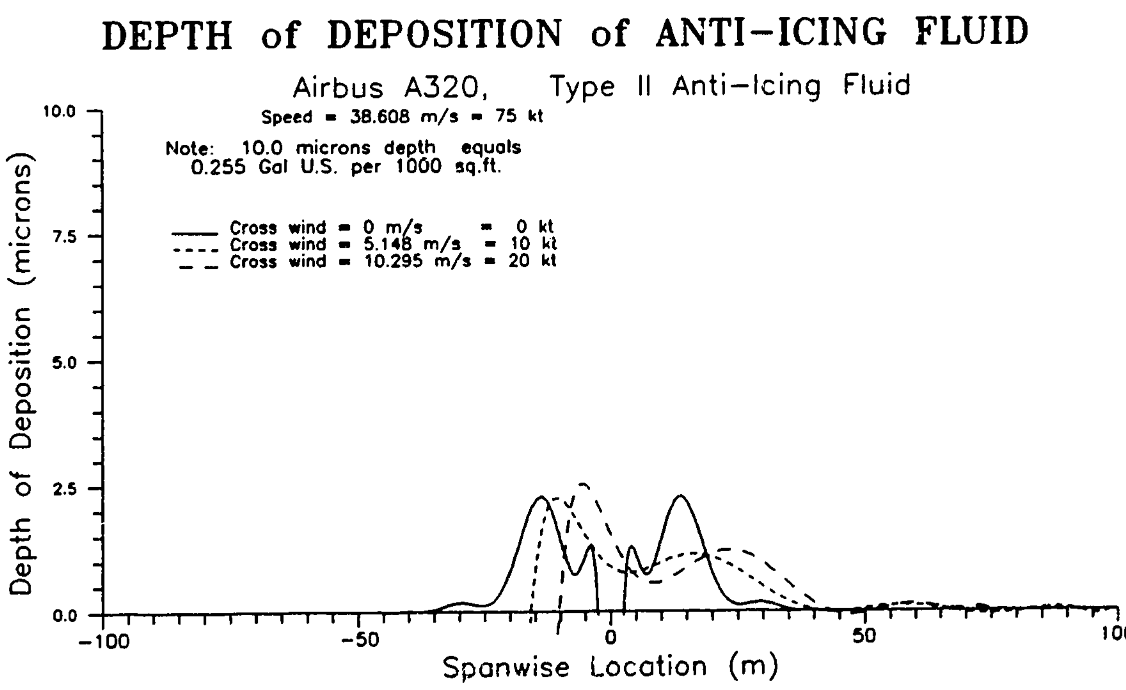

Figure 5.67 Depth of Deposition, Airbus A320, Speed = 38.608 m/s, Type II Anti-Icing Fluid.

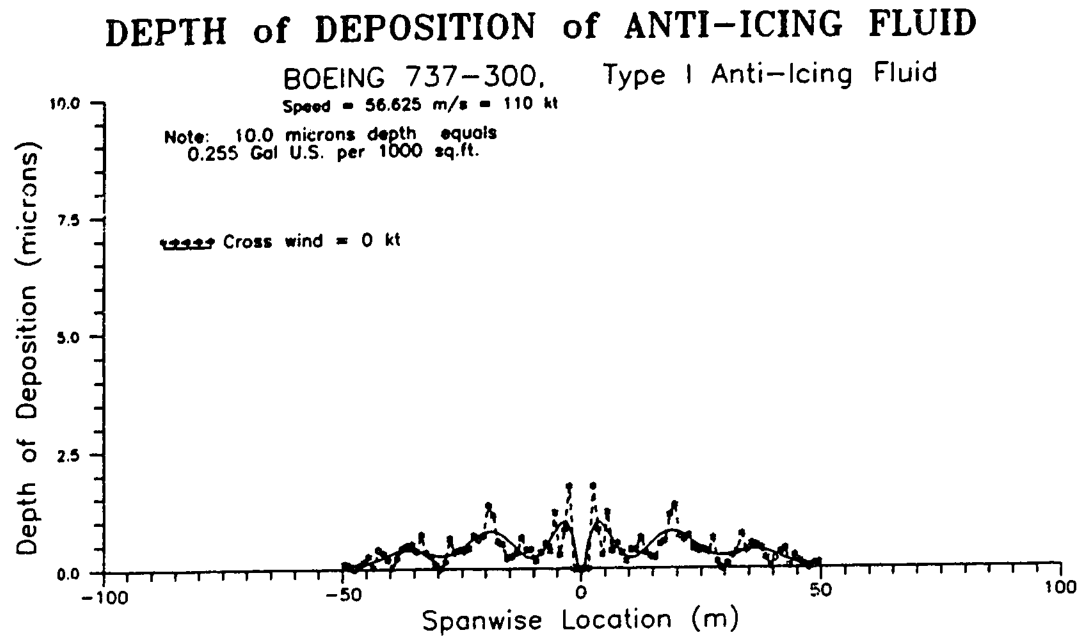

Figure 5.68 Spanwise Deposition, BOEING 737-300, Speed = 56.625 m/s, Crosswind = 0 kt, Type I Fluid.

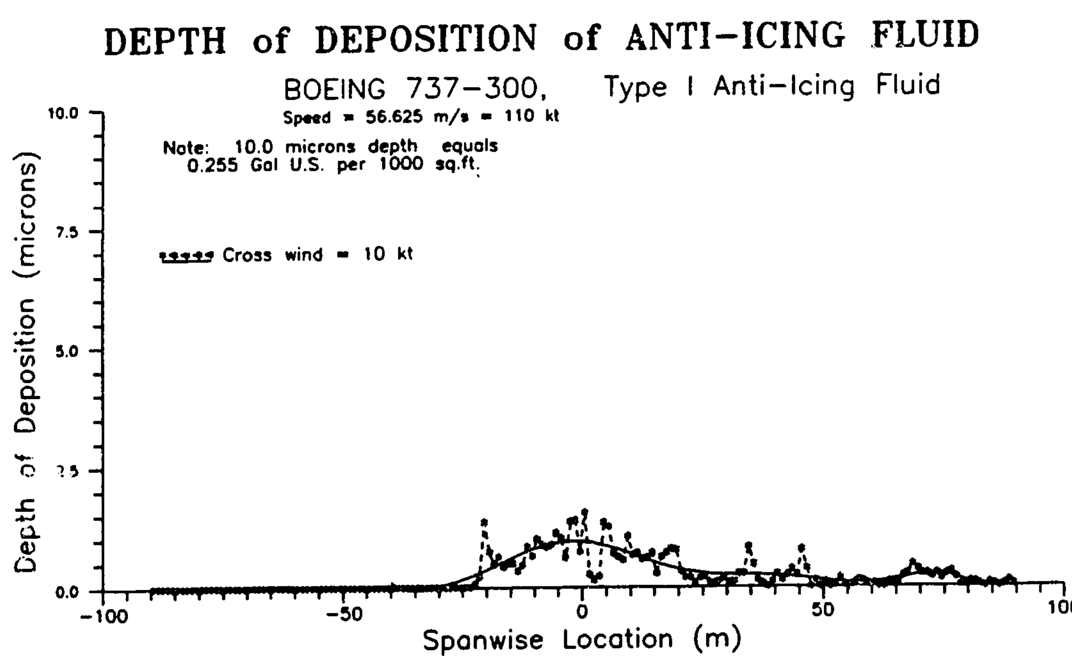

Figure 5.69 Spanwise Deposition, BOEING 737-300, Speed = 56.625 m/s, Crosswind = 10 kt, Type I Fluid.

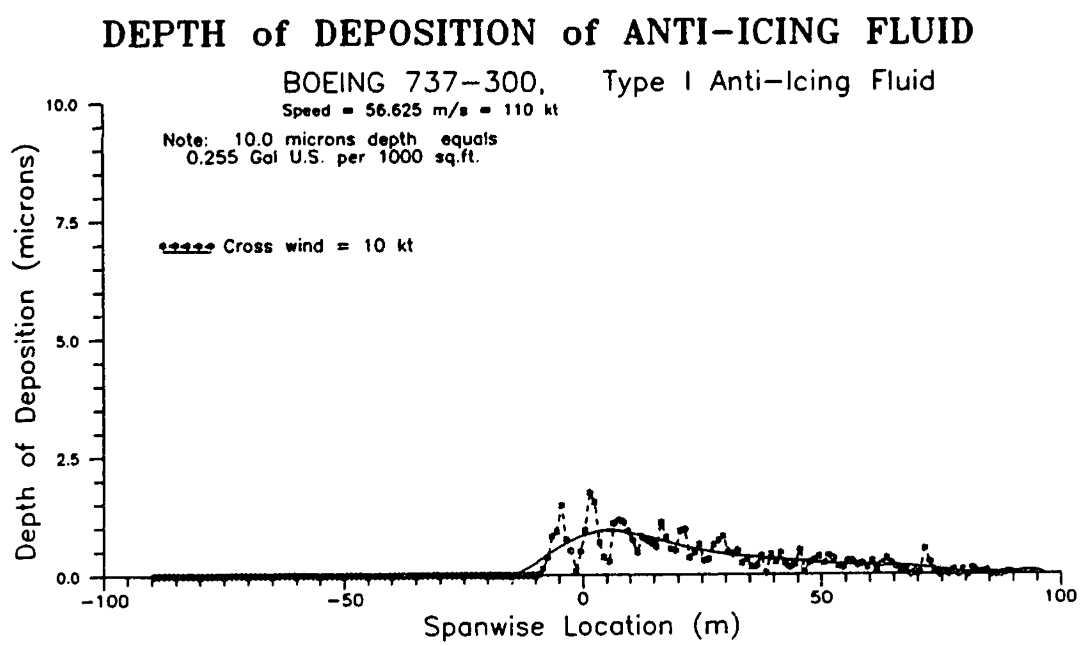

Figure 5.70 Spanwise Deposition. BOEING 737-300. Speed = 56.625 m/s. Crosswind = 20 kt. Type I Fluid.

APPENDIX 5.A. DROP SIMULATION ASSUMPTIONS

Much of this section is similar to the work of Merkl (1989).

Drag Theory As Applied To Droplets

The theory for drag on droplets has been quite well developed in the past few decades. This has been the result of research for the application of sprays using nozzles, and as a result of the desire to improve understanding of the formation and development of clouds in the atmosphere. For the purposes of this study certain assumptions are made about the anti-icing fluid droplets themselves. The majority stem from the fact that most droplets of concern with anti-icing fluid are less than 1000 microns in diameter. Others are more related to the movement of the mass of the anti-icing fluid droplets after departure from the wing.

Forces on a Drop and Drop Acceleration

There are two forces on the droplet which dominate its motion, that due to gravity and that due to drag. The forces on droplets due to static pressure gradients can be neglected for aerial spraying since, in general, the small diameter of the drops result in negligible static pressure differences across the droplet. Hence the droplet movement is determined by these two forces and the inertia of the droplet. Gravity has the obvious effect of pulling the drop toward the ground. The drag force on the drops tend to move the drops along with the local airflow. The resultant drag force, F_D, on the droplet is due to the relative velocity of the droplet with respect to the air, V_{rel}.

$$F_D = \frac{1}{2}\,\rho_{air}\,V_{rel}^2\,A\,C_D \tag{5.A.1}$$

where ρ_{air} is the air density, A is the cross-sectional area of the droplet, and C_D is the droplet drag coefficient. The total drag can be split into the component forces. These component forces acting on a spray droplet as defined here are in the cartesian reference frame, the axes of which are coincident with those for the aircraft and droplet computer model.

$$F_{Dx} = \frac{1}{2}\,\rho_{air}\,V_{xrel}\,V_{rel}\,A\,C_D \tag{5.A.2}$$

$$F_{Dy} = \frac{1}{2}\,\rho_{air}\,V_{yrel}\,V_{rel}\,A\,C_D \tag{5.A.3}$$

$$F_{Dz} = \frac{1}{2}\,\rho_{air}\,V_{zrel}\,V_{rel}\,A\,C_D \tag{5.A.4}$$

where $V_{x\,rel}$, $V_{y\,rel}$, and $V_{z\,rel}$ are the component velocities of the droplet relative to the air. As well it should be noted that C_D is a function of the Reynolds number, R_e, in which velocity used is the resultant relative velocity of the droplet with respect to the air, V_{rel}.

$$C_D = f\,(R_e) \tag{5.A.5}$$

When gravity is considered, the resultant force on a drop of mass, m, may be broken into its three component forces, giving the components of the acceleration of the drop as follows.

$$a_x = \frac{F_{Dx}}{m} \tag{5.A.6}$$

$$a_y = \frac{F_{Dy}}{m} \tag{5.A.7}$$

$$a_z = \frac{F_{Dz} - mg}{m} \tag{5.A.8}$$

Spherical drop shape assumption

The droplets which are being considered are generally less than 1000 microns and are assumed to remain perfectly spherical in shape and, consequently, behave as rigid spheres. In agreement with this, the assumption also is made that the fluid in the drop itself undergoes no significant circulation. This would be important with larger droplet sizes, as the motion of the fluid adjacent to the surface could alter the air movement around the droplet and hence the drag of the droplet. Very closely linked to the fluid circulation, is the assumption that the droplets do not oscillate between oblate and prolate spheroids, as would be the case of larger droplets close to the point of release from a nozzle or the edge of a plate or the trailing edge of a wing. According to Hughes and Gilliland (1952), this is considered to be quite realistic for drops under the 1000 micron diameter range.

Note that the Type II anti-icing fluids produce drop diameters in the 1000 μm range, however only slight changes in the drag coefficient would occur. The non-spherical condition is neglected since the error introduced for that assumption is small in light of other approximations made in determining the size of the fluid drops. Consequently, the fluid drops can be treated as rigid spheres which simplifies the calculation of the drag coefficient of each drop, C_D. Under that assumption,

$$C_D = f(R_e) = f\left(\frac{\rho_{air} V_{rel} D_{drop}}{\mu_{air}}\right) \tag{5.A.9}$$

Drag Coefficients Of Droplets

The topic of drag coefficients of drops has been the subject of a significant amount of research. The first major work was done by Eisner (1930). Since the quality of his work was so high, his work has thereafter been referred to as the benchmark with which to compare most other studies. The shortfall of his work is that it was purely graphical in form. Hence, much work has been done to verify Eisner's work and to develop mathematical formulations for the drag coefficients for given intervals of Reynolds numbers.

Perhaps the most detailed and carefully done work has been that of Beard and Pruppacher (1969). They used a "well designed and controlled wind tunnel" (Mason, 1971) to study droplet movement for the purposes of cloud studies. Their formulation and development resulted in equations, determined by the least squares method at the 95 percent confidence level (regression coefficient = 0.95), as follows:

$$\frac{F_D}{F_{Ds}} = \frac{C_D}{C_{Ds}} \qquad \textbf{(5.A.10)}$$

$$= \frac{C_D\, R_e}{24} \qquad \textbf{(5.A.11)}$$

$$= 1 + 0.010\, R_e^{0.955}\ , \quad 0.2 \le R_e \le 2.0 \qquad \textbf{(5.A.12)}$$

$$= 1 + 0.115\, R_e^{0.802}\ , \quad 2.0 \le R_e \le 21 \qquad \textbf{(5.A.13)}$$

$$= 1 + 0.189\, R_e^{0.632}\ , \quad 21 \le R_e \le 400 \qquad \textbf{(5.A.14)}$$

where F_{Ds} = Stoke's drag, N, and C_{Ds} = Stoke's drag coefficient.

$$C_{Ds} = \frac{24}{R_e} \qquad \textbf{(5.A.15)}$$

In their work, Beard and Pruppacher (1969) showed that droplets do, in fact, remain spherical to $R_e \le 200$, and to a very good approximation also to $R_e \le 400$. This confirmed the assumption of spherical droplets which is made for drop modelling purposes.

For Reynolds numbers less than 50000, a formula developed by Langmuir and Blodgett (1946) commonly has been accepted,

$$\frac{F_D}{F_{Ds}} = 1 + 0.197\, R_e^{0.63} + 0.00026\, R_e^{1.38}\ , \quad 0 \le R_e \le 50000 \qquad \textbf{(5.A.16)}$$

Again, the droplets are assumed to be spherical and rigid even though many of the larger ones, for this range of Reynolds numbers, will actually be oblate spheroids according to Marshall (1954), and Hughes and Gilliland (1952).

Actually, there is some difference between the values of the drag coefficient as obtained by Langmuir and Blodgett (1946), and by Beard and Pruppacher (1969) in the interval for the Reynolds number up to 400. The more recent studies by Beard and Pruppacher (1969) apparently give more accurate formulas relating drag coefficients to Reynolds numbers for Reynolds numbers up to 400. Their work dealing with terminal velocities and Reynolds numbers compares more favorably with the Eisner curve across the range of values of concern than that of Langmuir and Blodgett (1946). However, Langmuir and Blodgett (1946) presented the formula for higher Reynolds numbers as well, hence the formula of Langmuir and Blodgett is used for $R_e \ge 400$. In the less certain region, $200 \le R_e \le 400$, linear interpolation between the two equations has been used in the computer model to avoid any discontinuity in the equation representing the drag coefficient in that interval.

For Reynolds numbers greater than 50000 the value

$$C_D = 0.500 \qquad \textbf{(5.A.17)}$$

is used, since an examination of the Eisner curve readily reveals that the drag coefficient does not change much from this value for Reynolds numbers up to about 2 x 10^5. At higher Reynolds numbers the departure is greater, but Reynolds numbers in this range will be of little concern for the topic at hand.

(Figure 2.2 of) Merkl (1989) shows the plot of the Eisner curve as well as the relation for C_D versus R_e used in the model. The correlation was seen to be very good in the range of Reynolds numbers of concern with anti-icing fluids. Some differences occurred between the curves at the higher Reynolds numbers (i.e. $R_e \geq 50000$) but is of little concern for the study at hand where typically $R_e \leq 500$.

Some typical values of D_o along with the C_D and R_e corresponding to the terminal velocities, are included in Table 5.A.1.

Table 5.A.1 Drop Diameters, Drag Coefficients, R_e and Terminal Velocity.

D_o (μm)	C_D	R_e	Terminal Velocity (m/s)
50	96.094	0.257	0.075
100	15.779	1.791	0.260
200	4.199	9.819	0.713
300	2.424	23.746	1.150
400	1.672	44.008	1.598
500	1.293	69.937	2.031
1000	0.691	270.441	3.928

Acceleration Effects on Drag Coefficients of Drops

Lapple and Shepherd (1940) were among the first to estimate drop movement and the time for a drop to decelerate from high initial velocity (as from a spray nozzle for spray seperation processes) to terminal velocity considering the instantaneous drag coefficient. However, they make no effort to explain the effects of deceleration on the drag coefficient.

As noted by Hughes and Gilliland (1952), the effects of acceleration on particles are most apparent at low Reynolds numbers. Although probably not a major concern here, it is worthwhile to note the rationale since there still may be some effect. As a fluid particle accelerates (decelerates) the flow pattern around the drop must vary continuously. The Eisner curve, the accepted norm, gives C_D versus R_e for steady state flow conditions. The flow around a drop at any point in time, especially as a drop is decelerating when first released from a wing, takes time to change. Hence, the flow is never actually in the steady state mode represented by the Eisner curve. Thus, the flow regime is always lagging behind what the steady state flow would be at the same instantaneous R_e. As the drag coefficient increases with decreasing R_e, it is apparent then that the drag coefficient at any time will be lower than that predicted by the instantaneous R_e. Hence, the C_D in the steady state case will tend to under predict the C_D of a decelerating drop. However, this is a very small amount and not entirely known, therefore the influence of the deceleration of the drop is neglected for calculations of the C_D.

Air Entrainment with Drop Stream and Drop Mutual Interference

Next, considering the droplet release from the wing, there can be observed a certain amount of entrainment of the air mass with the movement of the spray itself. This entrainment could cause significantly lower drag effects on the droplet near the point of release, where the stream of fluid leaving the wing is still relatively concentrated. Once the stream has proceeded further away from the wing there will be enough spreading of the stream to no longer cause any significant entrainment effects. Since this phenomena would be difficult to model accurately, and may be of negligible importance in this particular application, the assumption has been made that the entrainment effects are not significant at any point during droplet motion.

Similarly, the assumption is made that each droplet of fluid leaving the wing is acted on independently of all other droplets. This means that the wake of one droplet does not affect the movement of the next droplet. This simplifies the individual droplet drag calculations so that each droplet is treated as being the only droplet in the wake.

Apparent Acceleration Due To Evaporation

The concept of apparent acceleration due to evaporation from droplets was considered. For a full discussion of this phenomenon the reader is referred to Merkl (1989). For the present case, since most use of anti-icing fluid occurs during atmospheric conditions of high relative humidity and the fluid absorbs water, the evaporation from the fluid drops would be very small. Hence, the apparent acceleration due to evaporation was neglected in this model.

Evaporation From Drops

poration and Drop life

The concern of this section is that of the prediction of the life of a droplet of pure water under given conditions of evaporation. The drop life predictions are based on drops under free fall conditions, at terminal velocity. This is reasonable since droplets in the size range of concern will be moving at only slightly greater velocities behind the aircraft than they would at terminal velocity in free fall conditions (Ormsbee and Bragg, 1978).

Trayford and Welch (1977) have given a method to calculate the drop life and the diameter of a droplet at any time after formation.

$$\tau = \frac{D_o^2}{\beta \ \Delta T} \tag{5.A.18}$$

where, τ = droplet life, s, ΔT = wet bulb depression, °C, D_o = initial diameter, m, Pr = Prandtl number = 0.72, R_e = Reynolds number, and $\beta = 84.76\ (1.0 + 0.3\ Pr^{1/3}\ R_e^{1/2}) \times 10^{-12}$.

The Prandtl number has been shown to remain nearly constant at 0.72 for air over the temperature range 250 K to 1000 K (Ranz and Marshall, 1952a and 1952b). Here, the Reynolds number is that for the terminal velocity of the droplet at the initial diameter and density in a free fall state.Hence, this drop life is that for a drop which is continuing to fall at the terminal velocity corresponding to its instantaneous diameter.

Manning and Gauvin (1960) considered the problem of heat and mass transfer from decelerating, finely atomized sprays. They concluded that, if the feedwater temperature is not too different from the wet bulb temperature, the droplet will reach the wet bulb temperature within approximately 13 mm from the nozzle. Hence, it is reasonable to use the wet bulb depression of the air to give a measure of the mass transfer from a spray droplet. If the drop remained at a temperature different from the wet bulb temperature of the air, the droplife could not be based on the wet bulb depression.

Next, knowing the drop life, the drop diameter at any time after formation can be determined (Trayford and Welch, 1977).

$$\frac{D}{D_o} = (1 - \frac{t}{\tau})^{1/2} \tag{5.A.19}$$

where, t = time since formation of drop, s, and D = diameter of drop at time t, m.

Walton and Walker (1970) have given a treatment of the drop diameter at any time, similar to that of Trayford and Welch (1977) but in a slightly different form. These can be shown to be equivalent (Merkl, 1989).

(Figure 2.3 from) Merkl (1989) shows that at ΔT the time to reach $D/D_o = 0.5$ for most water drops is sufficiently large so as to be of no concern in conditions for anti-icing fluid usage. The figure showed, that drops with $D_o = 200$ would take about 25 s to evaporate and that drops with $D_o = 500$ would take about 90 s to evaporate. Also, results from Merkl (1989) showed that, for normal aerial spray conditions conducted at an aircraft height of near one half wingspan, most drops with D_o near to, or greater than, about 200 μm would hit the ground within approximately 2 seconds.

Effects of Impurities on Evaporation Rates

A considerable uncertainty in the evaporation rate of a water-based drop may develop due to the content of glycol or other less volatile or non-evaporating liquids in a spray. The problem exists because of the various possible distributions of the impurities throughout the droplet. This may range from the liquid moving to the surface, being evenly distributed throughout the droplet, or being confined inside and away from the droplet surface. However, again due to the high humidity conditions accompanying anti-icing fluid usage this concern is neglected for this model.

APPENDIX 5.B WAKE MODEL OPERATION

Program Input

The VORTINFO data set provides information on the aircraft geometry, i.e. the chord, sweep, twist, $dC_l/d\alpha$, C_{l_0}, and $C_{l_{max}}$ all as a function of spanwise location.

The program V-CSM-34.04L was used for all calculations of the aircraft loadings and vortex wake development. The program WAK7794T.FOR was used for all calculations of fluid droplet movement. The required input data is entered when the program are executed. As the programs run, the information is input for the aircraft geometry, the aircraft operation, atmospheric conditions and the fluid droplet statistics.

The needed information is entered via four data files. The first file contains the information about the aircraft and its operation, thus is appropriately labelled VORTINFO. The second file called VDATA1 is output from the previous program and contains the information concerning the vortex wake development. The third file is called SPRAYIN.DAT and contains the required information regarding the droplet, and pertinent atmospheric conditions. The fourth file is called WAKEINPU and contains information regarding anti-icing drop release locations, the numbers of drops, and other information.

Program Output

A complete file of data regarding the conditions for the particular run is written into a file called SPRAYOUT.DAT.

If droplet trajectories, velocities, drag coefficients, and Reynolds numbers for individual droplets are desired, the file DROPDATA.DAT will have the information regarding the individual droplet written to it. The file DROPLOC.DAT gives the just drop locations every 0.25 sec and the final drop position for each droplet.

Another file SWATHDIS.DAT has written into it the droplet distribution over the entire swath width. This information is recorded both on the basis of the volume as well as the number of droplets at each of the spanwise stations, in increments as given in the input (usually 1.0 m).

Lastly, the file UNIFORMT.DAT has written to it the drop distributions. Also given is the measure of uniformity, the amount of fluid (both number of drops and volume of spray) which is not lost from recovery area, and the amount of fluid not evaporated.

Depth of deposition on the runway is calculated by the program DEPTHDEP.BAS. This program gives the conversion for the depth of deposition across the runway for the aircraft velocity and the mass flow-off rate. The output file is SWATHDEP.OUT.

APPENDIX 5.C AIRCRAFT DATA and STATISTICS

Airbus A320 Information and Statistics

From the Airbus A320 Maintenance Manual, and the Airbus A320 Aircraft Operations Manual.
(some also from Jane's All the World's Aircraft 1993-94, pp 118-120.)

Exposed Wing Area, flaps retracted, calculated based on the statistics given in the VORTINFO data file.

Take-off conditions given here are considered to be 0° OAT, 2000 ft Pres. Alt., and dry runway.

Fuselage width at wing:	3.950 m (12 ft 11.5 in)
Wing Span:	33.91m (111 ft 3 in)
Wing Dihedral:	5.11° (0.08919 rad)
Wing chord at centerline:	7.0694 m (23 ft 2.3 in)
Wing chord at root:	6.07 m (19 ft 11 in)
Wing chord at tip:	1.50 m (4 ft 11 in)
Wing Area Gross:	122.4 m^2 (1317.5 ft^2)
Wing Area Exposed, Flaps Retracted	99.19 m^2 (1067.7 ft^2)
Wing Aspect Ratio:	9.4
	(A_R based on gross wing area)
Wing Root Height at Centerline:	2.67 m
	(measured from figure in Airbus Maintenance Manual)

Max Landing weight:	64,500 kg (142,195 lb)
Max T-O weight (Standard):	73,500 kg (162,040 lb)
Modelled T-O weight:	70,000 kg (154,324 lb)
Max wing loading (Standard):	600.5 kg/m^2 (123.0 lb/ft^2)

T-O Stall speed, 15° flaps down, gear up, at modelled T-O weight

V_s = 66.92 m/s (130.0 kt or 14[illegible].7 mph)

T-O Safety speed, 15° flaps down, at modelled T-O weight

V_2 = 65.89 m/s (128 kt or 147.4 mph)

T-O Rotation speed, 15[illegible]s down, at modelled T-O weight

V_R = 61.41 m/s (119.3 kt or 137.4 mph)

T-O Ground Roll speeds modelled, 15° flaps down, at modelled T-O weight

38.608 m/s (75 kt or 86.4 mph)

66.9205 m/s (130 kt or 149.7 mph)

VORTINFO file for Airbus A320:

```
38.60800  686463.500  2.6700  2.6700  1.9750
 4
 0.08919  7.06940  0.00000
 0.43633  0.06388  6.10000  1.70000  4.00000
 0.08919  6.07000  1.97500
 0.43633  0.06388  6.10000  1.70000  4.00000
 0.08919  3.76000  6.54000
 0.43633  0.06388  6.10000  1.70000  4.00000
 0.08919  2.27083 13.40600
 0.43633  0.06388  6.10000  0.50000  3.00000
 0.08919  1.50000 16.96000
 0.43633  0.06388  6.10000  0.25000  2.50000
  1   1
 1.57080  0.75000  0.37500  0.80000
 0.00000  0.00000  6.10000  0.25000  2.00000
 0.03000
 45  35  10
  1  45   1
 0.00010  0.10000 20.00000
```

Note: At the stall speed given above (130 kt), the Maximum Lift Coefficient based on the exposed wing area is:

$$C_{Lmax} = L \,/\, \tfrac{1}{2}\, \rho\, V_s^2\, S = 2.52$$

Note that this is in fair agreement with the data shown in Figure 4 of Flaig and Hilbig (1992) which shows the Airbus A320 producing a C_{Lmax} = 2.5 - 2.6. Hence, the approximated areas and spanwise loading seems reasonable.

BOEING 737-300 Information and Statistics

From the BOEING 737-300 Maintenance Manual, and the BOEING 737-300 Operations Manual. (some also from Jane's All the World's Aircraft 1993-94, pp 441-443.)

Exposed Wing Area, flaps retracted, calculated based on the statistics given in the VORTINFO data file.

Take-off conditions given here are considered to be 0° OAT, 2000 ft Pres. Alt., and dry runway.

Fuselage width at wing:	3.6190 m (11 ft 10.5 in)
Wing Span:	29.03 m (95 ft 3 in)
Wing Dihedral:	6.00° (0.10472 rad)
Wing chord at centerline:	7.318 m (24 ft 0.1 in)
Wing chord at root:	4.71 m (15 ft 5.6 in)
Wing chord at tip (theoretical):	1.621 m (5 ft 3.8 in)
Wing Area (gross):	105.4 m^2 (1135.0 ft^2)
Wing Area Exposed, Flaps Retracted	83.01 m^2 (893.5 ft^2)
Wing Aspect Ratio:	7.91
(A_R based on gross wing area)	
Wing Root Height at Centerline:	2.21 m (7 ft 3 in)
(measured from figure in BOEING 737-300 M.M.)	

Max T-O weight (Basic):	56,472 kg (124,500 lb)
Modelled T-O weight:	47,000 kg (103,617 lb)
Max wing loading (All models):	575.6 kg/m^2 (117.9 lb/ft^2)

T-O Stall speed, 15° flaps down, gear up, at modelled T-O weight

V_s = 54.82 m/s (106.5 kt or 122.6 mph)

T-O Safety speed, 15° flaps down, at modelled T-O weight

V_2 = 65.89 m/s (128 kt or 147.4 mph)

T-O Rotation speed, 15° flaps down, at modelled T-O weight

V_R = 61.41 m/s (119.3 kt or 137.4 mph)

T-O Ground Roll speeds modelled, 15° flaps down, at modelled T-O weight

38.608 m/s (75 kt or 86.4 mph)

56.625 m/s (110 kt or 126.7 mph)

VORTINFO file for BOEING 737-300D:

```
56.62507  460912.550  2.2100  2.2100  1.8095
 5
0.10472  7.31800  0.00000
0.43633  0.01745  6.10000  2.00000  4.00000
0.10472  4.01000  4.85100
0.43633  0.00000  6.10000  2.00000  4.00000
0.10472  2.50600  10.59200
0.43633  0.00000  6.10000  0.50000  3.00000
0.10472  1.80400  13.25900
0.43633  0.00000  6.10000  0.25000  3.00000
0.10472  1.62100  14.22400
0.43633  0.00000  6.10000  0.25000  2.50000
0.10472  0.69600  14.51600
0.43633  0.00000  6.10000  0.25000  2.00000
 0  0
0.02000
45  45  0
 1  45  1
0.00010  0.10000  20.00000
```

Note that this gives Aircraft $C_L \cong 1.90$. Therefore, rotation angle of $\sim 8°$ to produce $C_L \cong 2.32$ necessary for take-off at this speed (110 kt). This is within the acceptable angles for rotation at take-off.

Note: At the stall speed given above (106.5 kt), the Maximum Lift Coefficient based on the exposed wing area is:

$$C_{L_{max}} = L \; / \; \tfrac{1}{2} \, \rho \, V_s^2 \, S = 3.02$$

Note that this is in fair agreement with the data shown in Figure 4 of Flaig and Hilbig (1992) which shows the BOEING 737 producing a $C_{L_{max}} \simeq 2.8 - 2.9$. Hence, the approximated areas and spanwise loading seems reasonable.

BOEING 737-200 Information and Statistics

This is given since it was some of the only complete information available to determine complete aircraft performance for one of the represented aircraft.

(From Jane's All the World's Aircraft 1974-75, pp 283-285.)

Wing Span:	28.35m (93 ft 0 in)
Wing Dihedral:	6.00° (0.10472 rad)
Wing chord at root:	4.71 m (15 ft 5.6 in)
Wing chord at tip:	1.60 m (5 ft 3 in)
Wing Area Gross:	91.05 m^2 (980 ft^2)
Wing Aspect Ratio:	8.83
Wing Root Height at Centerline:	2.21 m (measured from figure)
Max landing weight (All models):	46,720 kg (103,000 lb)
Max T-O weight (All models):	52,390 kg (115,500 lb)
Max wing loading (All models):	575.6 kg/m^2 (117.9 lb/ft^2)
Stall speed, flaps down, at max landing weight	49.67 m/s (179 km/h; 111 mph; 97 kt)
T-O Stall speed, flaps down, at max T-O weight	??.?? m/s

This gives, for the aircraft as a whole, in *Landing condition*,

$$C_{Lmax} = L \,/\, \tfrac{1}{2}\,\rho\, V^2\, S$$

$$= (46{,}720\text{ kg})(9.80\text{ m/s}^2) \,/\, (\tfrac{1}{2})(1.2256\text{ kg/m}^3)(49.67\text{ m/s})^2\,(91.05\text{ m}^2)$$

$$= 3.326 \quad \text{(Landing at Max landing weight.)}$$

This is a complete aircraft C_{Lmax}, therefore since the outboard wing sections at the ailerons would not be producing this high C_L locally, it is reasonable to assume that the inboard flapped stations will produce greater than $C_L = 3.326$ locally. Note that for *landing* the aircraft may deploy greater flap deflection in order to achieve a greater C_{Lmax} even though the trailing vortex drag would be greater. Therefore, it seems reasonable that for the take-off condition, the C_{Lmax} would not be as great as for the landing condition given above. For the purposes of this report, at take-off condition the assumption will be that local wing sections may achieve not greater than $C_{Lmax} = 4.0$.

BOEING 747 Information and Statistics:

Most information taken from the BOEING 747 Maintenance Manual and the BOEING 747 Aircraft Operations Manual.
(and some from Jane's All the World's Aircraft 1993-94, pp 443-446.)

Exposed Wing Area, flaps retracted, calculated based on the statistics given in the VORTINFO data file. Note that the wing area (gross) given in the BOEING 747 Maintenance Manual is 5500 ft^2 (511 m^2) appears to be the area of the wing including that area extending into the fuselage, but not including the area of the triangle composing the root strengthening region at the trailing edge (i.e. take the outboard trailing edge of the wing and project it to the centerline).

Take-off conditions given here are considered to be 0° OAT, 2000 ft Pres. Alt., and dry runway.

Fuselage width at wing:	6.5024 m (21 ft 4 in)
Wing Span:	59.6392 m (195 ft 8 in)
Wing Dihedral:	7.00° (0.12217 rad)
Wing chord at centerline:	16.516 m (54 ft 2.2 in)
Wing chord at root:	14.623 m (48 ft 1 in)
Wing chord at tip:	4.064 m (13 ft 4 in)
Wing Area (gross):	511.0 m^2 (5500 ft^2)
Wing Area Exposed, Flaps Retracted	439.8 m^2 (<5500 ft^2)
Wing Aspect Ratio:	6.96
	(A_R based on gross wing area)
Wing Root Height AGL at Centerline:	3.48 m (measured from figure)

Max T-O weight (most models):	>335,658 kg (>740,000 lb)
Modelled T-O weight:	335,658 kg (740,000 lb)

T-O Stall speed, 10° flaps down, gear up, at modelled T-O weight
V_s = 74.64213 m/s (145 kt. or 167 mph)

T-O Safety speed, 10° flaps down, at modelled T-O weight
V_2 = 89.57 m/s (174 kt or 200.4 mph)

T-O Rotation speed, 10° flaps down, at modelled T-O weight
V_R = 86.22 m/s (167.5 kt or 192.9 mph)

T-O Ground Roll speeds modelled, 10° flaps down, at modelled T-O weight
38.608 m/s (75 kt or 86.4 mph)
77.216 m/s (150 kt or 172.7 mph)

VORTINFO file for BOEING 747:

```
77.21600 3291681.310   3.4800   3.4800   3.2512
 4
 0.12217 16.56160  0.00000
 0.65450  0.03491  6.10000  1.80000  4.00000
 0.12217  9.55220 11.93800
 0.65450  0.03491  6.10000  1.80000  4.00000
 0.12217  6.17270 21.18360
 0.65450  0.03491  6.10000  0.50000  3.00000
 0.12217  4.40390 28.32100
 0.65450  0.03491  6.10000  0.25000  3.00000
 0.12217  4.06400 29.81960
 0.65450  0.03491  6.10000  0.25000  2.50000
  0  0
 0.00000
 42  42   0
  1  42   1
 0.00010  0.10000 20.00000
```

Note: At the stall speed given above (145 kt), the Maximum Lift Coefficient based on the exposed wing area is:

$$C_{L\max} = L \,/\, \tfrac{1}{2}\,\rho\, V_s^2\, S = 2.19$$

Note that this is in fair agreement with the data shown in Figure 4 of Flaig and Hilbig (1992) which shows the BOEING 747 producing a $C_{L\max} \simeq 2.2$ - 2.3. Hence, the approximated areas and spanwise loading seems reasonable.

Note that for *landing* the aircraft may deploy greater flap deflection in order to achieve a greater $C_{L\max}$ even though the trailing vortex drag would be greater. Therefore, it seems reasonable that for the take-off condition, the $C_{L\max}$ would not be as great as for the landing condition given above. For the purposes of this report, at take-off condition the assumption will be that $C_{L\max} = 4.0$ for the regions with the leading edge flaps or the leading edge slats, and trailing edge triple slotted flaps.

CHAPTER 6

CONCLUSIONS and FUTURE RESEARCH

SUMMARY of CONCLUSIONS

A simplified vortex lattice method (VLM) has been applied to three different problems in three dimensional aerodynamics. The use of even a simple model was shown to provide additional insight into each problem considered, hence, the VLM can still be considered a useful tool for engineering problems in aerodynamics.

Chapter 2 has reviewed and highlighted studies regarding vortex systems pertaining to lifting wings of moderate to high aspect ratio (6 to 20). The review discussed some vortex methods which have been used to determine aircraft wing loading and the development of the trailing vortex wake. The roll-up of the trailing vortex wake behind a lifting wing was shown to be dependent mostly on the spanwise wing loading. The development of the trailing vortex wake within ground effect was discussed.

The literature was also reviewed concerning the design of winglets for the use on the wing tips of aircraft. This review has shown that a significant amount of research has been done regarding winglet design. Most notably the revival of winglet research was prompted by Whitcomb's work published in 1976. Somewhat surprising is that throughout all of the research that has been done the question still remained as to exactly how winglets provide the drag reduction which they do produce. This uncertainty was the reason for the investigation performed for Chapter 3 of this work.

The literature review showed that winglets can be designed and constructed to produce a reduction of the total drag of a wing, hence, the drag reduction mechanism was investigated in Chapter 3. The vortex lattice model was able to provide significant insight into the problem. This study showed that by the proper design and application of winglets, some drag reduction is possible even for wings which were previously considered to be the optimum elliptical loading. The nonplanar winglet addition to a wing was the reason for the improvement of the Lift/Drag ratio by as much as 15% over the "supposed" optimum wing at high lift coefficients.

The investigation has provided insight into the importance of the forward thrust component of the total drag reduction due to a winglet. As well, the induced drag reduction along the span of the main wing winglet was shown to be a significant portion of any drag reduction caused by a winglet. The study has shown that winglets which are very small compared to the main wing tip chord produce most of the drag reduction by the forward thrust mechanism, while larger winglets provide most of the drag reduction by the induced drag reduction along the span of the main wing. The study showed the need to include both components of the induced drag reduction (forward thrust and the induced drag reduction along the span of the main wing) to explain the total drag reduction possible by winglets. Also, the results indicated that the forward thrust component of the drag reduction by a winglet is highly dependent on the main wing C_L. The forward thrust was shown to be 20% to 50% of the total drag reduction on a wing at high C_L, but at low C_L the forward thrust may become negligible or even negative. Thus, the induced drag along the main span of a wing was shown to be the dominant drag reduction mechanism by winglets at low C_L of the main wing. Another of the specific results showed a probable reason for much disagreement about if winglets work or why winglets actually can help on a particular aircraft. The reason is that the percentage improvement in the Lift/Drag ratio by using winglets on a given aircraft is dependent on the C_D-C_L curve for the main wing. The usefulness of this VLM can be to provide information for the design optimization of winglets for a particular aircraft wing.

Closely, related to the problem of aircraft wing loading is the development of the trailing vortex wake. The VLM was used in Chapter 4 to consider this problem. The development of the trailing vortex wake is dependent mainly on the wing spanwise loading. Additionally, the developing trailing vortex core was shown to be dependent on the wing boundary layer thickness which affects the vortex sheet thickness. The size of the developing core of the trailing vortex can be influenced by the vortex sheet thickness, hence the velocity profile through the vortex core was shown to be dependent on the boundary layer thickness. Modelling of the vortex sheet with multiple rows of vorticity has provided new insight into the stretching and thinning of the vortex sheet near the developing core. Also, the vorticity from the upper surface of the wing was seen to roll-up into the developing vortex core at the very beginning of the roll-up sequence, a result which was different from assumptions used by other researchers.

Chapter 5 has examined the problem of determining the deposition of anti-icing fluid on airport runways and adjacent areas. The problem involves the flow-off of anti-icing fluid from aircraft during the take-off ground run. Three specific aircraft were examined which were considered to be the aircraft which would typically be used in Canada during conditions requiring the use of anti-icing fluid. The wing loading and the trailing vortex wake of these aircraft are complex due to the wing slat and flap settings for the take off condition. The study revealed that the movement of anti-icing fluid is significantly affected by the developing wake of the aircraft, as well as any crosswinds during the take-off ground roll. Deposition of fluid on the runway, and especially near the runway centerline, during light crosswinds was seen to increase as compared to the no wind condition. Small span aircraft gave higher percentages of the initial fluid amounts deposited on the runway surface, while larger span aircraft produced greater off runway deposition. The amount of anti-icing fluid deposited on the runway by only a few aircraft was seen to be sufficient to produce a potential for the reduction of the runway friction coefficient.

This research has shown that valuable insight and design information may be gained by the application of a vortex lattice method to problems of three dimensional aerodynamics. Sometimes the abundance of data provided through the opportunity to apply more complicated computer modelling techniques can obscure the ultimate goal of developing insight into the particular problem being analyzed. Clearly, by the careful observation of results there is still much that can be learned by the application of a relatively simple model such as the VLM to these particular areas of aerodynamics.

RECOMMENDATIONS for FUTURE RESEARCH

Some possibilities for future work include the following in line with each of the research areas.

More comprehensive computer modelling of wing and winglet combinations should be done, with the focus on developing a more generalized formula for the drag reduction by a winglet.

This winglet study has been done with the assumption of a rigid wake. Obviously, this does not correspond to the real world situation. Further investigation should be done with the incorporation of a rolling up trailing vortex wake. Results due to both assumptions could then be compared to give the improvement of prediction of the aerodynamics of winglets with a more realistic model. Specifically, any information would be valuable which pertains to the effect on the induced drag reduction components due to including the relaxed wake. Comparisons of the results of this vortex lattice method should be made with a full vortex panel method and even perhaps with more robust CFD methods. Such a comparison would [illegible] whether there is a need for a more complex computer model.

Additionally, wind tunnel modelling of winglet configurations for comparison with computer predictions of winglet effectiveness would help to provide greater confidence in the results of these computer models.

Other applications of this work regarding winglet design include the improvement of aileron effectiveness due to winglet addition especially during the critical flight phase at high C_L near stall conditions of the main wing. The potential for using winglets to enhance aircraft aileron response, and hence flight safety, warrants further research.

The trailing vortex wake hazard to aircraft is still a major concern for air traffic safety. Better understanding of the vortex wake is necessary to tailor aircraft wings and wing tips to reduce that hazard. The vortex sheet roll-up model provided some interesting insight into the vortex sheet stretching and thinning. Wind tunnel work would be useful to provide some more confirmation of the accuracy of this vortex core development, and the effect of a wing boundary layer thickness on the developing vortex core. The effects of winglet addition on wing tips should also be investigated with special notice given to the winglet boundary layer thickness.

This work examined the deposition of anti-icing fluid on runways and adjacent areas. The study showed that significant amounts of fluid land on the runway surface. However, more work needs to be done to determine the effect of anti-icing fluid on an airport runway, especially concerning the runway friction coefficients and the effects on landing aircraft. Also, the ability to predict the deposition and accumulation of anti-icing fluid, which is generally a glycol based fluid, lends itself to the possibility of improved methods of reclaiming the fluid. As well, the environmental impact of off runway deposition should be addressed.